Developing Quantum-Classical Hybrid Interfaces for Solving Realistic Atomic Scale Chemical Problems

Tomoya Shiota

September, 2025

Developing Quantum-Classical Hybrid Interfaces for Solving Realistic Atomic Scale Chemical Problems

A dissertation submitted to
THE GRADUATE SCHOOL OF ENGINEERING SCIENCE
THE UNIVERSITY OF OSAKA
in partial fulfillment of the requirements for the degree of
DOCTOR OF PHILOSOPHY IN SCIENCE

BY

TOMOYA SHIOTA

SEPTEMBER, 2025

Abstract

Quantum computers are expected to offer a new computational paradigm that accelerates and enhances quantum-chemical calculations and machine learning (ML), thereby enabling the understanding and prediction of chemical phenomena at atomic and electronic scales. However, today's quantum computers remain limited by their small number of physical qubits. Even as early fault-tolerant quantum computing (FTQC) or FTQC emerges, classical computing will remain crucial for tasks that do not require quantum resources because of its high clock speeds. Accordingly, applying quantum algorithms to practical chemical problems requires complementary classical algorithms. The quantum–classical hybrid interfaces that bridge quantum and classical computing will play a pivotal role in fully leveraging the potential of quantum computing.

This dissertation builds such a framework. It links high-accuracy results from quantum algorithms to classical methods, such as molecular dynamics simulations and materials informatics. For example, it connects highly-parallelized classical quantum chemistry software with quantum computing. By integrating quantum and state-of-the-art classical computing, it becomes possible to combine more accurate results from quantum computing with existing large-scale classical simulations. This framework enables quantum computing to be applied across a wide range of systems—from single molecules to catalyst surfaces and biological systems. Furthermore, this dissertation introduces methodologies to incorporate quantum-chemical data from quantum computing into materials informatics. We develop a technique for merging datasets obtained from different protocols and demonstrate that quantum-chemical data generated at different levels of theory can be integrated seamlessly. Using the unified quantum chemical dataset, we constructed a single universal ML interatomic potential (MLIP) capable of handling both molecular and crystalline systems. Furthermore, we show that by using the internal representations of the MLIP as novel descriptors, superior quantum ML models can be constructed for properties such as nuclear magnetic resonance chemical shifts and catalytic activity—even when the available qubit count is limited. The developed quantum-classical hybrid interfaces open a way for applying quantum computing to real-world atomic-scale problems without compromising its potential.

Abbreviations

Acronym	Description
1-RDM	One-particle Reduced Density Matrix
2-RDM	Two-particle Reduced Density Matrix
ADF	Amsterdam Density Functional
AEC	Atomization Energy Correction
AIMD	Ab Initio Molecular Dynamics
AO	Atomic Orbital
ASE	Atomic Simulation Environment
BCC	Body Centered Cubic
BFGS	Broyden–Fletcher–Goldfarb–Shanno
BPNN	Behler–Parrinello Neural Network
CAS	Complete Active Space
CASCI	Complete Active Space Configuration Interaction
CASPT2	Complete Active Space Second-Order Perturbation Theory
CBS	Complete Basis Set
CC	Coupled Cluster
CCSD	Coupled Cluster Singles and Doubles
CCSD(T)	Coupled Cluster Singles and Doubles with perturbative Triples
CG	Conjugate Gradient
CI	Configuration Interaction
CISD	Configuration Interaction Singles and Doubles
CM	Coulomb Matrix
CPHF	Coupled Perturbed Hartree-Fock
DF	Density-Fitting
DFT	Density Functional Theory
DLPNO	Domain-based Local Pair Natural Orbital
EDA	Energy Density Analysis
FCC	Face Centered Cubic
FCHL	Faber–Christensen–Huang–Lilienfeld
FeMoco	FeMo cofactor (FeMoco)
FQE	Fermionic Quantum Emulator
FS	Final State
FTQC	Fault-Tolerant Quantum Computing
Full-CI	Full Configuration Interaction

Acronym	**Description**
GAP	Gaussian Approximation Potential
GAPW	Gaussian Augmented Plane Wave
GCN	Generalized Coordination Number
GGA	Generalized Gradient Approximation
GIAO	Gauge-Including Atomic Orbital
GNN	Graph Neural Network
GNN-TL	Graph Neural Network Transfer Learning
GPR	Gaussian Process Regression
GPW	Gaussian and Plane Wave
GTH	Goedecker–Teter–Hutter
GTO	Gaussian-Type Orbital
HEA	High-Entropy Alloy
HF	Hartree–Fock
I-LSE	Improved-LSE
IAP	Interatomic Potential
IAP	Interatomic Potential
ICEA	Inner Core Energy Alignment
IQR	Interquartile Range
IS	Initial State
KRR	Kernel Ridge Regression
LC	Lattice Constant
LDA	Local Density Approximation
LSE	Local Surface Energy
MAE	Mean Absolute Error
MaxAE	Maximum Absolute Error
MBPT	Many-Body Perturbation Theory
MD	Molecular Dynamics
ME	Mean Error
MEP	Minimum Energy Path
meta-GGA	meta-Generalized Gradient Approximation
ML	Machine Learning
MLIP	Machine Learning Interatomic Potential
MLP	Multilayer Perceptron
MM	Molecular Mechanics
MO	Molecular Orbital
MP2	Møller-Plesset perturbation theory at second order
MPn	Møller-Plesset perturbation theory
NMR	Nuclear Magnetic Resonance
NN	Neural Network
NNP	Neural Network Potential
NP	Nanoparticle
NPQC	Natural Parameterized Quantum Circuit
OT	Orbital Transformation
PAW	Projector-Augmented Wave
PBC	Periodic Boundary Condition

Acronym	Description
PBE	Perdew–Burke–Ernzerhof
PES	Potential Energy Surface
PFAS	Per- and Poly-FluoroAlkyl Substances
PQC	Parameterized Quantum Circuit
PW	Plane Wave
QCL	Quantum Circuit Learning
QKRR	Quantum Kernel Ridge Regression
QM	Quantum Mechanics
QM/MM	Quantum Mechanics/Molecular Mechanics
QML	Quantum Machine Learning
QPE	Quantum Phase Estimation
RDF	Radial Distribution Function
RMSE	Root Mean Square Error
SCF	Self-Consistent Field
SOAP	Smooth Overlap of Atomic Positions
STD	Standard Deviation
STO	Slater-Type Orbital
TADF	Thermally Activated Delayed Fluorescence
TEA	Total Energy Alignment
TS	Transition State
TST	Transition State Theory
UCC	Unitary Coupled Cluster
UCCSD	Unitary Coupled Cluster with Singles and Doubles
VASP	Vienna Ab initio Simulation Package
VQA	Variational Quantum Algorithm
VQE	Variational Quantum Eigensolver

Contents

Chapter 1

Introduction

Quantum computers are computing devices that operate according to quantum mechanical principles. They hold the potential to outperform classical machines in certain tasks, including factoring large integers via Shor's algorithm [1, 2], calculating the ground-state energies of molecules and crystals through quantum phase estimation (QPE) [3, 4, 5, 6, 7], and leveraging the exponentially large Hilbert space of qubits for quantum machine learning (ML) [8, 9, 10, 11]. Driven by these expectations, recent years have witnessed notable progress in both quantum hardware [12, 13, 14, 15, 16] and quantum software [17, 18, 19]. Nevertheless, current quantum devices suffer from limited qubit counts and noise, encouraging many researchers to explore quantum-classical hybrid strategies [20, 21, 22]. Even in the era of early fault-tolerant quantum computing (FTQC) or FTQC, classical computing will remain crucial for tasks where quantum computation is not essential, due to its high clock speed [23]. For these reasons, quantum–classical hybrid approaches are indispensable for applying quantum computers to practical problems. In these strategies, the inherently quantum components—those that truly require quantum resources—run on quantum computers, while classical computers handle the remaining tasks.

One of the key motivations for quantum computing has long been addressing the challenges of quantum many-body problems in chemistry and physics [24, 25, 4, 5, 26]. In quantum chemistry, accurately solving the Schrödinger equation is vital for understanding molecular and materials properties. Full configuration interaction (Full-CI), also known as exact diagonalization in physics, solves the Schrödinger equation exactly for a given Hamiltonian. However, its computational cost scales exponentially with system size on classical hardware [27, 28]. In principle, FTQC devices can execute Full-CI in polynomial time [4, 5], thereby enabling the accurate calculation of properties for systems that classical computers have been unable to solve so far. For instance, it is estimated that the ground-state energy of molecules such as FeMo cofactor (FeMoco)—found in the reaction center of a nitrogen-fixing enzyme—and a cytochrome P450 enzyme active site can be computed using QPE within a few days on a superconducting quantum computer with

several million qubits [6, 29]. Despite the constraints of today's noisy quantum processors [18, 30], variational quantum algorithms (VQAs) [17] and other quantum-assisted classical-computing techniques are being actively developed for chemical applications [31, 32, 33, 34, 35].

Although concurrent advances in both quantum hardware and algorithms have made it increasingly feasible to tackle quantum-chemistry problems, significant challenges remain for realistic atomic-scale chemical applications. First, preparing the Hamiltonian to be solved by a quantum algorithm still relies on classical computing, which can become a bottleneck for large-scale or periodic systems [36]. Exploring potential energy surfaces and simulating real-time chemical reactions require many energy and force evaluations [37, 36, 38]. Running all of these evaluations purely through quantum chemistry calculations on a quantum computer is not practical, making it essential to minimize the computational load on quantum processing as much as possible. Second, designing molecules or materials with desired chemical properties requires not only the prediction of energies and forces but also other chemical properties such as nuclear magnetic resonance (NMR) chemical shifts [39] and catalytic activities [40]. Furthermore, the discovery of molecules and materials necessitates efficiently exploring vast chemical spaces [41]. To address the challenges of predicting various chemical properties and efficiently exploring vast chemical spaces, materials informatics—integrating computational chemistry with ML—has emerged as a powerful approach [42]. Research aimed at solving chemical problems with quantum ML is beginning to emerge [43, 44]. However, constructing practical quantum ML models on today's quantum computers requires the development of input descriptors that are both accurate and compact.

In this dissertation, we attempt to develop quantum–classical hybrid interfaces that seamlessly bridge state-of-the-art classical computing with quantum computing, thereby opening a practical route to solving realistic atomic-scale chemical problems. One key technological component toward this goal is a framework that interfaces a highly parallelized low scaling classical quantum chemistry software with quantum computing. Another essential element involves leveraging ML interatomic potentials (MLIPs) [45, 46, 47, 48, 49]—an interdisciplinary advance between computational chemistry and ML—as a platform for making productive use of quantum calculations and as an interface to quantum ML for materials informatics. By learning the large amount of energies from the Schrödinger equation, MLIPs can effectively avoid solving the Schrödinger equation directly. As a result, they can provide near-quantum-chemical accuracy for energies and forces at speeds orders of magnitude faster than traditional quantum chemistry calculations. To incorporate the high-accuracy quantum-chemical data produced on quantum computers into MLIPs alongside existing large quantum-chemical datasets [50], we propose a protocol that integrates quantum-chemical data obtained from different electronic-structure methods. Moreover, to enable MLIPs to serve as inputs for quantum ML on today's limited-qubit quantum computers, we explore repurposing their intermediate information as compact descriptors. By combining these interfaces, we aim to seamlessly integrate quantum computing for quantum chemistry

and materials informatics—both of which have evolved at the intersection of computational chemistry, quantum information, and ML.

Dissertation Overview

Chapter 2: Preliminaries

We offer a unified perspective on computational chemistry, quantum computing, and ML, laying the quantum–classical hybrid interfaces developed in this dissertation. First, we introduce the fundamentals of quantum computing (Section 2.1). We then briefly review the basis of quantum chemical calculations, contrasting classical and quantum algorithms while highlighting their respective limitations (Section 2.2). Finally, we explore how ML techniques, including both classical and quantum methodologies, are employed to predict molecular and materials properties, and we outline the current challenges and opportunities in these areas (Section 2.3).

Chapter 3: Integrating Classical and Quantum Software for Enhanced Quantum Chemical Simulation of Realistic Chemical Systems

We develop practical implementations that link a classical high-peformance-computing quantum chemistry software with quantum circuit emulators, enabling efficient evaluation of chemical systems ranging from water clusters and semiconductor surfaces to biological enzymes. This approach combines large-scale force computation and Hamiltonian preparation in a parallelized classical computing with quantum subroutines for quantum classical hybrid algorithms. We demonstrate that the classical computations required for running quantum–classical hybrid algorithms have low scaling in this framework.

Chapter 4: Taming Multi-Domain,-Fidelity Data: Towards Foundation Models for Atomistic Scale Simulations

We develop a method to combine quantum chemical calculation data from various sources in preparation for the future era of quantum computing. When FTQC becomes available, it will likely produce small but highly accurate energy datasets due to its high computational costs. It will, therefore, be essential to develop methods that effectively integrate such high-quality data with existing classical calculations. To this end, we develop an integration method by proposing a total energy alignment (TEA) approach that can combine data from various computational sources (e.g., density functional theory (DFT), coupled cluster (CC) methods, Full-CI and so on). We discuss new dataset integration techniques and universal MLIPs, with examples involving molecular and crystalline systems. This chapter covers integration of multiple data sources, MLIP training, and the resulting performance in energy evaluations.

Chapter 5: Universal Neural Network Potentials as Descriptors: Towards Scalable Chemical Property Prediction Using Quantum and Classical Computers

To build practical quantum ML models that can predict diverse chemical properties on today's small-qubit quantum computers, we propose a new compact descriptor—the graph neural network (GNN) transfer learning (GNN-TL) descriptor—derived from pre-trained GNN-based MLIPs. Conventional high-accuracy descriptors that capture the local environments of atoms in molecular and crystalline systems typically scale quadratically with the number of chemical elements, so descriptors that cover most of the periodic table. We show that GNN-TL descriptors, extracted from a variety of pre-trained MLIPs, match the predictive power of state-of-the-art descriptors for NMR chemical shift prediction while remaining compact. Furthermore, a quantum kernel model implemented with only ten qubits achieves performance on par with its classical kernel counterpart, demonstrating that accurate, descriptor-based quantum ML is feasible even on current limited qubit quantum computer.

Chapter 6: Lowering the Exponential Wall: Accelerating High-Entropy Alloy Catalysts Screening using Local Surface Energy Descriptors from Neural Network Potentials

To demonstrate how MLIPs combined with quantum computing can accelerate materials discovery, we develop local surface energy (LSE) descriptors to screen high-entropy alloy (HEA) catalysts—one of today's most challenging material classes because of their vast compositional space. We illustrate that LSE-based predictions can drastically reduce computational costs, enabling large-scale screening of adsorption energies. Then, we demonstrate that quantum ML with a small number of qubits can improve prediction accuracy with a small amount of the training data. Furthermore, we compare conventional descriptor-based models in terms of accuracy.

Chapter 7: Conclusions

We conclude this dissertation with a discussion of future directions.

Chapter 2

Preliminaries

This chapter introduces preliminary concepts that span computational chemistry [36], quantum computing [51], and machine learning (ML) [52], laying the foundation for the quantum–classical hybrid interfaces developed in this dissertation. Although each field has historically advanced through largely independent trajectories, recent studies highlight that their integration fosters new approaches to overcoming computational limitations.

Quantum computing opens the possibility of polynomial-time solutions to electronic structure problems in quantum chemistry that are otherwise intractable on classical computers [53, 28, 27]. The synergy between computational chemistry and ML has led to materials informatics to accelerate atomistic simulations [54, 55, 46, 56, 48] and the digital screening of candidates for new materials [41, 57, 58] without using quantum chemical calculations. Quantum ML uses superposition and entanglement to enhance ML algorithms [8, 59, 11].

In Section 2.1, the fundamentals of quantum computing are introduced. In Section 2.2, the basics of quantum chemical calculations using classical and quantum algorithms are explained. Then, we explain the current limitations of both classical and quantum algorithms. In Section 2.3, we present ML approaches for predicting atomic- and molecular-scale phenomena as well as associated chemical properties. The section also provides an overview of classical and quantum ML and examines their respective challenges.

2.1 Fundamentals of Quantum Computing

2.1.1 Qubit and Quantum Gates

Quantum computing exploits quantum mechanical phenomena, such as superposition and entanglement, aiming to solve certain computational problems that are intractable for classical computers. In contrast to the classical bit, which can only take values in $\{0, 1\}$, quantum computers employ the quantum bit, commonly called a qubit, as their fundamental units of computation. A qubit is a two-level quantum system. Mathematically, the state of a qubit $|\psi\rangle$ is

represented as a normalized state vector in a two-dimensional complex Hilbert space. Typically, $|0\rangle$ and $|1\rangle$ form an orthonormal basis, so that

$$|\psi\rangle \;=\; \mu\,|0\rangle \;+\; \nu\,|1\rangle, \quad \text{where} \quad |\mu|^2 + |\nu|^2 = 1. \tag{2.1}$$

Here, $\mu, \nu \in \mathbb{C}$ are the complex probability amplitudes, and the squared magnitudes $|\mu|^2$ and $|\nu|^2$ can be interpreted as measurement probabilities in the respective basis states. In a two-dimensional complex Hilbert space, the basis vectors $|0\rangle$ and $|1\rangle$ can be written explicitly as:

$$|0\rangle = \begin{pmatrix} 1 \\ 0 \end{pmatrix}, \quad |1\rangle = \begin{pmatrix} 0 \\ 1 \end{pmatrix}. \tag{2.2}$$

When multiple qubits are considered together, they can exist in general superpositions of tensor products of single-qubit basis states. For example, the state of an n-qubit system all initialized to $|0\rangle$ is expressed as $|0\rangle^{\otimes n}$. Moreover, multiple qubits can become entangled, meaning that the global state cannot be expressed as a product of individual qubit states.

A quantum computer performs computations by applying quantum gates on qubits. The operations allowed in a quantum computer are linear transformations of the state vector. Quantum gate operations on qubits are all described by unitary operators. Single-qubit gates such as the Pauli operators X, Y and Z are among the most basic and commonly used:

$$X \;=\; \begin{pmatrix} 0 & 1 \\ 1 & 0 \end{pmatrix}, \quad Y \;=\; \begin{pmatrix} 0 & -i \\ i & 0 \end{pmatrix}, \quad Z \;=\; \begin{pmatrix} 1 & 0 \\ 0 & -1 \end{pmatrix}. \tag{2.3}$$

Each of these matrices is both unitary and Hermitian, with eigenvalues ± 1. For instance, the X gate swaps the states $|0\rangle$ and $|1\rangle$, analogous to the classical NOT gate operation, while the Z gate imparts a phase of -1 to the state $|1\rangle$. The Y gate applies a bit flip combined with a phase i. By combining these gates, one can perform arbitrary rotations on the Bloch sphere, effectively navigating the entire space of single-qubit states. Another fundamental single-qubit gate is the Hadamard gate which transforms $|0\rangle$ into $\frac{1}{\sqrt{2}}(|0\rangle + |1\rangle)$ and $|1\rangle$ into $\frac{1}{\sqrt{2}}(|0\rangle - |1\rangle)$. Furthermore, phase shift gates such as S gate and T gate introduce specific complex phases to $|1\rangle$, playing a crucial role in universal gate sets [60, 61]. To operate on multiple qubits, it is necessary to use controlled gates. A representative example is the CNOT (Controlled-NOT) gate, defined by the 4×4 matrix

$$\text{CNOT} \;=\; \begin{pmatrix} 1 & 0 & 0 & 0 \\ 0 & 1 & 0 & 0 \\ 0 & 0 & 0 & 1 \\ 0 & 0 & 1 & 0 \end{pmatrix}, \tag{2.4}$$

which applies the X gate to the target qubit if and only if the control qubit is in the state $|1\rangle$. By employing controlled gates, one can generate and manipulate entanglement, which is essential for quantum computing. It is known that any desired unitary operation can be composed from only a small set of one-qubit and

two-qubit gates [62, 63]. The minimal collections that allow such approximations to arbitrary precision are called universal gate sets. A canonical example is the three-element gate set $\{\text{Hadamard}, T, \text{CNOT}\}$, which is a universal gate set capable of approximating any quantum operation with arbitrary accuracy [60, 61].

As seen above, quantum computing can be performed by applying quantum gate operations to qubits. Quantum algorithms are described as sequences of quantum gates, i.e., quantum circuits. Some of them can accelerate tasks that are intractable for classical computers.

2.1.2 Variational Quantum Algorithms

Variational quantum algorithms (VQAs) [17] combine quantum and classical computing in a hybrid optimization loop. Despite the severe limitations on circuit depth and qubit count, they can still operate to some extent on today's noisy quantum devices. A VQA optimizes an n-qubit parameterized quantum circuit (PQC), $U(\boldsymbol{\theta})$, which has variational parameters $\boldsymbol{\theta}$. A PQC (whose circuit structure is often referred to as the ansatz) generates an n-qubit parameterized quantum state $|\Psi(\boldsymbol{\theta})\rangle$:

$$|\Psi(\boldsymbol{\theta})\rangle = U(\boldsymbol{\theta})|0\rangle^{\otimes n}. \tag{2.5}$$

One typical definition of a cost function $C(\boldsymbol{\theta})$ in a VQA is the expectation value of an observable O related to the problem, which is measured on the quantum processor:

$$C(\boldsymbol{\theta}) = \langle 0|^{\otimes n} U^{\dagger}(\boldsymbol{\theta})\, O\, U(\boldsymbol{\theta})|0\rangle^{\otimes n} = \langle \Psi(\boldsymbol{\theta}) \mid O \mid \Psi(\boldsymbol{\theta})\rangle. \tag{2.6}$$

A classical optimizer then updates $\boldsymbol{\theta}$ to minimize $C(\boldsymbol{\theta})$. The updated parameters are subsequently fed back into the PQC, and this cycle is repeated until convergence. Repeating this cycle converges to $\boldsymbol{\theta}^*$, which optimizes the cost function. In this dissertation, two VQA-based methods are applied. The first is variational quantum eigensolver (VQE) [64], widely used in quantum chemistry for estimating ground state energies of molecules and materials. The second is quantum circuit learning (QCL) [9], which employs VQAs for ML tasks.

2.1.3 Quantum Phase Estimation Algorithm

Quantum phase estimation (QPE) is an algorithm that estimates the phases of the eigenvalues of a given unitary matrix U as binary fractions. [3] If $|\Psi\rangle$ is an eigenstate of unitary matrix U, we have the eigenvalue equation

$$U\,|\Psi\rangle = e^{2\pi i\gamma}\,|\Psi\rangle, \tag{2.7}$$

with a phase γ in the range $0 \leq \gamma < 1$. The goal of QPE is to estimate the phase γ with high precision using finite number of qubits. In Kitaev's original QPE algorithm [3], n-qubit phase register and an m-qubit system register are required. One initializes the phase register in $|0\rangle^{\otimes n}$ and the system register in

the eigenstate $|\Psi\rangle$. After all operations in QPE, the state of the phase register encodes the phase of the eigenvalue of a given unitary U:

$$|0\rangle^{\otimes n} \otimes |\Psi\rangle \rightarrow |\tilde{\gamma}\rangle \otimes |\Psi\rangle. \tag{2.8}$$

If γ has an exact n-bit representation, then the phase-register state $|\tilde{\gamma}\rangle$ encodes the n-bit exact binary fraction of the phase γ. Otherwise, the phase-register state $|\tilde{\gamma}\rangle$ encodes an approximation using the n-bit binary fraction of γ. Finally, one measures the phase register $|\tilde{\gamma}\rangle$, obtaining an n-bit string which represents an estimate of γ. QPE is especially important for addressing large-scale eigenvalue problems that cannot be efficiently solved on classical computers alone. Consequently, QPE serves as a fundamental subroutine in various quantum algorithms, including Shor's factoring algorithm [1] and quantum chemical calculations [4, 5].

2.2 Quantum Chemical Calculations

2.2.1 Electronic Structure Theory

In the chemistry of molecules and materials, one can understand various properties by solving fundamental equations of quantum mechanics. At the atomic level, where interactions among electrons and nuclei are crucial, one typically solves the basic equations of quantum mechanics—specifically, the non-relativistic, time-independent Schrödinger equation—to obtain the system's wave function and its corresponding eigenenergy. The Schrödinger equation for an N-atom, n-electron system can be written in compact form as:

$$H\Psi(\mathbf{r},\mathbf{R}) \;=\; E\,\Psi(\mathbf{r},\mathbf{R}), \tag{2.9}$$

where H is the Hamiltonian operator of the system, $\Psi(\mathbf{r},\mathbf{R})$ is the eigenfunction (eigen wave function) depending on the electronic coordinates (including spin coordinates) $\mathbf{r} = \{\mathbf{r}_i\}_{i=1}^{n}$ and the nuclear coordinates $\mathbf{R} = \{\mathbf{R}_I\}_{I=1}^{N}$ and E is the eigenenergy.

For a non-relativistic system, the Hamiltonian is commonly expressed in the following form, using the atomic units introduced below (with T_{n} as nuclear kinetic energy operator, T_{e} as electronic kinetic energy operator, V_{nn} as nuclear–nuclear interaction, V_{ee} as electron–electron interaction, and V_{en} as electron–nuclear interaction),

$$\begin{aligned} H = &\underbrace{-\sum_I \frac{1}{2M_I}\nabla^2_{\mathbf{R}_I}}_{T_{\mathrm{n}}} \quad \underbrace{-\sum_i \frac{1}{2}\nabla^2_{\mathbf{r}_i}}_{T_{\mathrm{e}}} \\ &+\underbrace{\sum_{I<J}\frac{Z_I Z_J}{|\mathbf{R}_I-\mathbf{R}_J|}}_{V_{\mathrm{nn}}} + \underbrace{\sum_{i<j}\frac{1}{|\mathbf{r}_i-\mathbf{r}_j|}}_{V_{\mathrm{ee}}} - \underbrace{\sum_{i,I}\frac{Z_I}{|\mathbf{r}_i-\mathbf{R}_I|}}_{V_{\mathrm{en}}}, \end{aligned} \tag{2.10}$$

where M_I is the nuclear mass in units of the electron mass, and Z_I is the nuclear charge. By atomic units, we mean that the following fundamental constants are set to unity:

$$\hbar \;=\; m_{\mathrm{e}} \;=\; e \;=\; 4\pi\varepsilon_0 \;=\; 1. \tag{2.11}$$

Here, $\hbar$ is the reduced Planck constant, m_{e} is the electron mass, e is the elementary charge, and ε_0 is the permittivity of free space. In these units, factors of $\hbar$, m_{e}, e, and $4\pi\varepsilon_0$ do not appear explicitly, leading to the simplified Hamiltonian shown above.

Because electrons and nuclei differ greatly in mass, it is standard to separate their motions via the Born-Oppenheimer approximation. In this approach, the nuclei are assumed to be fixed, with their coordinates $\mathbf{R}$ treated as constants. Consequently, the nuclear kinetic-energy operator T_{n} is neglected, and the nuclear–nuclear repulsion V_{nn} is treated as a constant that depends only on the fixed nuclear coordinates $\mathbf{R}$. By common convention, V_{nn} is omitted when formulating the electronic Hamiltonian, so one solves:

$$H_{\mathrm{e}}\Psi_{\mathrm{e}}(\mathbf{r};\mathbf{R}) \;=\; \big(T_{\mathrm{e}} + V_{\mathrm{ee}} + V_{\mathrm{en}}\big)\,\Psi_{\mathrm{e}}(\mathbf{r};\mathbf{R}) \;=\; E_{\mathrm{e}}(\mathbf{R})\,\Psi_{\mathrm{e}}(\mathbf{r};\mathbf{R}), \tag{2.12}$$

where $\Psi_{\mathrm{e}}(\mathbf{r};\mathbf{R})$ is the electronic wave function for fixed nuclear coordinates $\mathbf{R}$, and $E_{\mathrm{e}}(\mathbf{R})$ is the resulting electronic energy excluding the nuclear–nuclear repulsion. To obtain the total energy of the system at a given $\mathbf{R}$ (still ignoring nuclear motion), one then adds the nuclear–nuclear repulsion:

$$E_{\mathrm{tot}}(\mathbf{R}) \;=\; E_{\mathrm{e}}(\mathbf{R}) \;+\; V_{\mathrm{nn}}(\mathbf{R}). \tag{2.13}$$

This function $E_{\mathrm{tot}}(\mathbf{R})$ is referred to as the potential energy surface (PES). Analysis of PES enables the discussion of molecular structure, stability, and reaction pathways. For example, by examining the PES using quantum chemical calculations, one can predict whether a chemical reaction will occur via transition state theory (TST). [65, 66]. According to the Eyring equation of TST, the reaction rate at temperature T is proportional to $\exp(-\Delta E/(k_B T))$, where ΔE is the activation-energy barrier and k_B is the Boltzmann constant [65]. For example, at 300 K, the reaction rate for $\Delta E = 20$ kcal/mol differs appreciably—by roughly a factor of five—from that for $\Delta E = 21$ kcal/mol. In contrast, when ΔE increases from 20 kcal/mol to 30 kcal/mol, the reaction rate can drop by seven orders of magnitude. Because the reaction rate is highly sensitive to ΔE, an accuracy of about 1 kcal/mol is required for quantitatively reliable predictions of chemical reactivity. This level of accuracy is commonly referred to as "chemical accuracy" [67].

2.2.2 Classical Algorithms

2.2.2.1 Wave Function Methods

The principal goal in quantum chemistry is to solve Equation (2.12) numerically, to predict properties such as the total energy and the related properties. Since

exact solutions are only feasible for very simple systems (e.g., the hydrogen atom), any general many-electron system inevitably requires approximate methods.

Approximate computational methods in quantum chemistry can be broadly classified into perturbation theory and variational methods. In perturbation theory, one begins with a Hamiltonian that can be solved easily and then treats the electron–electron correlation as a small perturbation, typically using Rayleigh-Schrödinger perturbation theory (e.g., Møller-Plesset perturbation theory (MPn) methods). By contrast, the variational method defines a trial wave function $\Psi_{\mathrm{e}}(\{\theta_i\})$ that depends on parameters $\{\theta_i\}$ and seeks to minimize the energy functional

$$E_{\mathrm{e}}[\Psi_{\mathrm{e}}] \;=\; \frac{\langle \Psi_{\mathrm{e}} \mid H_{\mathrm{e}} \mid \Psi_{\mathrm{e}} \rangle}{\langle \Psi_{\mathrm{e}} \mid \Psi_{\mathrm{e}} \rangle}. \tag{2.14}$$

Because of the variational principle, the resulting energy can never be lower than the true ground-state energy. The better the trial wave function, the closer one approaches the exact solution.

One of the most fundamental wave function methods in electronic structure theory is the Hartree-Fock (HF) method, which approximates the many-electron wave function by a single Slater determinant $|\Phi_{\mathrm{HF}}\rangle$:

$$|\Phi_{\mathrm{HF}}\rangle \;=\; \frac{1}{\sqrt{n!}} \begin{vmatrix} \psi_1(\mathbf{r}_1) & \cdots & \psi_n(\mathbf{r}_1) \\ \vdots & \ddots & \vdots \\ \psi_1(\mathbf{r}_n) & \cdots & \psi_n(\mathbf{r}_n) \end{vmatrix} \quad ; \quad \langle \psi_i \mid \psi_j \rangle = \delta_{ij}, \tag{2.15}$$

where n is the number of electrons of the system, and $\psi_i(\mathbf{r}_j)$ is the i-th spin-orbital (referred to as a molecular orbital for molecular systems) evaluated at the electronic coordinate (including spin coordinates) $\mathbf{r}_j$ of the j-th electron. Electrons are fermions and therefore obey antisymmetry; the Slater determinant–an antisymmetrized product–is constructed to satisfy this property. The HF scheme treats electron-electron repulsion by assuming each electron experiences the mean-field of the others. In the HF method, the wave function expressed by a single Slater determinant is variationally optimized by solving the Hartree–Fock equation:

$$F(\mathbf{r})\,\psi_i(\mathbf{r}) \;=\; \varepsilon_i\,\psi_i(\mathbf{r}), \tag{2.16}$$

where $F(\mathbf{r})$ is the Fock operator, ε_i is the i-th orbital energy corresponding to the i-th spin-orbital $\psi_i(\mathbf{r})$. For practical calculations, spin-orbitals corresponding to either α or β spin are expressed in terms of one-electron (spatial) basis functions so that each spatial part of spin-orbital $\psi_i(\mathbf{r})$ can be written as $\psi_i(\mathbf{r}) = \sum_{\kappa=1}^{N_{\mathrm{bas}}} c_{\kappa i}\phi_\kappa(\mathbf{r})$, where N_{bas} is the number of basis functions $\{\phi_\kappa(\mathbf{r})\}$, and $c_{\kappa i}$ is the orbital coefficients. The number of spin-orbitals m is $2N_{\mathrm{bas}}$. In a finite basis, the Fock operator becomes a matrix F whose diagonalization yields the orbital energies ε_i. Constructing F typically scales as $O(m^4)$, while its diagonalization scales as $O(m^3)$, making the latter step the main bottleneck in self-consistent field (SCF) HF calculations. HF solution is a mean-field approximation that neglects electron correlation beyond the exchange term. Although HF typically recovers more than 99% of a molecule's total energy, the

remaining 1% can significantly affect energy differences relevant for chemical reactions [36]. Consequently, electron correlation must be taken into account for quantitative predictions at chemical accuracy. Many post-HF methods (e.g., perturbation theory, coupled cluster (CC) theory [68, 69, 70], and configuration interaction (CI) methods) build upon the HF solution.

In the CI method, the many-electron wave function $|\Psi_{\mathrm{CI}}\rangle$ is written as a linear combination of Slater determinants (configurations) built from a single reference determinant using the same set of spin-orbitals:

$$|\Psi_{\mathrm{CI}}\rangle \;=\; C_0\,|\Phi_0\rangle + \sum_{i,a} C_i^a\,|\Phi_i^a\rangle + \sum_{i<j,a<b} C_{ij}^{ab}\,|\Phi_{ij}^{ab}\rangle + \ldots \;=\; \sum_k C_k\,|\Phi_k\rangle, \quad (2.17)$$

where $|\Phi_0\rangle$ denotes the reference configuration, typically taken to be the HF Slater determinant [71, 72]. The singly excited determinant $|\Phi_i^a\rangle$ is constructed by promoting one electron from an occupied spin-orbital i to an unoccupied spin-orbital a. The doubly excited determinant $|\Phi_{ij}^{ab}\rangle$ similarly involves promoting electrons from occupied spin-orbitals i, j to unoccupied spin-orbitals a, b. Higher excitations (triples, quadruples, etc.) follow the same pattern. The CI coefficients $\{C_0, C_i^a, C_{ij}^{ab}, \ldots\}$, collectively denoted $\{C_k\}$, are determined variationally by diagonalizing the electronic Hamiltonian in this configuration space. The resulting wave function corresponds to the solution of the variational principle in Equation (2.14) for the given basis set. The notation $\{|\Phi_k\rangle\}$ represents the complete set of Slater determinants and $\{C_k\}$ the corresponding CI coefficients. In the Full-CI limit, all possible Slater determinants formed by distributing n electrons among m spin-orbitals are included, so the number of configurations scales as $\binom{m}{n}$. As a result, the dimension of the Hamiltonian matrix is on the order of $\binom{m}{n} \times \binom{m}{n}$. Because $\binom{m}{n}$ grows combinatorially with both n and m, this leads to an exponential increase in computational cost, making Full-CI unfeasible for large systems. A straightforward approximation to avoid the exponential cost is the truncated CI method, where the expansion is cut off at a certain excitation level. Truncating the expansion at double excitations is known as CI with singles and doubles (CISD), which scales as $O(m^6)$. However, because truncated CI is not size-consistent, it becomes unsuitable for large systems.

In the CC method, the many-electron wave function $|\Psi_{\mathrm{CC}}\rangle$ is expressed as

$$|\Psi_{\mathrm{CC}}\rangle = e^{T}\,|\Phi_0\rangle = e^{T_1+T_2+T_3+\cdots}\,|\Phi_0\rangle, \quad (2.18)$$

where T is the cluster (excitation) operator that can, in principle, include single T_1, double T_2, triple T_3, and higher excitations [68, 68, 70]. $|\Phi_0\rangle$ is the reference wave function, typically taken to be the HF solution. By incorporating all excitation levels, CC becomes equivalent to the Full-CI limit, but suffers from exponential scaling in computational cost [70]. Hence, practical implementations rely on truncated CC methods such as CC with singles and doubles (CCSD) and CCSD with perturbative triples method CCSD(T), where CCSD scales as $O(m^6)$ with respect to the number of spin-orbitals m and typically offers greater accuracy than CISD due to its exponential ansatz, while remaining size-consistent and thus applicable to larger systems. CCSD(T) augments CCSD

with a perturbative treatment of triple excitations, raising the computational cost to $O(m^7)$; nevertheless, for weakly correlated systems it is known to reach chemical accuracy and is therefore often called the gold standard in quantum chemistry [73]. In this dissertation, CCSD(T) is employed as the reference for the torsional PES of an organic molecule in Chapter 4. Although truncated CC is not variational—meaning the computed energy may lie below the exact ground state if the reference is poor—it retains size-consistency and efficiently captures electron correlation.

2.2.2.2 Active Space Approximation

Despite the formal exactness of the Full-CI approach, its computational cost grows exponentially with the system size, rendering it impractical for most applications. A widely adopted method to mitigate this is the active space approximation, wherein one selects a subset of orbitals, termed the active space, that are most critical for describing strong correlation effects and performs a high-level (near-exact) calculation only in this subset. The remaining orbitals are treated at a simpler level (e.g., kept doubly occupied or unoccupied), thereby dramatically reducing the combinatorial explosion of configurations in Equation (2.17). A prominent example of this strategy is the complete active space configuration interaction (CASCI) method, which performs Full-CI within the chosen active space. By confining the combinatorial expansion to orbitals directly involved in near-degeneracies, bond-breaking processes, or other strong correlation phenomena, CASCI captures the static (strong) electron correlation that arises from multiple, nearly degenerate determinants. However, to achieve quantitative predictions at chemical accuracy, the dynamic correlation outside the active space must also be recovered [74, 75]. For example, many-body perturbation theory (e.g., complete active space second-order perturbation theory (CASPT2) [76]) is widely used to recover the electronic correlation lost through the active space approximation. One should note, however, that CASPT2 is only a second-order perturbative method and does not achieve the quantitative accuracy of CCSD(T).

2.2.2.3 Density Functional Theory

In this section, we introduce density functional theory (DFT), a quantum-mechanical framework that employs the electron density—rather than the many-body wave function—as its fundamental variable. Because DFT strikes a favorable balance between computational accuracy and computational cost, it has become the de facto standard for quantum chemical (first-principles) calculations of molecules and materials. The theoretical foundation of DFT was established by the Hohenberg–Kohn theorem [77], and most modern, practical DFT calculations are based on the Kohn–Sham formulation [78].

The Hohenberg-Kohn theorem [77] states that for a non-degenerate ground state, the external potential $v(\mathbf{r})$ (up to an additive constant) is uniquely determined by the ground-state n-electron density $\rho(\mathbf{r})$. Consequently, every

physical quantity, including the ground-state energy, can be expressed as a functional of $\rho(\mathbf{r})$. For a given external potential $v(\mathbf{r})$, the ground-state energy of the system $E_{\mathrm{e}}[\rho(\mathbf{r})]$ is written as a functional of the ground-state electron density $\rho(\mathbf{r})$:

$$E_{\mathrm{e}}[\rho(\mathbf{r})] = \int v(\mathbf{r})\,\rho(\mathbf{r})\,d\mathbf{r} \;+\; F[\rho(\mathbf{r})]. \tag{2.19}$$

The term $F[\rho(\mathbf{r})]$ is called the universal functional because it does not depend on the specific form of $v(\mathbf{r})$; rather, it reflects the internal contributions to the ground-state energy. More specifically, it is commonly decomposed as

$$F[\rho(\mathbf{r})] \;\equiv\; T[\rho(\mathbf{r})] \;+\; E_{\mathrm{ee}}[\rho(\mathbf{r})], \tag{2.20}$$

where $T[\rho(\mathbf{r})]$ is the kinetic-energy functional of the electrons and $E_{\mathrm{ee}}[\rho(\mathbf{r})]$ accounts for electron-electron interaction. Because $F[\rho(\mathbf{r})]$ does not explicitly depend on the external potential, it is considered universal in the sense that its form remains the same for any choice of $v(\mathbf{r})$. However, while the exact forms of both $T[\rho(\mathbf{r})]$ and $E_{\mathrm{ee}}[\rho(\mathbf{r})]$ are in principle uniquely determined by the ground-state electron density, neither is generally known in closed form.

The Kohn-Sham method is a practical formulation of Hohenberg-Kohn DFT, in which one introduces a set of m one-electron spin-orbitals (so-called Kohn-Sham orbitals) $\{\psi_i(\mathbf{r})\}_{i=1}^{m}$ from a fictitious non-interacting system as auxiliary variables. This approach, commonly referred to as Kohn-Sham DFT, allows for tractable calculations on real materials and molecules. Specifically, the ground-state electron density $\rho(\mathbf{r})$ is reconstructed from the $\{\psi_i(\mathbf{r})\}$ via

$$\rho(\mathbf{r}) \;=\; \sum_{i}^{n} |\psi_i(\mathbf{r})|^2. \tag{2.21}$$

These orbitals are obtained by solving a set of self-consistent equations that have the same mathematical form as the HF method of Equation (2.16) (often called the Kohn-Sham equations). Because orbital orthogonalization scales similarly to the HF method, the computational cost is typically on the order of $O(m^3)$. Using this electron density, the Hohenberg-Kohn universal functional is conventionally written in the form

$$F[\rho(\mathbf{r})] \;=\; T_{\mathrm{s}}[\rho(\mathbf{r})] \;+\; E_{\mathrm{H}}[\rho(\mathbf{r})] \;+\; E_{\mathrm{XC}}[\rho(\mathbf{r})], \tag{2.22}$$

where $T_{\mathrm{s}}[\rho(\mathbf{r})]$ is the kinetic energy of the non-interacting reference system, $E_{\mathrm{H}}[\rho(\mathbf{r})]$ is the classical Hartree energy, and $E_{\mathrm{XC}}[\rho(\mathbf{r})]$ is the electron-electron exchange-correlation functional. In practice, $T_{\mathrm{s}}[\rho(\mathbf{r})]$ is computed from the Kohn-Sham orbitals as

$$T_{\mathrm{s}}[\rho(\mathbf{r})] \;=\; -\frac{1}{2}\sum_{i} \int \psi_i^*(\mathbf{r})\,\nabla_{\mathbf{r}}^2 \psi_i(\mathbf{r})\,d\mathbf{r}, \tag{2.23}$$

and the Hartree energy is given by

$$E_{\mathrm{H}}[\rho(\mathbf{r})] \;=\; \frac{1}{2}\iint \frac{\rho(\mathbf{r})\,\rho(\mathbf{r}')}{|\mathbf{r}-\mathbf{r}'|}\,d\mathbf{r}\,d\mathbf{r}'. \tag{2.24}$$

The exchange-correlation functional $E_{\mathrm{XC}}[\rho(\mathbf{r})]$ accounts for all remaining many-body effects beyond the $v(\mathbf{r})$, $E_{\mathrm{H}}[\rho]$, and $T_{\mathrm{s}}[\rho(\mathbf{r})]$. In principle, if $E_{\mathrm{XC}}[\rho(\mathbf{r})]$ were known exactly, Kohn-Sham DFT would yield the exact ground-state energy for any system.

In order to apply Kohn-Sham DFT for practical studies, the exchange-correlation functional $E_{\mathrm{XC}}[\rho(\mathbf{r})]$ must be approximated. In practice, a variety of approximations have been proposed, such as the local density approximation (LDA), which applies the properties of a uniform electron gas locally, the generalized gradient approximation (GGA), which incorporates gradient information of the electron density, and the meta-generalized gradient approximation (meta-GGA), which uses second-order derivative information [79]. Moreover, hybrid functionals that include a portion of the exact exchange from HF theory have been introduced to improve accuracy, although these often come with higher computational costs [79]. The choice of which functional to employ depends on the target system and the objectives of the calculation, and there is frequently no single best approximation for all cases. Furthermore, systematically improving the accuracy of exchange-correlation functionals remains challenging: progressing from LDA to GGA, meta-GGA, or hybrid functionals does not guarantee uniform improvements in precision across all systems [79, 80]. This is due to the interplay of complex quantum many-body effects and specific structural or material properties, forcing researchers to balance computational cost and reproducibility in selecting the most suitable exchange-correlation approximation.

2.2.2.4 Limitations of Classical Algorithms

Quantum chemistry methods such as Full-CI or CC that include all electronic excitations can, in principle, provide exact solutions within a given basis set. However, their computational cost grows exponentially with system size, rendering them impractical for many chemically relevant systems. DFT could theoretically offer exact ground-state energies if the exact form of the exchange-correlation functional were known. In practice, because the exact functional remains unknown, numerous approximate functionals have been proposed [79]. For example, GGA-based exchange-correlation functionals have demonstrated predictive capability for certain solid-surface reactions [81]. Striking a balance between accuracy and computational expense, DFT has become one of the most widely employed methodologies in quantum chemistry. Despite these successes, DFT struggles to provide reliable predictions for strongly correlated systems such as the FeMo cofactor (FeMoco) cluster in nitrogenase [82]. For example, on the PES of the chromium dimer (Cr_2)—a prototypical transition-metal molecule—the hybrid functional B3LYP overestimates the binding energy by more than 1 eV ($\approx$ 23 kcal/mol) in the binding energy at the experimental bond length of about 1.68 Å, and it even predicts an artificial minimum near Å [83, 84]. CCSD(T) is often called the "gold standard" in quantum chemistry because it reliably achieves chemical accuracy across a wide range of chemical systems. However, as a single-reference method, CCSD(T) is unreliable for

strongly correlated systems where a single Slater determinant does not offer a satisfactory reference state. Furthermore, CCSD(T) does not satisfy the variational principle, sometimes yielding unphysical results such as total energies lower than those predicted by Full-CI in stretched bond regions of diatomic molecules. CASCI can provide a qualitatively correct description of systems if the active space is chosen appropriately. Nonetheless, for strongly correlated systems like FeMoco, a very large active space (e.g., 113 electrons in 152 spin-orbitals) may be required [85]. In contrast, the largest Full-CI calculation performed on a classical computer to date is limited to propane, involving 26 electrons in 46 spin-orbitals [86]. Given these constraints in computational resources and execution time, achieving even a qualitative description of systems such as FeMoco remains prohibitively challenging on classical hardware.

In summary, classical algorithms can provide semi-quantitative accuracy with DFT and even quantitative accuracy with CCSD(T) for weakly correlated systems, yet for large, strongly correlated complexes such as FeMoco they are unable to capture even qualitative features.

2.2.3 Quantum Algorithms

2.2.3.1 Pre-processing for Quantum Algorithms

The electronic Hamiltonian H_e given by Equation (2.12) cannot be handled directly on a quantum computer. In this subsection, we first express the electronic Hamiltonian in terms of creation and annihilation operators through second quantization, then explain how to convert these fermionic operators into Pauli operators for implementation on quantum hardware.

In second quantization, a set of spin-orbitals, $\{\psi_p(\mathbf{r})\}_{p=1}^m$, is required. These spin-orbitals are typically obtained by solving the Hartree-Fock equation of Equation (2.16). The index p labels spin-orbitals, and the corresponding creation and annihilation operators $c_p^\dagger$ and c_p satisfy the anticommutation relations $\{c_i, \hat{c}_j^\dagger\} = \delta_{ij}$ and $\{c_i, c_j\} = \{c_i^\dagger, c_j^\dagger\} = 0$. These relations ensure that the sign change arising from the exchange of fermions (reflecting the Pauli exclusion principle) is correctly incorporated. To write down the Hamiltonian using these operators, it is necessary to pre-compute the one- and two-electron integrals, h_{pq} and h_{pqrs}, respectively. The one-electron integral is defined as

$$h_{pq} = \int \psi_p^*(\mathbf{r}) \left(-\frac{1}{2}\nabla_\mathbf{r}^2 - \sum_I \frac{Z_I}{|\mathbf{r} - \mathbf{R}_I|} \right) \psi_q(\mathbf{r})\, d\mathbf{r}. \tag{2.25}$$

The two-electron integral,

$$h_{pqrs} = \iint \psi_p^*(\mathbf{r}_1)\, \psi_q(\mathbf{r}_1)\, \frac{1}{|\mathbf{r}_1 - \mathbf{r}_2|}\, \psi_r^*(\mathbf{r}_2)\, \psi_s(\mathbf{r}_2)\, d\mathbf{r}_1\, d\mathbf{r}_2, \tag{2.26}$$

accounts for the Coulomb repulsion between electrons, and its specific value depends on the choice of spin-orbitals and the basis functions used. The indices p,

q, r, and s denote spin-orbitals. Employing these integrals, the second-quantized electronic (fermionic) Hamiltonian H_e typically takes the form

$$H_\mathrm{e} = \sum_{p,q} h_{pq}\, c_p^\dagger c_q + \frac{1}{2} \sum_{p,q,r,s} h_{pqrs}\, c_p^\dagger c_r^\dagger c_s c_q. \tag{2.27}$$

This operator is physically equivalent to the (first-quantized) electronic Hamiltonian expressed in the same spin-orbital basis and therefore denoted by the same symbol H_e, as in Equation (2.12).

Because the hardware of a quantum computer naturally implements spin-1/2 operators (Pauli matrices), these fermionic operators cannot be used directly. Consequently, a procedure called fermion-to-qubit mapping is needed to convert the fermionic operators into products of Pauli matrices. The Jordan-Wigner transformation [87] is one of the most straightforward techniques for mapping the fermionic operators $c_p^\dagger$ and c_q into Pauli operators X, Y, and Z. It preserves the necessary anticommutation relations by introducing additional phase factors (strings of Z operators).

Under the Jordan-Wigner transformation, each fermionic operator is represented as

$$c_p^\dagger = \left(\prod_{t=1}^{p-1} Z_t \right) \frac{X_p - iY_p}{2}, \tag{2.28}$$

$$c_q = \left(\prod_{t=1}^{q-1} Z_t \right) \frac{X_q + iY_q}{2}. \tag{2.29}$$

Here, X_i, Y_i, and Z_i act on the i-th qubit, and the product (string) of Z operators is crucial for maintaining the fermionic anticommutation relations. When two fermionic operators are exchanged, they gain a factor of -1. The string of Z operators enforces this sign change within the qubit representation. Then, the second-quantized fermionic Hamiltonian H_e is transformed into a linear combination of Pauli operators—commonly called the qubit Hamiltonian $H_\mathrm{e}^\mathrm{qubit}$. In the Jordan-Wigner transformation, the creation–annihilation-operator terms in the second-quantized Hamiltonian are transformed as follows:

$$h_{pq} c_p^\dagger c_q = \frac{h_{pq}}{4} \left(X_p - iY_p\right) \prod_{t=p+1}^{q-1} Z_t \left(X_q + iY_q\right), \tag{2.30}$$

$$\begin{aligned} h_{pqrs} c_p^\dagger c_r^\dagger c_s c_q = & \frac{h_{pqrs}}{16} \left(X_p - iY_p\right) \\ & \times \prod_{t=p+1}^{r-1} Z_t \left(X_r - iY_r\right) \left(X_s + iY_s\right) \prod_{u=s+1}^{q-1} Z_u \left(X_q + iY_q\right), \end{aligned} \tag{2.31}$$

where $(p < r < s < q)$, though the precise details depend on the chosen basis and indexing. Once written as Pauli operators, the Hamiltonian can be simulated on a quantum computer via its time evolution or by variational methods such as VQE.

While the Jordan-Wigner transformation is conceptually simple and direct, it may introduce long strings of Z operators of length $O(m)$ when acting on m qubits (one qubit per spin-orbital). This can increase circuit depth, making the simulation more difficult on near-term quantum devices. Alternative methods, such as the Bravyi-Kitaev transformation [88], reduce the length of these strings to $O(\log m)$ by distributing the phase factors more efficiently at the cost of a slightly more complicated construction.

2.2.3.2 Variational Quantum Eigensolver for Quantum Chemistry

VQE [64] is a VQA that uses the variational principle to compute the ground-state energy E_e of the electronic Hamiltonian H_e. Concretely, one uses ansatz (PQC) to prepare a parametrized wave function $|\Psi_\mathrm{e}(\boldsymbol{\theta})\rangle$, where $\boldsymbol{\theta}$ represents the variational parameters. According to the previous section, the second-quantized Hamiltonian H_e after a fermion-to-qubit mapping, which is so called qubit Hamiltonian $H_\mathrm{e}^\mathrm{qubit}$, is expressed as

$$H_\mathrm{e}^\mathrm{qubit} = \sum_j h_j \, P_j, \tag{2.32}$$

where each P_j is a tensor product of Pauli operators and $h_j \in \mathbb{R}$ are the corresponding coefficients. The goal is to minimize the energy expectation value

$$E_\mathrm{e}(\boldsymbol{\theta}) = \langle \Psi_\mathrm{e}(\boldsymbol{\theta}) \mid H_\mathrm{e}^\mathrm{qubit} \mid \Psi_\mathrm{e}(\boldsymbol{\theta}) \rangle = \sum_j h_j \, \langle \Psi_\mathrm{e}(\boldsymbol{\theta}) \mid P_j \mid \Psi_\mathrm{e}(\boldsymbol{\theta}) \rangle. \tag{2.33}$$

In other words, VQE solves

$$\boldsymbol{\theta}^\star = \operatorname*{argmin}_{\boldsymbol{\theta}} E_\mathrm{e}(\boldsymbol{\theta}), \tag{2.34}$$

by iteratively updating $\boldsymbol{\theta}$ via a classical optimizer.

In VQE, the choice of ansatz crucially affects both computational accuracy and circuit depth, as it must capture electron correlation efficiently. A prominent chemically motivated ansatz is the unitary coupled cluster (UCC), derived from conventional CC theory [89, 90, 91, 92, 93, 94, 95]. In UCC, a reference state—typically the Hartree–Fock wave function $|\Phi_\mathrm{HF}\rangle$—is transformed by the exponential of an anti-Hermitian operator composed of excitation and de-excitation operators. Specifically, the excitation operator $T = \sum_{i=1}^{n} T_i$ includes up to n-fold electron excitations, where each T_i represents an i-body excitation operator. The overall transformation is then given by $\exp\big(T - T^\dagger\big)$, where $T^\dagger$ denotes the de-excitation operator, which is the Hermitian conjugate of T. In theory, including triple, quadruple, or higher-order excitations systematically improves accuracy, eventually converging to the exact ground state. However, circuit depth and parameter counts grow quickly, making these higher-order expansions challenging for current hardware. For instance, when truncated to single and double excitations (denoted as unitary coupled cluster singles and

doubles, UCCSD), the excitation operators are

$$T_1 = \sum_{i,a} \theta_i^a \, c_a^\dagger c_i, \quad T_2 = \sum_{i<j,a<b} \theta_{ij}^{ab} \, c_a^\dagger c_b^\dagger c_i c_j, \tag{2.35}$$

where i, j label occupied spin-orbitals, a, b label unoccupied spin-orbitals, $c_a^\dagger$ and $c_b^\dagger$ are creation operators, c_i and c_j are annihilation operators, and $\boldsymbol{\theta} = \{\theta_i^a \text{ (all } i, a), \; \theta_{ij}^{ab} \text{ (all } i < j, \; a < b)\}$ are variational parameters.

2.2.3.3 Quantum Phase Estimation for Quantum Chemistry

Full-CI provides the exact solution to the Schrödinger equation for the electronic Hamiltonian of Equation (2.12) within a basis set expansion, but its computational cost grows exponentially with system size, as explained in Section 2.2.2. QPE offers a way to address this issue in polynomial time [4, 5], if an initial wave function that closely matches the target eigenstates (i.e. the ground-state wave function) can be efficiently prepared [96]. In this section, we explain how QPE can be applied to solve the Schrödinger equation for the electronic Hamiltonian and present runtime estimates for implementations on superconducting quantum computers.

Although QPE, as introduced in Section 2.1.3, is designed for unitary operators, most Hamiltonians in quantum chemistry are Hermitian but generally not unitary. Therefore, an additional procedure is necessary to map a Hermitian operator to a form suitable for QPE. A widely adopted strategy is to use the time-evolution operator, which connects the phase to an eigenenergy E_e of the electronic Hamiltonian H_e:

$$e^{-iH_\mathrm{e}t}|\Psi_\mathrm{e}\rangle = e^{-iE_\mathrm{e}t}|\Psi_\mathrm{e}\rangle, \tag{2.36}$$

where t is the evolution time and $|\Psi_\mathrm{e}\rangle$ is the prepared target eigenstate [4, 5, 82]. In general, the electronic Hamiltonian is written as a sum of Pauli operators as shown in Equation (2.32), which often do not commute. Because of this, it cannot be implemented directly in a quantum circuit. To accurately determine ground-state energies via QPE, the time-evolution operator e^{-iHt} must be implemented with high precision. One common approach is the Suzuki–Trotter decomposition [97], which splits the Hamiltonian into multiple parts and approximates the time evolution in small increments. Reducing the step size τ controls the simulation error ϵ, but this increases the number of steps in proportion to $\frac{t}{\tau}$. In many scenarios, this leads to a polynomial increase in complexity with respect to $\frac{1}{\epsilon}$. The growing circuit depth and gate count make it hard to use Trotter-based Hamiltonian simulation.

An alternative approach called qubitization avoids decomposition errors by applying a walk operator,

$$e^{i \arccos\left(\frac{H_\mathrm{e}}{\lambda}\right)}|\Psi_\mathrm{e}\rangle = e^{i \arccos\left(\frac{E_\mathrm{e}}{\lambda}\right)}|\Psi_\mathrm{e}\rangle, \tag{2.37}$$

instead of the time evolution operator [98]. Performing phase estimation on this walk operator provides the same information as the time-evolution operator

because the spectra of these operators are isomorphic. In this approach, λ is the L^1 norm of the electronic Hamiltonian [98]. The computational cost of QPE through Qubitization is proportional to λ, which motivates ongoing efforts to reduce this norm [99, 100, 6].

We now turn to runtime estimates for QPE-based simulations of the FeMoco system. In 2017, Reiher and coauthors estimated that time-evolution-based QPE could be used to calculate the ground-state energy of FeMoco with an active space of 54 electrons and 108 spin-orbitals in about 15 days on a superconducting quantum computer, assuming a 10 ns T-gate cycle [82]. Since then, researchers have deemed that estimate far too optimistic. Updated resource analyses indicate that, even with one million physical qubits, the same calculation would take on the order of 40 years [6]. In 2021, Lee and colleagues applied the low-rank approximation method named the tensor hypercontraction [101, 102, 103] to reduce the L^1 norm of the Hamiltonian, indicating that a larger FeMoco system with an active space of 113 electrons and 152 spin-orbitals could be simulated in roughly four days on a superconducting device [6]. Although progress in quantum computing hardware continues, improvements in algorithms and Hamiltonian representations also play an essential role in making large-scale quantum chemical calculations more tractable and in overcoming the prohibitive cost of Full-CI on classical computers.

2.2.3.4 Limitations of Current Quantum Algorithms

Quantum algorithms, particularly those based on the VQE and QPE for quantum chemical calculations, have been the subject of intensive research but still face significant limitations. Noise in current quantum hardware critically constrains the size of the active space that can be handled by VQE, rendering large-scale calculations impractical at this stage. Although quantum error-correction techniques are expected to mitigate noise problems in the future, they will do so at the expense of substantial resource overhead.

Although theoretical runtime estimates for QPE-based methods have improved, they remain prohibitive in practice. For example, Lee et al. demonstrated that a single energy evaluation for the FeMoco Hamiltonian—incorporating 113 electrons and 152 spin-orbitals active space—could still take several days, making routine simulations time-consuming [6]. Indeed, quantum computing has the potential to address problems that are intractable for classical hardware. However, its computational cost is far from negligible. To make quantum algorithms practically useful, effective strategies must be devised to manage this high cost.

Furthermore, simulating realistic systems—including liquids, solids, and large molecular complexes—requires constructing the relevant Hamiltonian from the HF solution. Even with active-space approximations, constructing the Hamiltonian on classical hardware typically scales as $O(m^4)$ with the number of spin-orbitals m, and thus constitutes a major bottleneck. To enable truly atomistic simulations via quantum algorithms, an efficient quantum–classical hybrid interface for pre- and post-processing is indispensable. This challenge is addressed in Chapter 3.

2.2.4 Potential Energy Surface

As explained in Section 2.2.1, exploring the PES given by Equation (2.13) enables us to predict chemical reactions at the atomic-scale. In this section, we consider a system consisting of N atoms. The PES is a $3N$-dimensional hypersurface that, due to translational and rotational invariance, has $3N-6$ degrees of freedom ($3N-5$ in the case of a linear molecule). For example, the FeMoco molecule, which consists of 39 atoms, has a 111-dimensional PES [82]. As N increases, the dimension of the PES increases, making a manual exhaustive search impractical. To analyze finite-temperature, finite-time reactions at the atomic level, one can track the motion of the nuclei by solving Newton's equations of motion on the PES. This technique is known as molecular dynamics (MD) simulations. Evaluating the negative gradient of the potential energy surface $E_{\mathrm{tot}}(\mathbf{R})$ with respect to the atomic coordinates $\mathbf{R} = \{\mathbf{R}_I\}_{I=1}^N$, that is, the forces acting on each of the N atoms, $\{\mathbf{F}_I\}_{I=1}^N$, is crucial for both of these PES exploration methods. In this section, we will describe the fundamental PES exploration methods, geometry optimization and MD. Furthermore, we will discuss how to evaluate the forces using quantum chemical calculations.

2.2.4.1 Geometry Optimization

In quantum chemical calculations, geometry optimization is a fundamental procedure. This is because the geometries that actually occur correspond to near minima on the PES. The goal of geometry optimization is to find the configuration $\mathbf{R}^*$ that satisfies

$$\mathbf{F}_I = -\left.\frac{\partial E_{\mathrm{tot}}}{\partial \mathbf{R}_I}\right|_{\mathbf{R}=\mathbf{R}^*} = \mathbf{0} \quad \forall I. \tag{2.38}$$

Geometry optimization in quantum chemistry typically employs numerical optimizers that utilize the gradient (i.e., force) information. Concretely, one iteratively updates the geometry based on gradients calculated in various coordinate representations—whether internal, redundant internal, or Cartesian—in order to systematically reduce the total energy of the system. In practice, geometry optimization is often deemed converged when the magnitude of the force on each atom falls below a specified threshold. In this dissertation, the convergence criterion is similarly defined by requiring

$$\|\mathbf{F}_I\|_2 < F_{\max}^{\mathrm{th}} \quad \forall I, \tag{2.39}$$

where $\|\cdot\|_2$ is the Euclidean norm and $F_{\max}^{\mathrm{th}}$ is a user-defined threshold.

2.2.4.2 Molecular Dynamics

In MD simulations, the time evolution of the atomic coordinates can be described by numerically integrating Newton's equations of motion. In standard MD, the PES is typically given by empirical interatomic potentials—referred to

as molecular mechanics (MM). By replacing these empirical potentials with quantum-mechanical (QM) calculations (i.e., quantum chemistry methods), it is called *ab initio* molecular dynamics (AIMD) [104].

The equations of motion solved in MD simulation are written as

$$M_I \frac{d^2\mathbf{R}_I(t)}{dt^2} \;=\; \mathbf{F}_I \;=\; -\frac{\partial E_{\text{tot}}}{\partial \mathbf{R}_I}. \tag{2.40}$$

In MD simulation, atomic positions $\mathbf{R}(t)$ and velocities $\mathbf{v}(t)$ are updated at each time step Δt. In the MD calculations employed in Chapters 3 and 4 of this dissertation, the method used for the time evolution is the Velocity Verlet method [105]. The Velocity Verlet method, derivable via a second-order Taylor expansion of the classical equations of motion, provides second-order accuracy in Δt. To set up the update, one begins by assuming that the force at time t, $\mathbf{F}(t)$, has already been computed. The velocity at t is then obtained from the velocity and force at the previous time $(t - \Delta t)$ according to

$$\mathbf{v}_I(t) \;=\; \mathbf{v}_I(t - \Delta t) \;+\; \frac{1}{2M_I}\left[\mathbf{F}_I(t - \Delta t) + \mathbf{F}_I(t)\right]\Delta t. \tag{2.41}$$

Once $\mathbf{v}_I(t)$ has been established, the positions at $t + \Delta t$ are updated by

$$\mathbf{R}_I(t + \Delta t) \;=\; \mathbf{R}_I(t) \;+\; \mathbf{v}_I(t)\,\Delta t \;+\; \frac{1}{2M_I}\,\mathbf{F}_I(t)\,\Delta t^2. \tag{2.42}$$

2.2.4.3 Force Evaluation

To perform geometry optimization or MD simulations with quantum chemical methods, one must evaluate the atomic forces, i.e., the derivatives of the total energy with respect to atomic positions. A straightforward approach is to use finite-difference numerical derivatives, but this requires multiple energy calculations for each atomic coordinate and can become prohibitively expensive as system size grows. An alternative to finite-difference numerical derivatives is to compute atomic forces analytically. When the wave function $|\Psi_{\text{e}}\rangle$ is fully variational with respect to all parameters, the Hellmann-Feynman theorem [106] ensures that the force $\mathbf{F}_I$ on the I-th nucleus can be obtained as follows:

$$\mathbf{F}_I \;=\; -\frac{\partial E_{\text{tot}}}{\partial \mathbf{R}_I} \;=\; -\frac{\partial V_{\text{nn}}}{\partial \mathbf{R}_I} - \left\langle \Psi_{\text{e}} \,\middle|\, \frac{\partial H_{\text{e}}}{\partial \mathbf{R}_I} \,\middle|\, \Psi_{\text{e}} \right\rangle, \tag{2.43}$$

where E_{tot} is the total energy of the system, V_{nn} is the nuclear-nuclear repulsion, $|\Psi_{\text{e}}\rangle$ is the many-electron wave function, H_{e} is the electronic Hamiltonian, and $\mathbf{R}_I$ is the position of I-th atom. In this ideal variational scenario, no additional derivative terms appear because all variational parameters have already been optimized. In practice, however, many approximate wave functions are not obtained from a single global variational principle. Specifically, it becomes necessary to evaluate the orbital response term with respect to the atomic coordinates [107, 108, 109, 110].

2.2.5 Handling Condensed-Phase Systems

2.2.5.1 Periodic Boundary Conditions

In real condensed phases—crystalline solids, solid surfaces, liquids, and biomolecular assemblies—the number of constituent atoms is on the order of Avogadro's number ($\approx 6.02 \times 10^{23}$). Direct quantum-chemical treatment of such enormous systems is impractical. Even if a calculation involving 10^6 atoms were technically feasible, the simulation cell would terminate in vacuum, creating artificial surfaces that disrupt bulk properties; finite-size effects would therefore remain significant. Periodic boundary conditions (PBC) provide a robust solution: By tiling a finite simulation cell (unit cell) infinitely in space, PBCs suppress finite-size artifacts while keeping the computational workload tractable. When periodicity is applied only in two directions and a sufficiently thick vacuum layer is introduced along the third, a slab model is obtained, enabling realistic simulation of solid surfaces—an approach indispensable for studies of heterogeneous catalysis and other surface phenomena. PBCs are equally valuable in MD simulations performed at controlled volume or pressure, where they allow reliable evaluation of finite-temperature statistical properties—such as the radial distribution function and diffusion coefficient of liquid water. Thus, PBCs are an essential technique for modeling condensed-phase systems in quantum-chemical and atomistic simulations within finite computational resources.

2.2.5.2 Quantum Mechanics/Molecular Mechanics

When dealing with large condensed-phase systems with the nuclear coordinates $\mathbf{R}$ such as biomolecules, fully applying quantum chemical calculations is typically infeasible due to excessive computational costs. To overcome this limitation, quantum mechanics/molecular mechanics (QM/MM) methods have been developed, enabling quantum chemical treatment of electronic effects in selected regions (QM region, $\mathbf{R}_{\mathrm{QM}}$) (e.g., reactive sites) while describing the remaining parts of the system (MM region, $\mathbf{R}_{\mathrm{MM}}$) (e.g., protein backbones or solvent) using a classical force field [111, 112, 113]. A common way to represent QM/MM methods is through a partitioned total energy (PES) of the system $E_{\mathrm{tot}}(\mathbf{R})$,

$$E_{\mathrm{tot}}(\mathbf{R}) = E_{\mathrm{QM}}(\mathbf{R}_{\mathrm{QM}}) + E_{\mathrm{MM}}(\mathbf{R}_{\mathrm{MM}}) + E_{\mathrm{QM/MM}}(\mathbf{R}_{\mathrm{QM}}, \mathbf{R}_{\mathrm{MM}}), \tag{2.44}$$

where E_{QM} handle the QM region, and E_{MM} deal with the MM region, and $E_{\mathrm{QM/MM}}$ describe interactions between these two subsystems.

2.3 Machine Learning for Atomic-Scale Simulations and Property Predictions in Chemistry

2.3.1 Machine Learning for Atomic-Scale Simulations

The intersection of computational chemistry and ML is actively studied under the field of materials informatics. In particular, ML has been applied to tasks such as energy prediction, molecular design, and materials property prediction, where models constructed from experimental or quantum chemistry data offer high approximation accuracy at relatively low cost. Among these approaches, ML interatomic potentials (MLIPs) are becoming a standard computational chemistry tool, as they can act as surrogates for quantum chemical calculations while maintaining much lower computational costs, thereby striking a balance between accuracy and efficiency. In this dissertation, MLIPs are treated as an interface that bridges quantum chemical calculations using quantum computing and quantum ML applications to chemical problems.

2.3.1.1 Universal Machine Learning Interatomic Potentials

Quantum chemical methods incur large computational costs, posing significant challenges for large-scale or long-time simulations—such as AIMD and for exhaustive screening of material candidates. In recent years, MLIPs have attracted considerable attention as a means to alleviate these bottlenecks. Instead of solving the Schrödinger equation directly, MLIPs learn the relationship between atomic coordinates (element types and positions) and the total energy (as well as its derivatives) from first-principles reference data. This enables energies and forces to be predicted at speeds orders of magnitude faster than conventional quantum chemical calculations, while retaining first-principles level accuracy. Among MLIPs, universal MLIPs that cover a broad region of the periodic table have advanced rapidly in recent years.

Most of today's advanced MLIPs are based on the Behler-Parrinello neural network (BPNN) framework [45] and graph neural network (GNN) [114]. In the BPNN approach, the total energy of the system is expressed as a sum of atomic energies $\{E_I\}_{I=1}^{N}$, each of which depends on the local environment around a single atom. Formally, if $\{Z_I, \mathbf{R}_I\}_{I=1}^{N}$ denotes the elemental type Z_I and position $\mathbf{R}_I$ of each I-th atom in the system, then the total energy E_{tot} is written as

$$E_{\text{tot}}(\{Z_I, \mathbf{R}_I\}) \;=\; \sum_{I=1}^{N} E_I\Big(\mathbf{G}_I(\{Z_J, \mathbf{R}_J\}_{J\in\mathcal{N}(I)})\Big), \tag{2.45}$$

where $\mathbf{G}_I$ represents a set of atomic descriptors (typically vectors) that encode the local environment of I-th atom, considering the neighbor set $\mathcal{N}(I)$ of atoms lying within a certain cutoff radius. In other words, $\mathbf{G}_I$ transforms the raw coordinates and elemental identities of all atoms into features that reflect how I-th atom is bonded to or neighbored by others—while preserving essential symmetries such as translational, rotational, and permutational invariances.

These features $\mathbf{G}_I$ then serve as inputs to multi-layer perceptron (e.g. feed forward neural network), which outputs an atomic energy E_I. Summing over all atomic energies yields the total energy. One of the advantages of the BPNN framework is that, by evaluating the total energy as a sum of atomic energies using a high-dimensional neural network architecture, the number of parameters does not increase with the size of the system or the amount of training data.

In GNN-based MLIPs, atoms are treated as nodes, and interatomic connections are treated as edges in a graph. It allows to learn (update) atomic feature vectors $\{\mathbf{G}_I\}_{I=1}^{N}$ via message passing [114]. Although many GNN-based MLIPs incorporate strategies to maintain a certain degree of invariance or equivariance to E(3), i.e. the group of rotations, reflections, and translations in 3-dimentional space, they may not strictly preserve E(3) equivariance. E(3)-equivariant GNNs, however, are explicitly designed to be equivariant under E(3) ensuring that if the atomic positions are transformed, the corresponding output vectors (features) transform in the same manner [115]. This design ensures that the predicted energies and forces remain physically consistent under spatial transformations, leading to an accurate and data efficient MLIP [115].

2.3.1.2 Quantum Chemical Datasets for Machine Learning Interatomic Potentials

The performance of a universal MLIP depends heavily on the quality and quantity of training data, typically energies and forces obtained from quantum chemical calculations [50]. Recent MLIP architectures often employ hundreds of thousands to millions of parameters, necessitating large-scale datasets to fully exploit their capacity. In practice, many state-of-the-art MLIPs are trained on hundreds of thousands or even millions of data points, and datasets comprising hundreds of millions of data points have also been introduced. Performance improvements have generally been observed when the dataset size is increased, highlighting that dataset augmentation—alongside architectural advances—plays a pivotal role in building more universally applicable MLIPs [49].

Quantum chemical datasets are available for a variety of systems (domains). For crystalline materials under PBCs at the GGA level of DFT, prominent examples include MPtrj (1.6 million data points) [116] and OMat24 (110 million data points) [117]. In the surface domain, OC20 (265 million data points) is a large-scale dataset of adsorption systems, also generated under PBC and at the GGA level of DFT [118]. For molecular systems, where calculations are typically performed on isolated structures at the hybrid GGA level of DFT, key datasets include SPICE [119] (larger than 1 million data points) aimed at training MLIPs, as well as Transition1x [120] (9.6 million data points) encompassing a range of organic reaction pathways.

2.3.1.3 Limitations of Universal Machine Learning Interatomic Potentials

In practice, DFT calculations for organic systems commonly employ hybrid GGA functionals as a standard computational level (e.g. SPICE [119], Transiton1x [120]), whereas GGA functionals are typically used for inorganic systems (e.g. OC20 [118], MPtrj [116]). One limitation arising from this difference in computational protocols—particularly in the choice of functional and the treatment of core electrons—is the lack of a consistent PES across both domains. These inconsistencies can manifest as discontinuities in the PES, making direct comparisons of absolute energies meaningless.

As a consequence, universal MLIPs are typically trained on data confined to either organic (e.g. ANI-1 [121], AIMNet2 [122], GEMS [123]) or inorganic systems (e.g. M3GNet [124], MACE-MP-0 [47], GemNet-OC [125]), with limited interoperability. This separation has impeded the development of a truly universal MLIP framework. Moreover, in future applications where quantum-chemistry data generated by quantum algorithms may become available, the problem of aligning absolute energy values remains unresolved. In particular, combining quantum chemical data derived under heterogeneous computational conditions demands robust techniques to unify these datasets and integrate them effectively.

To address these challenges, new models and workflows are required to harmonize quantum chemical data from various sources—ranging from different exchange–correlation functionals to quantum algorithm outputs. Such a platform would function as a quantum–classical hybrid interface, facilitating the pre-processing, post-processing, and integration of diverse data into a single, universal MLIP framework that can handle both organic and inorganic systems at a reliable accuracy.

2.3.2 Machine Learning for Atomic-Scale Property Predictions

2.3.2.1 Atomic-Scale Chemical Properties

Atomic- and molecular-level chemical properties can often be derived from energy or its derivatives [126]. For instance, adsorption energy is defined based on energy differences and serves as an important metric for assessing the stability and reactivity of atoms or molecules adsorbed onto catalyst surfaces [127, 128, 129]. In contrast, nuclear magnetic resonance (NMR) chemical shifts are derivative properties, obtained as the mixed second derivative of the total energy with respect to an external magnetic field and a nuclear magnetic dipole moment. NMR chemical shifts provide a key spectroscopic fingerprint of the local chemical environment [130].

In recent years, large-scale datasets have been proposed to facilitate ML predictions of these atomic-scale properties. A well-known example is the QM9 dataset, which contains molecular structures and corresponding energies alongside other chemical attributes for a variety of small molecules (primarily composed

of C, O, N, F, and H) [131]. QM9 includes molecular orbital energies, dipole moments, and numerous other chemical quantities. Moreover, extended datasets such as QM9NMR incorporate NMR chemical shift information, enabling more detailed learning and analysis of atomic-scale properties [132].

Accurately predicting and analyzing atomic-scale properties—such as adsorption energy and NMR chemical shifts—is crucial in a wide range of fields, from materials science to drug discovery. Although large-scale, high-precision quantum chemical calculations remain challenging, advances in ML methods and the increasing availability of relevant datasets have opened up opportunities for more efficient exploration of broader chemical spaces.

2.3.2.2 Atomic Descriptors for Chemical Property Predictions

Atomic descriptors convert local chemical environments into numerical features for predicting various properties, including NMR chemical shifts, partial charges, and molecular spectra [133, 134, 135]. They often incorporate physical symmetries (translation, rotation, permutation) and can be constructed from explicit physical principles. Descriptor families like smooth overlap of atomic positions (SOAP) [134, 136, 137, 138, 139] and Faber–Christensen–Huang–Lilienfeld (FCHL) [132, 140, 141, 142] rely on carefully designed functions of distances, angles, or density projections to ensure rotational and translational invariance. They have been widely used to predict NMR chemical shifts [143, 144, 136, 145] as well as other properties such as energetics and partial charges [146, 138, 58]. When additional elements or complex bonding motifs are introduced, the dimensionality of these descriptors can grow rapidly, often scaling at least quadratically with the number of distinct element types [147, 148, 149]. This growth can lead to computational overhead and may reduce transferability across diverse chemical domains. Consequently, balancing efficiency and accuracy in descriptor design remains an open challenge. Such complex classical descriptors impose a high embedding cost on quantum hardware, rendering them unsuitable for the quantum ML methods introduced later. Ongoing efforts focus on refining existing descriptors or combining them with complementary techniques to capture a broad range of chemical spaces without incurring prohibitive computational costs.

2.3.3 Quantum Machine Learning

2.3.3.1 Quantum Circuit Learning

QCL is a VQA designed for ML tasks [9]. It can be regarded as a VQA analogous to neural networks. This section describes QCL in the context of supervised ML. Let the training dataset be $\{\boldsymbol{x}_i, y_i\}_{i=1}^{\mathcal{N}}$, where $\boldsymbol{x}_i$ is the input (descriptor) vector for sample i, y_i is its corresponding target value, and $\mathcal{N}$ is the total number of training data; let n denote the number of qubits. First, each input $\boldsymbol{x}_i$ is encoded into a quantum state via the data encoding circuit $\mathcal{E}(\boldsymbol{x}_i)$. Embedding data into the qubit Hilbert space holds the potential to realize feature maps unattainable

by classical computers, thereby heightening expectations for quantum ML. A subsequent PQC $U(\boldsymbol{\theta})$ then transforms the encoded data into the quantum state $|\psi(\boldsymbol{x}_i, \boldsymbol{\theta})\rangle$ so as to yield the desired output:

$$|\psi(\boldsymbol{x}_i, \boldsymbol{\theta})\rangle = U(\boldsymbol{\theta})\, \mathcal{E}(\boldsymbol{x_i})\, |0\rangle^{\otimes n}. \tag{2.46}$$

The parameters $\boldsymbol{\theta}$ of this PQC correspond to those of a neural network. The prediction of QCL is given by the expectation value of an observable measured on the resulting quantum state $|\psi(\boldsymbol{x_i}, \boldsymbol{\theta})\rangle$, denoted $f(\boldsymbol{x}_i, \boldsymbol{\theta})$. During training, the parameters $\boldsymbol{\theta}$ of the PQC are iteratively updated according to a cost function, ensuring that the output matches the target value. A common choice for the cost function is the mean square error $\sum_i^{\mathcal{N}} \|f(\boldsymbol{x}_i, \boldsymbol{\theta}) - y_i\|^2/\mathcal{N}$. The predictive model is given by $f(\boldsymbol{x}, \boldsymbol{\theta}^*)$, where $\boldsymbol{x}$ is a new input vector and $\boldsymbol{\theta}^*$ is the set of optimized parameters that minimize the cost function. Quantum ML models in which the quantum circuit itself serves as the predictive model such as a QCL are referred to as "explicit models." In Chapter 6, QCL is applied to the prediction of catalytic properties of metallic nanoparticle systems.

2.3.3.2 Quantum Kernel Learning

Another important family of quantum ML algorithms is that of quantum kernel methods [10]. One encodes classical input vectors $\boldsymbol{x}$ into quantum states $|\phi(\boldsymbol{x})\rangle$, and then leverages the overlap of these states as a kernel. Specifically, given two inputs $\boldsymbol{x}$ and $\boldsymbol{x}'$, the quantum kernel is defined by

$$k(\boldsymbol{x}, \boldsymbol{x}') = \left|\langle \phi(\boldsymbol{x}) \mid \phi(\boldsymbol{x}')\rangle\right|^2. \tag{2.47}$$

Because the dimension of the Hilbert space can grow exponentially with the number of qubits, a simple linear model in this high-dimensional feature space is expected to be capable of addressing problems that are computationally challenging for classical methods. In chemistry, such quantum kernel approaches are particularly appealing when dealing with molecular conformations, subtle reaction pathways, or correlated electronic states, as these may carry inherently quantum features that a suitable kernel map could exploit. Quantum kernel methods use quantum computation exclusively for kernel evaluation, and the resulting model is defined implicitly through these kernel values. Consequently, the models obtained in this approach are called "implicit models". A quantum kernel can be integrated into any kernel-based learning algorithm, such as support vector machines or kernel ridge regression. In Chapter 5, this approach is applied to kernel ridge regression.

2.3.3.3 Challenges of Quantum Machine Learning for Chemical Property Predictions

One overarching goal in quantum ML is to demonstrate quantum advantages: a scenario in which quantum ML outperforms classical methods on specific datasets or tasks. Recent efforts to facilitate such demonstrations include

generating quantum datasets via VQE, as proposed by Nakayama *et al.* [150], and adapting classical image benchmarks such as MNIST into a quantum circuit-friendly dataset known as MNISQ [151]. While these advances provide intriguing testbeds for quantum ML algorithms, relatively few large-scale or chemically oriented datasets have been proposed. In particular, there is still a pressing need for carefully crafted benchmarks that capitalize on the intrinsically quantum aspects of molecular structures and properties.

At present, efforts focus on specific tasks—like small-scale classification or chemical simulations—combining noise-robust circuit designs and efficient parameter tuning to achieve useful results even under limited hardware conditions. For example, Hatakeyama-Sato et al. applied QCL to predict chemical properties, comparing it with classical kernel methods and reporting results that suggest superior generalization performance for QCL [43]. On the other hand, because they employed principal component analysis for dimensionality reduction, there are concerns about accuracy. To apply QCL or quantum kernel method to practical chemical tasks, designing low-dimensional yet accurate descriptor remains a key challenge. This challenge is addressed in Chapter 5.

Chapter 3

Integrating Classical and Quantum Software for Enhanced Quantum Chemical Simulation of Realistic Chemical Systems

3.1 Abstract

We demonstrate the feasibility of quantum computing for large-scale, realistic chemical systems through the development of a new interface using a quantum circuit simulator and CP2K, a highly efficient first-principles calculation software. Quantum chemistry calculations using quantum computers require Hamiltonians prepared on classical computers. Moreover, to compute forces beyond just single-point energy calculations, one- and two-electron integral derivatives and response equations are also to be computed on classical computers. Our developed interface allows for efficient evaluation of forces with the quantum-classical hybrid framework for large chemical systems. We performed geometry optimizations and first-principles molecular dynamics calculations on typical condensed-phase systems. These included liquid water, molecular adsorption on solid surfaces, and biological enzymes. In water benchmarks with periodic boundary conditions, we confirmed that the cost of preparing second-quantized Hamiltonians and evaluating forces scales almost linearly with the simulation box size. This study marks a step towards the practical application of quantum-classical hybrid calculations, expanding the scope of quantum computing to realistic and complex chemical phenomena. This chapter is based on Ref. [Shiota, Gunst, Mori, Shiozaki and Mizukami, arXiv:2506.18877 (2025)].

3.2 Introduction

Computational chemistry has emerged as an indispensable tool for understanding chemical phenomena that occur in various phases [36, 53]. Today, quantum chemical calculations, particularly those based on first-principles, facilitate (semi-)quantutitative simulations of nanoscale world. Recently, quantum computers have garnered significant attention for their potential to advance quantum chemical calculations [93, 53, 27, 17, 28, 152, 153]. Over the past decade, especially in the last five years, a diverse array of quantum algorithms for quantum chemistry has been developed [64, 154, 155, 156, 157, 98, 158, 100, 99, 6, 159, 160, 161, 162, 163, 161, 164, 165, 166, 167, 168, 169, 170, 7, 32, 33, 171, 172, 173, 174, 175, 176, 177], with numerous demonstrations using actual quantum devices [64, 154, 178, 174, 34].

Despite these advancements, the scope of quantum chemical calculations employing quantum algorithms has largely been confined to small molecules in the gas phase or crystals with small unit cells, barring a few exceptions. While calculations on surface chemical reactions [179], thermally activated delayed fluorescence (TADF) systems [180], and per- and poly-fluoroalkyl substances (PFAS) [181] have been reported, these still represent relatively small molecular systems by today's quantum chemistry standards [182, 183, 184, 185, 186, 187, 188, 189, 190, 191, 81, 192, 193, 194, 195]. Moreover, the majority of these studies have been limited to single-point energy calculations using geometries structures pre-optimized with density functional theory (DFT).

Notably, there are few studies applying quantum algorithms to practical materials for common quantum chemical tasks such as transition state searches, geometry optimizations, and *ab initio* molecular dynamics (AIMD) simulations [196, 179, 166]. The work of Hohenstein et al. stands as a rare exception, yet even their results pertain to finite systems [166]. To date, no reports exist of AIMD simulations or geometry optimizations using quantum algorithms for condensed-phase systems under periodic boundary conditions (PBCs).

This current state of affairs stems not from limitations in quantum algorithms, but rather from constraints in classical computing. Electronic structure calculations using quantum computers, whether employing quantum phase estimation (QPE) [5, 155] or the variational quantum eigensolver (VQE) [64, 197, 17, 198], are inherently quantum-classical hybrid computations. These methods virtually utilize second-quantized Hamiltonians prepared on classical computers. Even with a limited number of qubits, quantum algorithms can be applied to larger systems through active space approximations, provided that an appropriate active orbital space Hamiltonian is available. The computational cost of generating electronic Hamiltonians formally scales as $O(m^5)$ with respect to the number of spin-orbitals m, or $O(m^4)$ when employing the active space approximation. Furthermore, force calculations essential for geometry optimization and AIMD simulations necessitate the computation of nuclear coordinate derivatives of one- and two-electron integrals and orbital response terms [199]. The cost of these calculations for large-scale systems on

classical computers is substantial, particularly under PBC [200, 201, 202].

Addressing the classical computational cost issue in quantum chemical calculations using quantum algorithms is crucial for applying quantum computers to systems of interest in materials science. Tackling this challenge requires the use of software implementing more sophisticated algorithms on the classical side.

In this chapter, we have developed an interface between the large-scale quantum chemistry program package CP2K version 8.2 [190] and quantum computation. While Battaglia et al. [203] have already developed a interface between CP2K and a quantum computing software Qiskit [204], their research primarily focused on realizing single-point energy calculations, particularly in the framework of a wavefunction-in-DFT embedding method [205]. Similarly, Lukas Schreder and Sandra Luber have built an interface between CP2K and OpenMolcas [206], implementing the wavefunction-in-DFT embedding method [207]. In contrast, our interface emphasizes force calculations in quantum chemical computations using quantum algorithms. Consequently, we have achieved, for the first time using quantum algorithms in first-principles calculations, under PBC, the exploration of molecular adsorption structures on solid surfaces and AIMD simulations of water in the liquid phase.

The remainder of this chapter is organized as follows. In Section 3.3, we describe the interface for the quantum-classical hybrid algorithm for quantum chemistry integrating CP2K and quantum circuit simulators. In Section 3.4, we demonstrate the application of our developed interface in case of representative systems in gas, solid, and liquid phases. Further, we discuss the computational efficiency in terms of the system size. Section 3.5 concludes with a summary of this chapter and its implications for the advancement of quantum computing in computational chemistry.

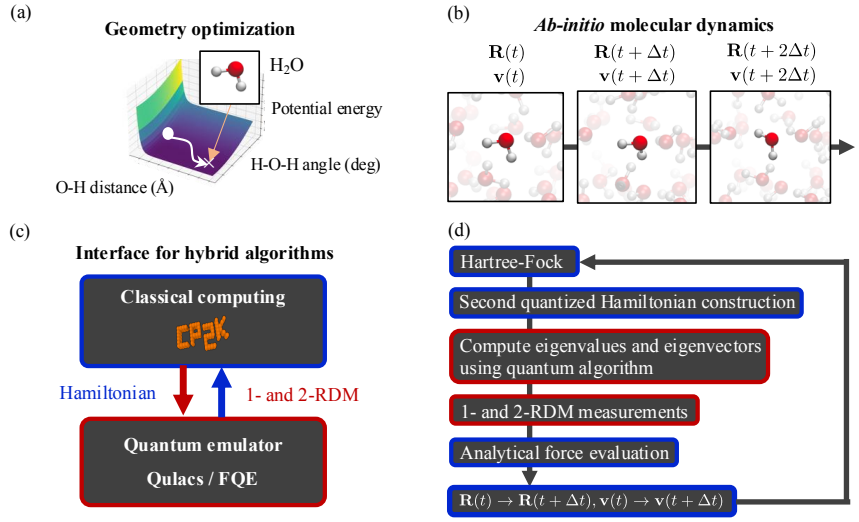

Figure 3.1: (a) Geometry optimization for a water molecule, illustrating the potential energy surfaces as functions of the O-H bond distance and H-O-H bond angle. Geometry optimization follows the forces from the initial geometry, indicated by a white circle, to the equilibrium geometry, marked via a cross. (b) *Ab initio* molecular dynamics (MD) simulations, highlighting the finite-temperature dynamical trajectories of liquid water. In MD, the evaluation of velocity $\mathbf{v}$, which is derived from the forces based on the gradient of the total energy E_{tot} with respect to atomic coordinates $\mathbf{R}$ at the time t must be evaluated. (c) Interface between classical computing using the CP2K package and quantum emulators Qulacs and FQE. The interface is designed to facilitate a two-way exchange between CP2K and quantum emulators such as FQE or Qulacs. Specifically, it enables the transfer of second-quantized Hamiltonians generated by CP2K to the quantum emulator. Subsequently, the reduced density matrices computed by the quantum emulator are returned to CP2K for further processing.(d) The workflow for the MD simulation using the interface. The colors of the borders correspond to classical (blue) and quantum (red) components, as shown in panel (c).

3.3 Methods

This section outlines the interface developed in our research, whilst reviewing a methodology for force calculations with quantum computing.

Quantum chemistry calculations on quantum computers typically begin with a Hartree-Fock calculation performed on conventional quantum chemistry software. Then, a second-quantized fermionic Hamiltonian H_e of the following form is computed:

$$H_\mathrm{e} = \sum_{p,q} h_{pq} c_p^\dagger c_q + \frac{1}{2} \sum_{p,q,r,s} h_{pqrs} c_p^\dagger c_r^\dagger c_s c_q \tag{3.1}$$

Here, h_{pq} and h_{pqrs} represent one-electron and two-electron integrals, respectively. The indices p, q, r, and s denote molecular orbitals. $c_p^\dagger$ and $c_q^\dagger$ are fermionic creation operators, whilst c_r and c_s are annihilation operators.

Quantum computers operate on spin-1/2 systems and cannot directly manipulate fermionic operators. A fermionic Hamiltonian, therefore, must be transformed into a qubit-representation Hamiltonian $H_\mathrm{e}^\mathrm{qubit}$ using a fermion-to-spin mapping such as the Jordan-Wigner transformation [208]. A qubit Hamiltonian $H_\mathrm{e}^\mathrm{qubit}$ is written as

$$H_\mathrm{e}^\mathrm{qubit} = \sum_j h_j P_j \tag{3.2}$$

where P_j represents the tensor product of Pauli operators and h_j are the corresponding coefficients.

Once $H_\mathrm{e}^\mathrm{qubit}$ is obtained, various quantum algorithms can be employed to prepare the wave function. For instance, the QPE can directly yield the eigenvalues and eigenvectors of $H_\mathrm{e}^\mathrm{qubit}$. Alternatively, the VQE can approximate these values variationally.

For variationally calculated wave functions, the Hellmann-Feynman theorem allows us to compute forces as the expectation value of the Hamiltonian differentiated with respect to nuclear coordinates. However, when employing active space approximations, the Hellmann-Feynman theorem no longer holds. In such cases, orbital response terms must be calculated by solving the Coupled Perturbed Hartree-Fock (CPHF) equations [199].

In either scenario, the calculation requires the one-particle reduced density matrix (1-RDM) d_{pq}^full, the two-particle reduced density matrix (2-RDM) $D_{pq,rs}^\mathrm{full}$, and the nuclear coordinate derivatives of one- and two-electron integrals. The latter relies solely on classical computation, whilst RDMs are obtained by measuring the expectation values of operators $c_p^\dagger c_q$ and $c_p^\dagger c_r^\dagger c_s c_q$ for the quantum-computed state $|\Psi_\mathrm{e}\rangle$.

Our implementation, as illustrated in Figure 3.1(c), employs CP2K to generate the second-quantized Hamiltonian for the active orbital space. This Hamiltonian is then passed to either the Qulacs quantum circuit simulator [209] or the fermionic quantum emulator (FQE) [210]. These tools generate the 1-RDM and 2-RDM, which are subsequently returned to CP2K. Within CP2K, the

second-quantized Hamiltonian is stored in the FCIDUMP format, which is then read by Qulacs or FQE. When using Qulacs, the OpenFermion package [211] is utilized to convert the Hamiltonian (operator) from the fermionic form to a qubit form. Throughout this research, we exclusively employed the Jordan-Wigner transformation [87]. For AIMD simulations, as shown in Figure 3.1(d), this force calculation is followed by an update of atomic positions and velocities. The process then loops back to the initial Hartree-Fock step, repeating the cycle as necessary.

The diagonalization of the second-quantized Hamiltonian was performed using both the VQE implemented in Qulacs and FQE. For the VQE ansatz, we adopted the unitary coupled cluster with singles and doubles (UCCSD) [89, 90, 91, 92, 93, 94, 95]. For large-scale systems, an active space approximation was employed, restricting the electronic orbital degrees of freedom to regions critical for reactivity. The active space was selected by choosing an equal number of occupied and unoccupied orbitals near the Fermi level. When diagonalizing a second-quantized Hamiltonian with a 4-electron 4-orbital (eight spin-orbitals) active space using VQE and FQE, the notations UCCSD($4e$, $4o$) and FQE($4e$, $4o$) are used, respectively.

3.4 Results and Discussion

This section presents the results of the simulations conducted using the developed interface with the VQE and FQE methods under the active space approximation. We demonstrated the application of our approach to representative condensed matter systems, as follows. Section 3.4.1 examines water clusters, Section 3.4.2 investigates H_2O on the Si(001) surface, Section 3.4.3 explores liquid water, and Section 3.4.4 analyzes chorismate mutase. For the systems discussed in Sections 3.4.1, 3.4.2, and 3.4.4, we performed geometry optimizations. Whereas, for the system in Section 3.4.3, AIMD simulations were conducted to evaluate the oxygen-oxygen (O-O) radial distribution function (RDF), which is a key statistical property of liquid water. Further, in Section 3.4.5, we assess the computational efficiency of the proposed interface. This was done by examining the system-size dependence of the VQE calculation time using the UCCSD ansatz for liquid water simulations at a density of $1\,\mathrm{g/cm^3}$ for various sizes of the PBC box. Computational details can be found in Appendix A.2.

3.4.1 Water Clusters

Geometry optimizations were performed for the water cluster, that is, the water n-mer $(H_2O)_n$ ($n = 2 \cdots 30$). Figure 3.2 shows the geometry optimization at the UCCSD($2e$, $2o$) level starting from $(H_2O)_{30}$, which was preoptimized using the HF method. The energy decreased uniformly, and after approximately the 20th optimization step, the force decreased with oscillations below 0.05 Hartree/Bohr. In the 102nd optimization step, the force reduced to below the convergence threshold of 0.45×10^{-3} Hartree/Bohr, and convergence was achieved. The

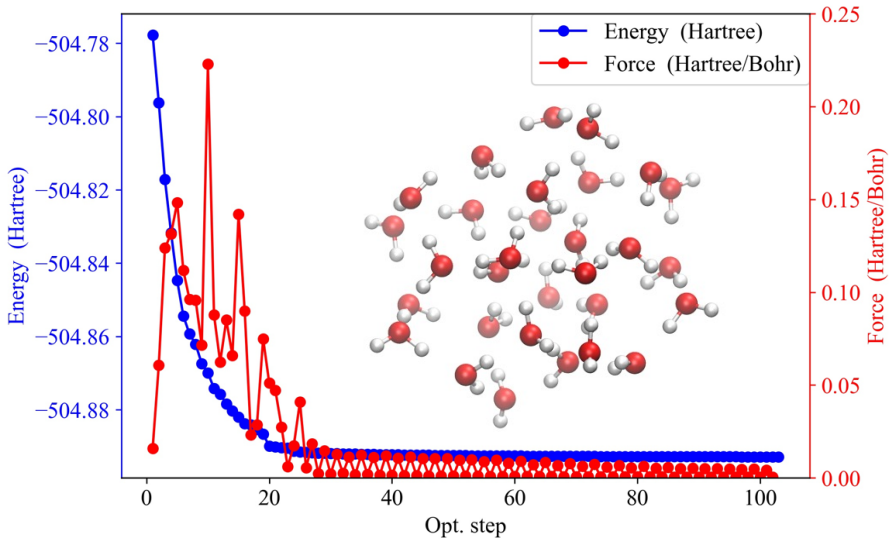

Figure 3.2: Geometry optimization of the water cluster $(H_2O)_{30}$ at the UCCSD($2e$, $2o$) level. The left axis and blue dots represent the total energy. Whereas, the right axis and red dots illustrate the force as a function of the optimization step (opt. step).

optimized structure of $(H_2O)_{30}$ is shown in Figure 3.2. The binding energies per H_2O of the water cluster $(H_2O)_n$ ($n = 2 \cdots 30$) before and after geometry optimization are shown in Figure 3.3. The binding energies of all the water clusters increased with geometry optimization, thereby confirming the possibility of identifying stable structures via geometry optimization. As presented in Appendix A.2, the structures before and after optimization for $n = 2 \cdots 30$ are very similar. However, the binding energies exhibited a change greater than 1 kcal/mol, which is beyond the chemical accuracy. Thus, the equilibrium geometry must be determined for calculating binding energies or other relative chemical quantities with chemical accuracy.

In the case of $(H_2O)_2$, the binding energy before geometry optimization was negative (-0.50 kcal/mol/H_2O). This implied that the water molecule was more stable when it existed by itself. The binding energy in the optimized geometry was 2.48 kcal/mol/H_2O, which indicated stabilization via hydrogen bonding. The full configuration interaction calculation for the water dimer at the complete basis set limit yielded 5.1 kcal/mol (2.55 kcal/mol/H_2O) [212] and experimental measurements of 5.4 $\pm$ 0.7 kcal/mol (2.7 $\pm$ 0.35 kcal/mol/H_2O). These values are consistent with the present calculation. The energy difference can be attributed to the size of the chosen basis set 6-31G(d) not sufficiently large, and the effect of the zero-point energy.

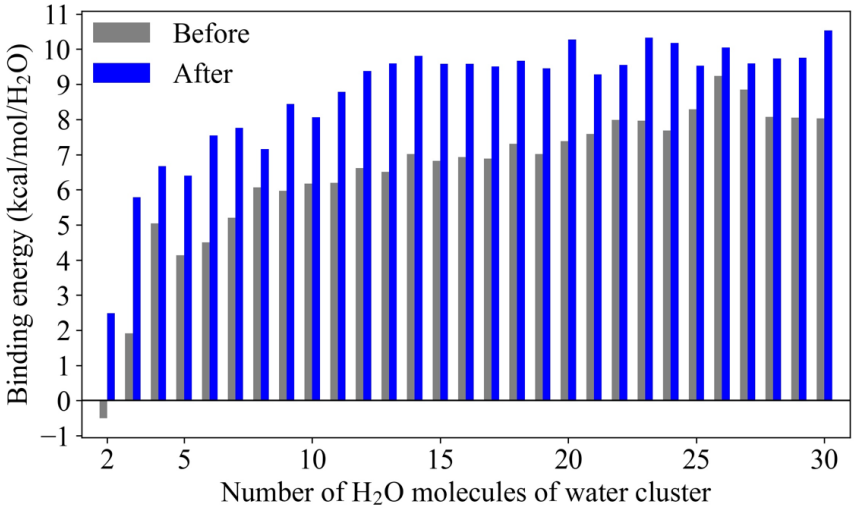

Figure 3.3: Binding energy per water molecule of water clusters $(H_2O)_n$ with ($n = 2 \cdots 30$) before (gray) and after (blue) geometry optimization at the UCCSD($2e$, $2o$) level.

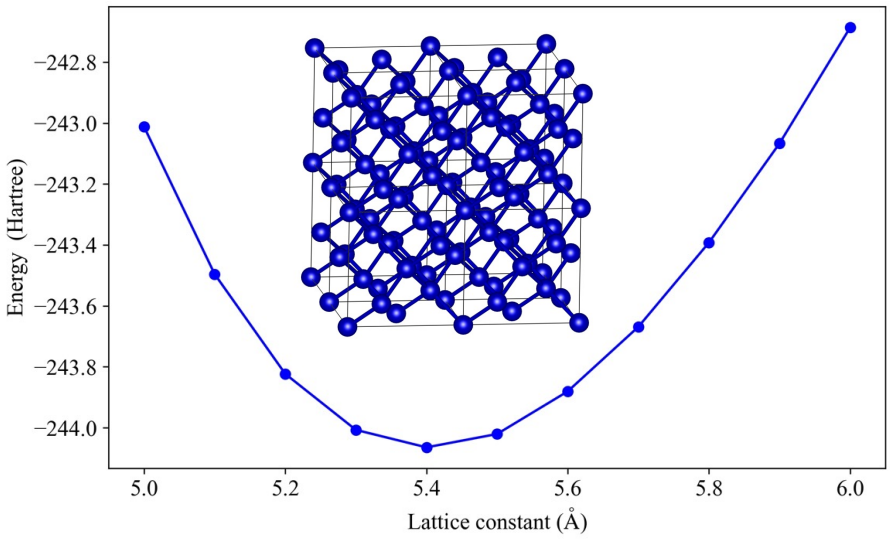

Figure 3.4: Energy versus lattice constant for bulk silicon. The calculated energy is shown as a function of the lattice constant. The minimum energy is observed at a lattice constant of 5.4 Å, which is the value adopted for subsequent modeling of the Si surface. The inset illustrates the crystal structure of bulk silicon used in the calculations.

3.4.2 Defect on Semiconductor Surface

Next, to apply the surface/interface systems, we calculated the adsorption energies for the dissociative adsorption of H_2O molecule on the Si(001) surface. In particular, we calculated the adsorption energy of the adsorption structure known as a type-C defect [213]. The Si(001) surface is stabilized by an alternating arrangement of inclined dimers that reconstruct a $c(4\times2)$ periodic structure [214, 215, 216]. Scanning tunneling microscopy measurements indicated that residual water molecules were dissociatively adsorbed onto the Si(001)-$c(4\times2)$ surface. The dominant structures were H-Si and HO-Si bonds formed on the same side Si atoms for neighboring Si dimers [213]. For modeling the Si(001) surface, single-point calculations were performed at the FQE($4e$, $4o$) level by varying the diamond Si lattice constant (Figure 3.4). The most stable lattice constant 5.4 Å was consistent with the experimental value of 5.43 Å. Thus, this lattice constant was used to model the Si(001)-$c(4\times2)$ surface in the hydrogen-terminated five-layer slab model, as shown in the bird's eye view in Figure 3.5.

Figure 3.5 shows the geometry optimization of the dissociative adsorption of H_2O on the Si(001) surface at the UCCSD($4e$, $4o$) level. Similar to the molecular system, the periodic surface system demonstrated an appropriate

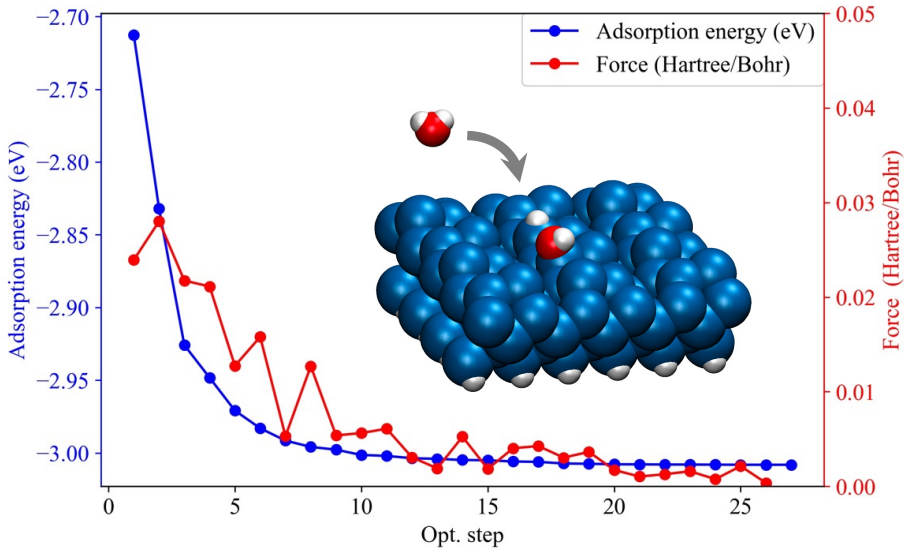

Figure 3.5: Geometry optimization of the dissociative adsorption of a H_2O molecule on the Si(001)-$c(4\times2)$ reconstruction surface at the UCCSD($4e$, $4o$) level. The red axis and points on the left indicate the adsorption energies calculated using the energies of water molecules and Si(001)-$c(4\times2)$ clean surfaces. The blue axis and points on the right present the force as a function of the optimization step.

decrease in energy at each geometry optimization step. The force converged below a threshold value of 0.45×10^{-3} Hartree/Bohr at the 26th step. Further, the adsorption energy after geometry optimization was -3.11 eV. The DFT calculation using the 6-layer slab model with plane-wave basis functions and PBE functionals estimated the adsorption energy to be -2.12 eV [213]. However, our calculations overestimated the adsorption energy by approximately -1.01 eV. To determine the reason for this difference, the stable structure was calculated using DFT calculations with the PBE functional. This yielded -2.72 eV, which was close to the value of -2.12 eV. The remaining energy difference cfould be attributed to the difference in the basis functions, GPW basis functions (6-31G(d), Gaussian basis sets with auxiliary plane-wave basis functions), and plane-wave basis functions. To the best of knowledge, no experimental data have been reported, and quantum chemical calculations of adsorption energies are scarce. Thus numerical experiments on a wide range of surface adsorption systems using various levels of theory are required to realize theoretical prediction accuracy compared to the experimental measurements.

3.4.3 Liquid Water

The results of a 10 ps UCCSD($2e$, $2o$) NVE AIMD simulation of liquid water at 300 K are presented in Figure 3.6. Figure 3.6(a) shows the obtained results, and Figure 3.6(b) shows the trajectories at 10 ps, including the periodic boundary box. The conservation of total energy, as indicated by the black line, confirmed the accurate evaluation of the forces through the analytical gradient calculations. Subsequently, we examined the RDF of the oxygen atoms in the 10 ps NVE simulations performed using the DFT, HF, and UCCSD($2e$, $2o$) methods (Figure 3.6(c)). The RDFs obtained from the HF and UCCSD($2e$, $2o$) simulations exhibited strikingly similar profiles with two major peaks. This similarity may be attributed to the employment of a relatively small active space. This similarity may be attributed to the employment of a relatively small active space. This yielded accuracy levels comparable to the HF calculations because the active space is tiny relative to the full system, which contains 512 electrons distributed over 1,152 orbitals. These results were consistent with those of a previous study that used the HF potential [217]. In contrast, the RDF derived from the DFT simulations exhibited prominent peaks that spanned from the first to the third hydration sphere, thereby successfully reproducing the number of major peaks observed in the experimental measurements [218]. These findings demonstrate that HF and UCCSD with limited active spaces do not accurately replicate the RDF of oxygen atoms in liquid water.

3.4.4 Chorismate Mutase Enzyme

Chorismate mutase is an essential enzyme found in various organisms, including plants and bacteria [219]. It plays a crucial role in specific physiological functions. It functions as a catalyst in certain biochemical reactions and facilitates the conversion of shikimic acid (chorismate) to prephenate, which is a significant

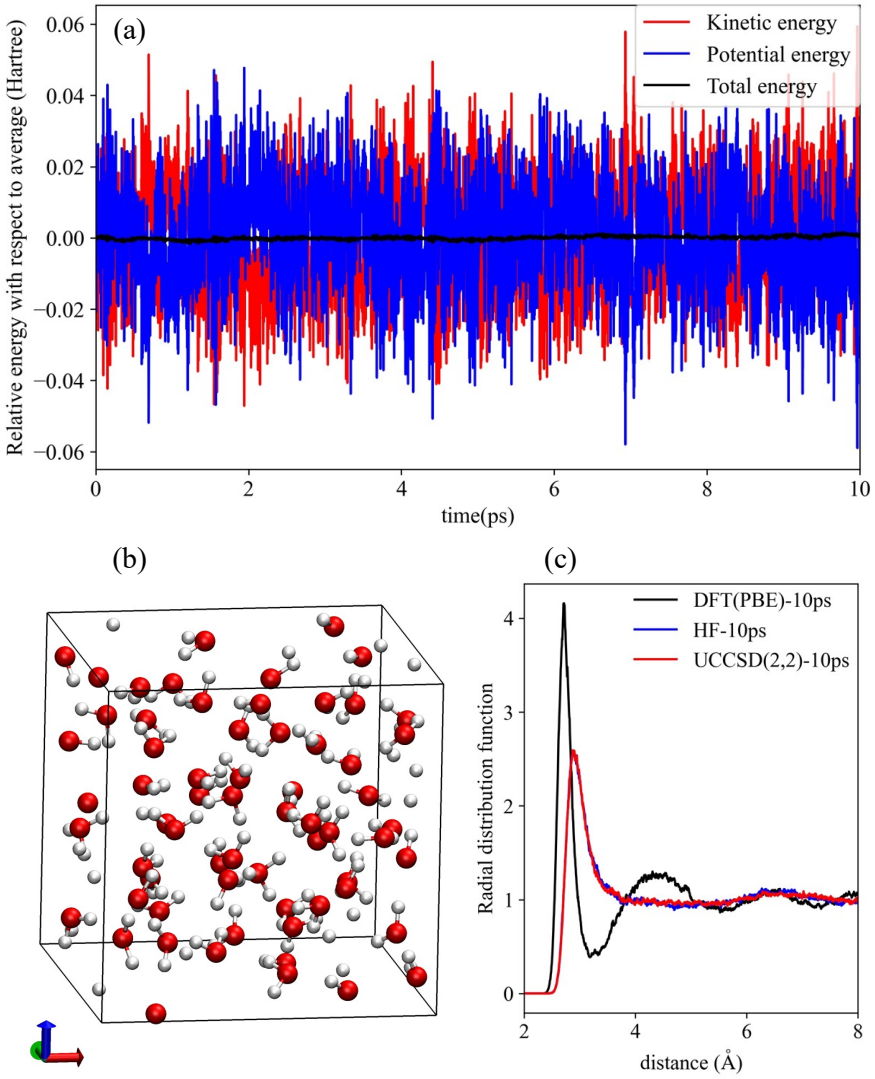

Figure 3.6: Results of a 10 ps NVE simulation of liquid water at 300 K at the UCCSD($2e$, $2o$) level. (a) Plot of kinetic energy (red line) and potential energy (blue line) and their sum (sum) with respect to their respective averages (b) Snap-shot of the liquid water at 10 ps with PBC box. (c) Radial distribution function (RDF) of oxygen atoms calculated via NVE simulations of 10 ps for a total of 20,000 trajectories using DFT (black), HF (blue), and UCCSD($2e$, $2o$) (red), respectively.

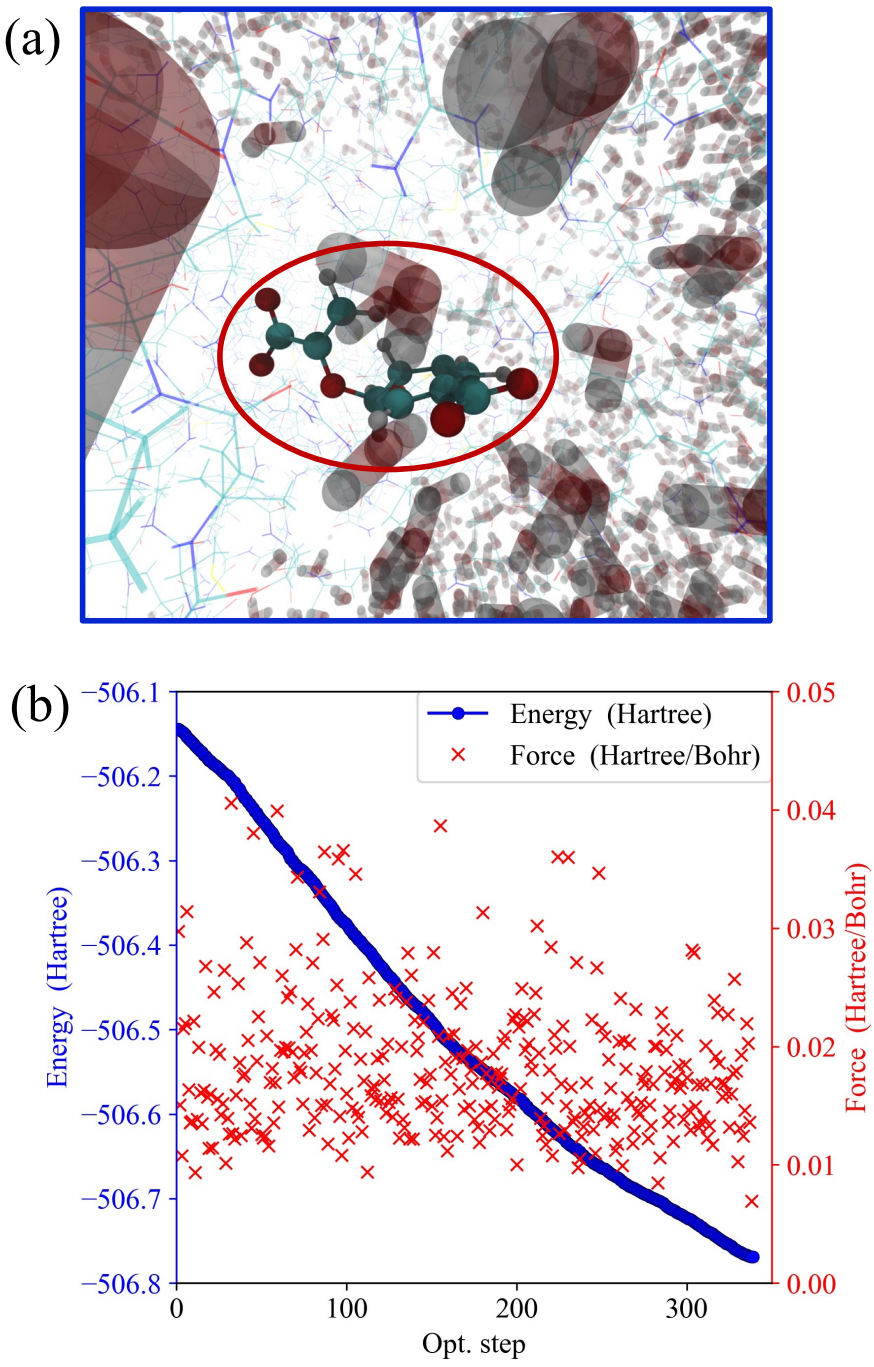

Figure 3.7: Chorismate mutase. The chorismate circled in red is the QM region and the others are the MM region. (b) Geometry optimization of chorismate mutase. The blue axis and blue dots on the left indicate the energy, and the red axis and red × symbol indicate the force on the right of the QM region.

step in the aromatic amino acid biosynthesis pathway. In this dissertation, we took the first step towards simulating this enzyme reaction by performing a geometry optimization of the reactant, chorismate, within the framework of quantum mechanics/molecular mechanics (QM/MM) [113]. The QM region comprised the substrate chorismate, whereas the MM region represents the enzyme environment (see Figure 3.7(a)). Detailed information on the model setup and the classical force field settings can be found in [220]. For the QM calculations, we employed the UCCSD ($4e$, $4o$) level of theory. The progress of geometry optimization is illustrated in Figure 3.7(b). The geometry optimization using QM/MM proceeded stably. The energy decreased consistently throughout the optimization process. Although the change in forces did not stabilize until immediately before converging to 0.01 Hartree/Bohr, this behavior was attributable to the perturbation of the QM region owing to interactions with the MM region. However, with the progression of the optimization, the fluctuation diminished. We anticipate that implementing more stringent convergence criteria for the forces will result in smaller fluctuations. Thus, these results demonstrate the feasibility of the VQE simulation within the QM/MM framework.

3.4.5 Computational Efficiency

We evaluated the performance of the VQE simulation using the interface developed in this chapter. Specifically, we focused on the system size dependence of the UCCSD($2e$, $2o$) level calculations for liquid water at 300K. Figure 3.8 illustrates the scalability of various components involved in the UCCSD($2e$, $2o$) calculations, including the HF calculations, second-quantized Hamiltonian construction, and the evaluation of forces using analytical differentiation as a function of the number of water molecules. HF calculations performed using CP2K exhibited approximately linear scaling with an increase in the number of H_2O molecules in the unit cell. This was consistent with the linear scaling reported in the benchmarks of Kühne et al. for AIMD calculations of liquid water [183]. Similarly, the costs associated with the second-quantized Hamiltonian construction and force evaluation scaled linearly with the number of molecules. The computation time for the UCCSD calculations was significantly shorter than that for the other processes performed on the CP2K side. This is because the active space for execution on a quantum computer is limited to four qubits. In the future, as the scale of accessible quantum devices increases, it is expected that the degrees of freedom of orbitals handled in quantum calculations will increase, which would facilitate the addressal of more meaningful tasks.

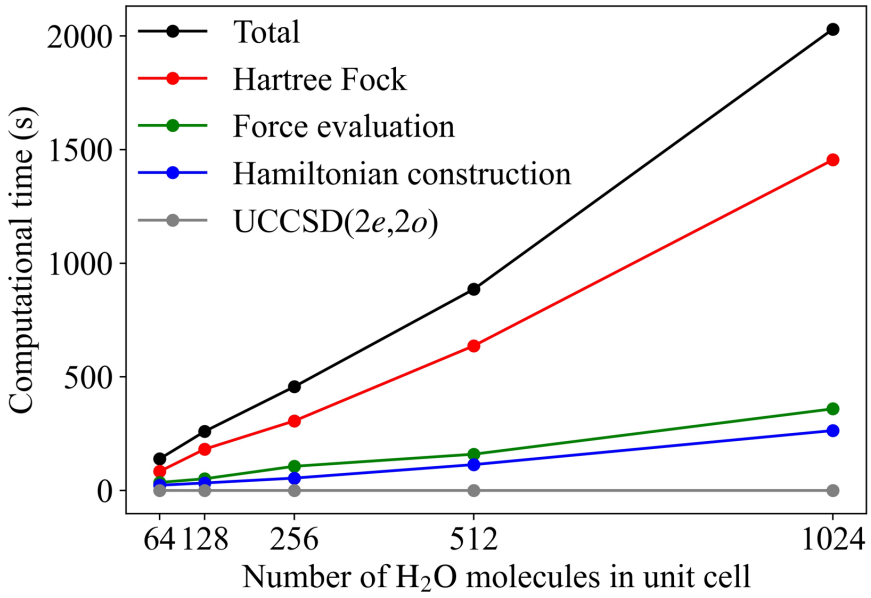

Figure 3.8: Single-point calculation benchmarks for bulk water of 1 g/cm^3 at UCCSD(2e, 2o) level, modeled considering different simulation box sizes of 64, 128, 256, 512, and 1024 H_2O molecules. Different stages of computations are distinguished: total computation time (black circles), HF computation time (red circles), analytic derivative computation time (green circles), second-quantized Hamiltonian construction time (blue circles) and UCCSD(2e,2o) calculations. All calculations are performed using 4 Intel(R) Xeon(R) Platinum 9242 CPUs with 96 CPU cores in message passing interface (MPI) parallel, for a total of 384 CPU cores.

3.5 Conclusion

This chapter developed an interface between CP2K, a linear-scaling quantum chemical calculation package, and Qulacs and FQE, which are state vector-based quantum simulators, to facilitate efficient quantum-classical hybrid calculations for realistic chemical problems. The developed interface facilitated the evaluation of analytical gradients with respect to the atomic coordinates using the 1-RDMs and 2-RDMs obtained from the VQE simulations. Water clusters, liquid water, dissociative adsorption structures of water molecules on the reconstructed Si(001)-$c(4\times2)$ surface, a well-known defect in silicon wafers, and chorismate mutase, an important enzymatic reaction in biological systems, were selected to conduct simulations on realistic materials. The computational efficiency of the developed interface was evaluated at the UCCSD($2e$, $2o$) level for liquid water with a density of $1\,\mathrm{g/cm^3}$ and a PBC box containing 64–1024 molecules. The developed interface appropriately elicited a near-linear performance from CP2K, which facilitated the second-quantized Hamiltonian construction and analytical force evaluation at a near-linear cost with respect to the number of molecules and simulation box size.

However, issues regarding accuracy were observed. The RDF of water at 300K obtained at the UCCSD($2e$, $2o$) level was almost identical to that at the HF level. The adsorption energy of H_2O on the Si(001)-$c(4\times2)$ surface differed significantly from that obtained using DFT. These accuracy issues suggest that the orbital degrees of freedom for electron correlation included in quantum calculations were insufficient for large systems involving tens to thousands of atoms. These problems may be resolved by employing several sophisticated quantum-classical hybrid algorithms. For example, the methods proposed by Erhart et al. [175] and Scheurer et al. [221] efficiently solved the active space problem in quantum algorithms, and incorporated dynamic correlations using methods such as CCSD. Furthermore, in molecular adsorption systems, improvements can be achieved through the application of quantum embedding methods [205, 203] that handle only the region close to the adsorption site with quantum calculations while treating the remaining using DFT. Using the interface we developed to implement these quantum-classical hybrid algorithms, it is expected that the computational burden on classical computing can be minimized, thereby enabling efficient quantum-classical hybrid algorithms.

Chapter 4

Taming Multi-Domain,-Fidelity Data: Towards Foundation Models for Atomistic Scale Simulations

4.1 Abstract

Machine learning interatomic potentials (MLIPs) are changing atomistic simulations in chemistry and materials science. Yet, building a single, universal MLIP—capable of accurately modeling both molecular and crystalline systems—remains challenging. A central obstacle lies in integrating the diverse datasets generated under different computational conditions. This difficulty creates an accessibility barrier, allowing only institutions with substantial computational resources—those able to perform costly recalculations to standardize data—to contribute meaningfully to the advancement of universal MLIPs. Here, we present total energy alignment (TEA), an approach that enables the seamless integration of heterogeneous quantum chemical datasets almost without redundant calculations. Using TEA, we have trained MACE-Osaka24, the first open-source neural network potential model based on a unified dataset covering both molecular and crystalline systems, utilizing the MACE architecture developed by Batatia et al. This universal model shows strong performance across diverse chemical systems, exhibiting comparable or improved accuracy in predicting organic reaction barriers compared to specialized models, while effectively maintaining state-of-the-art accuracy for inorganic systems. Our method democratizes the development of universal MLIPs, enabling researchers

across academia and industry to contribute to and benefit from high-accuracy potential energy surface models, regardless of their computational resources. This advancement paves the way for accelerated discovery in chemistry and materials science through genuinely foundation models for chemistry. This chapter is based on Ref. [Shiota, Ishihara, Do, Mori and Mizukami, arXiv:2412.13088 (2024)].

4.2 Introduction

Recent advances in machine learning interatomic potentials (MLIPs) have opened new opportunities in computational chemistry and materials science. Researchers can now perform atomistic simulations with nearly first-principles accuracy at orders of magnitude lower computational cost [48, 222, 223, 224, 225, 46, 56, 54, 226, 55, 227, 146, 45]. This paradigm shift has been propelled by increasingly sophisticated architectures—ranging from high-order equivariant neural networks to multi-scale graph neural representations—and an expanding wealth of large, first-principles-based datasets [45, 228, 229, 230, 231, 232, 233, 234, 235, 115, 236, 237, 238, 239, 240, 241, 242, 243, 244, 245, 246, 247, 248, 249, 250, 118, 251, 252, 253, 120, 131, 254, 255, 256, 119, 257, 258, 259, 260, 261, 262]. Inorganic-focused MLIPs now span much of the periodic table, making it easier to survey crystal structures and discover new phenomena in catalysis, semiconductor, and beyond [124, 263, 264, 116, 265, 47, 266, 267, 117, 268, 269, 270, 271, 272]. At the same time, MLIPs for molecular systems have grown more versatile, achieving near hybrid density functional theory (DFT) accuracy across a range of organic, pharmaceutical, and biomolecular targets [121, 273, 274, 275, 276, 122, 119, 258, 257, 233, 123, 239, 277, 278, 236].

Yet despite these advances, the pursuit of a truly "universal" MLIP—one that seamlessly unites the organic and inorganic realms—remains challenging. Molecular and crystalline datasets often differ in their computational methods, choice of DFT functionals, and basis sets, making their resulting potential energy surfaces (PESs) incompatible [279, 280, 281, 282, 283, 182, 284, 285, 189, 286, 287, 288]. For example, inorganic datasets typically use plane-wave basis sets and generalized gradient approximations, while organic datasets rely on localized basis sets and hybrid functionals. Merging these heterogeneous sources—without recalculating vast portions of data—has been difficult, placing the development of foundation models in chemistry out of reach for many research groups with limited computational resources.

Here, we introduce a general strategy called total energy alignment (TEA) that addresses this long-standing problem by harmonizing datasets generated under different computational settings. TEA uses a two-step approach—first aligning inner-core reference energies, then scaling atomization energies—to integrate datasets that previously could not be combined. Applying TEA to unify a large inorganic dataset (MPtrj) [116] and a broad organic set (OFF23 [278], consisting of SPICE [119, 258], QMug [257], water clusters, and Tripeptides datasets), we have constructed MACE-Osaka24: a single open-source neural network potential capable of accurately modeling both

organic molecular reactions and extended crystalline systems. Unlike previous multi-task approaches that simply switch between domains [264, 289], MACE-Osaka24 handles organic and inorganic PESs with a single model. It not only outperforms specialized potentials in predicting reaction barriers for drug-like organic molecules, but also maintains state-of-the-art accuracy for inorganic systems.

This work has two key implications. First, by removing the need for costly recalculations, TEA helps democratize the creation of foundation models in chemistry, enabling research groups with limited computational resources to contribute more effectively. Second, MACE-Osaka24 shows that a single model can achieve high accuracy across both molecular and inorganic domains, suggesting a new level of interoperability. As data-driven discovery expands, the ability to seamlessly handle both organic and inorganic chemical spaces will accelerate catalyst design, functional material development, and the exploration of complex reactions. Together, the TEA framework and MACE-Osaka24 point the way toward truly universal MLIPs, enabling the next generation of foundation models to go beyond traditional domain boundaries.

The remainder of this chapter is organized as follows. In Section 4.3, we review related works on learning from datasets generated under different computational conditions. Section 4.4 introduces our TEA method, followed by details of the integrated datasets and the process of building multi-domain universal MLIPs. In Section 4.5, we assess the accuracy of the constructed multi-domain universal MLIP using a range of benchmarks: we compare predicted reaction barriers for organic molecules, evaluate lattice constants for inorganic crystals, and perform molecular dynamics simulations for liquid water. Section 4.6 discusses the implications of our findings and suggests directions for future research. Finally, we present our conclusions in Section 4.7.

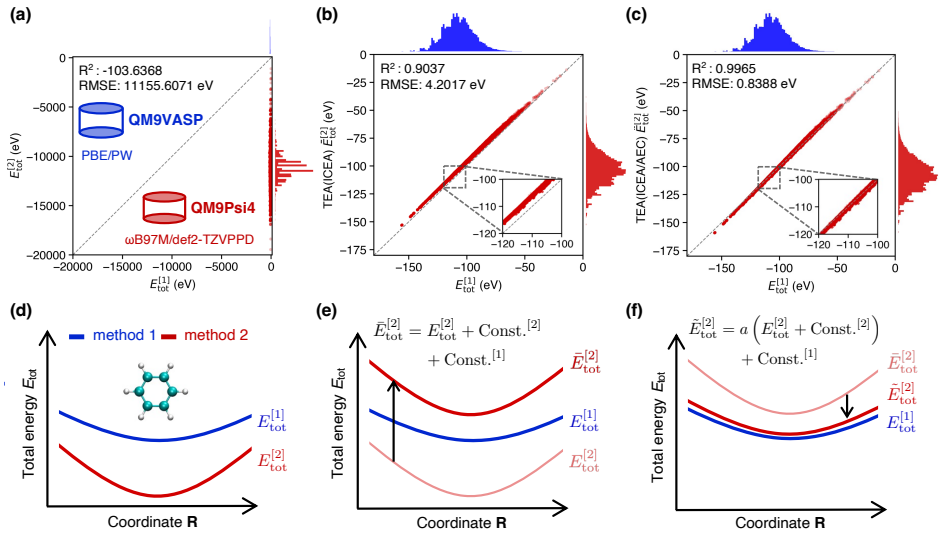

Figure 4.1: (a) Scatter plot comparing the total energies of about 143 000 QM9 geometries obtained with Method 1 (PBE/PW via VASP; "QM9VASP") and Method 2 (ωB97M/def2-TZVPPD via Psi4; "QM9Psi4"). The very poor correlation (R^2 = –103.6, root mean square error (RMSE) = 11 156 eV) underscores the large systematic difference between the two levels of theory; marginal histograms are shown on the axes. (b) Same data after the first stage of Total Energy Alignment (TEA)—Inner Core Energy Alignment (ICEA)—is applied to the total energies of the QM9Psi4. (c) Total energies after the second stage of TEA—Atomization Energy Correction (AEC)—which brings the datasets into close agreement (R^2 = 0.9965, RMSE = 0.839 eV). Insets in (b) and (c) enlarge the boxed regions. (d) Schematic potential-energy surfaces (PESs) for a representative molecule (benzene) calculated with Methods 1 (blue) and 2 (red), corresponding to one data point in (a). (e) Illustration of ICEA: for species with identical stoichiometry, ICEA acts as a constant vertical shift of the Method 2 PES. (f) Illustration of AEC: after ICEA, AEC rescales the shifted Method 2 PES by a factor a, yielding the fully aligned PES that matches the Method 1 reference.

4.3 Related Work

A goal of MLIPs has been to achieve first-principles accuracy in simulating chemical and materials systems while greatly reducing computational costs. Early methods, like Behler-Parrinello networks and Gaussian Approximation Potentials, showed that machine learning can reproduce high-level quantum chemistry results without directly solving the Schrödinger equation for every geometry [45, 146]. Since then, more advanced E(3)-equivariant graph neural networks and message-passing models have emerged, improving both accuracy and transferability [229, 230, 232, 233, 234, 115, 236, 237]. Concurrently, large-scale first-principles datasets—ranging from the Materials Project's extensive inorganic databases [244, 245, 124, 116, 47] to molecular sets such as the QM9 [131], OFF23 [119, 257, 258, 278], and SPICE [119] datasets – have enabled the training of increasingly universal MLIPs. As a result, models such as MACE-MP-0 [236, 47] and CHGNet [116] now approach state-of-the-art performance for inorganic crystals, while others, like MACE-OFF23 [278] and AIMNet2 [276, 122], deliver high accuracy across diverse organic and biomolecular systems.

A major challenge in advancing universal MLIPs lies in the integration of these heterogeneous datasets – each constructed under different computational protocols, basis sets, and exchange-correlation functionals – into a single, cohesive training set. These differences affect reference energies, force field definitions, and whether the calculations include periodic conditions, making it hard to combine data directly [279, 280]. To date, several strategies have been attempted to bridge these discrepancies. For example, Δ-machine learning and multi-fidelity learning approaches learn corrections from lower- to higher-level references, allowing them to blend datasets at different accuracy levels [290, 291, 292, 293]. However, these methods often need a reference dataset covering both fidelity/domain ranges and still face difficulties when data come from different software or fundamentally different computational setups. As a result, many solutions remain specialized to a specific domain, for example, to either molecular systems or periodic solids, but not both simultaneously.

When it comes to spanning organic and inorganic domains within a single MLIP, only a handful of attempts exist. For instance, PFP [264] uses multi-task learning to handle molecular and crystalline data together, but treats them as separate 'modes' rather than unifying their energy scales. Similarly, DPA-2 [289] improves generalization by pretraining on multiple tasks—including molecules, crystals, and surfaces—but still depends on carefully managed workflows and fine-tuning, rather than directly merging heterogeneous datasets. These approaches highlight the advantages of multi-domain learning, such as better transferability, fewer data requirements, and stronger PES exploration. However, they have yet to solve the core issue of integrating data generated under different computational conditions into one consistent PES without extensive recalculations.

Another line of research has sought to align different datasets using physically meaningful reference values. For inorganic materials, methods like the fitted elemental reference energies (FERE) approach compare formation energies and elemental reference energies across various exchange-correlation functionals

and calculation setups [294, 295, 296, 297]. Recently, Gabellini et al. [261] introduced a large molecular dataset by converting total energies into atomization energies (analogous to formation energies), which helps reduce reliance on absolute reference values that differ among computational codes. However, atomization energies carry systematic errors depending on the computational protocol [298, 299]. As a result, simply transforming existing datasets into atomization energies does not guarantee more effective MLIP training. While these strategies offer promising leads, applying them to integrate large-scale organic and inorganic datasets—where both computational fidelity and the nature of the systems (extended solids vs. finite molecules) differ—remains non-trivial.

4.4 Methods

4.4.1 Total Energy Alignment

Developing a truly universal MLIP that can handle molecular and extended solid systems requires the unified treatment of datasets generated under diverse computational conditions. However, directly merging these heterogeneous datasets is challenging because their total energies are often incomparable, as shown in Fig. 4.1(a) and (d). Here, we introduce the TEA framework, which is a two-step procedure designed to seamlessly reconcile datasets computed using different quantum chemical approaches, as shown in Fig. 6.1(e) and (f).

TEA comprises two key steps: (I) Inner Core Energy Alignment (ICEA) and (II) Atomization Energy Correction (AEC). ICEA corrects for systematic energy offsets caused by differences in the treatment of core electrons, such as the use of effective core potentials or projector-augmented wave (PAW) methods, without altering the relative energy differences. AEC subsequently scales the atomization energies to account for discrepancies in the computational fidelities or basis sets or exchange-correlation functionals used across different datasets. By initially aligning the core-level energies and then applying a scalable correction to the atomization energies, TEA provides a straightforward route for use in integrating previously incompatible datasets into a single coherent training platform, as shown schematically.

In the following explanation of TEA method, we adopt the problem setting and assumptions that a dataset of total energies and forces has been generated with method 2, labeled [2] in the equations, and that isolated atomic energies for every element in the dataset are available from both method 1 ([1]) and method 2. TEA's goal is to transform the total energy and force dataset produced by Method 2 into the form that would be obtained with Method 1, without recomputing the dataset with Method 1. For simplicity, we now outline the procedure for converting the data of an N-atom system, taken from the dataset obtained with Method 2, into the corresponding data that would be produced with Method 1, as shown in Fig. 4.1(d)–(f).

4.4.1.1 Inner Core Energy Alignment

Different computational methods often treat inner-core electrons differently, leading to systematic shifts in their total energies. These differences do not generally affect chemical reactivity, but they hamper direct comparisons or combinations of datasets. To address this, we first assume that the relative quantities, such as atomization energies, remain consistent between Methods 1 and 2.

For a system of N atoms, the atomization energy E_{at} is defined as:

$$E_{\mathrm{at}} = \sum_{i=1}^{N} E_i^{P_i} - E_{\mathrm{tot}}, \tag{4.1}$$

where $E_i^{P_i}$ is the energy of an isolated atom of species P_i, and E_{tot} is the total energy of the system.

Under the assumption that the atomization energies obtained using Methods 1 and 2 are equivalent,

$$E_{\mathrm{at}}^{[1]} = E_{\mathrm{at}}^{[2]}, \tag{4.2}$$

the ICEA-shifted total energy of Method 2, $\bar{E}_{\mathrm{tot}}^{[2]}$, is given as

$$\begin{aligned} \bar{E}_{\mathrm{tot}}^{[2]} &= \sum_{i=1}^{N} E_i^{P_i,[1]} - E_{\mathrm{at}}^{[2]} \\ &= \left(\sum_{i=1}^{N} E_i^{P_i,[1]} - \sum_{i=1}^{N} E_i^{P_i,[2]} \right) + E_{\mathrm{tot}}^{[2]}. \end{aligned} \tag{4.3}$$

This relation shows that we can shift the total energies from Method 2 onto the reference scale of Method 1 using only isolated-atom energies. In practice, ICEA sets a common baseline for both datasets, ensuring that differences arise from meaningful chemical effects rather than arbitrary computational choices.

4.4.1.2 Atomization Energy Correction

After applying ICEA, certain residual differences in the atomization energies still remain if the two datasets originate from different calculation protocols (e.g., distinct levels of theory, different basis sets, or contrasting exchange-correlation functionals). These differences manifest as systematic offsets that must be corrected before the datasets can be fully integrated.

We introduce a correction function f that relates the atomization energies obtained via the two methods:

$$E_{\mathrm{at}}^{[1]} = f\left(E_{\mathrm{at}}^{[2]}\right). \tag{4.4}$$

To maintain simplicity and ensure a robust performance, we adopt a single scaling factor a:

$$f\left(E_{\mathrm{at}}^{[2]}\right) = a\, E_{\mathrm{at}}^{[2]}. \tag{4.5}$$

In fact, previous studies have reported a linear relationship between the magnitude of the atomization energy and the systematic errors present [298, 299], making a simple scaling approach a practical choice. Using the correction function defined by the scaling factor a, the AEC-aligned total energy $\tilde{E}_{\text{tot}}^{[2]}$ is expressed as follows:

$$\tilde{E}_{\text{tot}}^{[2]} = \sum_{i=1}^{N} E_i^{P_i,[1]} - a\, E_{\text{at}}^{[2]}. \tag{4.6}$$

Because forces $\{\mathbf{F}_i\}_{i=1}^{N}$ are negative gradients of the total energy E_{tot} with respect to atomic coordinates $\{\mathbf{R}_i\}_{i=1}^{N}$, this correction consistently adjusts forces $\mathbf{F}_i^{[2]}$ as well:

$$\tilde{\mathbf{F}}_i^{[2]} = -\frac{\partial \tilde{E}_{\text{tot}}^{[2]}}{\partial \mathbf{R}_i} = -a\frac{\partial E_{\text{tot}}^{[2]}}{\partial \mathbf{R}_i} = a\mathbf{F}_i^{[2]}, \tag{4.7}$$

where $\tilde{\mathbf{F}}_i^{[2]}$ is AEC-aligned forces. This ensures that the entire PES is appropriately rescaled. Together, ICEA and AEC yield a coherent PES alignment that preserves relative energy differences and accuracies across heterogeneous datasets.

4.4.2 Datasets

To demonstrate the effectiveness of TEA, we integrated two large-scale datasets: the MPtrj dataset, which provides inorganic structures calculated at the PBE [300] functional with plane-wave basis sets (PBE/PW) using Vienna Ab initio Simulation Package (VASP) [281, 282, 283, 182], and the OFF23 dataset, an extensive organic dataset computed at the ωB97M-D3(BJ)/def2-TZVPPD [301, 302, 303, 304] level using Psi4 [189]. Prior to integration, we remove the D3(BJ) dispersion correction from the OFF23 data to avoid double-counting dispersion effects in the final MLIP.

To determine the scaling factor a used in the AEC step and assess uncertainties, we also employed the QM9 dataset [131], originally computed at B3LYP [305]/6-31G(2df,p) level using Gaussian09 [288]. We recalculated QM9 using VASP (PBE/PW) and Psi4 (ωB97M-D3(BJ)/def2-TZVPPD) to generate QM9VASP and QM9Psi4 subsets, ensuring consistent reference points for establishing a. Full details of dataset preparation and integration, including corrections and final merged sets, are provided in Appendix B.1. The fully integrated organic-inorganic dataset is publicly available at https://github.com/qiqb-osaka/mace-osaka24.

4.4.3 Machine Learning Interatomic Potential Training

With TEA-enabled integration, we trained MLIPs using the MACE framework [236, 47], specifically employing mace v0.3.6 (https://github.com/ACEsuit/mace). We leveraged the integrated MPtrj/OFF23 dataset after applying TEA, and refer to the resulting MLIP as MACE-Osaka24. The model and the

final training data are available at https://github.com/qiqb-osaka/mace-osaka24.

Our training followed the hyperparameters, cost functions, and optimizers of MACE-MP-0-small and MACE-MP-0-large models described in Ref. [47], with a few modifications. For all models, we set a cutoff radius of 4.5 Å for constructing the atomic neighborhood graph. We used isolated atomic energies computed with spin polarization via VASP as references for the atomic species included in OFF23. Model training was performed using 32 A100 GPUs in parallel. Details of the MACE-Osaka24 model training procedure and hyperparameter settings can be found in Appendix B.2.

By unifying heterogeneous datasets under the TEA framework and leveraging advanced MLIP architectures, our approach yields a single universal potential model that can accurately describe both molecular and crystalline systems. This lays a critical foundation for accessible, high-fidelity PES modeling across the chemical and materials sciences.

4.5 Results

To evaluate the performance of TEA between datasets that employed the different fidelity functionals and differed in core electron treatments, basis sets, and boundary conditions, we conducted TEA for QM9 datasets re-calculated using the VASP [281, 282, 283, 182] and Psi4 [189], named QM9VASP and QM9Psi4, respectively. Fig. 4.1(a) shows a parity plot comparing QM9VASP and QM9Psi4. No clear trend in the total energy between the two datasets is observed, and the data points are scattered. This is because QM9Psi4 is calculated using an all-electron method, where the total energy is the energy of all electrons, whereas QM9VASP represents the total energy of the valence electrons only. As shown in Fig. 4.1(b), by performing TEA using ICEA, we succeed in aligning the total energies to be comparable. However, the precision is as high as the root mean square error (RMSE) 4.2017 eV and the reliability is low. This is mainly because of the differences in fidelity caused by the different functionals. As shown in Fig. 4.1(c), TEA using ICEA/AEC captures the systematic differences due to fidelity variations and significantly improves the RMSE to 0.8388 eV.

We evaluate the performance of the constructed multi-domain universal MLIPs, MACE-Osaka24-small and MACE-Osaka24-large. For comparison, we also performed simulations using MACE-MP-0 and MACE-OFF23, where feasible. Furthermore, we present simulation results obtained using other universal MLIPs, as well as DFT, and semiempirical and classical force fields, for additional reference.

First, we present the benchmark results for organic molecular systems. Table 4.1 shows the mean absolute errors (MAEs) of barrier heights for 78 drug-like biaryl torsions, compared against high fidelity reference energies at the coupled cluster level of theory provided in biaryl torsion benchmark [306]. Compared with the RMSEs in the benchmark by Kovács et al. [278], the approximately 0.1 kcal/mol difference in the accuracy of MACE-OFF23 models

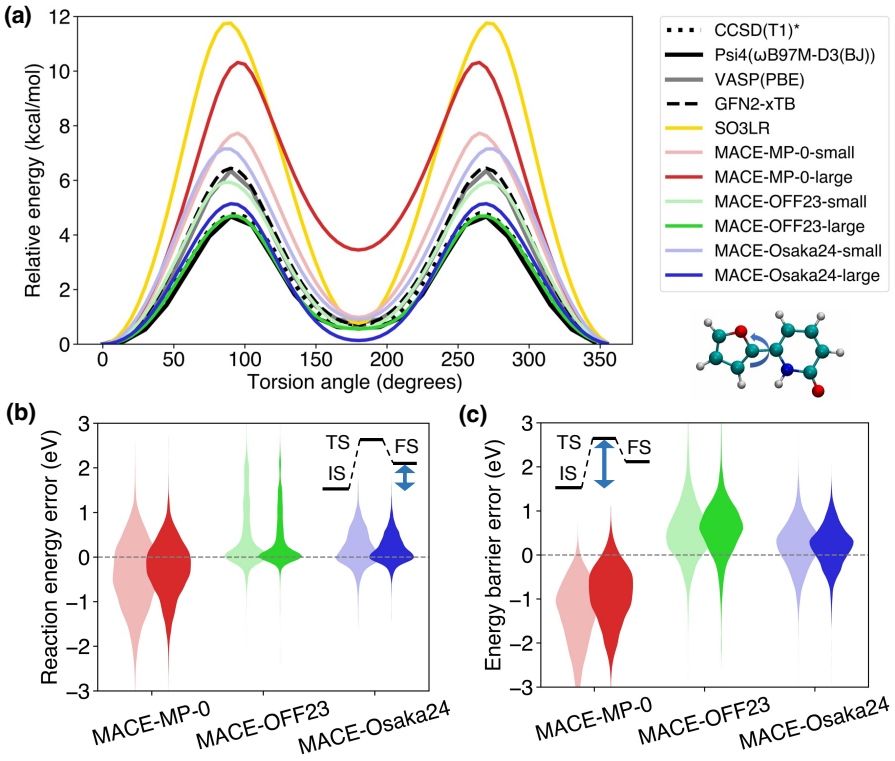

Figure 4.2: (a) The optimized torsional potential energy surface (PES) of dihedral torsion in a representative organic molecule in biaryl torsion dataset [306] shown on the right side the figure, comparing results across various machine learning interatomic potentials (MLIPs), including SO3LR, MACE-MP-0, MACE-OFF23, and MACE-Osaka24 models, alongside reference calculations from Psi4 (ωB97M-D3(BJ)), VASP (PBE) and ORCA (CCSD(T1)*). The CCSD(T1)* values are taken from biaryl torsion benchmark [306]. (b) A violin plot of reaction energy errors, where the reaction energy is defined as the energy difference between the initial state (IS) and the final state (FS). The errors are calculated based on single-point energy calculations obtained using the MACE-MP-0, MACE-OFF23, and MACE-Osaka24 models, compared to single-point energy at the ωB97M-D3(BJ) level with Psi4 for the 10,073 organic reactions of Transition1x dataset. The results for small models are shown with lighter colors, while those for large models are shown with darker colors. (c) Violin plot of energy barrier errors, where the energy barrier is defined as the energy difference between the IS and transition state (TS), compared to single-point energy at the ωB97M-D3(BJ) level with Psi4 for the 10,073 organic reactions of Transition1x dataset for the same models as in (b), with lighter and darker colors representing small and large models, respectively.

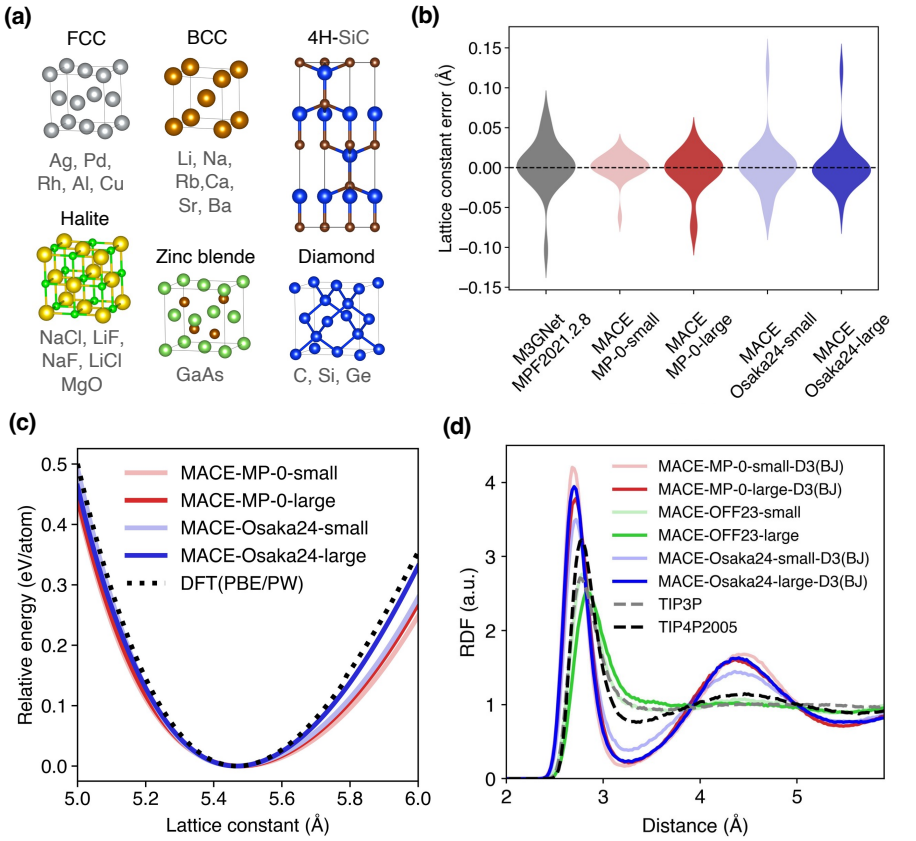

Figure 4.3: (a) Crystal structures and their representative materials used in the lattice constant benchmark shown in (b): Face centered cubic (FCC) (e.g., Ag, Pd), body centered cubic (BCC) (e.g., Li, Na), Halite (e.g., NaCl), Zinc blende (e.g., GaAs), and Diamond (e.g., C, Si). (b) Violin plot showing the lattice constant error (Å) for different models, including MACE-MP-0-small, MACE-MP-0-large, MACE-Osaka24-small, MACE-Osaka24-large, and M3GNet trained on the MPF.2021.2.8 dataset. The errors are calculated with respect to lattice constants optimized using VASP with the PBE functional, employing the MPRelaxSet input provided by pymatgen from the Materials Project. (c) Relative energy (eV/atom) as a function of the lattice constant (Å) for Diamond Si crystal, predicted using MACE models (MP-0 and Osaka24 variants) and compared with VASP calculations. The VASP calculations at level were performed using the MPStaticSet input provided by pymatgen. (d) Radial distribution function (RDF, a.u.) for liquid water obtained from NVT simulations. Results are shown for MACE-MP-0 and MACE-Osaka24 models with D3(BJ) corrections, as well as for classical MD simulations using TIP3P and TIP4P/2005 force fields.

is likely attributable to differences in the optimizer used for the torsional PES. Details of the biaryl torsion benchmark, including the computational settings for DFT and universal MLIPs, are described in Appendix B.c. The MACE-Osaka24-small and -large models achieved predictions that are 2.69 and 1.45 kcal/mol more accurate, respectively, compared to the predictions of MACE-MP-0-small and -large in torsion reactions of molecules. As shown in the study by Kovács et al. [278], the MACE-OFF23 models and semiempirical GFN2-xTB [307] method provide quantitative predictions within chemical accuracy (1 kcal/mol) with respect to calculations at the level of coupled cluster theory. Similarly, our MACE-Osaka24 models also achieve chemical accuracy, demonstrating its effectiveness in providing precise predictions for molecular torsions. Figure 4.2(a) shows the torsional PES of one of the molecules in the biaryl torsion benchmark. The MACE-MP-0-large model overestimates the barrier height of the torsion reaction by about twice. Compared to the PES calculated at the PBE level using VASP, the difference is large. This result suggests that for MLIPs trained only on inorganic crystal domains, quantitative prediction of organic molecular domains is difficult. The MACE-OFF23-small model gives predictions almost equivalent to the PBE level results. Our MACE-Osaka24-small model shows predictive performance almost equivalent to MACE-MP-0-small. The MACE-Osaka24-large model achieves predictive accuracy close to the high-fidelity ωB97M-D3(BJ), exceeding the predictive accuracy of the PBE level. These results suggest that learning datasets integrated by TEA allows the single model to inherit the accuracy of the original datasets.

Then, we evaluated the performance of universal MLIPs on the Transition1x dataset, focusing on their ability to predict reaction energies and energy barriers for 10,073 organic reactions. Details of the calculations are shown in Appendix B.d. Figure 4.2(b) shows the distribution of reaction energy prediction errors, where MACE-Osaka24 achieved the lowest error spread compared to MACE-MP-0 and MACE-OFF23. Similarly, Figure 4.2(c) highlights the performance on energy barrier prediction errors, indicating that MACE-Osaka24 consistently outperformed the other models, particularly in capturing transition state

Table 4.1: Mean absolute errors (MAEs) of barrier heights for 78 drug-like biaryl torsions, compared against high-fidelity reference energies. The values inside the parentheses were taken from Ref. [278].

Universal MLIP	MAE (kcal/mol)
MACE-OFF23-large	0.403 (0.3)
MACE-Osaka24-large	0.457
MACE-OFF23-small	0.598 (0.5)
MACE-Osaka24-small	0.695
GFN2-xTB	0.898
MACE-MP-0-large	1.909
SO3LR	2.451
MACE-MP-0-small	3.386

Table 4.2: Mean absolute errors (MAEs) of reaction energy and energy barrier predictions of 10,073 reactions in Transition1x dataset. The units are all in eV.

Universal MLIPs	Reaction energy	Energy barrier
MACE-Osaka24-large	0.265	0.404
MACE-Osaka24-small	0.336	0.457
MACE-OFF23-large	0.436	0.711
MACE-OFF23-small	0.544	0.672
MACE-MP-0-large	0.519	0.937
MACE-MP-0-small	0.686	1.333

(TS) regions with higher accuracy. Table 4.2 quantitatively supports these observations. The MAEs of the reaction energies predicted using MACE-MP-0-small, MACE-OFF23-small, and MACE-Osaka24-small are 0.686, 0.544, and 0.336 eV, respectively, and the respective MAEs of the predicted energy barriers are 1.333, 0.672, and 0.457 eV. The larger models of each potential exhibit further improvements, with MACE-Osaka24-large yielding the lowest MAEs of 0.265 and 0.404 eV for the reaction energies and energy barriers, respectively. These results demonstrate that MACE-Osaka24, especially in its large model, offers superior predictive accuracy for both reaction energy and energy barrier predictions in the Transition1x dataset. This highlights the importance of tailored model architectures and training datasets that explicitly include transition state regions, enabling MLIPs to achieve high accuracy even for reactive systems far from equilibrium.

Next, we present the results of accuracy verification of universal MLIPs for crystalline systems listed in Figure 4.3(a). The crystals used for the benchmark were those adopted in Section B.4 of the Supporting Information in the paper by Batatia et al [47]. Details of the calculation conditions for the crystal benchmarks can be found in Appendix B.3.e. The benchmark results for each crystal and crystal structure are discussed in detail in Appendix B.4. Figure 4.3(b) shows the error distributions of lattice constant predictions calculated using various universal MLIPs and VASP at the same computational level as the training data, specifically the PBE functional. The MAEs of the MACE-Osaka24 models are

Table 4.3: Mean absolute errors (MAEs) of lattice constants predicted by universal machine learning interatomic potentials (MLIPs) compared to PBE-level DFT calculations for bulk crystals

Universal MLIP	MAE (Å)
MACE-MP-0-small	0.012
MACE-MP-0-large	0.016
MACE-Osaka24-large	0.018
MACE-Osaka24-small	0.020
M3GNet-MPF2021.2.8	0.021

larger than those of the MACE-MP-0 models. However, as shown in Table 4.3, the MAEs of the predictions made by both the MACE-MP-0 and MACE-Osaka24 models are lower than those of the predictions made by the pretrained M3GNet model. The differences in predictive accuracy between MACE-MP-0 and MACE-Osaka24 were 0.008 Å and 0.002 Å for small and large models, respectively. This suggests that integrating data of organic molecules with different fidelities and domains using TEA does not deteriorate the original predictive accuracy. Figure 4.3(c) shows the PES for the lattice constant of diamond Si as an example. All models accurately predict the equilibrium lattice constant at the PBE level calculated using VASP (calculation conditions of the MPStaticSet of the Materials Project). Furthermore, the performance of PES description was better in MACE-Osaka24 compared to MACE-MP-0 with respect to the VASP calculation results. This is likely coincidental but demonstrates the high robustness of multi-domain universal MLIPs.

Finally, Figure 4.3(d) shows the radial distribution function (RDF) of O–O atoms obtained by MD of bulk liquid water at room temperature (300 K), which is important for both organic and inorganic materials. The MACE-MP-0 and MACE-Osaka24 models apply the D3(BJ) correction. Details of the MD calculations using MLIPs and classical force fields are provided in Appendix B.3.f. The MACE-OFF23 model describes the properties of liquid water at room temperature well [278]. MACE-MP-0-D3(BJ) reproduces the RDF at the PBE-D3(BJ) level [47]. Our MACE-Osaka24-large-D3(BJ) provides RDF descriptions almost equivalent to MACE-MP0-D3(BJ). On the other hand, MACE-Osaka24-small-D3(BJ) gives an RDF that is approximately intermediate between MACE-MP-0 and MACE-OFF23. This suggests that the ability to describe dynamic properties changes significantly depending on the complexity of the architecture and the balance of the dataset.

4.6 Discussion

Our results show that TEA is an effective way to combine different datasets. By aligning inner-core reference energies and adjusting atomization energies, TEA bridges differences caused by varying computational details such as basis sets and exchange-correlation functionals. Using TEA, we merged the MPtrj inorganic crystal dataset with the OFF23 organic dataset to train MACE-Osaka24—a multi-domain MLIP that achieves accuracy on par with specialized models like MACE-MP-0 and MACE-OFF23, while covering a much wider range of chemical systems.

The key advantage of TEA is that it simplifies data integration without changing the MLIP's architecture. Unlike methods such as Δ-machine learning or multi-fidelity SevenNet, which often target specific domains or fidelity levels, TEA offers a general, straightforward way to combine datasets. This approach allows researchers to use existing data from various sources without extensive recalculations. By showing that a single model—MACE-Osaka24—can accurately predict molecular reaction energies, lattice constants in inorganic crystals, and

the properties of liquid water, we confirm that the resulting PES maintains physical consistency and meaningful energy gradients across diverse chemical environments.

Nonetheless, some limitations and challenges remain. The current implementation relies on the availability of suitable reference atomic energies and reference geometries, which can be more difficult for systems with strong electron correlations, charged species, or relativistic effects. While using a single global scaling factor for atomization energies worked well here, certain specialized cases may need more nuanced correction schemes. Future improvements might include adaptive correction functions or machine learning models that predict fidelity differences, further enhancing TEA's generality and accuracy.

Future work could test TEA on datasets obtained from higher-level quantum chemical methods or directly include correlation and relativistic effects. Continued advances in neural network architectures, training methods, and hyperparameter optimization will also likely improve the robustness and accuracy of universal MLIPs. As research communities produce larger and more varied first-principles datasets, the concepts demonstrated by TEA and MACE-Osaka24 can guide the development of more fully integrated and widely accessible foundation models. Such models, firmly based on reliable first-principles accuracy yet adaptable to different computational approaches, will help us better explore and understand increasingly complex chemical systems.

4.7 Conclusion

We introduced the total energy alignment (TEA) methodology as a robust and efficient framework for unifying heterogeneous quantum chemical datasets into a single-level potential energy surface. Using TEA, we created MACE-Osaka24, a single universal MLIP that achieves state-of-the-art accuracy for both molecular and crystalline systems. It matches the performance of specialized models like MACE-MP-0 for inorganic solids and MACE-OFF23 for organic molecules, all without expensive recalculations under a single theoretical framework.

The impact of TEA goes beyond its technical contributions. By enabling the integration of diverse datasets without expensive recalculations, it helps democratize the development of foundation models in chemistry. This approach aligns with the move toward open science, where using a wide range of data sources is increasingly essential. As the chemistry and materials science communities continue to produce larger, more varied datasets, TEA provides a practical route to truly universal MLIPs, accelerating the discovery of materials, drugs, and catalysts through collaborative, data-driven research.

Chapter 5

Universal Neural Network Potentials as Descriptors: Towards Scalable Chemical Property Prediction Using Quantum and Classical Computers

5.1 Abstract

Accurate prediction of diverse chemical properties is crucial for advancing molecular design and materials discovery. Here we present a versatile approach that uses the intermediate information of a universal neural network potential as a general-purpose descriptor for chemical property prediction. Our method is based on the insight that by training a sophisticated neural network architecture for universal force fields, it learns transferable representations of atomic environments. We show that transfer learning with graph neural network potentials such as M3GNet and MACE achieves accuracy comparable to state-of-the-art methods for predicting the NMR chemical shifts of using quantum machine learning as well as a standard classical regression model, despite the compactness of its descriptors. In particular, the MACE descriptor demonstrates the highest accuracy to date on the ^{13}C NMR chemical shift benchmarks for drug molecules. This work provides an efficient way to accurately predict properties, potentially accelerating the discovery of new molecules and materials. This chapter is based on Ref. [Shiota, Ishihara, Mizukami, Digital Discovery, **3**, 1714-1728 (2024)].

5.2 Introduction

As evidenced by the enumeration of 166.4 billion possible organic molecules containing up to 17 heavy elements, such as C, N, O, S, and halogens (excluding hydrogen), the expansion of the chemical space is astronomical with the increase in types and numbers of elements [308, 309]. This vast landscape has given rise to multidisciplinary approaches to combining experimental and computational chemistry for the discovery of new chemical substances and materials in a wide range of fields, including material, catalysis, and drug design [308, 309, 310, 311, 312, 313]. Although quantum chemistry and first-principles calculations offer accurate descriptions of chemical substances, their high computational demands make an exhaustive exploration of the chemical space impractical [314, 315, 316, 124, 39, 317, 313]. However, machine- and deep-learning techniques are overcoming these limitations to enable a more extensive exploration [318, 58, 143, 44, 319, 124, 139, 148, 320, 138, 311, 56, 135, 321, 266, 322, 323, 313].

With machine learning, physics-inspired descriptors that characterize the chemical space have been developed and serve as the cornerstone for building efficient and highly accurate models [134, 132, 324, 137, 325, 140, 141, 147, 326, 146, 138, 142, 135, 327, 133]. Smooth overlap of atomic positions (SOAP) [134, 58, 136, 137, 325, 139, 138], Faber–Christensen–Huang–Lilienfeld (FCHL) [132, 324, 140, 141, 142], and similar descriptors offer atom-level descriptions within molecular or material environments based on physical insights and are effective in regressing chemical quantities, such as interatomic potentials (IAP) and nuclear magnetic resonance (NMR) chemical shifts [134, 58, 136, 328, 132, 324, 143, 137, 325, 140, 141, 147, 326, 39, 146, 138, 142, 135, 321, 145]. Notably, IAPs built using descriptors and Gaussian process regression (GPR) [58] have been termed Gaussian approximation potentials (GAP) and have found success in the exploration of the chemical space of molecules and materials [58, 146, 138]. Both kernel ridge regression (KRR) and GPR have been employed to improve the accuracy of NMR chemical shift prediction [144, 136, 328, 132, 324, 145]. However, the dimensionality of the descriptors becomes a barrier to generalization and high accuracy as the molecular or material composition becomes more diverse owing to the addition of different types of elements [147, 148, 149, 327].

Recently, deep-learning models based on graph neural networks (GNNs) have been proposed to describe chemical spaces using graph representations [329, 330, 331, 332, 333, 316, 319, 139, 229, 231, 148, 232, 334, 335, 320, 149, 336, 337, 338, 321, 266, 339, 264, 124, 237, 236, 278, 47]. In most GNN-based IAPs, atoms within a molecular or material environment are represented as nodes, and their local connectivity as edges in a graph. The graph is then convolved to embed atom-specific information within each node, and further processed using multilayer perceptrons (MLP) to predict target observables. In molecular and materials simulation and modeling, the consideration of symmetry is extremely important. It is desirable for GNNs to be invariant or equivariant to symmetry operations such as translation, rotation, and reflection for the models to make

physically meaningful predictions. GNNs that possess these properties are referred to as invariant GNNs or equivariant GNNs. The universal GNN-based IAPs proposed thus far have been designed to satisfy these symmetries. Recently, E(3) or SE(3) equivariant GNN-based IAPs (e.g., Allegro [237], GNoME [266], MACE [236, 278, 47]) have demonstrated superior performance compared to E(3) invariant GNN-based IAPs [115, 340] (e.g., MEGNet [231], M3GNet [124]).

Similarly, GNN-based models have been developed to predict NMR chemical shifts [329, 330, 332, 333, 341, 339]. DFT-level calculations of NMR chemical shifts for ^{1}H and ^{13}C have demonstrated the ability to predict within a target accuracy range of 1-2% relative to the possible ranges of approximately 10 ppm and 200 ppm, respectively [342, 343]. Therefore, the uncertainty in machine learning models using DFT-level datasets is this level of precision, with the target accuracy of 0.2 ppm for ^{1}H and 2 ppm for ^{13}C [324]. For example, Yanfei Guan et al. achieved the target accuracy of 0.16 ppm for ^{1}H and 1.26 ppm for ^{13}C by training the SchNet architecture [229] on molecular NMR chemical shifts (CASCADE) [329].

However, the scalability remains an issue due to the increasing optimization costs of GNN and MLP parameters when the size of datasets increase. Han et al. addressed this issue by constraining the nodes in a GNN to heavy elements only, thereby rendering the construction of scalable GNN-based NMR chemical shift models feasible while achieving a state-of-the-art prediction accuracy comparable to that of CASCADE [341]. Furthermore, NMR chemical shifts of various nuclei beyond hydrogen and carbon have become crucial for understanding systems involving a wide range of elements, such as proteins and solids [344, 345, 346, 347, 348, 349, 350]. Consequently, efforts are being made to develop machine learning models for NMR chemical shifts of nuclei such as ^{15}N, ^{17}O, and ^{19}F [348, 349, 346, 347]. These elements exhibit wide chemical shift ranges, with about 600, 2500, 500 ppm for ^{15}N, ^{17}O, and ^{19}F, respectively. The target accuracy for these nuclei is set at 6 ppm for ^{15}N, 25 ppm for ^{17}O, and 5 ppm for ^{19}F [344, 345, 346, 347, 348, 349, 350].

Notably, both descriptor-based and GNN-based methods face challenges. The former faces increased learning costs as the composition becomes more complex, and the latter faces increasing parameter optimization costs with larger training datasets. To address these issues simultaneously, we focused on the potential utility of the outputs from pre-trained GNN-based IAPs as descriptors. We considered these outputs GNN transfer learning (GNN-TL) descriptors and built machine-learning models for predicting chemical properties. Note that there are existing studies attempting to apply pre-trained GNN potentials to other tasks, particularly to generative modeling [351, 352, 353, 354].

The remainder of this chapter is organized as follows. Section 5.3 details the GNN-TL descriptor and the kernel method, implemented on both classical and quantum computers, for predicting NMR chemical shifts of ^{1}H, ^{13}C, ^{15}N, ^{17}O, and ^{19}F. Section 5.4 presents the performance of our developed machine learning models. Section 5.5 discusses the benefits and applications of the GNN-TL descriptor. Finally, Section 5.6 concludes this chapter.

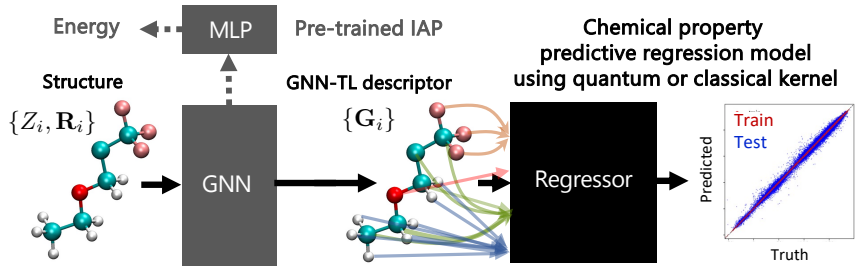

Figure 5.1: Schematic diagram of our proposed graph neural network transfer learning for predicting chemical properties. The black arrows depict the flow of our transfer learning process. The gray area is a pre-trained IAP (NNP) designed for predicting the energy of the system and composed of a GNN and an MLP. The initial step in our learning procedure involves obtaining the pre-trained GNN block output a set of vectors, $\{\mathbf{G}_i\}$, using the atomic coordinates of a molecule with N atoms, $\{Z_i, \mathbf{R}_i\}$ as input. Subsequently, we construct a regression model to predict the chemical properties *e.g.* NMR shielding constants, using this GNN output $\{\mathbf{G}_i\}$ as a descriptor.

5.3 Method: Transfer Learning Using Pre-Trained Graph Neural Networks

In this section, we discuss the transfer learning of a pre-trained GNN-based IAP. This approach integrates the outputs from the GNN layer of the IAP as shown in Figure 5.1. The architecture of a GNN-based IAP can be broadly segmented into a GNN layer and an MLP layer (gray area of Figure 5.1). For the E(3) invariant GNN-based IAP, we opted for two backbones: a MEGNet pre-trained on the QM9 dataset [131] and a M3GNet trained on the MPF.2021.2.8 dataset, which encompasses compounds covering all 89 elements from the Materials Project [124]. The parameters of the GNN layer in the M3GNet IAP were optimized to predict system energy, forces, and stress tensors. Additionally, we incorporated the E(3) equivariant GNN-based IAPs, namely MACE [236, 47, 278], into our study. We employed two types of pre-trained MACE IAPs: one trained on a larger dataset named MPtrj [116] from Materials Project, referred to as the MACE-MP-0 model [47], and another trained on an organic molecule dataset covering 10 types of elements including SPICE [119] and QMug [257], termed the MACE-OFF23 model [278]. Each model has variations in parameter size, and for this chapter, we utilized the "small" and "large" versions [47, 278].

When fed with the atomic coordinates of a molecule with N atoms, denoted by $\{Z_i, \mathbf{R}_i\}$, where Z_i represents the atomic number indicating the type of each atom, and $\mathbf{R}_i$ is the three-dimensional position vector of the ith atom, the GNN layer generates a set of vectors, $\{\mathbf{G}_i\}$, which mirrors the environment of the ith atom in the molecule. This is referred to as the GNN-TL descriptor. The

GNN layer for both MEGNet and M3GNet outputs GNN-TL descriptors with dimensions of 32 and 64 per atom, respectively. On the other hand, MACE is a GNN architecture that predicts energy in the form of atomic cluster expansion. As in Ref.[355], only the output of the 1st layer of the GNN layer, corresponding to the one-body term of the many-body expansion, is used as the GNN-TL descriptor. The dimensions of this GNN-TL descriptor are 128, 256, 96, and 224 per atom for MACE-MP-0-small, MACE-MP-0-large, MACE-OFF23-small, and MACE-OFF23-large, respectively.

Using GNN-TL descriptors as input, a regression model was constructed to predict NMR chemical shielding constants. For the regressor, one can choose methodologies, such as GPR, KRR, or feed-forward neural network (NNs), which are contingent on the specific task. To ensure a maximally fair comparison with other descriptor-based techniques, we adopted KRR.

KRR combines the merits of ridge regression, which offers regularization to mitigate overfitting, with the kernel method, facilitating nonlinear regression. In kernel methods, the data —in the context of this study, the GNN-TL descriptors— are mapped into a high-dimensional feature space through a non-linear kernel function. The Laplacian and Gaussian kernels were applied:

$$k\left(\mathbf{G}_i, \mathbf{G}_j\right) = \exp\left(-\gamma \left\|\mathbf{G}_i - \mathbf{G}_j\right\|_p^p\right), \tag{5.1}$$

where γ is the hyperparameter of the kernel and p is the norm parameter that differentiates the type of kernel: $p = 1$ for the Laplacian kernel and $p = 2$ for the Gaussian kernel. In KRR, the predicted value $\hat{\sigma}_t$ for the target chemical property of the target atom is derived from the GNN-TL descriptor $\mathbf{G}_t$ as follows:

$$\hat{\sigma}_t\left(\mathbf{G}_t\right) = \sum_i^N \alpha_i k\left(\mathbf{G}_i, \mathbf{G}_t\right) \tag{5.2}$$

Here, α_i represents the i^{th} element of the regression coefficient vector, $\boldsymbol{\alpha}$, of size N. The regression coefficients are determined by solving a ridge-regularized least-squares problem, which can be reduced to:

$$\boldsymbol{\alpha} = (\mathbf{K} + \lambda \mathbf{I})^{-1} \boldsymbol{\sigma} \tag{5.3}$$

where $\mathbf{I}$ denotes the identity matrix, $\boldsymbol{\sigma}$ denotes the chemical properties of each N training data samples, and λ denotes the regularization parameter. The matrix $\mathbf{K}$, is a kernel matrix, with elements given by $k\left(\mathbf{G}_i, \mathbf{G}_j\right)$.

All computations related to the KRR were executed using Scikit-learn v.1.2.2 [356], and the hyperparameters of each model were tuned using Optuna v.2.10 [357]. For dataset sizes of up to 50,000 items, we conducted hyperparameter optimization for 100 iterations with ten-fold cross-validation, while for those at 100,000, we limited the optimization to 10 iterations.

The quantum-kernel method leverages quantum computers to compute kernels [44, 10, 358], which is achieved by embedding feature vectors generated by classical computers into quantum states. This method calculates the inner

product of these quantum states to derive the desired kernels. Embedding feature vectors into quantum states corresponds to mapping them onto a Hilbert space with dimensions raised to the power of two quantum bits (qubits). Using the kernel matrix constructed on a quantum computer, we performed a KRR, denoted as quantum KRR (QKRR).

In this study, we adopted the natural parameterized quantum circuits (NPQC) kernel, which has been demonstrated to possess performance characteristics similar to the Gaussian kernel, both theoretically and in actual hardware experiments [359, 360, 361]. All computations were conducted using Scikit-qulacs [356, 362, 209]. The quantum kernel was constructed in a 10-qubit space. Hyperparameters for the quantum kernel were determined through grid search. The determined parameters of NPQC kernel were $c = 1.5$ and the repetition times of embedding 40. The regularization hyperparameter in QKRR was determined using 10 iterations of randomized search.

5.4 Results

In Section 5.4.1, because we deal with many elements, we compared the dimensional efficiency of our proposed GNN-TL descriptor to well-established physics-inspired descriptors. Note that the GNN-TL descriptor can better handle complex chemical systems by exploiting the GNN-based IAP architecture.

In Section 5.4.2, we focused on the accuracy of the GNN-TL descriptor in predicting NMR chemical shifts, which are key to understanding molecular details (*e.g.*, interatomic distances and bond angles). This scenario provides an appropriate test to determine how well the GNN-TL descriptor works.

Our analysis began by comparing quantum kernel learning, in which the kernels are tested using a quantum computer emulator with traditional kernel learning methods. We then checked the accuracy of the GNN-TL descriptors across the different pre-trained GNN models.

Finally, we juxtaposed our GNN-TL descriptor using well-established physics-inspired descriptors. This comparison demonstrates the superiority of the proposed descriptor in terms of efficiency and accuracy. Furthermore, it highlights its potential for accurately predicting chemical properties, which is crucial for advancing research in the molecular and material sciences.

5.4.1 Dimensional Efficiency

At the atomic level, descriptors are tools designed to encode information about atoms within molecules or crystalline materials into vectors. Popular descriptors, such as SOAP and FCHL18, excel at intricately capturing the environment within an atom's cutoff radius. Although these descriptors have achieved significant success in various accuracy benchmarks, they also present challenges due to their large dimensions. Various strategies have been developed to address these challenges [364, 365, 366, 141], including refining the descriptor itself, using principal component analysis for dimensionality reduction, and exploring NNs

to encode them. In particular, Christensen et al. applied Behler's method of the atom-centered symmetry function [228] for NN potential to discretize FCHL18 [140] to derive a compact and accurate FCHL19 [141].

In Table 5.1, we present the scaling of the SOAP, FCHL19 and various GNN-TL descriptors in response to an increase in the number of elemental species considered. Additionally, for the QM9, QMugs [257], and MPF.2021.8 or MPtrj datasets [124], the descriptor dimensions corresponding to 5, 10, and 89 elemental species comprising each dataset are summarized, respectively. Remarkably, with an increase in the number of element types, both SOAP and FCHL19 exhibited quadratic scaling. As a snapshot, when representing five elements in the QM9 dataset, the SOAP and FCHL19 methods have dimensions of 5,740 and 740, respectively. This dimensional disparity increases with the number of elemental types. Hence, to represent the 89 elements, the dimensions increased to 1,737,120 and 162,336, respectively. These dimensions are hundreds to tens of thousands of times larger than the compact GNN-TL descriptors, which ranges from 64 to 256 dimensions. Owing to its consistent dimensionality, irrespective of the increase in elements, the GNN-TL descriptors are overwhelmingly compact.

5.4.2 Prediction Accuracy: Nuclear Magnetic Resonance Chemical Shifts

The NMR chemical shifts, δ, were predicted using the chemical shielding constant of the reference substance, σ_{ref}, as the baseline. The NMR chemical shift was calculated using the following equation:

$$\delta = \sigma_{\text{ref}} - \sigma. \tag{5.4}$$

The reference substances selected for the various nuclei in this study are widely recognized and commonly adopted in the literature [367, 368, 369, 370, 132]. Specifically, tetramethylsilane was selected for both ^{1}H and ^{13}C, nitromethane ($MeNO_2$) for ^{15}N, water-^{17}O ($H_2{}^{17}O$) for ^{17}O, and trichlorofluoromethane ($CFCl_3$) for ^{19}F. We determined the chemical shielding constants for these well-established reference substances as follows: 31.7608 ppm for ^{1}H, 187.0521 ppm for ^{13}C, -147.8164 ppm for ^{15}N, 325.8642 ppm for ^{17}O, and 171.2621 ppm for ^{19}F. These constants were evaluated by calculations at the mPW1PW91 [371]/6-311+G(2d,p) level using density functional theory (DFT) and gauge-including atomic orbital (GIAO) [130] methods. Structure optimization was conducted at the B3LYP [305]/6-31G(2df,p) level in alignment with the methodologies employed for the QM9 NMR dataset. All calculations were performed using the Gaussian 16 software suite [288].

In this study, we utilized the QM9NMR dataset, which contains approximately 134K small organic molecules containing C, N, O, and F (excluding H), with each molecule having no more than nine atoms [132, 131]. This dataset provides the detailed NMR chemical shielding constants for these molecules. To analyze how the model accuracy changes with training data size, we adopted an approach similar to that used in the original publication of the QM9NMR dataset [132].

Specifically, for ^{13}C, of a total of 831K data points, we randomly withheld 50,000 data points to build our test set. Subsequently, from the remaining ^{13}C NMR chemical shifts, we randomly selected subsets containing 100, 200, 500, 1000, 2000, 5000, 10,000, 50,000 and 100,000 data points to create various training sets. For the other isotopes (*i.e.*, ^{1}H, ^{15}N, ^{17}O, and ^{19}F), the test sets were similarly established by withholding 50,000, 30,000, 50,000, and 1000 data points, respectively. The training size for ^{19}F was set to 2K, whereas the other isotopes were trained on datasets of 100,000 data points. In addition to the QM9 NMR dataset, we sought to validate the performance of our model on external datasets. Hence, we employed the two sets of molecules provided in another study [132]; one consisting of 40 drug molecules from the GDB17 universe and another containing 12 drugs with 17 or more heavy atoms.

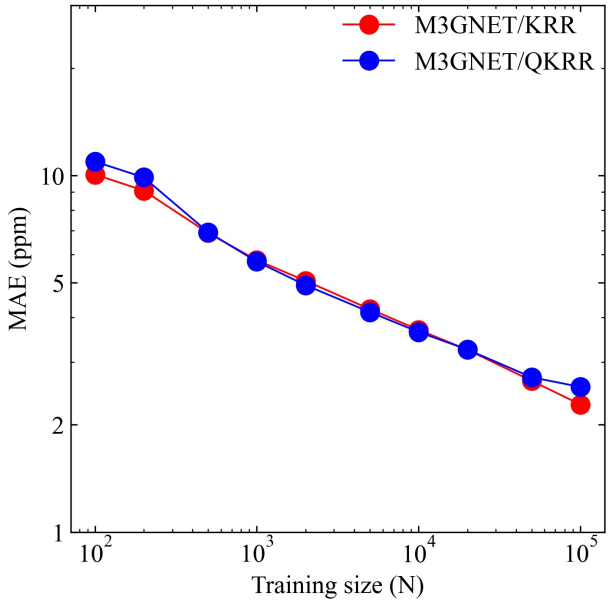

Figure 5.2: Log-log plot of the training size (N) and MAE for the ^{13}C NMR chemical shielding constant prediction model. The red and blue colors represent the results of the KRR with the Laplacian kernel and QKRR with the NPQC kernel using GNN-TL descriptors from the pre-trained M3GNet model, respectively.

Figure 5.2 shows the relationship between the mean absolute error (MAE) for the ^{13}C NMR shielding constant predictions and the training data size. Both QKRR and KRR demonstrated consistent improvements in predictive accuracy with an increase in training size. Notably, the quantum kernel exhibited a performance comparable to that of the Laplacian kernel. For a training size of 100,000, the MAE for the ^{13}C predictions was 2.28 ppm when using Laplacian-

kernel KRR, while NPQC-kernel QKRR yielded an MAE of 2.55 ppm. In a comparative study by Gupta et al., the KRR models using the Coulomb matrix (CM) [372], SOAP, and FCHL descriptors reported MAEs of approximately 4, 2.1, and 1.88 ppm, respectively, for the same training size [132]. Compared with the CM descriptor, our GNN-TL descriptor showed significantly better predictive capabilities, achieving an MAE that was nearly half that of the CM descriptor. Although our method did not exceed the accuracy levels of SOAP and FCHL, the performance of the GNN-TL descriptor was competitive, highlighting its potential as a robust descriptor.

Next, we compared the performance of the GNN-TL descriptors derived from different IAP architectures. Recently, independent of our work, a predictive model for ^{13}C NMR chemical shielding was proposed using a pre-trained IAP known as SchNet, which is a pioneering GNN used as a descriptor [373]. This model was trained on 400 data points of ^{13}C NMR chemical shielding constants of the molecules in QM9 dataset [131], with the SchNet GNN-TL descriptor as an input to a feed-forward NN for regression. The predictive accuracy of the SchNet/NN was a root mean-squared error (RMSE) of 12.8 ppm. In pursuit of a fair comparison with their model, we applied KRR using pre-trained MEGNet, M3GNet and MACE GNN-TL descriptors, setting our training data size to 400 data points of ^{13}C NMR chemical shielding constants. To account for the influence of random sampling, we created 10 different training sets, each comprising 400 data points. The effect of potential data bias was then quantified by calculating the mean RMSE and standard deviation (STD) for each model. Detailed verification including kernel function dependencies can be found in the Appendix. The results of this comparative study are summarized in Table 5.2. In Table 5.2, the results for KRR using the Gaussian kernel, which showed superior accuracy compared to the Laplacian kernel, are presented.

In contrast to the SchNet/NN model's RMSE of 12.8 ppm, the MEGNet/KRR model shows significantly lower predictive accuracy with an RMSE of 20.08 $\pm$ 0.55 ppm, suggesting that the MEGNet descriptor is less effective for ^{13}C NMR chemical shielding data. The M3GNet/KRR model demonstrates a substantial improvement with an RMSE of 10.02 $\pm$ 0.37 ppm. Models using MACE descriptors show even greater accuracy: the MACE-MP-0-small/KRR and MACE-MP-0-large/KRR models achieve RMSEs of 9.77 $\pm$ 0.34 ppm and 9.74 $\pm$ 0.27 ppm, respectively. The best performance is observed with the MACE-OFF23-small/KRR model, which has an RMSE of 8.05 $\pm$ 0.19 ppm, with the MACE-OFF23-large/KRR model close behind at 8.15 $\pm$ 0.42 ppm. These results highlight the superior performance of the MACE descriptors, particularly MACE-OFF23-small, in enhancing the accuracy of KRR models for predicting ^{13}C NMR chemical shielding. A more detailed discussion of the nuances of these architectural differences is presented in Section 5.5.1.

The accuracy of KRR models incorporating the M3GNet GNN-TL descriptor with a Laplacian kernel for NMR chemical shifts was evaluated for each test set of the five different nuclei. Table 5.3 lists the statistical performance metrics for predicting NMR chemical shifts. Across all elements, the MAE for the test set remained below 5 ppm. The MAE for ^{1}H and ^{19}F were notably low at 0.18 ppm

and 2.65 ppm, respectively, indicating a high degree of prediction accuracy for these nuclei in the unseen molecular environments. The MAE for ^{17}O, although higher at 4.95 ppm, still reflects a reasonable predictive capability, given the complexity of the oxygen chemical shifts. The STD and interquartile range (IQR) values in the Table 5.3 represent the distribution of chemical shifts within the training data, rather than the accuracy of the model itself. Thus, the higher STD and IQR values for ^{17}O do not indicate a lack of model precision but rather the natural variability inherent in the ^{17}O chemical shifts within the training data. The MAE/STD ratio can still offer insights into model performance relative to data variability. For example, the relatively low ratio of ^{17}O (2.21%) suggests that the model predictions are consistent with the diversity of the training data. On the other hand, the higher ratios for ^{1}H (9.09%) and ^{19}F (7.78%) indicate that the accuracy of the models are not as high as desired, particularly when considering the range of chemical shifts represented in the training dataset. The maximum absolute error (MaxAE) for all nuclei is comparable to the STD of the training data. This is attributed to random sampling and is expected to improve with the application of more sophisticated data point sampling techniques, such as active learning.

Subsequently, these models were employed to predict the NMR chemical shifts of a single molecule $C_5H_5N_2OF$ containing five elements that was not included in the training data. The results are shown in Figure 5.3. The MAE for each nucleus were found to be 0.08 ppm for ^{1}H, 1.03 ppm for ^{13}C, 6.45 ppm for ^{15}N, 2.86 ppm for ^{17}O, and 6.73 ppm for ^{19}F. The remarkably low MAE for ^{1}H and ^{13}C underscores the high accuracy of our model for these nuclei, with predictions that closely mirror the calculated values. The model performed well for the more challenging ^{15}N and ^{17}O nuclei, where the chemical shifts can be significantly affected by subtle changes in the molecular structure and environment, as indicated by the MAE values. The ^{19}F nucleus, while having a higher MAE, showed excellent agreement with the DFT/GIAO calculations, suggesting that the model predictions were robust, even for nuclei with typically higher chemical shift ranges. These results demonstrate the strong predictive power and potential of the model as a reliable tool for accurately predicting NMR chemical shifts across a variety of nuclei, even in molecules beyond the scope of the training data.

We then expanded our assessment to evaluate the predictive ability of our model for molecules larger than those in the QM9 NMR dataset. As such, we incorporate the test sets provided in Ref. [132], which comprised 40 drug molecules from the GDB17 universe and another set containing 12 drugs with 17 or more heavy atoms. See Ref. [132] for the structures of these molecules.

Table 5.4 presents the benchmark results for each test set using our M3GNet GNN-TL descriptor and MACE-OFF23-small GNN-TL descriptor. For comparison, we used the FCHL descriptor from Gupta's study [132]. To ensure a fair comparison, we employed our GNN-TL descriptor models trained on a size of 100,000 ^{13}C chemical shielding constants. For both models, an increased molecular size in the dataset correlated with deterioration of the MAE value. Notably, although our M3GNet GNN-TL descriptor did not match the

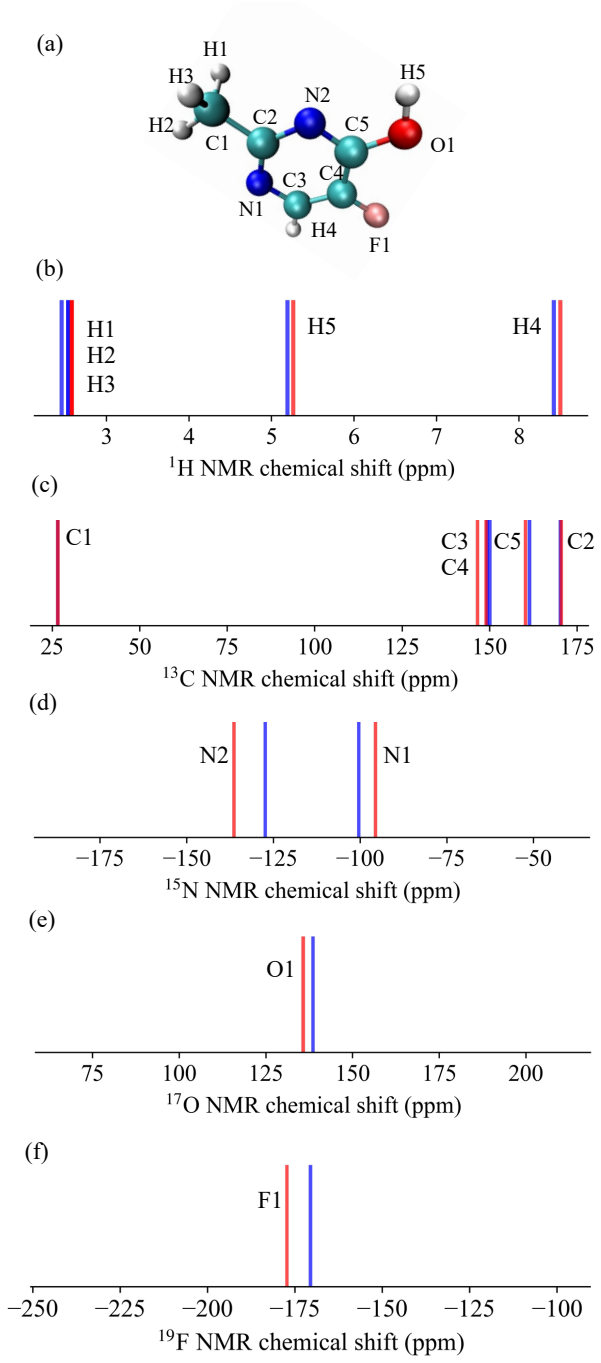

Figure 5.3: Predicted NMR chemical shifts for (a) a single molecule, randomly selected from the QM9NMR dataset and not included in the training data, for (b) ^{1}H, (c) ^{13}C, (d) ^{15}N, (e) ^{17}O, and (f) ^{19}F. These predictions (represented by red lines) are compared with the calculated values at the DFT/GIAO level, which are considered as the correct values (depicted by blue lines).

1.88 ppm value achieved by the FCHL descriptor for the QM9 50,000 test set, our model exhibited an MAE value that was approximately 0.3 ppm lower for the 40 GDB17 dataset test. The MACE-OFF23-small GNN-TL descriptor showed even better performance, with an MAE of 1.87 ppm for the QM9 50,000 test set, closely matching the FCHL descriptor, and significantly outperforming it for the 40 GDB17 dataset with an MAE of 2.83 ppm. For the set of 12 drugs with 17 or more heavy atoms, the M3GNet descriptor showed an MAE of 4.21 ppm, while the MACE-OFF23-small descriptor showed an MAE of 3.85 ppm. Notably, the M3GNet descriptor's accuracy is comparable to the FCHL descriptor. The results were nearly identical for the set of 12 drugs with 17 or more heavy atoms, highlighting that the M3GNet GNN-TL descriptor was less affected by increasing molecular size. On the other hand, the MACE-OFF23-small descriptor significantly outperforms FCHL with an MAE of 3.85 ppm, highlighting its superior predictive performance.

For a detailed comparison, Figure C11 illustrates the molecule-specific MAE values for both drug test sets. The molecular structures are provided in Ref. [132]. Our M3GNet and MACE-OFF23-small GNN-TL descriptor-based prediction models ensured that the highest MAE values for individual molecules across both test sets remained below 10 ppm. Intriguingly, the desflurane molecule, which posed the greatest challenge, showed MAE values of 53.3 ppm, 9.35 ppm and 8.31 ppm for the FCHL, M3GNet and MACE-OFF23-small GNN-TL descriptor models, respectively. This suggests an approximately 80% reduction in the MAE with our descriptor, which is likely attributable to differences in the encompassed descriptor domain.

The cutoff radius for the FCHL descriptor was determined through a grid search [132], which settled at 4.0 Å. In this scenario, the two fluorine atoms in the terminal trifluoromethyl group (CF_3) of the desflurane molecule, which lie beyond 4 Å from the CF_2H carbon, were neglected. In contrast, our M3GNet descriptor had a 5 Å cutoff radius during the initial graph configuration and a 4 Å cutoff for three-body interactions during graph convolution, capturing the entire CF_3 group. This suggests that the descriptor adequately accounts for the influence of the terminal trifluoromethyl group. Additionally, the intrinsic ability of GNN-TL descriptors to account for environments beyond their cutoff radius, owing to graph convolution, may have contributed to the substantial improvement in MAE. Notably, the MACE-OFF23-small model, with a cutoff value of 4.5 Å, achieves the highest accuracy, even though it does not capture the fluorine element at a distance of 4.65 Å in the CF_3 group. In summary, the proposed M3GNet and MACE GNN-TL descriptors demonstrate the capability of predicting ^{13}C NMR chemical shifts for molecules outside the training dataset with an accuracy comparable to that of the state-of-the-art FCHL descriptor.

Lastly, to explore further practical applications of the constructed models, we validated the NMR chemical shielding constants obtained using semi-empirical PM7-level geometries as inputs against the NMR chemical shift values obtained using DFT/GIAO-level structures from the training data. This validation was performed on the QM9 50,000 holdout set and two drug molecule test sets, as provided by Ref.[132]. The ^{13}C prediction model employed was the

M3GNet/KRR model. The MAE values for each molecule in the drug datasets can be found in Figures 6(b) and 6(d). For the QM9 50,000 holdout set, the result was 3.61 ppm, showing a significant deterioration of 1.33 ppm compared to when DFT-level geometries were used as inputs. Conversely, predictions for the 40 drugs and 12 drugs test sets showed only minor deteriorations of 0.23 ppm and 0.04 ppm, respectively. These results suggest that even when using more readily available PM7-level geometries as inputs, the transferability of the model remains robust for extrapolative predictions on larger molecules compared to the training data.

Table 5.1: Scaling of descriptor dimensions with respect to number of elemental species N_{elem}. SOAP descriptors were generated using Dscribe 0.4.0 [134] and FCHL19 descriptors using QML 0.4.0.12 [363], both with default hyperparameters as in the QM9NMR paper.

Method	N_{elem}	**Scaling**	**Dimension**
SOAP	5	$O(N_{\text{elem}}^2)$	5,740
	10	$O(N_{\text{elem}}^2)$	22,680
	89	$O(N_{\text{elem}}^2)$	1,737,120
FCHL19	5	$O(N_{\text{elem}}^2)$	740
	10	$O(N_{\text{elem}}^2)$	2,440
	89	$O(N_{\text{elem}}^2)$	162,336
SchNet GNN-TL	5	$O(1)$	128
	10	$O(1)$	-
	89	$O(1)$	-
MEGNet GNN-TL	5	$O(1)$	32
	10	$O(1)$	-
	89	$O(1)$	-
M3GNet GNN-TL	5	$O(1)$	64
	10	$O(1)$	64
	89	$O(1)$	64
MACE-MP-0-small GNN-TL	5	$O(1)$	128
	10	$O(1)$	128
	89	$O(1)$	128
MACE-MP-0-large GNN-TL	5	$O(1)$	256
	10	$O(1)$	256
	89	$O(1)$	256
MACE-OFF23-small GNN-TL	5	$O(1)$	96
	10	$O(1)$	96
	89	$O(1)$	-
MACE-OFF23-large GNN-TL	5	$O(1)$	224
	10	$O(1)$	224
	89	$O(1)$	-

Table 5.2: The architecture dependence of the predictive performance. For KRR, the Gaussian kernel was applied.

GNN-TL descriptor/Regressor	RMSE (ppm)
SchNet/NN [373]	12.8
MEGNet/KRR	20.08±0.55
M3GNet/KRR	10.02±0.37
MACE-MP-0-small/KRR	9.77±0.34
MACE-MP-0-large/KRR	9.74±0.27
MACE-OFF23-small/KRR	8.05±0.19
MACE-OFF23-large/KRR	8.15±0.42

Table 5.3: Predictive performance and data variability of NMR shielding constants for 5 elements

	^{1}H	^{13}C	^{15}N	^{17}O	^{19}F
MAE (ppm)	0.18	2.28	3.42	4.95	2.65
MaxAE (ppm)	7.50	68.58	71.62	279.84	39.31
STD (ppm)	1.98	51.96	119.58	224.40	34.07
IQR (ppm)	2.34	59.93	211.19	354.25	36.77
MAE/STD (%)	9.09	4.38	2.86	2.21	7.78

Table 5.4: The MAE values for the prediction of the 50,000 QM9NMR hold out set, 40 drug molecules from GDB17 Universe and the other containing 12 drugs with 17 or more heavy atoms. The values in parentheses indicate MaxAE. All units are in ppm.

	FCHL [132]	M3GNet GNN-TL	MACE-OFF23-small GNN-TL
50,000 QM9	1.88	2.28 (68.58)	1.87 (59.76)
40 drugs	3.7	3.46 (29.86)	2.83 (16.08)
12 drugs	4.2	4.21 (20.48)	3.85 (24.70)

5.5 Discussion

5.5.1 Influence of Architectural Choices on Graph Neural Network Transfer Learning Descriptor Performance

In our exploration of different architectures for generating GNN-TL descriptors, we observed several patterns. First, as shown in Table 5.1 and Table 5.2, it is important to note that the accuracy of GNN-TL descriptors does not necessarily improve with an increase in the dimensionality of the descriptors. With this in mind, we discuss the architecture of each GNN-based IAP. SchNet, which operates on GNN-based local descriptors to evaluate systems as summations of atomic energies, accounts only for pairwise interactions. This limited inclusion could potentially constrain expressions, leading to inadequate representational power. The subpar performance of MEGNet during transfer learning may be attributed to its architectural design as it integrates atomic (local) descriptors into molecular (global) descriptors through concatenation. This means that the final piece of information passed to the MLP is not extracted directly from the end of the model, which might not be the optimal representation for targeted atomic-wise property prediction; however, it is expected to be suitable for molecule-wise property predictions. Moreover, the M3GNet architecture, which considers three-body interactions, has the potential to capture the three-dimensional structure of molecules with high resolution. Additionally, the MACE model, an E(3) equivariant GNN, has demonstrated high performance as an IAP, suggesting that the outputs of its GNN layers are highly accurate in representing molecular structures. Furthermore, future improvements in accuracy may be achieved by leveraging the outputs of higher-order GNN layers in the MACE model, corresponding to the two-body and three-body terms in the atomic cluster expansion.

5.5.2 Significance of Dataset Size and Diversity

The M3GNet training regimen incorporates data from 187,687 ionic steps spanning 62,783 compounds, including 187,687 energies, 16,875,138 force components, and 1,689,183 stress components. This diverse dataset covers 89 elements from the periodic table. The model is not limited to learning only the energies associated with these elements but extends to atomic-level forces. Moreover, M3GNet training includes not only stable structures but also the processes of structure optimization. The ingestion of vast amounts of data from crystalline systems may have endowed the M3GNet with enhanced expression, potentially making it adept at interpolating molecular systems. The pre-trained MACE-MP-0 model was trained using ten times more energy data of crystalline systems, potentially contributing to the improved accuracy of the ^{13}C NMR chemical shift predictions shown in Table 5.2. On the other hand, the MACE-OFF23 model, which is specialized for molecules containing 10 elemental species, was trained on a dataset comprising about 1M energy data points, with structures containing up to 150 atoms. This extensive training dataset might

make it more suitable for predicting molecular NMR chemical shifts. Thus, the training data for IAPs, much like their architectures, could be a crucial factor in determining the performance of the descriptors.

5.5.3 Potential for Transfer Learning on Quantum Computers

There is a potential for leveraging quantum computation approaches [17]. Specifically, our 10 qubit QKRR, facilitated by a simulator, demonstrated a performance comparable to that of state-of-the-art KRR. This is underpinned by the theoretical equivalence of the NPQC with the Gaussian kernel. The quantum kernel method stands out because of its capability to compute with fewer measurement iterations than other quantum computation methodologies, such as quantum neural networks [9]. In particular, our proposed M3GNet GNN-TL descriptor can be feasibly realized with a minimum of six qubits, enabling evaluations with a quantum bit count that is more efficient than traditional descriptors, such as SOAP. However, embedding for higher-dimensional SOAP appears to be a challenge, possibly due to noise. From a futuristic perspective, there is excitement about the possibility of developing kernels that traditional computers cannot express, as well as accelerating the inversion calculations of kernel matrices using quantum algorithms. The constant scaling property of our proposed method concerning element number dimensions may significantly contribute to real-time material exploration powered by quantum-classical hybrid algorithms in the near future.

5.6 Conclusion

The dynamics of machine learning and its extensive applications across various domains are driving cutting-edge research. Our endeavor to integrate transfer learning with pre-trained IAP GNNs for NMR chemical shift prediction offers a paradigm shift in efficiency and scalability. The GNN-TL descriptor presents an unparalleled advantage in terms of scalability due to its consistent dimensionality, irrespective of the number of elements.

Comparative evaluations with other renowned descriptors, such as SOAP, suggest that the GNN-TL descriptor can match, if not surpass, the performance of its contemporaries while maintaining a more compact representation. This is especially important when factoring large datasets, where dimensionality can exponentially burgeon.

Architectural choice plays a pivotal role in the performance of GNN-TL descriptors. Moreover, the diversity and vastness of the training dataset, which encompasses myriad elemental types and structural configurations, augment the robustness and versatility of the GNN.

Our proposed model has immense potential for creating a unified framework capable of predicting various atomic and molecular properties simultaneously, presenting profound implications for accelerated material and molecular research.

This potential union of multiple predictions can usher in an era of comprehensive understanding and quicker innovations, possibly revolutionizing fields, such as catalysis, drug discovery, and material design.

The union of transfer learning with pre-trained GNNs not only augments prediction accuracy but also drastically reduces learning costs, presenting a cost-effective and efficient alternative to more computationally intensive methods. As we move toward an era in which data-driven insights and models govern the pace of innovation, the method proposed in this chapter offers a promising pathway for future endeavors in the domain of chemical property predictions with both classical and quantum computers.

Chapter 6

Lowering the Exponential Wall: Accelerating High-Entropy Alloy Catalysts Screening Using Local Surface Energy Descriptors from Neural Network Potentials

6.1 Abstract

Computational screening is indispensable for the efficient design of high-entropy alloys (HEAs), which hold considerable potential for catalytic applications. However, the chemical space of HEAs is exponentially vast with respect to the number of constituent elements, making even machine learning-based screening calculations time-intensive. To address this challenge, we propose a rapid method for predicting HEA properties using data from monometallic systems (or few-component alloys). Central to our approach is the newly introduced local surface energy (LSE) descriptor, which captures local surface reactivity at atomic resolution. We established a correlation between LSE and adsorption energies using monometallic systems. Using this correlation in a linear regression model, we successfully estimated molecular adsorption energies on HEAs with significantly higher accuracy than a conventional descriptor (i.e., generalized coordination numbers). Furthermore, we developed high-precision models by

employing both classical and quantum machine learning. Our method enabled CO adsorption-energy calculations for 1000 quinary nanoparticles, comprising 201 atoms each, within a few days, considerably faster than density functional theory, which would require hundreds of years or neural network potentials, which would have taken hundreds of days. The proposed approach accelerates the exploration of the vast HEA chemical space, facilitating the design of novel catalysts. This chapter is based on Ref. [Shiota, Ishihara, Mizukami, Digital Discovery, **4**, 738-751 (2025)].

6.2 Introduction

High-entropy alloys (HEAs), composed of five or more elemental species at concentrations ranging from 5 to 35 at%, have emerged as versatile materials with promising applications in catalysis and as functional materials [374, 375, 376, 377]. Their rich compositional diversity facilitates the way for the "cocktail effect", resulting in unexpected properties that often surpass those of traditional single-element systems [376, 378]. Recent advancements have highlighted their superior catalytic performance [379, 380, 381, 382]; however, the vast array of potential combinations of elements poses a significant challenge for experimental exploration.

To address this complexity, studies have focused on computational methods for efficient screening [383, 384, 385, 382, 386]. First-principles calculations, such as density functional theory (DFT) [127, 387, 81, 388], coupled cluster (CC) theory [389, 129, 390] and many-body perturbation theory (MBPT) [391, 128], describe chemical reactions on solid surfaces with high accuracy. Volcano plots, derived from first-principles calculations, illustrate the optimal adsorption energy range for catalytic activity, balancing between excessively strong and weak interactions [40, 392, 386]. However, the heterogeneous surfaces of HEAs complicate the molecular adsorption characteristics, making first-principles approaches computationally intensive..

To circumvent these limitations, neural network potentials (NNPs) based on the Behler-Parrinello framework [45, 228, 393, 394, 395] and graph neural networks [114, 396, 229, 230], offer promising solutions. Universal NNPs can encompass extensive elemental diversity and achieve high computational efficiency while maintaining accuracy on par with that of DFT [396, 229, 231, 397, 124, 264, 236, 116, 125, 251, 278, 47, 237, 335, 266]. Recently, NNPs specializing in HEAs have emerged, made more lightweight through knowledge distillation [398]. These advances have accelerated the prediction of catalytic properties; however, computational challenges remain.

In contrast, descriptor-based machine learning models offer scalability by predicting adsorption energies through generalized coordination numbers (GCNs), d-band centers, surface microstructural features, and local atomic environments, bypassing direct energy assessments [399, 400, 401, 402, 384, 403, 404, 405, 406, 383]. These models have been proposed for predicting the adsorption energies of the remaining candidates by regressing the adsorption energies obtained from

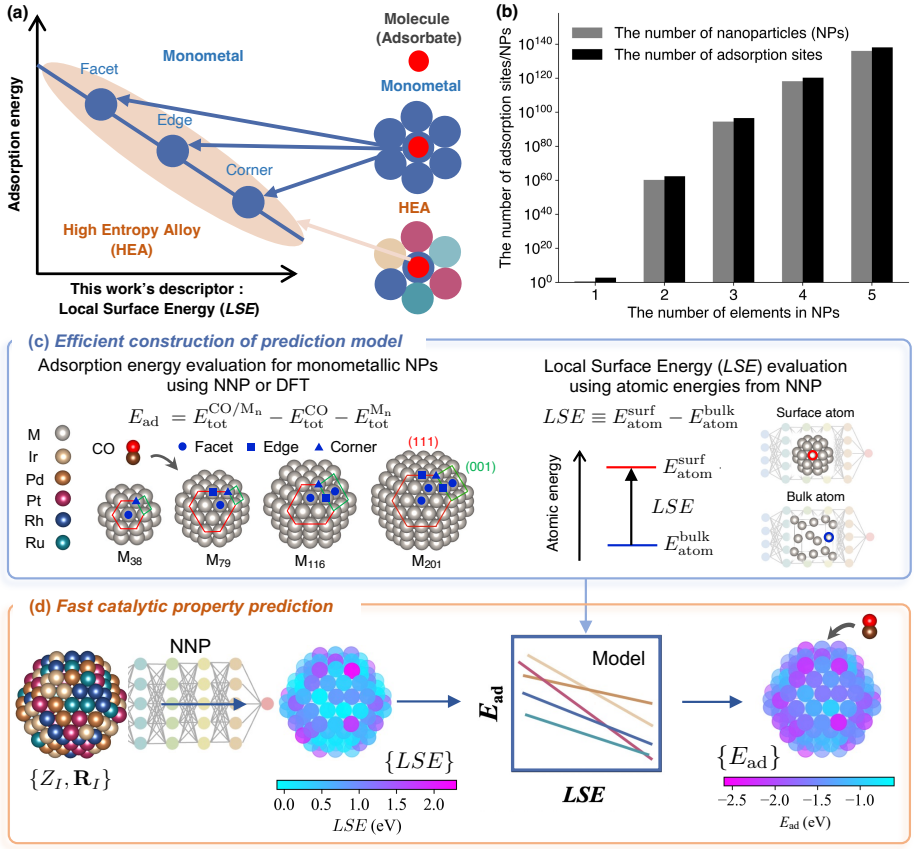

Figure 6.1: (a) Relationship between the molecular adsorption energy and the newly introduced descriptor, i.e., the local surface energy (LSE), for monometallic and high-entropy alloy (HEA) nanoparticle (NP) systems. The LSE descriptor developed in this chapter effectively captures the variation in adsorption energy across different adsorption sites and NP compositions. (b) Near-exponential increase in the number of NPs and adsorption sites as the number of elements in the NPs increases from monometallic to multicomponent systems. (c) The model is constructed through linear regression between the adsorption energies and the LSE using atomic energies from the NNP. The CO adsorption energies are evaluated on the ontop irreducible sites of facets (circles), edges (squares), and corners (triangles) of the monometallic NPs indicated by the blue symbols. (d) Fast catalytic property prediction workflow using neural network potentials (NNPs). The adsorption energy E_{ad} is predicted from the LSE of the HEA NP surface prior to adsorption.

several first-principles calculations. Nonetheless, their applicability to HEAs is hampered by the complexity of alloy compositions and their dependence on extensive first-principles calculations.

To address these challenges, we propose a methodology for predicting the molecular adsorption energies on multi-element surfaces, such as HEAs, without direct adsorption-energy computations. Our approach focuses on a new descriptor that reflects the local reactivity of solid surfaces at atomic resolution. A key feature of the proposed method is its ability to predict the properties of multi-element systems using models constructed from data on single-element systems. We validated our method by comparing it with DFT for predicting the adsorption energies of CO on IrPdPtRhRu HEA NPs.

6.3 Methods

In this section, we introduce a novel model that employs data on monometallic surfaces to predict molecular adsorption energies on multimetallic surfaces. In Section 6.3.1 2.1, we clarify the target systems and the problems addressed in this chapter. In Section 6.3.2, we introduce the LSE—a scalar descriptor that captures the atomic-level surface stability—which is the foundation of our model construction and prediction. Section 6.3.3 outlines the methodologies employed to develop and refine the prediction model using the newly introduced LSE descriptor and data derived from monometallic surfaces.

6.3.1 Target Systems and Problems

Designing new HEAs comprising five elements selected from a pool of approximately 40 different elemental candidates results in approximately 6.58×10^5 possible combinations. Moreover, even for a given set of five elements, an exponentially large degree of freedom exists in the distribution of these elements in the actual alloy. Furthermore, the catalysts synthesized in practice and use are NPs, which differ from ideal surfaces in that they contain sites with different coordination numbers, such as corners, edges, and facets (Figure 6.1(b)). These diverse surface environments are the source of the cocktail effect, which contributes to the variability in catalytic properties. However, considering all these degrees of freedom when screening new catalyst candidates is not feasible. In this chapter, our objective was to identify the distribution of molecular adsorption energies, assuming that the elemental composition, size, and shape of the HEA NPs were predetermined.

We made the following assumptions regarding the structure and composition of HEA NPs: the structure is a truncated octahedron NP with 201 atoms in a face-centered cubic (fcc) arrangement (see 6.1(d)), the elemental composition ratio is as uniform as possible, and the atomic arrangement is randomly determined following a uniform distribution. We also assumed that the molecule occupied only a single top site. In HEA_{201}, there are 122 sites. Even with these

assumptions, the number of adsorption sites on HEA NPs is approximately 1.3×10^{138} (Figure 6.1(a)).

As a specific demonstration system, we measured the adsorption energies of CO molecules on IrPdPtRhRu NPs. In 2020, Wu et al. successfully synthesized IrPdPtRhRu NPs with nearly identical experimental composition ratios [379]. The investigation of the adsorption characteristics of CO molecules is useful for evaluating the catalytic properties of HEAs [384, 407]. As precursor systems for developing predictive models for HEAs, the monometallic NPs are of the truncated octahedron type corresponding to M_n n=38, 79, 116, 201. For the on-top adsorption of the CO molecule on monometallic NPs M_{201}, only the irreducible adsorption sites are calculated as shown in Figure 6.1(c). The adsorption energy E_{ad} is calculated as follows:

$$E_{ad} = E_{tot}^{CO/M_n} - E_{tot}^{CO} - E_{tot}^{M_n}, \tag{6.1}$$

where E_{tot}^{CO/M_n}, E_{tot}^{CO}, and $E_{tot}^{M_n}$ denote the total energies of CO/M_n, CO, and M_n, respectively. The adsorption energies were computed using both the pretrained universal NNP M3GNet [124] and DFT at the Perdew-Burke-Ernzerhof (PBE) level.

6.3.2 Local Surface Energy Descriptor

The LSE descriptor is defined as follows:

$$LSE \equiv E_{atom}^{surf} - E_{atom}^{bulk}, \tag{6.2}$$

where E_{atom}^{surf} and E_{atom}^{bulk} denote the atomic energies in the surface and bulk environments, respectively. The LSE represents the energy loss caused by a single atom in a single-element (or unary) bulk environment when exposed to a single- or multi-element surface. This definition enables the quantification of the surface stability, even for surfaces in complex environments and multicomponent systems. The atomic energies in Equation (6.2) can be evaluated via energy density analysis (EDA) from first-principles calculations, such as DFT [408, 409, 410, 411, 412], which was introduced by Nakai in 2002 [408]. EDA is accurate because it is based on first-principles calculations; however, it is not suitable for exhaustive calculations, such as those in this chapter, because of its high computational cost. To reduce the computational cost, all the LSE values in this chapter were evaluated using a machine learning interatomic potential (MLIP), specifically the universal NNP M3GNet. In the previous chapter, we demonstrated that the intermediate information from M3GNet can efficiently and accurately represent the local environments of atoms in molecules [268]. In the Behler-Parrinello NNP framework, the total energy E_{tot} of a system comprising N atoms is calculated as the sum of the energies of the atoms.

$$E_{tot} = \sum_{I=1}^{N} E_{atom}^{I} \tag{6.3}$$

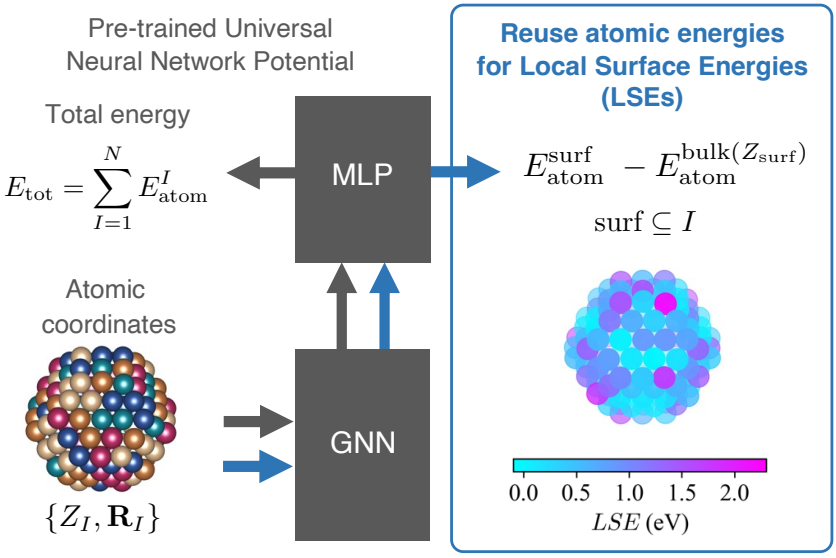

Figure 6.2: Framework for predicting Local Surface Energies (LSEs) using a pre-trained universal neural network potential (NNP). The gray arrow indicates the computational flow from the pre-trained universal NNP, and the blue arrow represents the flow that generates LSEs. Atomic coordinates $\{Z_I, R_I\}$ are processed by a graph neural network (GNN) layer to extract atomic features. A multi-Layer perceptron (MLP) layer predicts the atomic energies E^I_{atom}, which are reused to compute LSEs as the difference between surface atomic energies $E^{\text{surf}}_{\text{atom}}$ and bulk atomic energies $E^{\text{bulk}}_{\text{atom}}(Z_{\text{surf}})$. The resulting LSEs are visualized with a color map, highlighting local reactivity on the surface.

Yoo et al. demonstrated the ability to map the atomic energies obtained by NNPs onto NP and surface systems [413]. Deringer et al. utilized the Gaussian approximation potential model to compute the atomic energies, which were then used to explore the configurational space and investigate the nature of defects in crystals [414, 415]. MLIPs such as NNPs enable efficient evaluation of LSEs because the atomic energies of all adsorption sites in one system can be obtained in a single calculation. Figure 6.2 illustrates the workflow for evaluating the Local Surface Energy (LSE) using a pre-trained universal NNP.

6.3.3 Prediction Model Based on Monometallic Data

We introduce a predictive model for the adsorption energy of a molecule on a multi-element surface. This model is defined as a regression between the molecular adsorption energy on monometallic surfaces for each constituent element M of the multimetallic system and the LSE of the adsorption site prior to molecular adsorption. Figure 6.1(c) illustrates the workflow for constructing the predictive model. As the simplest model, we adopted the least-squares linear regression model expressed as follows:

$$E_{\mathrm{ad}}^{\mathrm{M}}(\mathrm{Predict.}) = \alpha_{\mathrm{M}} \times LSE + \beta_{\mathrm{M}}. \tag{6.4}$$

Here, α_{M} and β_{M} denote the regression coefficients and constants, respectively, for each element M. Simple regression makes the model explainable. α_{M} represents the magnitude of the adsorption energy response to a change in LSE. β_{M} represents the adsorption energy of a molecule when the LSE is 0, that is, when the surface atom has the same energy as that in the bulk environment. For prediction, the adsorption energy is estimated by substituting the LSE values of the multi-element alloy surface prior to molecular adsorption into Equation (6.4). Figure 6.1(d) illustrates the workflow for predicting CO adsorption energies on HEA NPs using the proposed model. Here, the prediction model using adsorption energies from the NNP for regression is referred to as the LSE-based prediction model, while the model using adsorption energies from DFT is referred to as the Improved-LSE (I-LSE) prediction model. Details of the model construction can be found in the Computational details section.

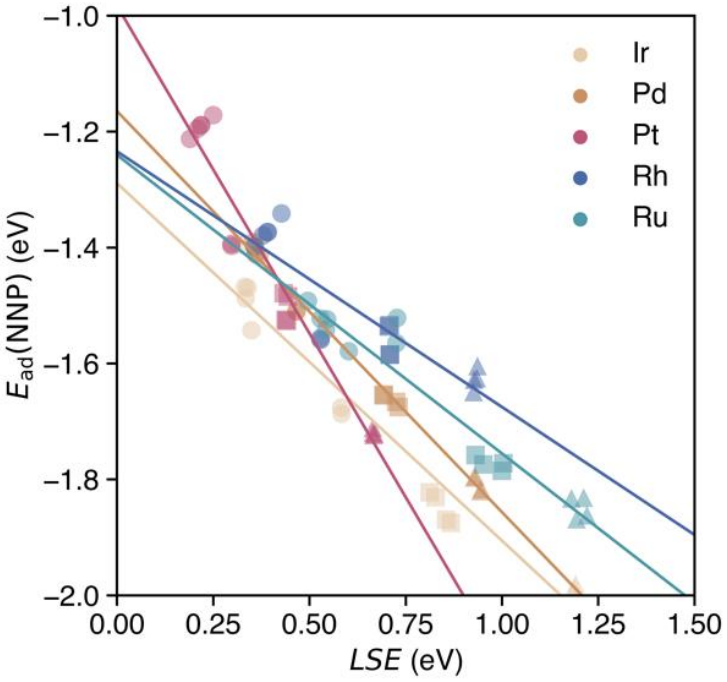

Figure 6.3: Adsorption energies of CO calculated using the NNP for each on-top adsorption site of monometallic NPs M_n with respect to the LSE. Solid lines represent the linear regressions of the adsorption energies of a CO molecule at the on-top sites of each monometallic NP according to Equation (6.4). Circles, squares, and triangles at each datapoint represent the facet, edge, and corner CO adsorption sites, respectively.

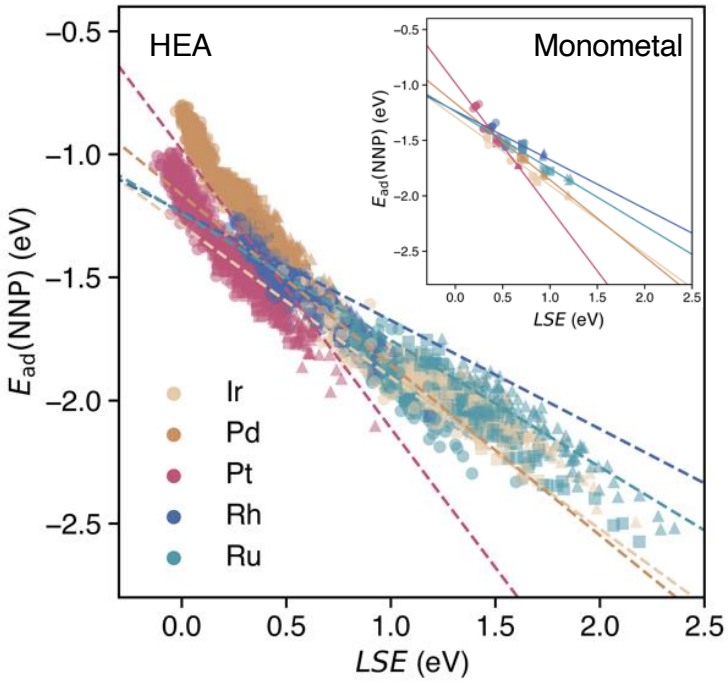

Figure 6.4: Adsorption energies of CO calculated using the NNP for each on-top adsorption site of 20 HEA_{201} NPs with respect to the LSE. The inset presents a comparison of the distribution of adsorption energies for CO between the HEA NPs and monometallic NPs, with the x- and y-axes rescaled from Figure 6.3 for consistency. Dashed lines represent the linear regressions of the adsorption energies of a CO molecule at the on-top sites of each monometallic NP based on Equation (6.4). Circles, squares, and triangles at each datapoint represent the facet, edge, and corner CO adsorption sites, respectively.

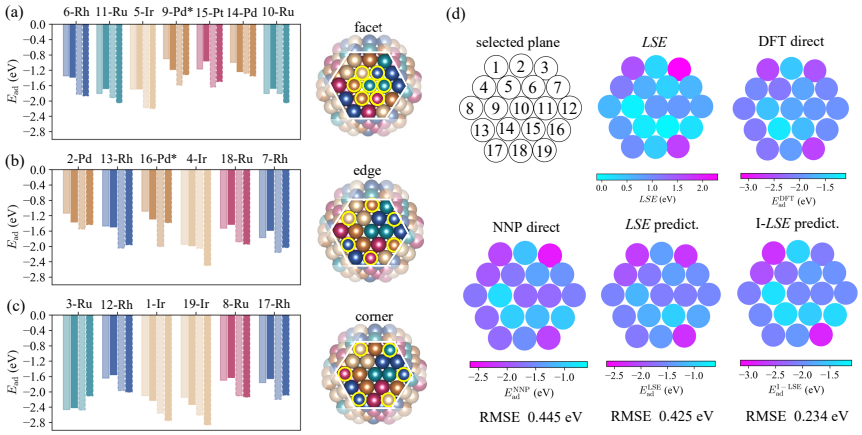

Figure 6.5: Bar graphs in (a), (b), and (c) show the evaluated adsorption energies of CO on the (111) plane of a randomly selected HEA_{201} at each on-top site of the facet, edge, and corner, respectively. The atoms of the selected plane are numbered as shown in (d). For each adsorption site, from left to right, the bar graph represents the adsorption energy obtained via direct evaluation using NNP (NNP direct), LSE-based prediction (LSE predict.), DFT, and LSE-based prediction parameterized by DFT data (I-LSE predict.). (d) Color mapping of the LSE values of the atoms on the selected plane and corresponding adsorption energies shown in (a), (b), and (c), along with the RMSE values relative to the DFT results. The asterisk indicates that the results of the structural optimization converge on the bridge site rather than the on-top site.

6.4 Results

In this section, we present the results for the prediction of the adsorption energy of HEA NPs using the proposed methods based on the LSE descriptor, focusing on the computational efficiency and precision. In Section 6.4.1, we demonstrate a strong correlation between the adsorption energy and the LSE descriptor, confirming that the LSE is a reliable descriptor of the adsorption energy between different sites in the NP. In Section 6.4.2, we verify the accuracy of LSE-based predictions by comparing them with DFT calculations, thereby proving the robustness of the prediction model. In Section 6.4.3, we analyze how the diverse surface structures and elemental compositions of 1000 different HEA NPs, comprising 122000 environments, lead to a wide range of adsorption-energy distributions. Finally, in Section 6.4.4, we compare the computational efficiency of our LSE-based adsorption energy predictions with that of direct adsorption-energy predictions using the traditional NNP and DFT methods.

6.4.1 Correlation Between Adsorption Energy and Local Surface Energy

The correlation between the LSE and the CO adsorption energy $E_{\mathrm{ad}}(\mathrm{NNP})$ of the monometallic NPs obtained using the NNP is shown in Figure 6.3. The solid lines represent linear regressions of the adsorption energies of a CO molecule at the top sites of each monometallic system. For all the metal elements, the relationship between the adsorption energy $E_{\mathrm{ad}}(\mathrm{NNP})$ of the CO molecule at the top site and the LSE is linear. The LSE values of all the adsorption sites for all elements range from approximately 0.2 to 1.2 eV. In other words, in all cases, the atomic energies are more unstable in the surface environment than in the bulk environment, which is reasonable given the lower coordination number in the surface environment. The adsorption energy $E_{\mathrm{ad}}(\mathrm{NNP})$ ranges from approximately -1.2 to -2.0 eV. Next, we examined the adsorption sites on the NPs. For all elements, the adsorption energy decreased in the following order: facets, edges, and corners. In contrast, the LSE values increased in the order of facets, edges, and corners. The LSE values and adsorption energies were concentrated at the facets, edges, and corners, and energy gaps existed between each group of adsorption sites. The RMSE was 0.035 eV, revealing a strong correlation between the LSE and the adsorption energy (see Figure D12 in the Details of the LSE-based regression models in Appendix).

Figure 6.4 presents the adsorption energies calculated directly using the NNP and their predicted values (dashed lines). The RMSE was 0.150 eV, which exceeded that of the unitary system. However, a strong correlation was observed between the LSE and adsorption energy in the HEA, indicating that the adsorption energy in a multicomponent environment can be effectively predicted (Figures D14(a) and (b) in the Appendix). This finding suggests that the LSE can efficiently and accurately predict the adsorption energies not only for unitary systems but also for complex systems such as HEAs. Notably, when we used the adsorption-energy range of -2.0 to -1.2 eV in the unitary system as the

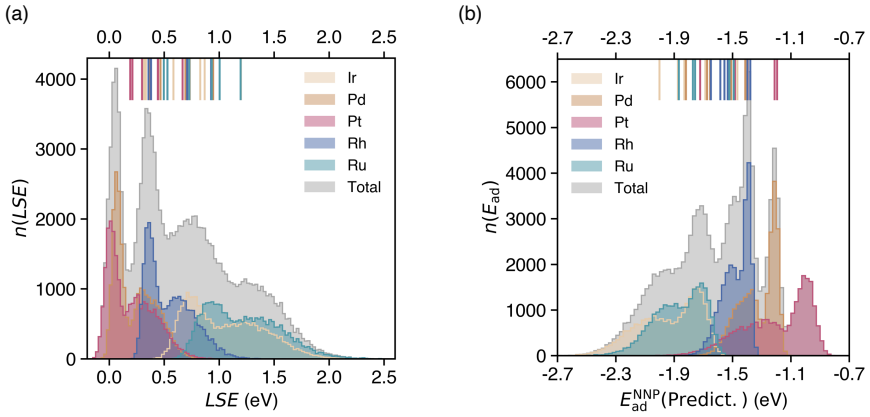

Figure 6.6: (a)Distributions of 122,000 LSE values of all the topmost layer atoms of the 1000 structure-optimized HEA_{201} NPs for each element and their sum, respectively. (b) Distributions of adsorption energies of CO for all the on-top adsorption sites predicted using the LSEs in (a) and Equation (6.4). Solid lines represent the values for monometallic NP M_{201} (M=Ir, Pd, Pt, Rh, and Ru).

interpolation region for E_{ad}(Predict.), the predictions were more reliable than those for other ranges. In the extrapolation region of E_{ad}(Predict.), the difference from E_{ad}(NNP) increased, and a maximum shift of approximately 0.5 eV was observed.

Next, we explored the trends for each elemental species. Figures 6.4 and D14(a) and (b) in the Appendix show that for all elemental species, the adsorption energies are nonlinearly estimated toward the unstable adsorption energy side. Additionally, the nonlinear region was dominated by adsorption at the facet sites. Pd atoms in HEA nanoparticles clearly show this non-linear behavior; unlike Pt atoms, they show a reversed pattern of adsorption energies. Compared to sites with low coordination numbers, such as corner and edge sites, the atoms on the facets were coordinated with eight or nine atoms. This increased coordination number renders them more sensitive to the surrounding environment than unitary systems. Consequently, the complex environment of HEAs may introduce unexpected nonlinearity into predictions. To show that this nonlinear trend can be captured by training the adsorption energies on HEA NPs, we applied kernel ridge regression (KRR) and quantum circuit learning (QCL) regression [9] to construct an adsorption energy prediction model for each elemental species at the HEA NP adsorption sites. Figures D14(c) and (d) in the Appendix show the correlation plots between the predicted and actual adsorption energies of CO on 14 HEA NP patterns generated by the regression model using KRR and QCL regression, respectively. The RMSEs of the adsorption energy predictions for all the adsorption sites provided by the KRR and QCL regression models were 0.0580 and 0.0579 eV, respectively, indicating comparable nonlinear

regression performance. Compared with the uncorrected predictions based on the LSE, the RMSE values were reduced by a factor of approximately three.

6.4.2 Density Functional Theory Verification of the Local Surface Energy Based Predictions

The accuracy of the adsorption energy predictions was verified using an NNP and the LSE with DFT calculations while seeking to increase the prediction accuracy. In our computing environment, the computation time for evaluating the adsorption energy via DFT was approximately 10^3 times that of the NNP, as indicated by Table 6.1. Therefore, we randomly selected one of the 20 structures of HEA_{201} discussed above and evaluated the adsorption energies for 19 sites on the (111) plane, as shown on the right side of Figure 6.5. The selected HEA_{201} was $Ir_{40}Pd_{40}Pt_{41}Rh_{40}Ru_{40}$. First, the prediction accuracy of the adsorption energies between the prediction based on the LSE and direct NNP calculation was compared with that of the DFT calculations. The RMSE of the adsorption energy for all sites obtained via the direct NNP calculation was 0.445 eV. The RMSE value of the prediction based on the LSE was 0.425 eV, corresponding to a slightly higher accuracy (0.020 eV) compared with the direct evaluation via the NNP. Thus, the accuracy of the prediction model using the LSE was close to that of the NNP. Although the RMSE of 0.445 eV for direct NNP calculations may appear large, the M3GNet NNP systematically overestimates CO adsorption energies, with a mean error (ME) of 0.388 eV relative to DFT as shown in Figure 6.5. A similar overestimation trend is observed for monometallic NPs, where the RMSE and ME against DFT are 0.439 eV and 0.379 eV, respectively. As a result, the LSE-based prediction also displays a systematic overestimation of the CO adsorption energy in comparison with DFT. Notably, the adsorption energy range for the 19 HEA sites spans from 1.329 eV to 1.567 eV (by DFT and NNP, respectively), indicating a broad distribution of possible adsorption energies. Given this wide range, a constant shift between NNP and DFT remains comparatively tolerable for high-throughput screening of HEA catalysts.

While the M3GNet NNP has difficulty quantitatively describing CO-adsorbed states, it effectively captures the atomic-level stability of the NPs. This is supported by the small RMSD (0.09 Å) between the DFT-relaxed and NNP-relaxed HEA NP structures, as well as the LSE RMSE of 0.026 eV for the 19 target sites, indicating that M3GNet—trained on diverse crystal environments—can reliably describe complex HEA NP configurations despite their absence from its original training set. Consequently, by combining DFT-derived adsorption energies for monometallic NPs with M3GNet-derived LSE (i.e., the I-LSE method), the prediction error is halved to an RMSE of 0.234 eV. This improvement arises because the LSEs are calculated from the NPs before adsorption, thereby avoiding the systematic overestimation of adsorption energy found in direct NNP calculations, while retaining the efficiency of an LSE-based framework.

6.4.3 Distribution of the Adsorption Energy on High-Entropy Alloy Nanoparticles

Figure 6.6(a) shows the 122000 LSE values of 1000 HEA NPs for each element and their total distribution. This distribution becomes smoother and converges as the number of NP patterns increases. The sum of all the elemental distributions shown in gray in Figure 6.6(a) can be considered as an indicator of the reactivity of the entire HEA NP surface of the given elements. In the monometallic system, the LSE ranged from approximately 0.2 to 1.2 eV. However, in the quintic HEA environment, these values underwent significant changes and ranged from approximately -0.1 to 2.4 eV. The distribution of each element exhibited two prominent peaks. For Pt and Pd, the LSE exhibited a major peak near 0 eV (or a slightly lower energy), indicating improved stability compared with that in the monometallic environment. Second, the smaller peak remained nearly unchanged for Pd, whereas the LSE range expanded by approximately 0.3 eV for Pt. For Ir and Ru, the LSE values shifted toward higher energies compared with those in the monometallic systems. For Rh, a slight increase in the LSE range was observed, lying between those of the stable Pt and Pd groups and the less stable Ir and Ru groups.

Figure 6.6(b) presents the predicted adsorption energies of CO on all the on-top sites of 1000 HEA_{201} NPs obtained using Equation (6.4) with LSE values. The range of the on-top adsorption energy E_{ad} for CO in the monometallic system (Figure 6.3) expanded by approximately 0.8 eV, from approximately -2.0 to -1.2 eV to -2.5 to -0.9 eV. This serves as an example of how adsorption characteristics diversify in a quintic HEA environment. The distribution of the adsorption energies for each element also exhibited two prominent peaks. Next, we examined the differences between the elemental species. For Pd and Pt, the LSE values were very close, but the range of adsorption energies was broader on the high-energy side by 0.2 eV for Pt. Similar trends were observed for Ir and Ru on the low-energy side. In the case of Rh, a slight extension in the range of both the high- and low-energy sides was observed compared with that of the monometallic system. In particular, the adsorption energy was concentrated in three adsorption site groups (corners, edges, and facets) in the monometallic NP environment, but these groups exhibited a broader range of values in the HEA NP environment. This representation as a distribution can help characterize and visualize the potential cocktail effect for efficient screening of novel HEAs across the periodic table.

6.4.4 Universality of the Local Surface Energy Based Method

In this section, we discuss the universality of the LSE-based prediction model constructed in this chapter. As described in Section 6.4.1, due to the vastness of the chemical space for HEA NPs, we restricted both the model construction and the target NP shape to truncated octahedra. However, the LSE-based model can be universally applied to any HEA NP shape, provided the structure is given.

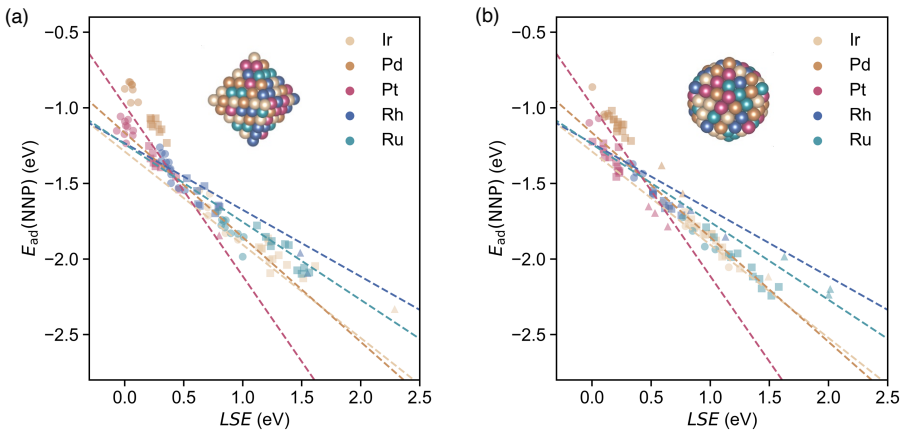

Figure 6.7: Universality of the LSE-based prediction model for CO adsorption energy across different HEA nanoparticle (NP) shapes. (a) Predicted adsorption energies from the NNP for all ontop sites on a regular octahedron-shaped HEA_{146}, plotted as a function of LSE. (b) Corresponding predictions for an icosahedron-shaped HEA_{147}. The dashed lines represent the LSE-based linear regression model constructed for monometallic truncated octahedron NPs.

This is because the universal NNP is capable of evaluating atomic energies for the given structure and thus computing the LSEs. The resulting LSEs can then be fed into the LSE-based model—originally constructed using monometallic data—to predict adsorption energies for the given HEA NP.

To verify the shape-independence of LSE-based prediction models, we evaluated its performance on two test sets: HEA_{146} in the form of a regular octahedron and HEA_{147} in the form of an icosahedron, as shown in the respective subsets in Figures 6.7(a) and (b). Figures 6.7(a) and (b) present the predicted CO adsorption energies from the NNP for all possible ontop sites on the regular octahedron and icosahedron, respectively. The corresponding LSE-based predictions are represented by the dashed lines as a function of LSE.

For both NP shapes, we found clear correlations with the predictions obtained from the LSE-based model. The RMSE were 0.156 eV for the regular octahedron and 0.142 eV for the icosahedron, comparable to the RMSE of 0.150 eV achieved for truncated octahedra. These results demonstrate that our predictive framework exhibits universality with respect to NP shape.

6.4.5 Comparison with Generalized Coordination Number Based Prediction Model

In this section, we employ a GCN descriptor—a scalar descriptor similar to LSE—to construct a prediction model based on monometallic data and compare its predictive accuracy. The GCN descriptor quantifies the environment of the

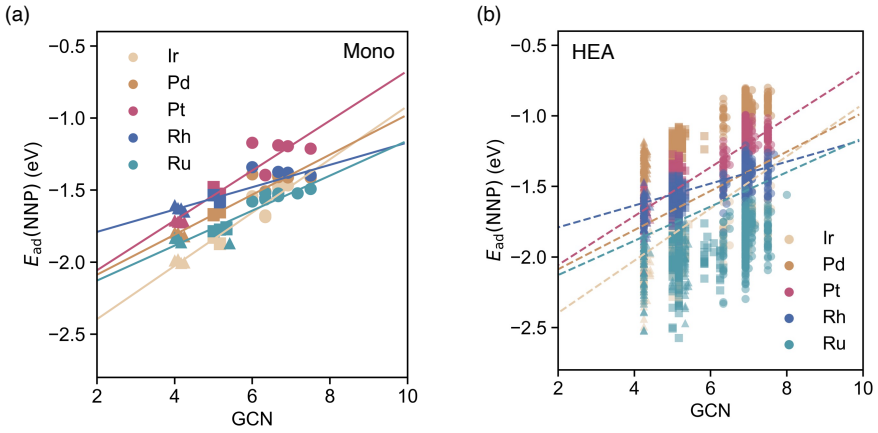

Figure 6.8: (a) Adsorption energies of CO calculated using the NNP for each on-top adsorption site of monometallic NPs M_n with respect to the GCN values. Solid lines represent the linear regressions of the adsorption energies of a CO molecule at the on-top sites of each monometallic NP and the GCN values. (b) Adsorption energies of CO calculated using the NNP for each on-top adsorption site of 20 HEA_{201} NPs with respect to the GCN values. The dashed lines represent the same linear regressions as in (a). Circles, squares, and triangles at each datapoint represent the facet, edge, and corner CO adsorption sites, respectively.

adsorption site by counting the coordination number of the nearest-neighbor atoms, and it is defined in Ref. [399] Following the same approach used for the LSE-based predictive model of Equation (6.4), we examined the correlation between CO adsorption energies on monometallic surfaces and GCN values. Linear regression models were then constructed for each element type. As shown in Figure 6.8(a), similar to LSE, a linear model accurately represents the relationship, achieving a precision of approximately 0.06 eV. The parameters of the linear regression models are summarized in Table 4 in Appendix section.

Subsequently, we applied these linear models to predict the adsorption energies of the 20 HEA NPs presented in the Results section to evaluate the prediction accuracy. As depicted in Figure 6.8(b), although the GCN-based predictions correlate with the directly computed adsorption energies, the discrete nature of GCN leads to variations of approximately from 1 to 1.5 eV even for identical GCN values. The resulting RMSE was 0.278 eV, approximately twice as large as that obtained using the LSE-based predictions, indicating that GCN alone is insufficient for capturing the environmental changes in multicomponent systems. This trend is consistent with findings reported by Namba et al. [401]. Nonetheless, future improvements may be possible by combining GCN with other descriptors, such as LSE, to enhance the predictive capabilities of monometallic data-based adsorption energy prediction models.

6.4.6 Computational Efficiency

Finally, we compared the computational performance of our method with that of conventional approaches for obtaining adsorption energy distributions. The time required to predict the adsorption energies of CO at 122000 sites across 1000 patterns of HEA_{201} using LSE was compared with the time required for direct calculations using the NNP and DFT. The use of the LSE eliminates the need for optimization of the adsorption structure for CO molecules. The computation times for the NNP and DFT are presented in Table 6.1. The computation time per structural optimization step with the NNP was approximately 1000 times shorter than that with DFT. However, as mentioned in Section 6.4.4, performing direct structural optimizations for 122000 adsorption sites requires approximately 171 days using the NNP and 188 years using DFT. These lengthy timescales were

[4] NNP calculations with M3GNet were performed using an AMD EPYC 7532 32-core processor with 64 CPUs.

[5] DFT calculations with VASP were performed using 10 Intel(R) Xeon(R) Platinum 9242 CPUs each with 96 CPUs in an MPI parallel configuration, for 960 CPUs.

Table 6.1: Computational costs for 19 geometry optimizations of CO adsorption on the (111) plane on $Ir_{40}Pd_{40}Pt_{41}Rh_{40}Ru_{40}$ HEA NP via NNP and DFT.

	total time[sec.]	total step[step]	sec./step
NNP[4]	2314	10480	0.22
DFT[5]	925518	5008	184.81

avoided by using the proposed method. The most time-consuming process in our approach is obtaining the LSE values through NNP structural optimization of 1000 HEA NPs, which was completed in just 1.4 days. The significant reduction in the execution time for adsorption energy predictions achievable with this method is expected to facilitate the screening of catalytic properties for HEAs with exponentially large combinations using the entire periodic table as candidates.

6.5 Discussion

We utilized the atomic energy obtained from the NNPs and introduced a metric called the LSE, which represents the surface energy per atom. Using the LSE, we determined the adsorption energy of CO molecules on the top sites of IrPdPtRhRu HEA_{201} NPs with a large number of atomic combinations as a distribution (Figure 6.6(b)). This approach offers a novel means of analyzing the atomic energies to evaluate various adsorption energies in multicomponent systems such as HEAs. The adsorption-energy distribution obtained via LSE prediction can help efficiently and effectively characterize and visualize unexpected cocktail effects induced by the vast chemical space of HEA NPs.

Notably, our calculations solely considered the adsorption energies on monometallic NPs and isolated multicomponent NPs, without the need for a direct evaluation of the CO molecular adsorption energy on the HEA. This approach enables the evaluation of adsorption energies approximately 10^5 times faster than direct DFT calculations, facilitating the visualization of the cocktail effect. Regarding accuracy, a comparison with DFT calculations revealed that the predictions based on the LSE were nearly an order of magnitude larger than the chemical accuracy, although they were not quantitatively accurate. Nonetheless, the relative energies exhibited a similar trend, indicating that qualitative comparisons that consider the influence of the surrounding environment on each element are feasible. Consequently, this method can be employed as a screening tool prior to applying DFT calculations or high-level quantum chemical methods such as CC theory.

The LSE-predicted adsorption energies were highly accurate, with an RMSE of 0.150 eV relative to the correct values, despite their low cost compared with direct evaluations. However, nonlinearity relative to the correct values was observed, indicating nonlinear behavior with respect to the LSE. We introduced a naïve method to capture this nonlinearity: nonlinear regression between the directly evaluated CO adsorption energy and the LSE. We modeled nonlinear regression with KRR and the classical quantum hybrid algorithm QCL regression. Learning the adsorption energies for only 732 sites for NPs in six patterns of structures improved the resulting LSE predictions thrice for the remaining 14 patterns tested for 1708 sites. The constraint that the norm of the parameters in QCL regression must equal 1 is expected to act as regularization. The results of the KRR and QCL regression models indicated similar regularization capabilities. Although our adsorption-energy correction model does not inherently require

quantum computing, its utility may be extended to a wider chemical space and the construction of models encompassing the entire periodic table. Furthermore, the adsorption energies of quintet systems were studied; it may be possible to systematically increase the accuracy by adding binary and ternary adsorption energies to the model.

Finally, we discuss potential applications of the proposed method for designing chemical reactions for catalyst and device development. Previous studies examined the role of atomic energy in increasing the accuracy and efficiency of NNPs and validated atomic-energy mapping results [413, 416, 417, 418, 419]. Recently, studies have attempted to gain chemical insight from atomic energies [420]. However, to the best of our knowledge, the proposed LSE prediction method is the first to demonstrate that atomic energy can serve as a descriptor for the efficient evaluation of catalytic properties. Moreover, in contrast to atomic energies, which are absolute quantities, LSEs are relative quantities and are thus expected to be less sensitive to differences in computational methods, such as the treatment of basis functions and inner-shell electrons. The proposed approach enhances chemical reaction design—a crucial component of machine learning-based material design—which has garnered significant attention in the scientific community over the past few years due to its promise to accelerate the discovery and development of useful materials [421, 422].

6.6 Conclusion

We developed a computational methodology for predicting the molecular adsorption energies on HEAs using the LSE descriptor derived from the NNPs calculated atomic energies. This method addresses the challenge of evaluating the vast chemical space of HEAs due to their compositional diversity and the computational expense associated with direct DFT and NNP calculations. The LSE descriptor efficiently captures the local reactivity of surface atoms, enabling rapid and accurate prediction of adsorption energies across a wide range of HEA configurations.

Our approach significantly accelerates the computational process, reducing the computation time from hundreds of years with DFT and hundreds of days with the NNP to only a few hours, which makes it a practical tool for materials discovery and catalyst design. The adoption of nonlinear regression techniques combined with advanced machine learning models, such as KRR and QCL regression, has increased the accuracy of adsorption-energy predictions, even in the face of the nonlinearity inherent in multicomponent systems.

Building upon this work, future research can extend the application of the LSE descriptor to other molecular species and reaction systems, validating and enhancing its predictive accuracy across a broader spectrum of catalytic processes. Integrating the LSE descriptor with advanced machine learning algorithms could facilitate large-scale screening of HEA compositions, accelerating the discovery of optimal catalysts for specific reactions. Moreover, combining the LSE descriptor with additional descriptors, such as surface microstructural features or GCN,

offers the potential to further refine predictive accuracy by accounting for local atomic environments in more detail [399, 400, 401, 402, 384, 403, 404, 405, 406, 383].

In this chapter, we assumed that the HEA NPs have random elemental configurations following a uniform distribution. However, short-range order is also important in high-entropy alloys [423, 424, 425]. By combining our method with techniques for quantifying short-range order using E(3)-equivariant graph neural networks [426], we can potentially obtain more accurate distributions of reactivity. This integration would allow us to capture the effects of atomic arrangements more precisely, leading to improved predictions of catalytic properties.

Moreover, this approach holds the potential to consider more realistic environmental conditions, including the behavior of catalysts in solution or under operational settings. Incorporating factors such as solvent effects, temperature, and pressure into the screening process would enhance the relevance and applicability of the predictions, leading to more effective and practical catalyst designs. Furthermore, applying the LSE framework to other material systems, such as high-entropy nitrides, oxides, and carbides, could further expand its impact on materials design.

In conclusion, the method proposed in this chapter not only paves the way for rapid and accurate computational screening of catalytic materials but also sets the stage for developing computational tools capable of handling the complexities of modern materials science—particularly in the realm of high-entropy materials.

Chapter 7

Conclusions

In this dissertation, we argue that extending quantum computation beyond toy models to real chemical problems requires sophisticated integration with state-of-the-art classical computing. Accordingly, we developed a suite of quantum-classical interfaces to achieve this integration. Whereas most quantum-classical hybrid algorithm research has focused on exploiting quantum speed-ups, the classical side—responsible for tasks such as Hamiltonian preparation and post-processing of quantum-computation outputs—has often been overlooked. For instance, constructing the second-quantized Hamiltonian scales as $O(m^{4–5})$, where m is the number of spin-orbitals, and developing practical generation schemes for condensed-phase systems has long been an overlooked challenge. Likewise, the classical post-processing required to evaluate energy derivatives after a quantum computation can become a significant bottleneck. Our first contribution integrated a highly parallelized, high-performance-computing–ready quantum-chemistry package with quantum processors, thereby mitigating both Hamiltonian construction and force evaluation costs. Second, anticipating an era in which fault-tolerant quantum computing (FTQC) will deliver small but high-accuracy datasets, we proposed a total energy alignment (TEA) protocol that reconciles heterogeneous data from multiple electronic structure methods. This protocol enabled the training of a universal machine learning interatomic potential (MLIP) capable of learning seamlessly across molecular and crystalline domains. Finally, we showed that the intermediate information of the pre-trained MLIPs can be repurposed as compact descriptors for materials-oriented quantum ML models, achieving rapid and accurate property predictions—even on present-day, qubit-limited hardware or quantum circuit emulators.

Collectively, these advances closed critical gaps on the classical side of hybrid workflows and charted a practical path toward deploying quantum computing for practical atomic-scale chemical problems. The remainder of this chapter revisits the specific contributions presented in each preceding chapter, offering a more in-depth discussion of their outstanding challenges and future prospects than was provided in the individual chapter conclusions.

Chapter 3 introduced a quantum-classical hybrid interface that combines

the massively parallel, low-scaling quantum-chemistry package CP2K with a quantum-circuit emulator. Classical hardware constructs large second-quantized Hamiltonians and evaluates analytic nuclear forces, while the quantum back-end efficiently diagonalizes those Hamiltonians with quantum algorithms such as variational quantum eigensolver and quantum phase estimation. Calculations on liquid water, semiconductor surfaces and an enzymatic active site showed that this approach already permits geometry optimization and ab-initio molecular dynamics for realistic condensed-phase systems using quantum computers. In particular, benchmark calculations on liquid-water cells containing 64-1,024 H_2O molecules revealed that Hartree–Fock (HF) calculations, Hamiltonian construction and analytic force evaluation scale almost linearly with system size and still finished within about 30 minutes even for the periodic cell containing 1,024 water. Conversely, the present study employed a minimal active space of 2 electrons in 4 spin-orbitals, which is too small to recover the second O–O peak observed in the 300 K radial distribution function; the overall accuracy therefore remained close to that of plain HF theory. This limitation can be alleviated by designing larger, chemistry-driven active spaces—e.g. via quantum-selected configuration interaction [32, 33]—or by combining the quantum region with an efficient density functional theory (DFT) embedding scheme [205, 203]. Taken together, these results showed that controlling the classical overhead makes it realistic to apply forthcoming quantum processors to chemically relevant condensed-phase problems.

Chapter 4 presented TEA, an efficient protocol that integrates heterogeneous quantum-chemical datasets with almost no redundant calculations. Constructing a universal MLIP that spans a broad range of the periodic table demands a large, high-accuracy quantum-chemical dataset covering an extensive domain. Applying TEA to merge a hybrid generalized gradient approximation (GGA) organic set with a large inorganic GGA set enabled the training of MACE-Osaka24—the first open-source universal MLIP spanning both molecular and crystalline systems—which matched or outperformed specialized models while lowered the computational barrier to universal MLIP development and use. Yet TEA still relies on suitable reference atomic energies and geometries—harder to secure for strongly correlated, charged, or relativistic systems—and on a single global scaling factor that may prove insufficient in niche cases, motivating adaptive corrections or ML surrogates that predict fidelity gaps. Future testing on higher-level quantum-chemical datasets, explicit inclusion of correlation and relativistic effects, and continued advances in neural-network architectures, training strategies, and hyperparameter optimization should bolster the robustness and accuracy of universal MLIPs. As ever-larger, more diverse quantum-chemical datasets emerge, TEA and models like MACE-Osaka24 can steer the creation of integrated, widely accessible foundation models that remain faithful to quantum chemical calculations yet flexibly interface with varied computational approaches, accelerating our exploration of increasingly complex chemical systems. Furthermore, once high-accuracy quantum-chemical data generated on quantum computers become widely available, we believe that our methodology will efficiently scale those quantum chemical calculations up to

atomistic simulations.

Chapter 5 demonstrated that the intermediate information at the graph neural network (GNN) layer of the pre-trained universal GNN-based MLIPs can be reused as general-purpose atomic descriptors named GNN transfer learning (GNN-TL) descriptors for chemical property predictions. Whereas traditional high-accuracy descriptors scale roughly with the square of the number of element types, GNN-TL descriptors keep their dimensionality constant. For a chemical space containing 89 elements, the M3GNet and MACE-MP-0 GNN-TL descriptors require only 64 to 256 dimensions, respectively, yet state-of-the-art SOAP and FCHL19 descriptors balloon to 10^5–10^6 dimensions. In the accuracy evaluation of M3GNet GNN-TL descriptor, for a training size of 100,000, the mean absolute error (MAE) for the ^{13}C nuclear magnetic resonance (NMR) chemical shift predictions was 2.28 ppm with Laplacian-kernel KRR, while natural parametrized quantum circuit (NPQC)-kernel QKRR achieved a comparable MAE of 2.55 ppm. The molecule-specific MLIP, MACE-OFF23-small GNN-TL descriptor, attained an MAE of 1.78 ppm, thereby meeting the experimental accuracy target of 2.00 ppm. For nuclei beyond carbon, the M3GNet GNN-TL descriptor-based KRR model kept the MAE for molecules in the test set below 5 ppm, thus met the target accuracy of remaining within 1 % of each nucleus's experimentally accessible NMR chemical-shift range. On an external set of forty drug molecules the MACE descriptor delivered the highest ^{13}C accuracy reported to date at 2.83 ppm, beating the state-of-the-art FCHL by nearly 1 ppm. The present QKRR model is capped at ten qubits, the study showed that intermediate representations learned by universal MLIPs already rival established descriptors while being dramatically lighter. Because the NPQC kernel largely mirrors a Gaussian kernel, quantum and classical ML models are limited to similar levels of performance. We believe that future advances in quantum kernel methods—such as designing kernels tailored specifically to NMR chemical-shift prediction—could surpass the performance of classical kernel approaches as larger quantum hardware becomes available.

Chapter 6 demonstrated that the atomic energies produced by the universal M3GNet MLIP could be repurposed as a local surface energy (LSE) descriptor for catalyst screening of high-entropy alloy (HEA) nanoparticles. Trained only on monometallic data, a linear LSE model predicted CO on-top adsorption energies for 1000 distinct IrPdPtRhRu HEA_{201} nanoparticles in a matter of days—an effort that exhaustive DFT would stretch to centuries—and a six-qubit quantum-circuit-learning (QCL) correction halved the residual error. The long-standing generalized coordination number (GCN) descriptor gave root-mean-square errors (RMSEs) of 0.06 eV for monometallic particles and 0.28 eV for these HEAs, whereas the linear LSE model tightened the errors to 0.035 eV and 0.150 eV, and the QCL-corrected model lowered the HEA error further to 0.058 eV. These results highlighted LSE's suitability for accelerated catalyst screening on today's quantum hardware. However, the model developed in this study was restricted to HEAs composed of five platinum-group metals—Ir, Pd, Pt, Rh, and Ru—and it was validated only for CO adsorption. Future work should broaden the model to include a much larger set of candidate elements across the periodic table and

to account for additional probe molecules, thereby providing a more rigorous test of the method's generality. We believe that such future studies, combined with screening based on the LSE descriptor, will facilitate the discovery of new HEA candidates.

In summary, we developed interfaces between quantum and classical computation that are indispensable for applying quantum computing to practical chemical problem solving. Specifically, the principal achievements can be summarized in the following three points. First, we successfully interfaced the quantum chemistry package CP2K with quantum computing. Using this interface, we demonstrated that a quantum–classical hybrid algorithm can run even on a periodic cell containing 1,024 water molecules. Second, we developed a TEA protocol that integrates quantum-chemical data obtained from different computational methods. Building on this protocol, we constructed MACE-Osaka24, a universal MLIP capable of treating both molecular and crystalline systems. Third, by introducing a compact descriptor, we achieved experimental-level accuracy in NMR chemical shift prediction using a quantum ML model that employs only ten qubits. On the other hand, the TEA protocol was limited to integrating results from different DFT calculations, and its application to quantum-chemical data generated by quantum computers remains to be validated in future work. This will be a critical first step towards constructing MLIPs capable of accurately describing strongly correlated systems. Moreover, the present work was validated entirely on emulators rather than on physical quantum hardware. However, real quantum processors have now surpassed the 100-qubit scale, making classical emulation impractical. Using this utility-scale hardware and, in the near future, early FTQC to validate and deploy the interfaces developed in this dissertation on actual quantum devices is therefore a key direction for future work.

Meanwhile, the advances reported here are already benefiting classical computational chemistry. For example, Nomura et al. demonstrated an MLIP that scales to systems comprising billions of atoms by employing the TEA protocol [427]. Increasingly, the MLIP descriptors proposed here are being applied in materials informatics via transfer-learning techniques [428]. Furthermore, the interface with CP2K is valuable not only for deploying quantum algorithms but also for utilizing classical methods such as the density matrix renormalization group (DMRG). Thus, although the series of studies presented in this dissertation began with the aim of applying quantum computing to chemistry, the resulting interfaces generated benefits that extend well beyond quantum computing itself. These results demonstrated that classical computing not only accelerates quantum computing but also benefits from valuable feedback in return. Driven by this mutually reinforcing cycle, the ongoing synergy between classical and quantum computing is expected to build a robust foundation for further advances in computational chemistry.

Appendix

Appendix A: Supporting Information for Chapter 3

1 Theoretical Implementation

The following has been written considering the spin-restricted case, although the code also applies to the spin-unrestricted case: All codes were implemented in a modified CP2K version 8.2 [190].

a Energy Evaluation

The subspace Hamiltonian within the active space is computed using the closed-shell Fock operator:

$$f^c_{xy} = h_{xy} + G(\mathbf{d}^c)_{xy}, \tag{A1}$$

$$V_{xy,zw} = (xy|zw) \tag{A2}$$

where x, y, z, and w run over the active orbitals. h_{xy} represents the one-electron Hamiltonian matrix elements in the basis of active orbitals. $G(\mathbf{d}^c)_{xy}$ denotes the Coulomb and exchange contributions from the density matrix of the closed (inactive) orbitals, $\mathbf{d}^c$. f^c_{xy} is the Fock matrix within the active space, accounting for the interactions with the closed-shell electrons. $V_{xy,zw} = (xy|zw)$ are the two-electron repulsion integrals between active orbitals. The two-electron integrals $V_{xy,zw}$ are computed by expanding each product of active orbital pairs $\phi_x\phi_y$ into plane waves (PWs), which is efficient for periodic systems.

An external active-space solver is used to obtain the correlation energy and the correlation contribution to one-particle reduced density matrix (1-RDM) and two-particle reduced density matrix (2-RDM) within the active space. We have implemented interfaces for both the fermionic quantum emulator (FQE) [210] and Qulacs [209], which compute

$$E^c = E^{\text{full}} - E^{\text{HF}}, \tag{A3}$$

$$d_{xy} = d^{\text{full}}_{xy} - d^{\text{HF}}_{xy}, \tag{A4}$$

$$D_{xy,zw} = D^{\text{full}}_{xy,zw} - D^{\text{HF}}_{xy,zw}, \tag{A5}$$

where E^{full} is the total energy obtained from the full configuration interaction (FCI) calculation within the active space. E^{HF} is the Hartree-Fock (HF) energy recomputed within the active space using the active-space solver. d^{full}_{xy} and $D^{\text{full}}_{xy,zw}$ are the 1-RDM and 2-RDM from the FCI calculation. d^{HF}_{xy} and $D^{\text{HF}}_{xy,zw}$ are the corresponding HF 1-RDM and 2-RDM within the active space. E^{c} is the correlation energy within the active space.d_{xy} and $D_{xy,zw}$ are the correlation contributions to the 1-RDM and 2-RDM, respectively. The integrals are passed to this solver using so-called FCIDUMP format and the resulting energy, 1-RDM, and 2-RDM are passed back in the same format. The total energy is expressed as follows:

$$E = E^{\text{ref}} + \frac{1}{2}\sum_{xy} f^{c}_{xy} d_{xy} + \frac{1}{2}\sum_{xy,zw} V_{xy,zw} D_{xy,zw} \tag{A6}$$

E^{ref} is the reference HF energy, which should not be confused with E^{HF}. In periodic cases, the plane-wave expansion involves reciprocal lattice vectors $\mathbf{g}$. The correlation contributions are computed under the approximation that the contributions from the $\mathbf{g} = \mathbf{0}$ reciprocal lattice vector are neglected. This is a common approximation in plane-wave-based calculations to avoid singularities associated with the long-range Coulomb interaction at $\mathbf{g} = \mathbf{0}$.

b Lagrangian and Multipliers

To discuss nuclear gradient formulation, it is worth noting that the total Lagrangian is expressed as

$$\begin{aligned} L \quad &= E + \sum_{ai} Z_{ai} \frac{\partial E_{\text{ref}}}{\partial \kappa_{ai}} + \frac{1}{2}\sum_{rs} X_{rs}(\mathbf{C}^{\dagger}\mathbf{S}\mathbf{C} - \mathbf{1})_{rs} \\ &\quad + \sum_{i}\sum_{x^o} z_{ix^o} f_{ix^o} + \sum_{a}\sum_{x^v} z_{ax^v} f_{ax^v}. \end{aligned} \tag{A7}$$

where r and s are the general molecular orbital (MO) indices and $\mathbf{C}$ is the MO coefficient matrix, $\mathbf{S}$ is the atomic orbital (AO) overlap integral. Hereafter, i, j, k, and l denote the closed (inactive) orbitals, i.e., occupied orbitals that are outside of the active space. a, b, c, and d denote virtual orbitals outside of the active space. This is performed on an AO basis. x^o and x^v denote the occupied and virtual parts of the active orbitals, respectively. In addition, κ_{ai} represents the orbital rotation parameters between occupied orbitals i and virtual orbitals a. The derivative $\partial E_{\text{ref}}/\partial \kappa_{ai}$ denotes the self-consistent field (SCF) condition.

The Z-vector equation is derived by taking the derivative of the Lagrangian with respect to the orbital rotation between virtual and occupied orbitals and make it stationary:

$$Y_{bj} + (\mathbf{fz} + \mathbf{fz}^{\dagger})_{bj} + \sum_{ai} Z_{ai} \frac{\partial^2 E_{\text{scf}}}{\partial \kappa_{ai} \kappa_{bj}} = 0 \tag{A8}$$

where $Y_{ai} = \partial E/\partial \kappa_{ai}$. The term with X does not appear here because it is symmetric (as opposed to anti-symmetric, such as Z). Because the SCF solution

is a minimum, the second derivatives in the third term are positive definite; therefore, this equation is well-conditioned.

Once the RDMs are read from the file, they are used to compute $\mathbf{Y}$. In CP2K, we do not store virtual MOs explicitly. Therefore, the input to the Z vector equation is in the format of occupied MO coefficients where the first index is an AO index:

$$Y_{\alpha i} = \sum_{\beta} 2P^{v}_{\alpha\beta} f^{t}_{\beta i} - \sum_{x^v} C_{\alpha x^v} \left[\sum_{y} f^{c}_{yi} d_{x^v y} + \sum_{y,zw} V_{yi,zw} D_{x^v y,zw} \right] \tag{A9}$$

$$Y_{\alpha x^o} = \sum_{\beta} P^{e}_{\alpha\beta} \left[\sum_{y} f^{c}_{\beta y} d_{x^o y} + \sum_{y,zw} V_{\beta y,zw} D_{x^o y,zw} \right] \tag{A10}$$

with

$$P^{v} = \mathbf{S}^{-1} - \frac{1}{2}\mathbf{d_{SCF}} \tag{A11}$$

$$P^{e} = \mathbf{S}^{-1} - \mathbf{C_{occ}}\mathbf{C}^{\dagger}_{\mathbf{occ}} \tag{A12}$$

where $\mathbf{C_{occ}}$ is the extended MO coefficients (including both inactive and active) and α and β are the AOs. We also introduce the so-called total Fock operator,

$$f^{t}_{rs} = h_{rs} + G(\mathbf{d}^{\mathrm{ref}} + \mathbf{d})_{rs}. \tag{A13}$$

In CP2K the linear equation is multiplied from the left by the overlap matrix $\mathbf{S^{-1}}$. Therefore, it is not necessary to compute the inverse of the overlap matrix. Because we do not want to construct the two electron integrals with a virtual index, we use the following algorithm for the last term. First, we back-transform the two electron density to AOs for each x^v and y, that is

$$D_{xy,zw} \equiv (\mathbf{d}^{xy})_{zw} \rightarrow (\mathbf{d}^{xy})_{\alpha\beta}. \tag{A14}$$

This density matrix is used to obtain the Coulomb operator using the code in the SCF, which is subsequently transformed into MOs. For each x and y, we compute

$$\sum_{zw} V_{yi,zw} D_{x^v,zw} = \sum_{g} J(\mathbf{d}^{x^v y})_g \phi_y(g) \phi_i(g) \tag{A15}$$

where J_g is the Hartree potential at grid g. The following quantities are introduced in the code:

$$g_{\alpha x} = \sum_{y} f^{c}_{\alpha y} d_{yx} + \sum_{y} \sum_{g} J(\mathbf{d}^{xy})_g \phi_\alpha(g) \phi_y(g) \tag{A16}$$

Using this quantity, Equations (A9) and (A10) can be simplified to

$$Y_{\alpha i} = \sum_{\beta} 2P^{v}_{\alpha\beta} f^{t}_{\beta i} - \sum_{x^v} C_{\alpha x^v} g_{i x^v} \tag{A17}$$

$$Y_{\alpha x^o} = P^{e}_{\alpha\beta g\beta x^o} \tag{A18}$$

The multipliers z associated with the active orbital selection using canonical orbitals are computed as follows:

$$z_{ij} = -\frac{Y_{ij} - Y_{ji}}{f_{ii} - f_{jj}} \tag{A19}$$

Because CP2K implementation does not explicitly compute the virtual orbitals, this is solved iteratively for the virtual part of $\mathbf{z}$. After obtaining $\mathbf{z}$, Equation (A8) is solved iteratively to obtain $\mathbf{Z}$.

c Relaxed Dipole Moment

Once the Z vector is obtained, the total relaxed density matrix can be computed as

$$\tilde{d}_{rs} = d_{rs}^{\text{ref}} + d_{rs} + d_{rs}^{z} \tag{A20}$$

where we introduced $\mathbf{d}^z = \mathbf{Z} + \mathbf{z}$, with $\mathbf{Z}$ and $\mathbf{z}$ being the Lagrange multipliers associated with the constraints in the Lagrangian. The relaxed density matrix is defined as the derivative of the Lagrangian

$$\tilde{d}_{rs} = \frac{\partial L}{\partial h_{rs}}. \tag{A21}$$

The dipole moment is calculated using this quantity. Under an external electric field, E, the Hamiltonian becomes $H \to H + \sum_{rs} \mu_{rs} \mathbf{E}_{rs}$, (i.e., the dipole operator appears whenever h appears), therefore,

$$\mu = \frac{\partial L}{\partial \mathbf{E}}\bigg|_{\mathbf{E}=0} = \sum_{\alpha\beta} M_{\alpha\beta} \tilde{d}_{\alpha\beta} \tag{A22}$$

where we implicitly back-transform the density matrix into AO, and $M_{\alpha\beta}$ are the dipole moment integrals between atomic orbitals. This dipole moment agrees exactly with the finite difference obtained using the finite $\mathbf{E}$.

d Evaluation of Nuclear Gradients

Once the relaxed density matrices are computed, the nuclear gradients are evaluated as follows.

e Relaxed One-Particle Reduced Density Matrix

Using the total density matrix defined in Equation (A21), the contribution to the nuclear gradients from the one-body part of the Hamiltonian can be expressed as

$$\frac{dE}{dR_A} = \frac{\partial L}{\partial R_A} \leftarrow 2 h_{rs}^{R_A} \tilde{d}_{rs} \tag{A23}$$

where $h_{rs}^{R_A} = \frac{\partial h_{rs}}{\partial R_A}$ represents the derivative of the one-electron Hamiltonian matrix elements with respect to the displacement of atom A in the Cartesian direction R. In practice, however, because nuclear attraction is handled together with the Hartree potential in CP2K, special care must be taken (see below).

f Non-separable Part of Two-Particle Reduced Density Matrix

The 2-RDM from the active-space solver is contracted to the two-electron gradient integrals and contributes to the nuclear gradient as follows:

$$\frac{\partial L}{\partial R_A} \leftarrow 2\left(i_{A_R} j \mid kl\right) \Gamma_{ij,kl} \tag{A24}$$

where R is the Cartesian direction, and A labels the atoms. i_{A_R} is the derivative of MO i with respect to the nuclear displacement (computed using the derivative basis functions and the same MO coefficients). $\Gamma_{ij,kl}$ is the 2-RDM element in the MO basis. This contribution is evaluated using the Hartree potential $J(\mathbf{d}^{xy})_g$ used to compute the intermediate quantities in Equation (A17) for each x and y pair:

$$\begin{aligned}
\frac{\partial L}{\partial R_A} \quad &\leftarrow \sum_{zw} \left(x_{A_R} y \mid zw\right) D_{xy,zw} \\
&= \sum_{g} J\left(\mathbf{d}^{xy}\right)_g \frac{\partial \phi_x(g)}{\partial R_A} \phi_y(g) \\
&= \sum_{g} \sum_{\alpha\beta} \sum_{g} J\left(\mathbf{d}^{xy}\right)_g \frac{\partial \phi_\alpha(g)}{\partial R_A} \phi_\beta(g) T^{xy}_{\alpha\beta}
\end{aligned} \tag{A25}$$

where $\phi_x(g)$ is the value of the active molecular orbital x at grid point g, and $\phi_\alpha(g)$ is the atomic orbital (AO) basis function at grid point g. $T^{xy}_{\alpha\beta} = C_{\alpha x} C_{\beta y}$, where $C_{\alpha x}$ and $C_{\beta y}$ are the MO coefficients relating AOs to MOs, i.e., $\phi_x = \sum_\alpha C_{\alpha x} \phi_\alpha$. Note that the last equation can be evaluated by the standard SCF nuclear gradient code.

g Separable Part of Two-Particle Reduced Density Matrix

The separable part of the 2-RDM is given by

$$\begin{aligned}
\Gamma^{\text{sep}}_{rs,tu} \quad &= d^{\text{ref}}_{rs} \left(2\mathbf{d}^z + \mathbf{d}^{\text{ref}}\right)_{tu} \\
&- \frac{1}{2} d^{\text{ref}}_{ru} \left(2\mathbf{d}^z + \mathbf{d}^{\text{ref}}\right)_{ts} \\
&+ d^c_{rs} d_{tu} - \frac{1}{2} d^c_{ru} d_{ts}
\end{aligned} \tag{A26}$$

where d^{ref}_{rs} is the 1-RDM from the reference Hartree-Fock calculation, $\mathbf{d}^z = \mathbf{Z} + \mathbf{z}$ (with $\mathbf{Z}$ and $\mathbf{z}$ being the Lagrange multipliers from the Z-vector equations). The indices r, s, t, u run over molecular orbitals. The density matrices are back-transformed into AOs before entering the gradient integral contraction. Using a short hand notation for the gradient contribution, we obtain

$$\begin{aligned}
f_{A_R}\left(\mathbf{d}^a, \mathbf{d}^b\right) \quad &= \sum_{xyzw} \left(x_{A_R} y \mid zw\right) \\
\times \Big(d^a_{xy} d^b_{zw} \quad &+ d^a_{zw} d^b_{xy} - \frac{1}{2} d^a_{xw} d^b_{zy} - \frac{1}{2} d^a_{zy} d^b_{xy}\Big).
\end{aligned} \tag{A27}$$

where x, y, z, w are AO indices, x_{A_R} denotes the derivative of AO x with respect to the displacement of atom A in Cartesian direction R, and $(x_{A_R} y \mid zw)$ are the derivative two-electron integrals involving the derivative of AO x. The above expressions are further expressed as follows:

$$\frac{\partial L}{\partial R_A} \leftarrow f_{AR}\left(\mathbf{d}^{\mathrm{ref}}, 2\mathbf{d}^{z} + \mathbf{d}^{\mathrm{ref}}\right) + f_{AR}\left(\mathbf{d}^{c}, \mathbf{d}\right). \tag{A28}$$

In CP2K, the code for evaluating the separable contribution is complicated because the Hartree potentials are handled in a complex manner (particularly in the Gaussian Augmented Plane Wave (GAPW) code). Therefore, we implemented these terms by taking advantage of the following relationship: dropping the subscript of f for simplicity we obtain

$$\begin{aligned} &f\left(\mathbf{d}^{a}, \mathbf{d}^{b}\right) + f\left(\mathbf{d}^{b}, \mathbf{d}^{a}\right) \\ &= f\left(\mathbf{d}^{a} + \mathbf{d}^{b}, \mathbf{d}^{a} + \mathbf{d}^{b}\right) - f\left(\mathbf{d}^{a}, \mathbf{d}^{a}\right) - f\left(\mathbf{d}^{b}, \mathbf{d}^{b}\right). \end{aligned} \tag{A29}$$

In the actual code, this idea is generalized such that the nuclear attraction potential which is handled together with the two-electron part, is appropriately handled. The working equation for the mixed term between $\mathbf{d}^{\mathrm{ref}}$ and $\mathbf{d}^{z}$ is expressed as

$$\begin{aligned} &f\left(-\varphi^{-1}\mathbf{d}^{\mathrm{ref}} + \varphi\mathbf{d}^{z}, -\varphi^{-1}\mathbf{d}^{\mathrm{ref}} + \varphi\mathbf{d}^{z}\right) - (1+\varphi) f\left(\mathbf{d}^{z}, \mathbf{d}^{z}\right) \\ &- f\left(-\varphi^{-1}\mathbf{d}^{\mathrm{ref}}, -\varphi^{-1}\mathbf{d}^{\mathrm{ref}}\right) + (1+\varphi) f(\mathbf{0}, \mathbf{0}) \end{aligned} \tag{A30}$$

where φ is the so-called golden ratio, $(1+\sqrt{5})/2$.

h Overlap Derivatives

The contribution, which depends on the derivative of the overlap integrals is expressed as

$$\frac{\partial L}{\partial R_A} \leftarrow X_{rs} S_{r_{R_A} s} \tag{A31}$$

where X_{rs} is calculated from the symmetric part of the $\mathbf{Y}$ matrix, and $S_{r_{A_R} s}$ denotes the derivative of the overlap matrix elements with respect to the displacement of atom A in Cartesian direction R.

2 Computational Details

The calculations were performed using a customized CP2K version 8.2 in conjunction with the quantum computer emulator Qulacs. The computational conditions employed for each of the systems analyzed are as follows:

a Water Cluster

The initial geometries of the water clusters $(H_2O)_n$ (n = 2–30), comprising of n water molecules were obtained from n = 2–20 [429] and n = 21–30 [430]. The periodic boundary condition (PBC) box size was chosen to ensure a vacuum layer between clusters of less than 8 Å, specifically $20 \times 20 \times 20 Å^3$. The HF calculations were performed using the Gaussian and PW (GPW) basis set under PBC. Further, the core electrons were treated with the corresponding Goedecker–Teter–Hutter (GTH) pseudopotential [431]. The Gaussian-type basis function employed was 6-31G(d). The cutoff energy for the auxiliary plane-wave and Gaussian-type basis functions were set to 240 and 40 Ry, respectively. Four multigrid levels were utilized for efficient integral calculations. Wave function optimization employed the conjugate gradient method (CG), with an SCF threshold of 1.0×10^{-8} Hartree. Further, orbital transformation (OT) was applied with an energy gap and step size of 0.08 Hartree. To enhance SCF convergence, the maximum number of loops for the outer SCF, which involved preconditioning at each step, was set to 10. In addition, the maximum number of loops for the inner SCF with a fixed preconditioner was set to 40. Moreover, to facilitate computational efficiency, two-electron integral (ERI) calculations were screened using the Schwarz inequality with a threshold below 1.0×10^{-10}.

Geometry optimization was performed using CG as the optimizer until the maximum force on an atom was less than 0.45×10^{-3} Hartree/Bohr. The binding energy per water molecule in the water cluster E_{bind} is defined as

$$E_{\text{bind}} = \frac{\text{n}E(\text{H}_2\text{O}) - E(\text{H}_2\text{O})_\text{n}}{\text{n}} \tag{A32}$$

where $E(H_2O)$ and $E(H_2O)_n$ represent the total energies of a water molecule and water cluster, respectively.

b Diamond Si Crystal

The diamond Si crystal was represented by a PBC box containing 64 atoms. HF calculations were performed employing the GPW basis set with core electrons treated using GTH pseudopotentials. The Gaussian-type basis function employed was 6-31G(d). The cutoff energy for the auxiliary plane-wave and Gaussian-type basis functions were set to 320 and 40 Ry, respectively. Four multigrid levels were utilized for efficient integral calculations. Wave function optimization employed the direct inversion in the iterative subspace (DIIS) method, with an SCF threshold of 1.0×10^{-7} Hartree. Further, OT with a full single inverse was applied utilizing an energy gap and a step size of 0.08 Hartree. To enhance the SCF convergence, the maximum number of loops for the outer SCF, which involved preconditioning at each step, was set to 10. The maximum number of loops for the inner SCF with a fixed preconditioner was set to 40. For ERI calculations, the Schwarz inequality was utilized to screen values below 1.0×10^{-8}. In addition, a Truncated Coulomb operator was employed with a cutoff radius of 5 Å.

c H_2O on Si(001) Surface

The Si(001)-c(4×2) reconstruction surface was modeled with a 4×4 size hydrogen-terminated 5-layer slab, where the vacuum layer was approximately 13 Å. The HF calculations were performed using the GPW basis set under PBC. The core electrons were treated with appropriate GTH pseudopotentials. The Gaussian-type basis function utilized was 6-31G(d). The cutoff energy for the auxiliary plane-wave and Gaussian-type basis functions were set to 400 and 60 Ry, respectively. To enhance the computational efficiency, four multigrid levels were employed for efficient integral calculations. Wave function optimization employed the DIIS method, with an SCF threshold of 1.0×10^{-7} Hartree. Further, OT with a full single inverse was applied utilizing an energy gap and a step size of 0.08 Hartree. To improve the SCF convergence, the maximum number of loops for the outer SCF, which involved preconditioning at each step, was set to 10. The maximum number of loops for the inner SCF with a fixed preconditioner was set to 40. For two-electron integral calculations, the Schwarz inequality was utilized to screen values below 1.0×10^{-8}. In addition, a Truncated Coulomb operator was applied with a cutoff radius of 6 Å. Further, geometry optimization was performed using the conjugate gradient (CG) method as the optimizer until the maximum force on the adsorbed molecules and atoms up to the second layer on the surface was less than 0.45×10^{-3} Hartree/Bohr. The adsorption energy of H_2O on the Si(001) surface E_{ad} was calculated using the following equation:

$$E_{\mathrm{ad}} = E(\mathrm{H_2O/Si(001)}) - E(\mathrm{H_2O}) - E(\mathrm{Si(001)}) \tag{A33}$$

where $E(\mathrm{H_2O/Si(001)})$, $E(\mathrm{H_2O})$, and $E(\mathrm{Si(001)})$ are the total energies of the H_2O/Si(001), H_2O, and Si(001), respectively.

d Liquid Water

Liquid water with a density of $1\,\mathrm{g/cm^3}$ was modeled in simulation boxes containing 64, 128, 256, 512, and 1024 H_2O. NVT equilibration at 300 K was performed for each liquid water model using a Nose–Hoover thermostat at 10 ps. The NVT equilibration to 300 K at 1 ns was performed using AmberTools22 [432] with the classical force field q-SPC/Fw [433]. Final snapshots of each NVT equilibration are shown in Figure A1. NVT equilibration at 300 K at 10 ps was performed using density functional theory (DFT) and HF. The step times were all set to 0.5 fs in this dissertation. Subsequently, the 10 ps AIMD simulation in the NVE ensemble was performed based on the DFT and HF NVT equilibration results. Further, the UCCSD($2e$,$2o$) NVE simulation was continued from the HF-level NVT equilibration.

The HF calculations were performed on a GPW basis under PBC, and the core electrons were treated with the corresponding GTH pseudopotential. The Gaussian-type basis function was 6-31G(d). The cutoff energy of the auxiliary plane-wave and Gaussian-type basis functions were set to 300 and 40 Ry, respectively. The number of multigrids was set to four for efficient integral calculations. Further, DIIS was adopted as the optimizer of the wave function,

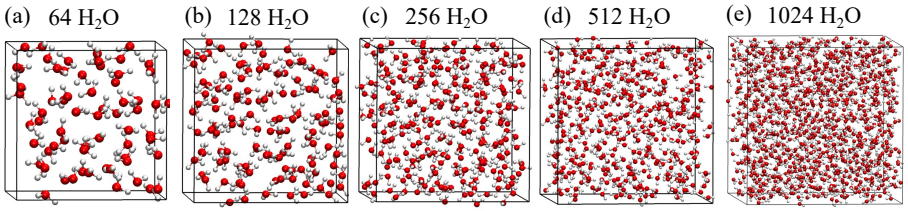

Figure A1: Liquid water unit cells with a density of $1\,g/cm^3$ used for benchmarking, as described in Section 3.4.5. The unit cells contain (a) 64 H_2O, (b) 128 H_2O, (c) 256 H_2O, (d) 512 H_2O, and (e) 1024 H_2O molecules. Each snapshot represents the final configuration obtained after 1 ns of NVT equilibration at 300 K using the classical force field q-SPC/Fw.

and the threshold of the SCF was set to 1.0×10^{-7} Hartree. OT with a full single inverse preconditioner was applied with an energy gap and step size of 0.08 Hartree to improve the efficiency of the SCF calculation. To improve the convergence of the SCF, we set the maximum number of loops of the outer SCF, wherein the preconditioner was applied at each step, to 10. In addition, the maximum number of loops of the inner SCF, in which the preconditioner was fixed, was set as 40. Further, we screened two-electron integrals below 1.0×10^{-10} using Schwarz's inequality to accelerate the computation. In the DFT calculations, the PBE functional [300] was selected as the exchange-correlation functional. The other calculation conditions were the same as those used for the HF calculation.

3 Geometries of Water Clusters

Figure A2 shows the water clusters before and after the geometry optimization. No convergence to non-physical structures was observed. Thus, the geometry optimization based on the analytical gradients via CP2K, utilizing the quantum calculation results obtained through our developed interface, was confirmed to operate correctly.

4 NVT Ensemble of Liquid Water

Figure A3 shows the results of the NVT simulations used to determine the initial structure and velocities for the 10 ps NVE simulation of water at 300 K, as shown in Figure 3.6. The simulation procedures are detailed in Appendix B.d. In each case, the system equilibrated at approximately 300 K within 10 ps. The equilibration behavior at the UCCSD($2e$,$2o$) level shown in Figure A2(c) resembled that of the HF method shown in Figure A2(b). This similarity was consistent with the radial distribution functions (RDFs) for O-O obtained from the NVE ensemble, which were similar for both HF and UCCSD($2e$,$2o$), as shown in Figure 3.6(c).

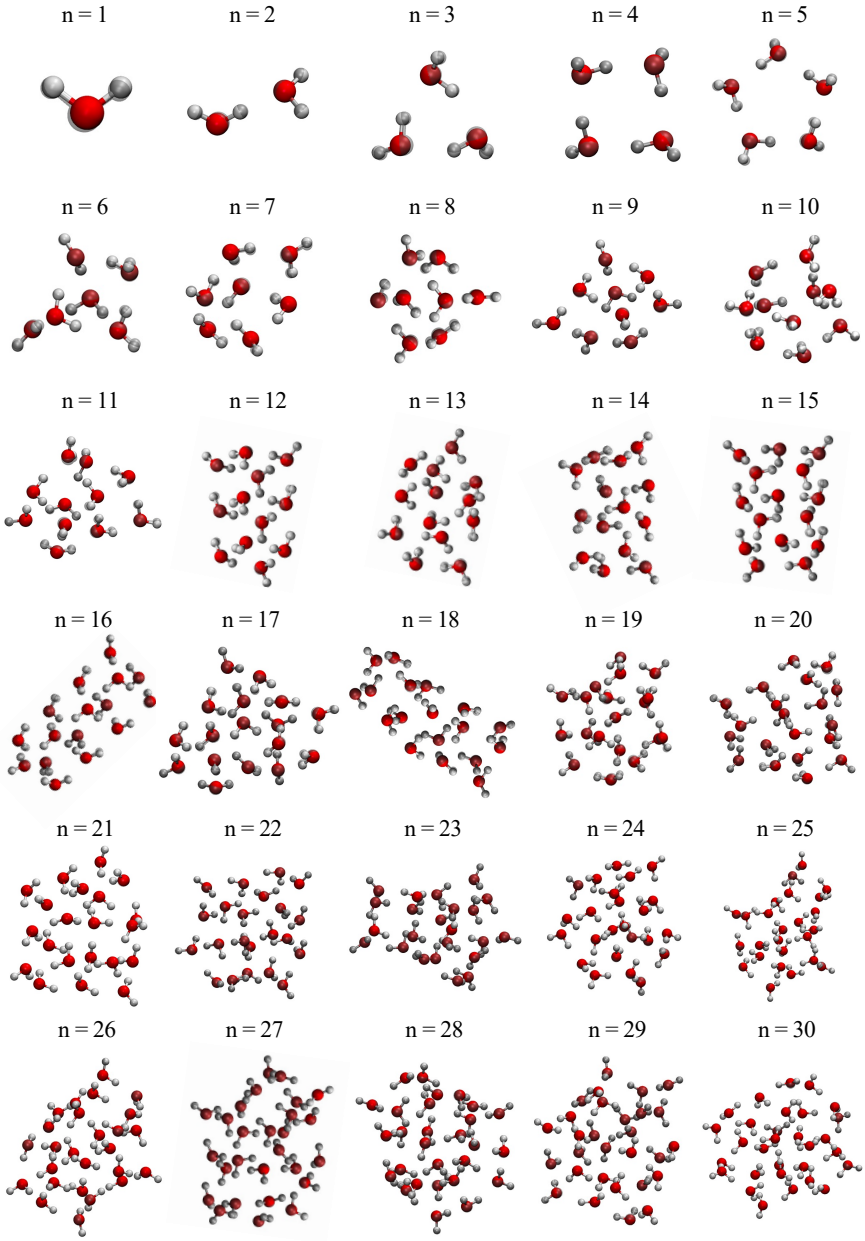

Figure A2: Optimized geometries of water clusters (n-mers) for $n = 2 \cdots 30$. Each subfigure displays the optimized geometry (with clear bonds and atoms) and the initial geometry used for the optimization (shown as shadows) using the UCCSD($2e$, $2o$) calculations.

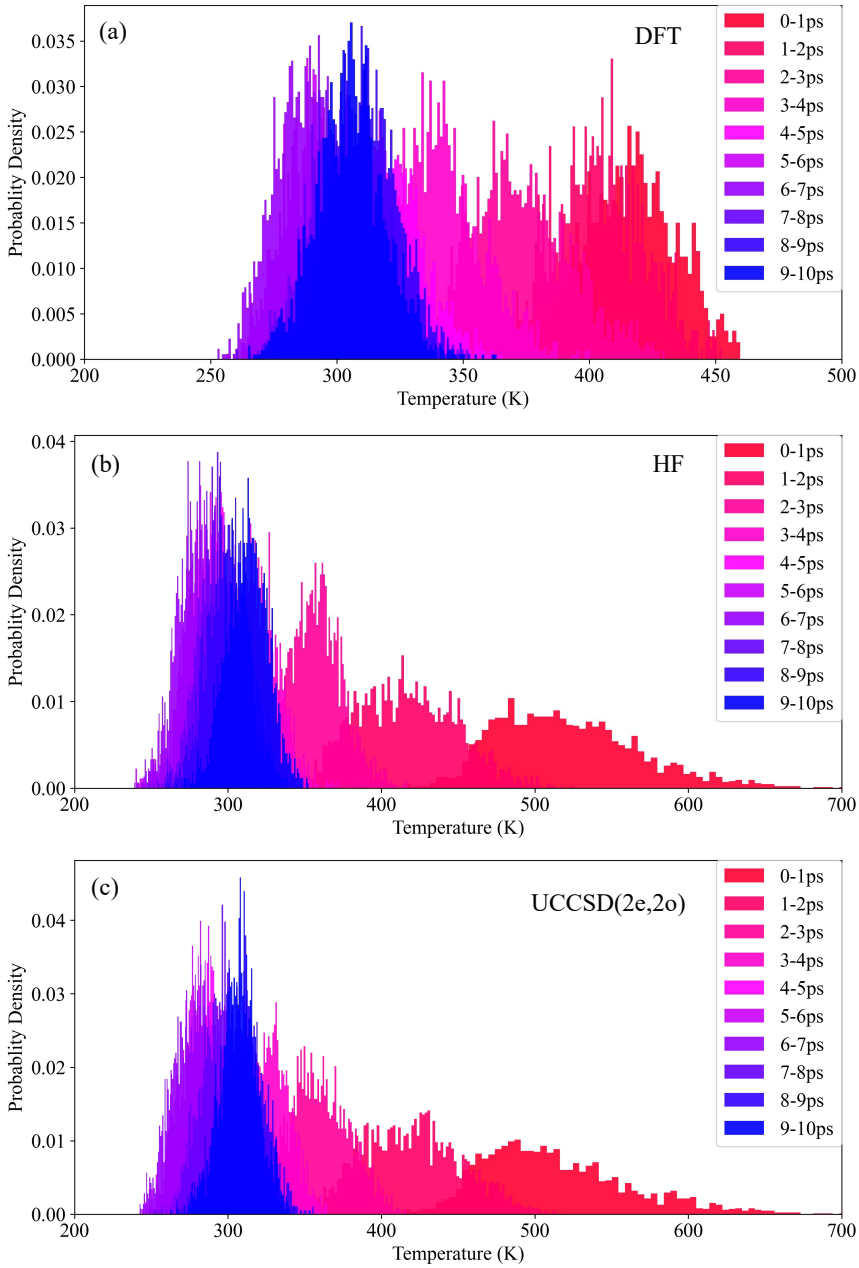

Figure A3: Temperature distribution changes during 10 ps NVT equilibration. The distributions are presented for every 1 ps interval. Each subplot represents a different computational method: (a) DFT, (b) HF, and (c) UCCSD(2e,2o). The x-and y-axes represent the temperature and probability density, respectively. The color gradient indicates the progression of time intervals, with each color corresponding to a specific 1 ps interval, as indicated in the legend.

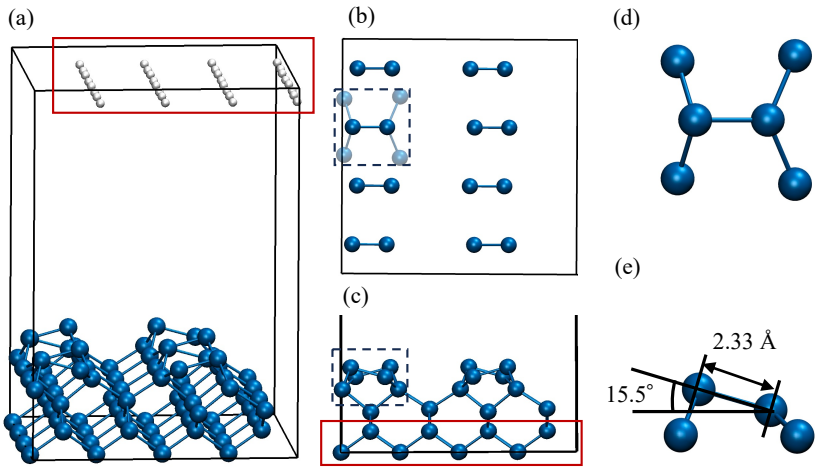

Figure A4: (a) Bird's eye view of the slab model of the Si(001)-c(4×2) reconstructed surface optimized at the UCCSD(4*e*,4*o*) level. The red box highlights the hydrogen termination for the fifth Si layer. (b) Top view and (c) side view of the Si(001)-c(4×2) reconstructed surface. In the top view, only the Si dimers of the reconstructed surface are shown for clarity. The black dashed box indicates the second layer of backbonding atoms (shown faintly) that bond with the Si dimers. In the side view, the red box indicates the fourth and fifth layers, where atomic positions are fixed during structural optimization, along with the hydrogen atoms in (a). (d) and (e) provide detailed views of the dashed box region in (c), with (e) presenting the Si dimer bond length and buckling angle.

5 Si(001)-c(4×2) Reconstructed Surface

Figure A4 shows the unit cell of the Si(001)-c(4×2) surface slab model optimized at the UCCSD(4*e*,4*o*) level. Shirasawa et al. studied this surface using low-energy electron diffraction experiments. They reported an Si dimer bond length of 2.4 ± 0.1 Å and a tilt angle of 18 ± 1° [216]. In this dissertation, the optimized Si dimer bond length and tilt angle were 2.33 Å and 15.1°, respectively, as shown in Figure A4(e). These values were slightly smaller than the experimental values. This discrepancy may have resulted from the limited degrees of freedom of the orbitals used in the quantum calculations. Healy et al. applied quantum Monte Carlo methods to cluster models of a Si(001) surface and concluded that both static and dynamic correlations were essential for Si dimer buckling [434]. We expect that simulations that can more efficiently and accurately incorporate electronic correlations, such as those using quantum embedding methods [205] or large active spaces accessible with actual quantum devices, will achieve better consistency with experimental measurements.

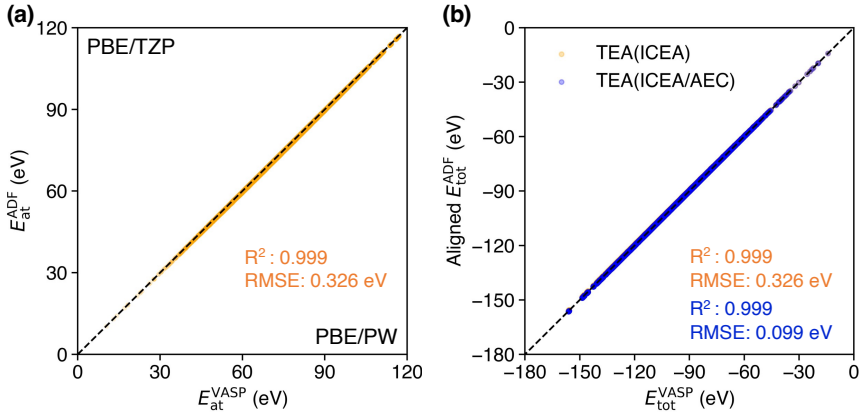

Figure B5: The total energy alignment (TEA) results for different datasets. (a) Parity plot of atomization energies between QM9VASP and QM9ADF datasets using the same PBE functional. (b) Parity plot of the total energies after applying Inner Core Energy Alignment (ICEA) and Atomization Energy Correction (AEC) to the QM9ADF dataset.

Appendix B: Supporting Information for Chapter 4

1 Total Energy Alignment for QM9 Dataset

a Verification of Total Energy Alignment Method

To evaluate the performance of the TEA method between datasets that, despite employing the same fidelity functionals, differ in core electron treatments, basis sets, and periodic boundary conditions, we conducted TEA between the quantum chemistry software packages VASP [281, 282, 283, 182] and Amsterdam Density Functional (ADF) [285]. We utilized the QM9 dataset, which comprises approximately 134,000 molecules optimized at the B3LYP/6-31G(d) level using Gaussian09 [131]. By performing single-point energy calculations at the PBE/PW level with VASP on the Gaussian09-optimized geometries, we generated a new dataset referred to as QM9VASP. For the TEA target, we adopted the PBE/TZP level dataset from MultiXC-QM9 [254]—calculated using ADF with various functionals—which excludes molecules involving charge separation [435]; we will hereafter refer to this dataset as QM9ADF.

Figure B5(a) shows the parity plot of the atomization energies of QM9VASP and QM9ADF. Although QM9VASP and QM9ADF are calculated using the same function, systematic differences are observed, with a root mean square error (RMSE) of 0.3258 eV. As shown in Figure B5(b), by performing TEA using Inner-Core Energy Alignment (ICEA), the total energies of both are consistent,

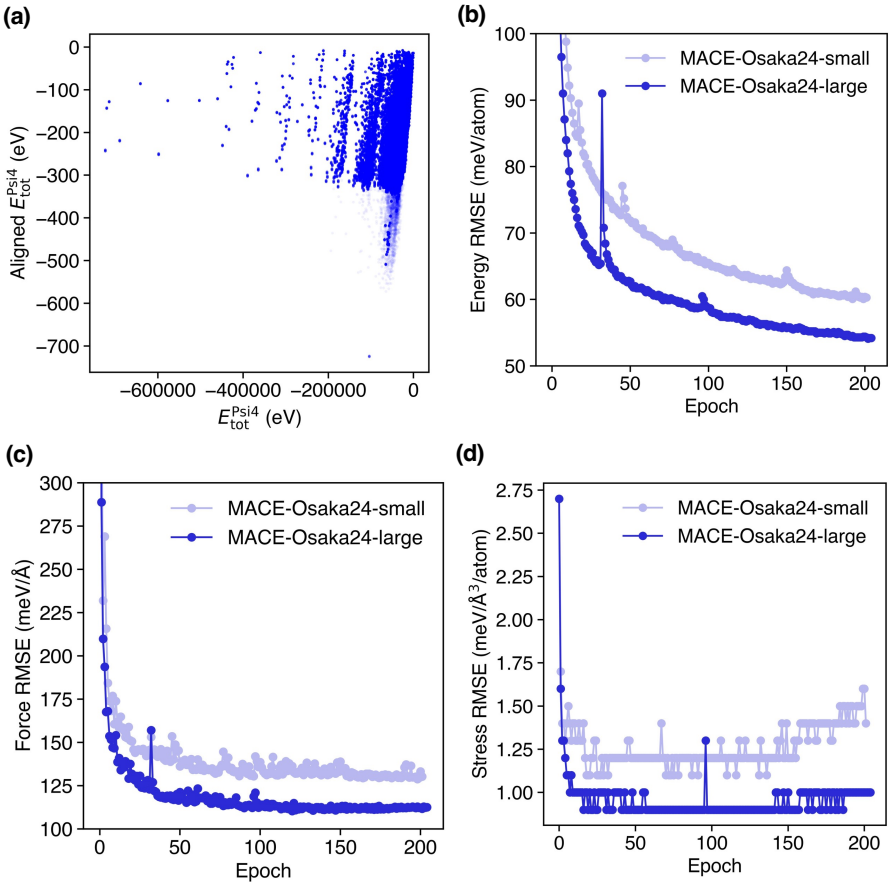

Figure B6: (a) Parity plot of total energies from the original OFF23 dataset and after application of total energy alignment (TEA). (b) Energy root mean square error (RMSE) during training of MACE-Osaka24-small and MACE-Osaka24-large models over 200 epochs. (c) Force RMSE during training of the same models. (d) Stress RMSE during training of the same models.

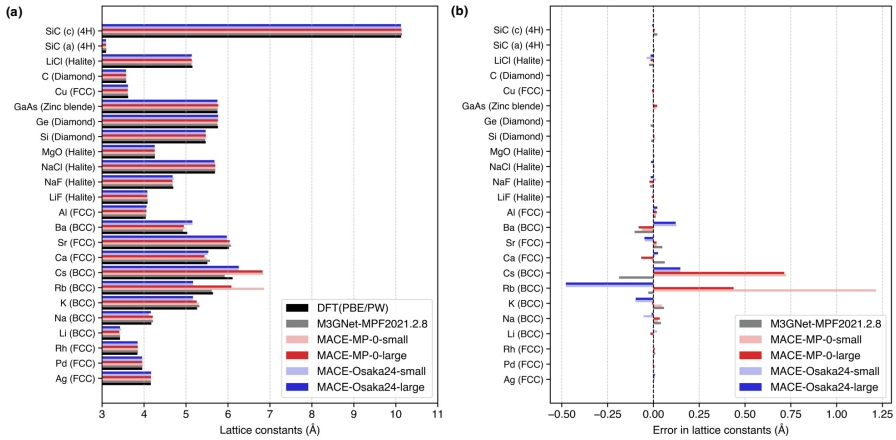

Figure B7: (a) Lattice constants of bulk crystals predicted by universal MLIPs and by DFT calculations using the PBE functional with VASP, which is at the same theoretical level as the training data of the universal MLIPs presented in Section 4.5 in Chapter 4. (b) Prediction errors of the universal MLIPs relative to the lattice constants predicted by DFT.

with an RMSE of 0.3258 eV. Therefore, TEA without correction is viable for functionals calculated at the same level. Furthermore, by performing TEA (ICEA/Atomization Energy Correction (AEC)), the RMSE of the total energy between the two improves to 0.0992 eV.

2 Training Multi-Domain Universal Machine Learning Interatomic Potentials

We demonstrate that stable training of universal MLIPs is possible by integrating datasets of the organic domain, to which TEA has been applied, into datasets of the inorganic domain. In this dissertation, as shown in Figure B6(a), we constructed a TEA-MPtrj/OFF23 dataset by integrating the TEA-OFF23 dataset, which uses the scaling factor of AEC to QM9, into MPtrj of the Materials Project. For the MLIP architecture, we adopted the MACE small and large architectures proposed by Batatia et al. [47]. The constructed multi-domain universal MLIPs are referred to as MACE-Osaka24-small and MACE-Osaka24-large, respectively. Figure B6(b)–(d) shows the learning curves of the MACE-Osaka24 models for energy, force, and stress. It was confirmed that the RMSEs tend to be smaller for the large model with a larger model size compared to the small model. This is in good agreement with the trend of learning curves shown in the paper by Batatia et al. [47].

3 Computational Details

a QM9VASP Dataset Generation

QM9VASP dataset was generated using the Vienna Ab initio Simulation Package (VASP) version 5.4.4. For the exchange-correlation functional, we adopted the PBE functional used in generating MPtrj dataset. A plane-wave energy cutoff of 400 eV was employed for the expansion of the electronic wave functions (ENCUT = 400). The geometries were taken from the original QM9 dataset. To prevent interactions between adjacent unit cells, a vacuum layer of 10 Åwas introduced in each unit cell. The electronic self-consistency loop was considered converged when the total energy change between successive iterations was less than 1×10^{-5} eV (EDIFF = 1e-05). Symmetry operations were disabled (ISYM = 0). High-precision settings were applied throughout the calculations (PREC = Accurate) to ensure reliable results. The Brillouin zone integrations were performed using the Gaussian smearing method with a smearing width of 0.1 eV (ISMEAR = 0, SIGMA = 0.1).

b QM9Psi4 Dataset Generation

The QM9Psi4 dataset was generated using Psi4 version 1.9. To ensure that the computational conditions are equivalent to those employed in generating the OFF23 dataset, we adopted the ωB97M-D3(BJ) functional, which adds the D3 dispersion correction with the Becke-Johnson (BJ) damping function to the exchange-correlation functional ωB97M. The def2-TZVPPD basis set was used in all calculations.

c Biaryl Torsion Benchmark

First, we introduce the method for generating the biaryl torsion dataset by Lahey et al. [306], which provides the reference energies at the coupled cluster level as shown in Table 4.1. The torsional PES were computed using density-fitting Møller-Plesset perturbation theory at second order (DF-MP2) with the def2-TZVP basis set (DF-MP2/def2-TZVP). CCSD(T1)*/CBS energies were obtained by combining the domain-based local pair natural orbital (DLPNO)-CCSD(T) (denoted as CCSD(T)*) [436], the complete basis set (CBS) correction scheme proposed by Smith et al. [274, 306], and iterative triples CCSD(T1) methods [436]. These torsional PES values serve as reference data for this dissertation.

We performed torsional PES optimizations using GFN2-xTB [307], MACE-MP-0, SO3LR [277], MACE-OFF23, MACE-Osaka24, VASP, and Psi4 on the dihedral torsions of 78 molecules presented in the biaryl torsion benchmark [306]. In calculations with GFN2-xTB and all MLIPs, the dihedral angles were varied in 5° increments, and structure relaxations were performed under the constraint that each dihedral angle remained fixed at its set value. For VASP and Psi4, the dihedral angle increments were set to 10°. In all methods, geometry relaxations were carried out until the force acting on each atom was less than 0.01 eV/Å. All

constrained geometry optimization calculations were implemented using Atomic Simulation Environment (ASE) version 3.23.0 [437]. It should be noted that in the work by Kovács et al. [278], the torsional PES optimization was performed using TorsionDrive [438] algorithm.

d Benchmark on Transition1x

The original Transition1x dataset was generated using ORCA version 5.0.2 with the exchange functional ωB97x and the basis set 6–31G(d). Since our constructed MACE-Osaka24 models are based on the OFF23 dataset computed with Psi4, we performed single-point calculations on the initial state, transition state, and final state geometries of the 10,073 reactions provided in Transition1x dataset using Psi4 under the computational conditions specified in Appendix b to ensure compatibility. Similarly, all validations using MLIPs and GFN2-xTB were carried out by performing single-point calculations on the IS, TS, and FS geometries provided in Transition1x.

e Bulk Crystal Lattice Constant

The crystals used for the benchmark were those adopted in Section B.4 of the Supporting Information in the paper by Batatia et al [47]. For the BCC materials K, Rb, and Cs, it was not possible to represent them using the 4.5 Å cutoff radius employed in the graph construction for the MACE-Osaka24 models, and therefore they were excluded for benchmark in Section 4.5. Further details can be found in Appendix B.4. The optimization of lattice constants through first-principles calculations was performed using VASP at PBE level. To ensure compatibility with the MPtrj dataset used for training the MACE-MP-0 and MACE-Osaka24 models, input parameters from the MPRelaxSet in the pymatgen [439] library of the Materials Project were utilized. For the MACE-MP-0 and MACE-Osaka24 models, the convergence criterion for unit cell optimization was set to 0.01 eV/Å. First-principle PES calculations for Si as a function of lattice constants, shown in Figure 4.3(c), were performed using single-point calculations with inputs from the MPStaticSet in pymatgen. The lattice constants were varied from 5 Å to 6 Å in increments of 0.01 Å.

f Molecular Dynamics of Liquid Water

Classical MD simulations were performed using GROMACS version 2023.3 [440]. The TIP3P [441] and TIP4P/2005 [442] water models were employed as the force fields. The TIP4P/2005 model was chosen as a reference for evaluating the accuracy of MLIPs because it reproduces the thermodynamic properties of water with high accuracy over a wide temperature range [443]. For ML-driven MD simulations, the interface with MACE was implemented using a modified version of OpenMM-ML [444], enabling the incorporation of D3(BJ) dispersion force corrections. Simulations were conducted in a PBC box containing 64 H_2O molecules with a density of 1 g/cm^3. For ML-driven MD, NVT ensemble

Table B1: Mean absolute errors (MAEs) of lattice constants (in Å) predicted by universal MLIPs compared to DFT with PBE using VASP, categorized by crystal structure type. The predictions from M3GNet-MPF2021.2.8, MACE-MP-0-small, MACE-MP-0-large, MACE-Osaka24-small, and MACE-Osaka24-large models are evaluated across various structures including 4H, BCC, Diamond, FCC, Halite, and Zinc blende. The errors correspond to the deviations shown in Figure B7(b).

Crystal structure	M3GNet-MPF2021.2.8	MACE-MP-0-small	MACE-MP-0-large	MACE-Osaka24-small	MACE-Osaka24-large
4H	0.0143	0.0036	0.0042	**0.0002**	0.0033
BCC	**0.0701**	0.3453	0.2153	0.1536	0.1423
Diamond	0.0100	0.0047	0.0031	**0.0020**	0.0029
FCC	0.0200	**0.0096**	0.0179	0.0118	0.0156
Halite	0.0111	**0.0036**	0.0108	0.0113	0.0100
Zinc blende	**0.0017**	0.0153	0.0205	0.0049	0.0031

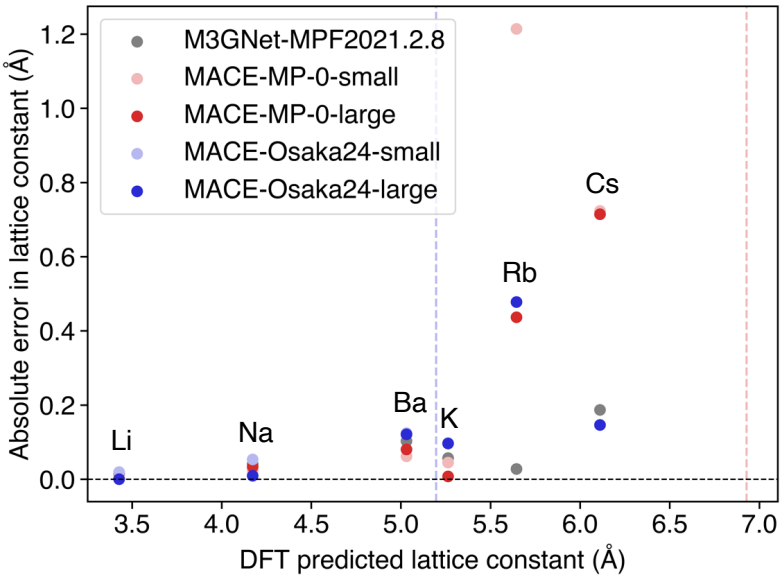

Figure B8: Absolute errors in lattice constant predictions as a function of DFT-predicted lattice constants for body centered cubic (BCC)-type crystals using various universal MLIPs. The models compared are M3GNet-MPF2021.2.8, MACE-MP-0 (small and large), and MACE-Osaka24 (small and large). The graph construction cutoff radii for the MACE-MP-0 and M3GNet models are 6.0 Å, with the range of lattice constants these models can consider indicated by the red dashed line. For the MACE-Osaka24 model, the cutoff radius is 4.5 Å, and the corresponding range of lattice constants is shown by the blue dashed line. Specific elements (Li, Na, K, Rb, Cs, Ba) are labeled for clarity.

simulations were performed for 100 ps, with the final 50 ps used for analysis. For classical MD, simulations were carried out in an NVT ensemble with 1,000 H_2O molecules for 1,000 ps, with the last 500 ps utilized for analysis.

4 Material-Specific Lattice Constants

In this section, we discuss the results of lattice constant predictions for representative bulk crystals presented in Section 4.5, as well as the predictive performance for each crystal structure. Figure B7 shows the predicted lattice constants obtained from DFT and universal MLIPs. As shown in Figure B7(b), the predictions by M3GNet-MPF2021.2.8 exhibit the fewest outliers among the models. As indicated in Table B1, the M3GNet-MPF2021.2.8, MACE-MP-0, and MACE-Osaka24 MLIPs achieve prediction accuracies with mean absolute errors (MAEs) below 0.02 Åfor crystal structures other than body-centered cubic (BCC). However, in predicting BCC-type crystal structures, they exhibit larger

prediction errors compared to other crystal structures. The poor predictive performance for BCC crystals may be related to the cutoff radius used in graph construction. Figure B8 shows the DFT-predicted lattice constants of BCC crystals and the absolute errors of the lattice constant predictions. As the lattice constant increases, the prediction errors of all models also increase. MACE-Osaka24 is constructed with a cutoff radius of 4.5 Å, while M3GNet-MPF2021.2.8 and MACE-MP-0 are constructed with a cutoff radius of 6.0 Å. Therefore, the maximum lattice constants of BCC crystals that each model can capture are 5.196 Åfor MACE-Osaka24 and 6.928 Åfor M3GNet-MPF2021.2.8 and MACE-MP-0. Predictions for larger lattice constants result in a superposition of isolated atoms and simple cubic lattice crystals, failing to properly capture the BCC crystal structure. Thus, MACE-Osaka24 cannot be applied to predict the lattice constants of K, Rb, and Cs. On the other hand, although M3GNet and MACE-MP-0 have cutoff radii exceeding the lattice constants of the target BCC crystals, their predictions tend to approach lattice constants near the cutoff radius, suggesting that using larger cutoff radii may be necessary for improvement.

Appendix C: Supporting Information for Chapter 5

1 Distribution of Datasets for Each Nuclear Magnetic Resonance Chemical Shift Prediction Model

The distributions of the training and test sets sampled from the QM9NMR dataset are shown in Figure C9. Figure C9(a) shows that above 5K, the distribution is in good agreement with the overall distribution of the ^{13}C NMR shielding constants. For the other elemental species, the distributions of the training and test sets were in good agreement with the overall distribution.

2 Kernel Function Dependency for Various Graph Neural Network Transfer Learning Descriptors

The accuracy of KRR models using Gaussian and Laplacian kernels was evaluated. Table C2 presents the mean RMSE and its standard deviation for predictions on the 50,000 holdout set by models trained on 400 data points of $^{\mathbf{13}}$C using Gaussian and Laplacian kernels. For all models using GNN-TL descriptors, the mean RMSE of models with Gaussian kernel was found to be more accurate than those with Laplacian kernel. However, the variation in accuracy due to dataset sampling (standard deviation) was found to have a greater impact than kernel choice in models with MEGNet and M3GNet GNN-TL descriptors. On the other hand, in models with MACE GNN-TL descriptors, the impact of kernel choice was more significant than the variation due to dataset sampling.

Next, Table C3 shows the accuracy of KRR models using M3GNet and MACE-OFF23-small GNN-TL descriptors trained on a 100,000 ^{13}C training set.

Unlike models trained on the 400 ^{13}C training set, the KRR models with M3GNet GNN-TL descriptors consistently showed higher accuracy with the Laplacian kernel compared to the Gaussian kernel. Conversely, the results for MACE-OFF23-small GNN-TL descriptors were similar to those for models trained on the 400 ^{13}C training set, with the Gaussian kernel models demonstrating higher accuracy. This suggests that the appropriate kernel function may vary depending on the size of the training data.

Finally, these results indicate the choice of kernel functions for KRR models as presented in Section 5.4 of Chapter 5. For models trained on 400 ^{13}C data points, all KRR models using GNN-TL descriptors employed the Gaussian kernel. In contrast, for models trained on 100,000 ^{13}C data points, the Laplacian kernel was used for KRR models with M3GNet GNN-TL descriptors, whereas the Gaussian kernel was employed for models with MACE-OFF23-small GNN-TL descriptors.

3 Validation of Learning Accuracy of Nuclear Magnetic Resonance Chemical Shift Prediction

Figure C10 illustrates the accuracy of the KRR models trained using the M3GNet GNN-TL descriptor for five elemental species. The MAE values for the NMR shielding constant, for train/test, are as follows: for ^{1}H, 0.0344/0.1767; ^{13}C, 0.1420/2.2798 ppm; ^{15}N, 0.3910/3.4157 ppm; ^{17}O 0.8881/4.9509 ppm; and ^{19}F 0.0864/2.6518 ppm.

The accuracy of the GNN-TL descriptors was also validated using the molecular structures of two drug molecule data sets reported in Ref 29. The predicted ^{13}C NMR shielding constants for each drug molecule using the M3GNet and MACE-OFF23 GNN-TL/KRR models are shown in Figure C11(a) and (c). These predictions are accompanied by the values predicted by the FCHL/KRR model [132]. The prediction results of the M3GNet/KRR model using PM7-level optimized geometries, along with the prediction results using DFT-level geometries, are shown in Figure C11(b) and (d).

Table C2: Accuracy (measured by RMSE) of GNN-TL/KRR models trained on 400 13C NMR chemical shift values for different kernel functions. All units are in ppm.

GNN-TL descriptor	Gaussian kernel	Laplacian kernel
MEGNet	**20.08±0.55**	21.12±0.56
M3GNet	**10.02±0.37**	10.31±0.38
MACE-MP-0-small	**9.77±0.34**	10.78±0.31
MACE-MP-0-large	**9.74±0.27**	10.17±0.30
MACE-OFF23-small	**8.05±0.19**	8.64±0.13
MACE-OFF23-large	**8.15±0.42**	8.77±0.21

Table C3: The kernel function dependency of accuracy (MAE) for the prediction of the 50,000 QM9NMR hold out set, 40 drug molecules from GDB17 Universe and the other containing 12 drugs with 17 or more heavy atoms. All units are in ppm.

	M3GNet		MACE-OFF23-small	
	Gaussian	Laplacian	Gaussian	Laplacian
50,000 QM9	2.35	**2.28**	**1.87**	2.10
40 drugs	3.98	**3.46**	**2.83**	3.21
12 drugs	5.14	**4.21**	**3.85**	3.93

4 Data Availability

Data and code required to reproduce the figures and tables related to the GNN-TL descriptors and the NMR shielding constants prediction models presented in the manuscript is publicly accessible on GitHub at https://github.com/TShiotaSS/gnn-tl. The dataset utilized for the prediction of NMR chemical shifts, specifically the QM9NMR dataset, is available at DOI: https://doi.org/10.17172/NOMAD/2021.10.16-1 and GitHub at https://moldis-group.github.io/qm9nmr/. Results of the DFT/GIAO calculations for isolated atoms, used for NMR chemical shift computations, are included within the manuscript. The GNN-TL descriptor vectors for the QM9NMR datasets are available at DOI: https://doi.org/10.6084/m9.figshare.25484068.v2. We have modified the code to extract GNN-TL descriptors from the pretrained M3GNet model on Github at https://github.com/materialsvirtuallab/m3gnet, and this adapted version can be found at https://github.com/TShiotaSS/gnn-tl/tree/main/scripts/m3gnet. The code used to extract GNN-TL descriptors from the pretrained MEGNet model can be found on GitHub at https://github.com/materialsvirtuallab/megnet/blob/master/megnet/utils/descriptor.py. The code used to generate descriptors from the pretrained MACE models can be found on GitHub at https://github.com/ACEsuit/mace/blob/main/mace/calculators/mace.py. The implementation for quantum kernel ridge regression used in this chapter is available at https://github.com/Qulacs-Osaka/scikit-qulacs/tree/main/skqulacs/qkrr.

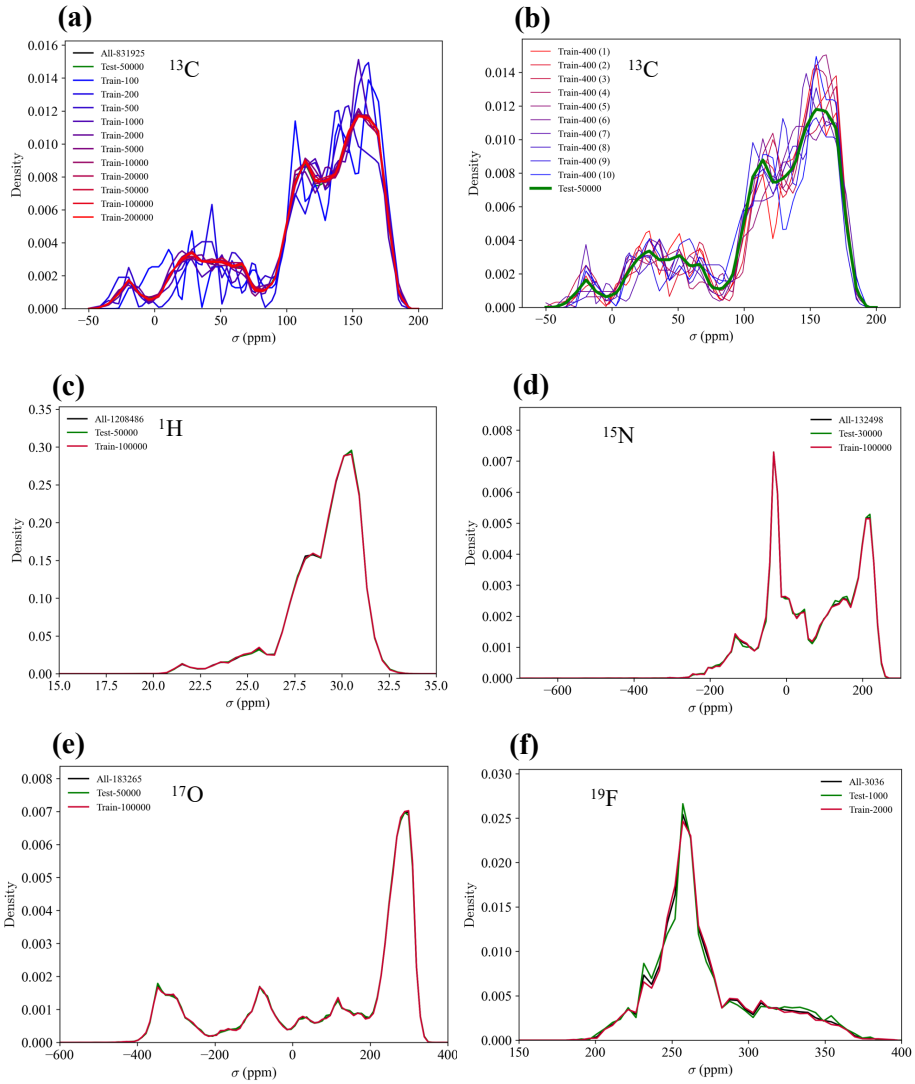

Figure C9: Distributions of the NMR shielding constants of the training subsets and test set sampled from the of the QM9NMR dataset for the five elemental species: (a) ^{13}C (for dataset size dependency), (b) ^{13}C (for potential data bias), (c) ^{1}H, (d) ^{15}N, (e) ^{17}O, and (f) ^{19}F, respectively.

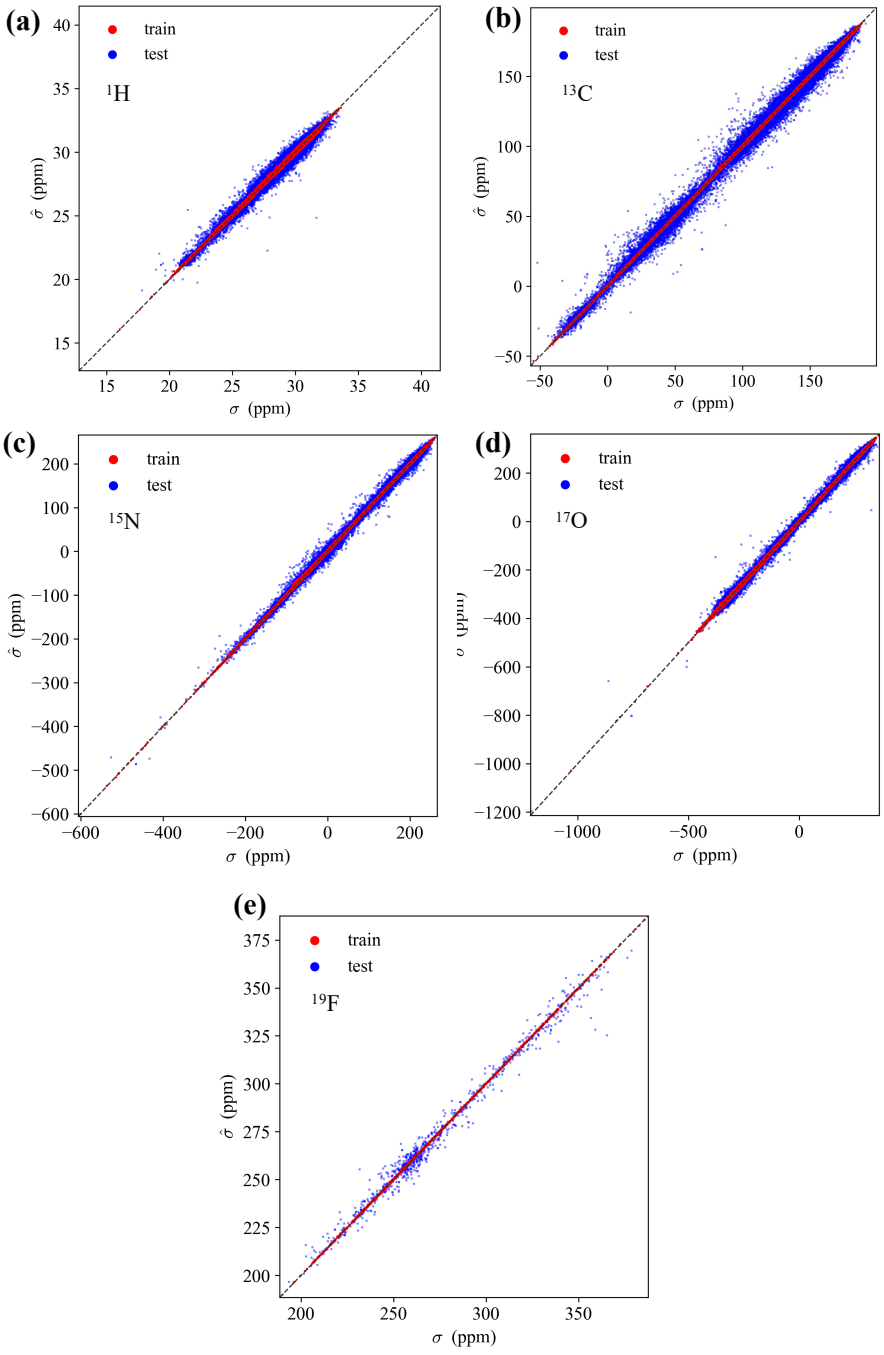

Figure C10: Scatterplots for the training set (red) and test set (blue) showing NMR chemical shifts from the QM9NMR dataset, using the M3GNet GNN-TL/KRR model constructed with QM9NMR data for the five elemental species: (a) ^{1}H, (b) ^{13}C, (c) ^{15}N, (d) ^{17}O, and (e) ^{19}F, respectively.

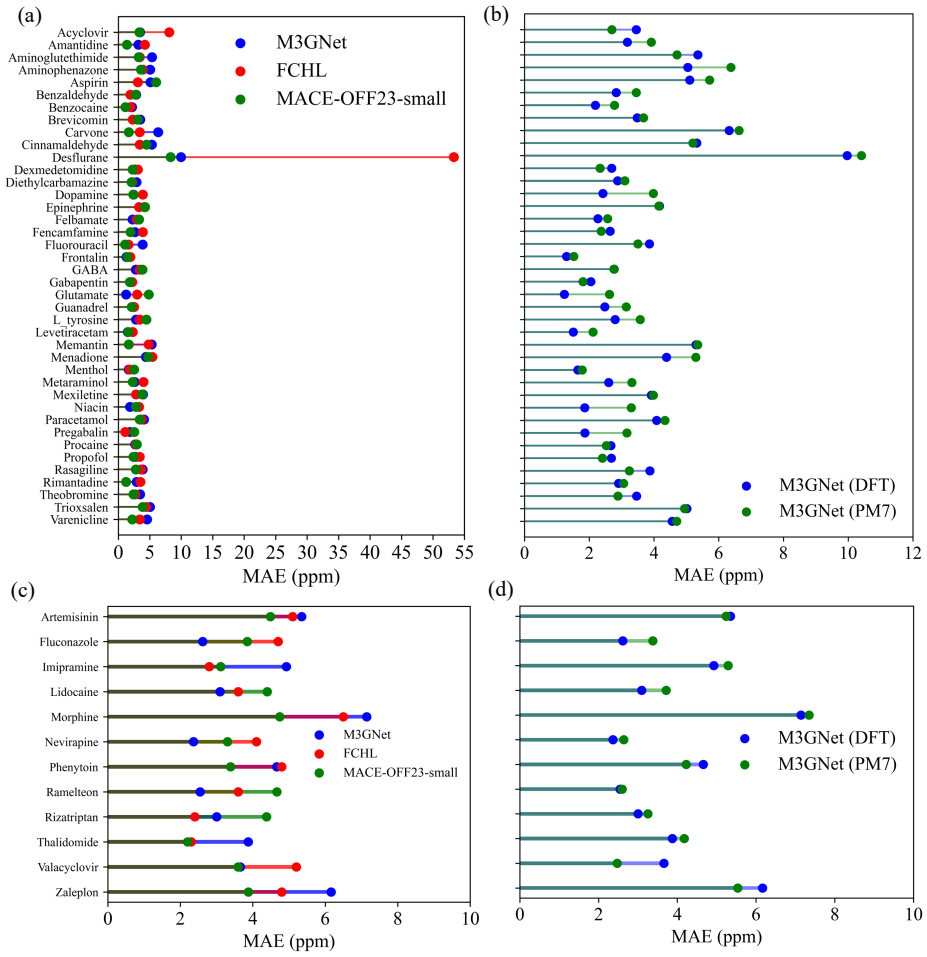

Figure C11: Comparison of ^{13}C NMR shielding constant predictions using different descriptors for (a) 40 drug molecules from the GDB17 universe and (d) 12 drugs with 17 or more heavy atoms. The predictions were made using the KRR model with the FCHL descriptor (red), the M3GNet GNN-TL descriptor (blue), and the MACE-OFF23-small GNN-TL descriptor (green). The FCHL results were taken from Ref. [132]. The results for the M3GNet/KRR model using DFT-level geometries and PM7-level geometries are shown in (b) and (d), respectively.

Appendix D: Supporting Information for Chapter 6

1 Computational Details

a Modeling

We modeled CO adsorption on the NPs, i.e., CO/M_n, using an atomic simulation environment (ASE) [445, 437]. The initial lattice constants (LCs) of M_n were determined via bulk calculations. For HEA_{201}, the largest bulk was used as the initial LC. A 15-Å vacuum region was inserted in all supercells to minimize cell-to-cell interactions. The initial structures of CO/M_n and CO/HEA_{201} were derived by placing CO on the on-top sites of the optimized structures of M_n and HEA_{201}, respectively, with the distance between the C atom and the adsorption-site metal atom M set as 2 Å.

b Neural Network Potential Calculations

The NNP used was M3GNet, a universal NNP proposed by Chen and Ong [124]. This M3GNet NNP was trained on approximately 180,000 crystal environments at the PBE or PBE+U levels of theory from the Materials Project [244], covering 89 elements. The crystal structures of the bulk $M = Ir, Pd, Pt, Rh, Ru$ were assumed to be fcc. Although Ru exhibits a hexagonal close-packed form at room temperature, Ru with an fcc structure can be created using NPs [446]. The atomic energy of the bulk fcc metal M was determined using the energy corresponding to the minimum value obtained when varying the LC of the material at intervals of approximately 0.01 Å. The resulting atomic-energy values and corresponding LCs are presented in Table D5. The Broyden-Fletcher-Goldfarb-Shanno (BFGS) algorithm was used for structural optimizations, with a maximum step of 0.005 Å. In the CO/M and CO/HEA structural optimization calculations, the M and HEA structures were fixed as stable isolated systems. Only the CO and adsorption-site atoms were relaxed, with the constraint that the adsorbed molecules occupy the top site. Structural optimizations were performed until the force acting on each atom was 0.001 eV/Å.

c Density Functional Theory Calculations

The DFT calculations were performed using the Vienna Ab initio Simulation Package (VASP), version 5.4.4 [447, 282, 182]. We employed the PBE generalized gradient approximation functional as the exchange-correlation functional [300]. The core electrons were treated using the projector-augmented wave method [448, 449]. Electronic structures were optimized using the blocked Davidson iteration scheme within a spin-restricted approximation. The cutoff energy for the plane-wave functions was set as 400 eV. Atomic coordinates were optimized using a conjugate-gradient algorithm with a convergence threshold of 0.01 eV/Å.

Table D4: Parameters α and β of the regression lines between the CO adsorption energy and the generalized coordination number (GCN) for monometallic systems. The values correspond to the lines in Figures 6.8(a) and (b)

	Ir	Pd	Pt	Rh	Ru
α(NNP)	0.185	0.139	0.173	0.078	0.121
β(NNP)	-2.766	-2.403	-1.073	-1.946	-2.371

d Generalized Coordination Number Evaluations

The GCN descriptor is evaluated according to the following equation, which is identical to the one defined in Ref. [399].

$$\mathrm{GCN}(i) = \sum_{j=1}^{n_i} \frac{cn(j)}{cn_{\max}}. \tag{D34}$$

Here, i represents the index of the surface atom of the NPs. n_i is the coordination number of the i-th atom, and $cn_{\max}$ is the coordination number of the i-th atom in its bulk environment, which is 12 for FCC metals considered in this chapter. $cn(j)$ represents the coordination number of each of the n_i atoms coordinated to the i-th atom. In this chapter, GCN was evaluated for structures optimized using the universal NNP M3GNet, following the same procedure as for the evaluation of the LSE.

e Nonlinear Regression

To capture the nonlinearity between LSE and CO adsorption energy, we trained a nonlinear regression model using all possible ontop adsorption sites (732 in total) from six randomly selected HEA nanoparticles out of the 20 used for validating the linear LSE-based model. For validation, all possible ontop adsorption sites on the remaining 14 HEA nanoparticles were utilized. KRRs were executed using scikit-learn version 1.2.2 [356]. A Gaussian kernel was selected as the kernel function of the KRR. The hyperparameters for each model were optimized over 100 iterations using a randomized search. QCL regressions were implemented using scikit-qulacs version 0.5.0 [362]. Qulacs version 0.5.6 was used as the quantum-circuit simulator [209]. The number of qubits in the QCL regression model was 4. The number of iterations of the parameterized variational quantum circuit of the model corresponding to the weights of the neural network was 6. The timestep for the time evolution operator in parameterized variational quantum circuits was set as 0.5. The BFGS algorithm was used to update the parameters of the QCL model.

Table D5: Atomic energies $E_{\text{atom}}^{\text{bulk}}$ and lattice constants (LC) of face-centered cubic (fcc) bulk metals M (M = Ir, Pd, Pt, Rh, Ru), obtained from M3GNet calculations and used for computing the local Surface Energy (LSE). The atomic energies are the minimum values determined by varying the lattice constant in intervals of approximately 0.01 Å.

fcc bulk M	Ir	Pd	Pt	Rh	Ru
$E_{\text{atom}}^{\text{bulk}}$(eV)	-8.941	-5.185	-6.069	-7.394	-9.305
LC (Å)	3.875	3.957	3.977	3.850	3.815

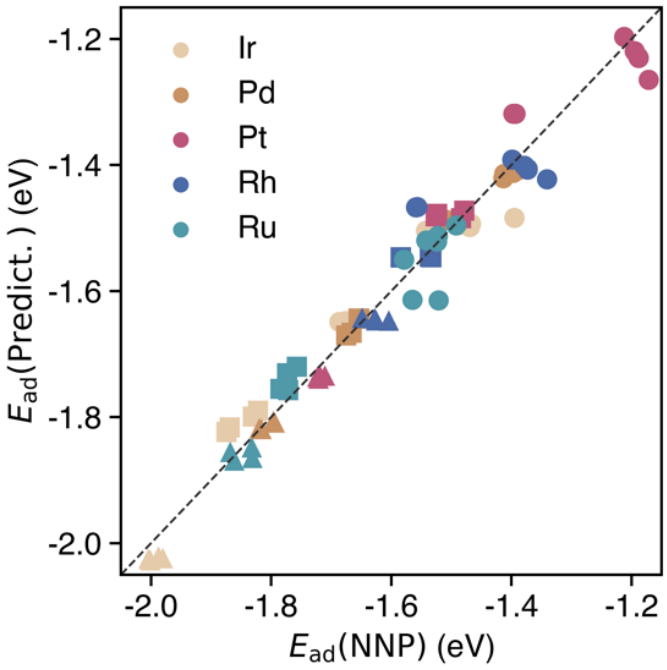

Figure D12: Correlation between the adsorption energies of a CO molecule on monometallic NPs calculated directly using the NNP and those predicted through regression. Circles, squares, and triangles at each datapoint represent the facet, edge, and corner CO adsorption sites, respectively.

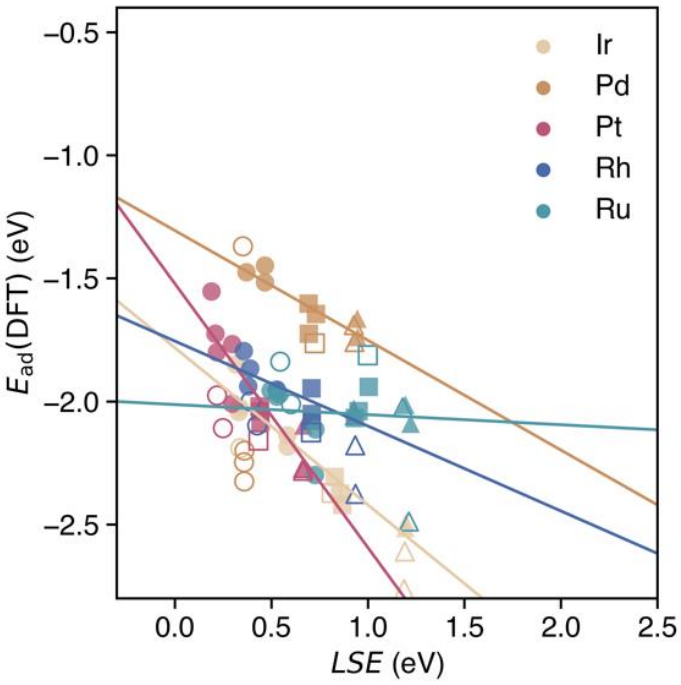

Figure D13: Correlation between adsorption energies of a CO molecule on monometallic NPs calculated directly via DFT and the LSEs corresponding to each adsorption site. The CO adsorption energies for the 38- and 79-atom NPs, as well as the datapoints corresponding to the hollow sites that converged on the Pd NPs, are shown as open markers, as they were not included in the linear regression data points. Circles, squares, and triangles at each datapoint represent the facet, edge, and corner CO adsorption sites, respectively.

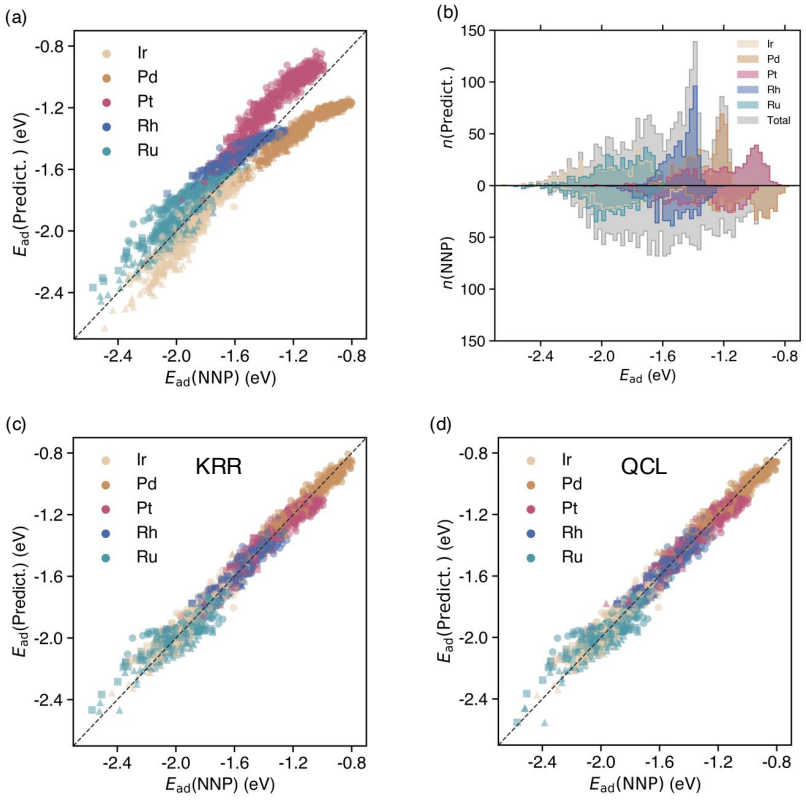

Figure D14: (a) Comparison and (b) correlation between the adsorption energy predicted via LSE and the adsorption energy of CO/HEA_{201} directly calculated using the NNP. We limit the comparison to 2440 sites, encompassing all on-top sites across the 20 structures. For each element (Ir, Pd, Pt, Rh, Ru) for 14 patterns of IrPdPtRhRu HEA_{201} NPs, the energies are corrected using non-linear regression models based on (c) KRR and (d) QCL regression. These values are plotted against values directly obtained using the NNP, which serve as the standard for accuracy.

Table D6: Parameters α and β of the regression lines between the CO adsorption energy and the local surface energy (LSE) for monometallic systems, obtained using NNP and DFT methods. The values correspond to Figures 6.3 and D13, respectively, where NNP and DFT in parentheses indicate the method used to obtain these parameters.

	Ir	Pd	Pt	Rh	Ru
α(DFT)	-0.639	-0.446	-1.073	-0.345	-0.041
α(NNP)	-0.617	-0.692	-1.131	-0.441	-0.515
β(DFT)	-1.782	-1.305	-1.521	-1.755	-2.012
β(NNP)	-1.289	-1.165	-0.983	-1.234	-1.240

2 Details of Models Based on Local Surface Energy and Generalized Coordination Number

Here, we summarize the parameters of the regression model for adsorption-energy prediction using the LSE descriptor as well as the results of the model accuracy validation. Figure D12 shows the parity plot of the training data and prediction results for the LSE linear regression model presented in Figure 2. The RMSE for predicting the training data was 0.035 eV. Figure D13 presents the regression results for the linear regression model between the CO adsorption energies on monometallic NPs obtained via DFT calculations and the LSE. Two datapoints corresponding to the hollow sites that converged on the facets of Pd in 38- and 79-atom monometallic NPs were excluded from the regression model. For small NPs, the entire system tended to exhibit molecular characteristics upon adsorption, making it difficult for a simple regression model to capture these effects. However, for larger NPs, a linear relationship with the LSE, similar to that observed for the NNP, was confirmed. The parameters of the regression models constructed using the adsorption energies from both the NNP and DFT are presented in Table D6. Figure D14 presents a parity plot of the prediction results for the data not included in the training data for the non-linear regression model of HEA NP adsorption energies evaluated directly using the NNP. The prediction accuracies were 0.0580 and 0.0579 eV, respectively, indicating that, as demonstrated in this chapter, the regression models using KRR and QCL had comparable accuracy. Finally, the regression parameters of the GCN-based prediction model are summarized in Table D4.

3 Data Availability

The data and code required to reproduce the figures and tables are publicly accessible on GitHub `https://github.com/TShiotaSS/lse`. NP datasets are available at DOI: `https://figshare.com/articles/dataset/Nano_particle_structures/26973409`. We modified the code to extract the atomic energies from the pretrained M3GNet model on Github at `https://github.com/materialsvirtuallab/m3gnet`, which can be found at

https://github.com/TShiotaSS/lse/tree/main/scripts/m3gnet_each_atom_energy. The implementation for QCL regression used in this chapter is available at https://github.com/Qulacs-Osaka/scikit-qulacs/tree/main.

Bibliography

[1] P. W. Shor, in *Proceedings of the 35th Annual Symposium on Foundations of Computer Science* (IEEE, 1994) pp. 124–134.

[2] P. W. Shor, SIAM review **41**, 303 (1999).

[3] A. Y. Kitaev, Quantum measurements and the abelian stabilizer problem (1995).

[4] D. S. Abrams and S. Lloyd, Physical Review Letters **83**, 5162 (1999).

[5] A. Aspuru-Guzik, A. D. Dutoi, P. J. Love, and M. Head-Gordon, Science **309**, 1704 (2005).

[6] J. Lee, D. W. Berry, C. Gidney, W. J. Huggins, J. R. McClean, N. Wiebe, and R. Babbush, PRX Quantum **2**, 030305 (2021).

[7] A. V. Ivanov, C. Sünderhauf, N. Holzmann, T. Ellaby, R. N. Kerber, G. Jones, and J. Camps, Physical Review Research **5**, 013200 (2023).

[8] J. Biamonte, P. Wittek, N. Pancotti, P. Rebentrost, N. Wiebe, and S. Lloyd, Nature **549**, 195 (2017).

[9] K. Mitarai, M. Negoro, M. Kitagawa, and K. Fujii, Physical Review A **98**, 032309 (2018).

[10] M. Schuld and N. Killoran, Physical Review Letters **122**, 040504 (2019).

[11] S. Jerbi, L. J. Fiderer, H. Poulsen Nautrup, J. M. Kübler, H. J. Briegel, and V. Dunjko, Nature Communications **14**, 1 (2023).

[12] F. Arute, K. Arya, R. Babbush, D. Bacon, J. C. Bardin, R. Barends, R. Biswas, S. Boixo, F. G. Brandao, D. A. Buell, *et al.*, Nature **574**, 505 (2019).

[13] M. Kjaergaard, M. E. Schwartz, J. Braumüller, P. Krantz, J. I.-J. Wang, S. Gustavsson, and W. D. Oliver, Annual Review of Condensed Matter Physics **11**, 369 (2020).

[14] T. Ichikawa, H. Hakoshima, K. Inui, K. Ito, R. Matsuda, K. Mitarai, K. Miyamoto, W. Mizukami, K. Mizuta, T. Mori, *et al.*, Nature Reviews Physics , 1 (2024).

[15] S. J. Evered, D. Bluvstein, M. Kalinowski, S. Ebadi, T. Manovitz, H. Zhou, S. H. Li, A. A. Geim, T. T. Wang, N. Maskara, *et al.*, Nature **622**, 268 (2023).

[16] R. Acharya, D. A. Abanin, L. Aghababaie-Beni, I. Aleiner, T. I. Andersen, M. Ansmann, F. Arute, K. Arya, A. Asfaw, N. Astrakhantsev, *et al.*, Nature **638**, 920–926 (2024).

[17] M. Cerezo, A. Arrasmith, R. Babbush, S. C. Benjamin, S. Endo, K. Fujii, J. R. McClean, K. Mitarai, X. Yuan, L. Cincio, *et al.*, Nature Reviews Physics **3**, 625 (2021).

[18] K. Bharti, A. Cervera-Lierta, T. H. Kyaw, T. Haug, S. Alperin-Lea, A. Anand, M. Degroote, H. Heimonen, J. S. Kottmann, T. Menke, W.-K. Mok, S. Sim, L.-C. Kwek, and A. Aspuru-Guzik, Rev. Mod. Phys. **94**, 015004 (2022).

[19] A. Gilyén, Y. Su, G. H. Low, and N. Wiebe, in *Proceedings of the 51st Annual ACM SIGACT Symposium on Theory of Computing* (2019) pp. 193–204.

[20] J. R. McClean, J. Romero, R. Babbush, and A. Aspuru-Guzik, New Journal of Physics **18**, 023023 (2016).

[21] S. Endo, Z. Cai, S. C. Benjamin, and X. Yuan, Journal of the Physical Society of Japan **90**, 032001 (2021).

[22] Y. Alexeev, M. Amsler, M. A. Barroca, S. Bassini, T. Battelle, D. Camps, D. Casanova, Y. J. Choi, F. T. Chong, C. Chung, *et al.*, Future Generation Computer Systems **160**, 666 (2024).

[23] R. Babbush, J. R. McClean, M. Newman, C. Gidney, S. Boixo, and H. Neven, PRX Quantum **2**, 010103 (2021).

[24] R. P. Feynman, International Journal of Theoretical Physics **21** (1982).

[25] D. S. Abrams and S. Lloyd, Physical Review Letters **79**, 2586 (1997).

[26] G. H. Low and I. L. Chuang, Physical Review Letters **118**, 010501 (2017).

[27] S. McArdle, S. Endo, A. Aspuru-Guzik, S. C. Benjamin, and X. Yuan, Reviews of Modern Physics **92**, 015003 (2020).

[28] B. Bauer, S. Bravyi, M. Motta, and G. K.-L. Chan, Chemical Reviews **120**, 12685 (2020).

[29] J. J. Goings, A. White, J. Lee, C. S. Tautermann, M. Degroote, C. Gidney, T. Shiozaki, R. Babbush, and N. C. Rubin, Proceedings of the National Academy of Sciences **119**, e2203533119 (2022).

[30] J. Preskill, Quantum **2**, 79 (2018).

[31] W. J. Huggins, B. A. O'Gorman, N. C. Rubin, D. R. Reichman, R. Babbush, and J. Lee, Nature **603**, 416 (2022).

[32] K. Kanno, M. Kohda, R. Imai, S. Koh, K. Mitarai, W. Mizukami, and Y. O. Nakagawa, arXiv preprint arXiv:2302.11320 (2023).

[33] Y. O. Nakagawa, M. Kamoshita, W. Mizukami, S. Sudo, and Y.-y. Ohnishi, Journal of Chemical Theory and Computation **20**, 10817– (2024).

[34] J. Robledo-Moreno, M. Motta, H. Haas, A. Javadi-Abhari, P. Jurcevic, W. Kirby, S. Martiel, K. Sharma, S. Sharma, T. Shirakawa, *et al.*, arXiv preprint arXiv:2405.05068 (2024).

[35] S. Kanno, H. Nakamura, T. Kobayashi, S. Gocho, M. Hatanaka, N. Yamamoto, and Q. Gao, npj Quantum Information **10**, 56 (2024).

[36] F. Jensen, *Introduction to computational chemistry* (John wiley & sons, 2017).

[37] G. Henkelman, B. P. Uberuaga, and H. Jónsson, The Journal of Chemical Physics **113**, 9901 (2000).

[38] M. P. Allen and D. J. Tildesley, *Computer Simulation of Liquids* (Oxford University Press, 2017).

[39] M. W. Lodewyk, M. R. Siebert, and D. J. Tantillo, Chemical Reviews **112**, 1839 (2012).

[40] T. Bligaard, J. Nørskov, S. Dahl, J. Matthiesen, C. Christensen, and J. Sehested, Journal of Catalysis **224**, 206 (2004).

[41] Y. Liu, T. Zhao, W. Ju, and S. Shi, Journal of Materiomics **3**, 159 (2017).

[42] R. Ramprasad, R. Batra, G. Pilania, A. Mannodi-Kanakkithodi, and C. Kim, npj Computational Materials **3**, 54 (2017).

[43] K. Hatakeyama-Sato, Y. Igarashi, T. Kashikawa, K. Kimura, and K. Oyaizu, Digital Discovery **2**, 165 (2023).

[44] M. Sajjan, J. Li, R. Selvarajan, S. H. Sureshbabu, S. S. Kale, R. Gupta, V. Singh, and S. Kais, Chemical Society Reviews **51**, 6475 (2022).

[45] J. Behler and M. Parrinello, Physical Review Letters **98**, 146401 (2007).

[46] O. T. Unke, S. Chmiela, H. E. Sauceda, M. Gastegger, I. Poltavsky, K. T. Schütt, A. Tkatchenko, and K.-R. Müller, Chemical Reviews **121**, 10142 (2021).

[47] I. Batatia, P. Benner, Y. Chiang, A. M. Elena, D. P. Kovács, J. Riebesell, X. R. Advincula, M. Asta, M. Avaylon, W. J. Baldwin, F. Berger, N. Bernstein, A. Bhowmik, S. M. Blau, V. Cărare, J. P. Darby, S. De, F. D. Pia, V. L. Deringer, R. Elijošius, Z. El-Machachi, F. Falcioni, E. Fako, A. C. Ferrari, A. Genreith-Schriever, J. George, R. E. A. Goodall, C. P. Grey, P. Grigorev, S. Han, W. Handley, H. H. Heenen, K. Hermansson, C. Holm, J. Jaafar, S. Hofmann, K. S. Jakob, H. Jung, V. Kapil, A. D. Kaplan, N. Karimitari, J. R. Kermode, N. Kroupa, J. Kullgren, M. C. Kuner, D. Kuryla, G. Liepuoniute, J. T. Margraf, I.-B. Magdău, A. Michaelides, J. H. Moore, A. A. Naik, S. P. Niblett, S. W. Norwood, N. O'Neill, C. Ortner, K. A. Persson, K. Reuter, A. S. Rosen, L. L. Schaaf, C. Schran, B. X. Shi, E. Sivonxay, T. K. Stenczel, V. Svahn, C. Sutton, T. D. Swinburne, J. Tilly, C. van der Oord, E. Varga-Umbrich, T. Vegge, M. Vondrák, Y. Wang, W. C. Witt, F. Zills, and G. Csányi, arXiv preprint arXiv:2401.00096 (2024).

[48] G. Wang, C. Wang, X. Zhang, Z. Li, J. Zhou, and Z. Sun, Iscience **27** (2024).

[49] R. Jacobs, D. Morgan, S. Attarian, J. Meng, C. Shen, Z. Wu, C. Y. Xie, J. H. Yang, N. Artrith, B. Blaiszik, *et al.*, Current Opinion in Solid State and Materials Science **35**, 101214 (2025).

[50] M. Kulichenko, B. Nebgen, N. Lubbers, J. S. Smith, K. Barros, A. E. Allen, A. Habib, E. Shinkle, N. Fedik, Y. W. Li, *et al.*, Chemical Reviews **124**, 13681 (2024).

[51] M. A. Nielsen and I. L. Chuang, *Quantum Computation and Quantum Information* (Cambridge University Press, 2010).

[52] C. M. Bishop, *Pattern Recognition and Machine Learning (Information Science and Statistics)*, 1st ed. (Springer, 2007).

[53] Y. Cao, J. Romero, J. P. Olson, M. Degroote, P. D. Johnson, M. Kieferová, I. D. Kivlichan, T. Menke, B. Peropadre, N. P. Sawaya, *et al.*, Chemical Reviews **119**, 10856 (2019).

[54] V. L. Deringer, M. A. Caro, and G. Csányi, Advanced Materials **31**, 1902765 (2019).

[55] T. Mueller, A. Hernandez, and C. Wang, The Journal of Chemical Physics **152** (2020).

[56] E. Kocer, T. W. Ko, and J. Behler, Annual Review of Physical Chemistry **73**, 163 (2022).

[57] K. T. Butler, D. W. Davies, H. Cartwright, O. Isayev, and A. Walsh, Nature **559**, 547 (2018).

[58] V. L. Deringer, A. P. Bartók, N. Bernstein, D. M. Wilkins, M. Ceriotti, and G. Csányi, Chemical Reviews **121**, 10073 (2021).

[59] V. Dunjko and H. J. Briegel, Reports on Progress in Physics **81**, 074001 (2018).

[60] A. Y. Kitaev, Russian Mathematical Surveys **52**, 1191 (1997).

[61] C. M. Dawson and M. A. Nielsen, arXiv preprint arXiv:quant-ph/0505030 (2005).

[62] S. Lloyd, Physical Review Letters **75**, 346 (1995).

[63] D. P. DiVincenzo, Physical Review A **51**, 1015 (1995).

[64] A. Peruzzo, J. McClean, P. Shadbolt, M.-H. Yung, X.-Q. Zhou, P. J. Love, A. Aspuru-Guzik, and J. L. O'Brien, Nature Communications **5**, 10.1038/ncomms5213 (2014).

[65] H. Eyring, The Journal of Chemical Physics **3**, 107 (1935).

[66] M. G. Evans and M. Polanyi, Transactions of the Faraday Society **31**, 875 (1935).

[67] J. A. Pople, Reviews of Modern Physics **71**, 1267 (1999).

[68] J. Čížek, The Journal of Chemical Physics **45**, 4256 (1966).

[69] J. Čížek, Advances in Chemical Physics **14**, 35 (1969).

[70] R. J. Bartlett and M. Musiał, Reviews of Modern Physics **79**, 291 (2007).

[71] R. Nesbet, Proceedings of the Royal Society of London. Series A. Mathematical and Physical Sciences **230**, 312 (1955).

[72] C. David Sherrill and H. F. Schaefer (Academic Press, 1999) pp. 143–269.

[73] K. Raghavachari, G. W. Trucks, J. A. Pople, and M. Head-Gordon, Chemical Physics Letters **157**, 479 (1989).

[74] O. Sinanoğlu, Advances in Chemical Physics , 315 (1964).

[75] E. Ramos-Cordoba, P. Salvador, and E. Matito, Physical Chemistry Chemical Physics **18**, 24015 (2016).

[76] K. Andersson, P.-Å. Malmqvist, and B. O. Roos, The Journal of Chemical Physics **96**, 1218 (1992).

[77] P. Hohenberg and W. Kohn, Physical Review **136**, B864 (1964).

[78] W. Kohn and L. J. Sham, Physical Review **140**, A1133 (1965).

[79] L. Goerigk, A. Hansen, C. Bauer, S. Ehrlich, A. Najibi, and S. Grimme, Physical Chemistry Chemical Physics **19**, 32184 (2017).

[80] M. G. Medvedev, I. S. Bushmarinov, J. Sun, J. P. Perdew, and K. A. Lyssenko, Science **355**, 49 (2017).

[81] T. Shiota, W. Mizukami, H. Tochihara, K. Yagyu, T. Suzuki, and Y. Aoki, The Journal of Physical Chemistry C **124**, 24704 (2020).

[82] M. Reiher, N. Wiebe, K. M. Svore, D. Wecker, and M. Troyer, Proceedings of the national academy of sciences **114**, 7555 (2017).

[83] W. Purwanto, S. Zhang, and H. Krakauer, The Journal of Chemical Physics **142** (2015).

[84] H. R. Larsson, H. Zhai, C. J. Umrigar, and G. K.-L. Chan, Journal of the American Chemical Society **144**, 15932 (2022).

[85] Z. Li, J. Li, N. S. Dattani, C. Umrigar, and G. K. Chan, The Journal of Chemical Physics **150** (2019).

[86] H. Gao, S. Imamura, A. Kasagi, and E. Yoshida, Journal of Chemical Theory and Computation **20**, 1185 (2024).

[87] P. Jordan and E. Wigner, Zeitschrift für Physik **47**, 631 (1928).

[88] S. B. Bravyi and A. Y. Kitaev, Annals of Physics **298**, 210 (2002).

[89] W. Kutzelnigg, The Journal of Chemical Physics **77**, 3081 (1982).

[90] M. R. Hoffmann and J. Simons, The Journal of Chemical Physics **88**, 993 (1988).

[91] R. J. Bartlett, S. A. Kucharski, and J. Noga, Chemical physics letters **155**, 133 (1989).

[92] A. G. Taube and R. J. Bartlett, International journal of quantum chemistry **106**, 3393 (2006).

[93] J. Romero, R. Babbush, J. R. McClean, C. Hempel, P. J. Love, and A. Aspuru-Guzik, Quantum Science and Technology **4**, 014008 (2018).

[94] A. Anand, P. Schleich, S. Alperin-Lea, P. W. K. Jensen, S. Sim, M. Díaz-Tinoco, J. S. Kottmann, M. Degroote, A. F. Izmaylov, and A. Aspuru-Guzik, Chemical Society Reviews **51**, 1659 (2022).

[95] H. Lim, H.-N. Jeon, J.-K. Rhee, B. Oh, and K. T. No, Scientific Reports **12**, 10.1038/s41598-022-11537-6 (2022).

[96] S. Lee, J. Lee, H. Zhai, Y. Tong, A. M. Dalzell, A. Kumar, P. Helms, J. Gray, Z.-H. Cui, W. Liu, *et al.*, Nature Communications **14**, 1952 (2023).

[97] M. Suzuki, Physics Letters A **180**, 232 (1993).

[98] G. H. Low and I. L. Chuang, Quantum **3**, 163 (2019).

[99] M. Motta, E. Ye, J. R. McClean, Z. Li, A. J. Minnich, R. Babbush, and G. K.-L. Chan, npj Quantum Information **7** (2021).

[100] V. von Burg, G. H. Low, T. Häner, D. S. Steiger, M. Reiher, M. Roetteler, and M. Troyer, Physical Review Research **3**, 033055 (2021).

[101] E. G. Hohenstein, R. M. Parrish, and T. J. Martínez, The Journal of Chemical Physics **137** (2012).

[102] R. M. Parrish, E. G. Hohenstein, T. J. Martínez, and C. D. Sherrill, The Journal of Chemical Physics **137** (2012).

[103] E. G. Hohenstein, R. M. Parrish, C. D. Sherrill, and T. J. Martínez, The Journal of Chemical Physics **137** (2012).

[104] R. Iftimie, P. Minary, and M. E. Tuckerman, Proceedings of the National Academy of Sciences **102**, 6654 (2005).

[105] W. C. Swope, H. C. Andersen, P. H. Berens, and K. R. Wilson, The Journal of Chemical Physics **76**, 637 (1982).

[106] J. Hellmann, *Einführung in die Quantenchemie* (Deuticke, Leipzig, 1937) pp. 285–286.

[107] J. Gerratt and I. M. Mills, The Journal of Chemical Physics **49**, 1719 (1968).

[108] P. Pulay, Mol. Phys. **17**, 197 (1969).

[109] N. C. Handy and H. F. Schaefer, The Journal of Chemical Physics **81**, 5031 (1984).

[110] T. Helgaker and P. Jørgensen, Theoretical Chemistry Accounts **75**, 111 (1989).

[111] A. Warshel and M. Levitt, Journal of Molecular Biology **103**, 227 (1976).

[112] M. J. Field, P. A. Bash, and M. Karplus, Journal of Computational Chemistry **11**, 700 (1990).

[113] H. M. Senn and W. Thiel, Angewandte Chemie International Edition **48**, 1198 (2009).

[114] J. Gilmer, S. S. Schoenholz, P. F. Riley, O. Vinyals, and G. E. Dahl, arXiv preprint arXiv:1704.01212 (2017).

[115] S. Batzner, A. Musaelian, L. Sun, M. Geiger, J. P. Mailoa, M. Kornbluth, N. Molinari, T. E. Smidt, and B. Kozinsky, Nature Communications **13**, 2453 (2022).

[116] B. Deng, P. Zhong, K. Jun, J. Riebesell, K. Han, C. J. Bartel, and G. Ceder, Nature Machine Intelligence **5**, 1031 (2023).

[117] L. Barroso-Luque, M. Shuaibi, X. Fu, B. M. Wood, M. Dzamba, M. Gao, A. Rizvi, C. L. Zitnick, and Z. W. Ulissi, arXiv preprint arXiv:2410.12771 (2024).

[118] L. Chanussot, A. Das, S. Goyal, T. Lavril, M. Shuaibi, M. Riviere, K. Tran, J. Heras-Domingo, C. Ho, W. Hu, *et al.*, ACS Catalysis **11**, 6059 (2021).

[119] P. Eastman, P. K. Behara, D. L. Dotson, R. Galvelis, J. E. Herr, J. T. Horton, Y. Mao, J. D. Chodera, B. P. Pritchard, Y. Wang, *et al.*, Scientific Data **10**, 11 (2023).

[120] M. Schreiner, A. Bhowmik, T. Vegge, J. Busk, and O. Winther, Scientific Data **9**, 779 (2022).

[121] J. S. Smith, O. Isayev, and A. E. Roitberg, Chemical Science **8**, 3192 (2017).

[122] D. Anstine, R. Zubatyuk, and O. Isayev, ChemRxiv preprint 10.26434/chemrxiv-2023-296ch-v2 (2024).

[123] O. T. Unke, M. Stöhr, S. Ganscha, T. Unterthiner, H. Maennel, S. Kashubin, D. Ahlin, M. Gastegger, L. Medrano Sandonas, J. T. Berryman, *et al.*, Science Advances **10**, eadn4397 (2024).

[124] C. Chen and S. P. Ong, Nature Computational Science **2**, 718 (2022).

[125] J. Gasteiger, M. Shuaibi, A. Sriram, S. Günnemann, Z. Ulissi, C. L. Zitnick, and A. Das, arXiv preprint arXiv:2204.02782 (2022).

[126] T. Helgaker, S. Coriani, P. Jørgensen, K. Kristensen, J. Olsen, and K. Ruud, Chemical Reviews **112**, 543 (2012).

[127] J. K. Nørskov, F. Abild-Pedersen, F. Studt, and T. Bligaard, Proceedings of the National Academy of Sciences **108**, 937 (2011).

[128] L. Schimka, J. Harl, A. Stroppa, A. Grüneis, M. Marsman, F. Mittendorfer, and G. Kresse, Nature materials **9**, 741 (2010).

[129] T. Gruber, K. Liao, T. Tsatsoulis, F. Hummel, and A. Grüneis, Physical Review X **8**, 021043 (2018).

[130] R. Ditchfield, The Journal of Chemical Physics **56**, 5688 (1972).

[131] R. Ramakrishnan, P. O. Dral, M. Rupp, and O. A. Von Lilienfeld, Scientific Data **1**, 1 (2014).

[132] A. Gupta, S. Chakraborty, and R. Ramakrishnan, Machine Learning: Science and Technology **2**, 035010 (2021).

[133] M. Rupp, R. Ramakrishnan, and O. A. von Lilienfeld, The Journal of Physical Chemistry Letters **6**, 3309 (2015).

[134] L. Himanen, M. O. Jäger, E. V. Morooka, F. Federici Canova, Y. S. Ranawat, D. Z. Gao, P. Rinke, and A. S. Foster, Computer Physics Communications **247**, 106949 (2020).

[135] M. F. Langer, A. Goeßmann, and M. Rupp, npj Computational Materials **8**, 41 (2022).

[136] M. Cordova, E. A. Engel, A. Stefaniuk, F. Paruzzo, A. Hofstetter, M. Ceriotti, and L. Emsley, The Journal of Physical Chemistry C **126**, 16710 (2022).

[137] M. J. Willatt, F. Musil, and M. Ceriotti, The Journal of Chemical Physics **150**, 154110 (2019).

[138] A. P. Bartók, S. De, C. Poelking, N. Bernstein, J. R. Kermode, G. Csányi, and M. Ceriotti, Science Advances **3**, e1701816 (2017).

[139] K. Wan, J. He, and X. Shi, Advanced Materials **36**, 2305758 (2024).

[140] F. A. Faber, A. S. Christensen, B. Huang, and O. A. von Lilienfeld, The Journal of Chemical Physics **148**, 241717 (2018).

[141] A. S. Christensen, L. A. Bratholm, F. A. Faber, and O. Anatole von Lilienfeld, The Journal of Chemical Physics **152**, 044107 (2020).

[142] B. Parsaeifard, D. Sankar De, A. S. Christensen, F. A. Faber, E. Kocer, S. De, J. Behler, O. Anatole von Lilienfeld, and S. Goedecker, Machine Learning: Science and Technology **2**, 015018 (2021).

[143] F. A. Faber, L. Hutchison, B. Huang, J. Gilmer, S. S. Schoenholz, G. E. Dahl, O. Vinyals, S. Kearnes, P. F. Riley, and O. A. von Lilienfeld, Journal of Chemical Theory and Computation **13**, 5255 (2017).

[144] F. M. Paruzzo, A. Hofstetter, F. Musil, S. De, M. Ceriotti, and L. Emsley, Nature Communications **9**, 4501 (2018).

[145] M. Tsitsvero, J. Pirillo, Y. Hijikata, and T. Komatsuzaki, The Journal of Chemical Physics **158**, 194108 (2023).

[146] A. P. Bartók, M. C. Payne, R. Kondor, and G. Csányi, Physical Review Letters **104**, 136403 (2010).

[147] A. Kabylda, V. Vassilev-Galindo, S. Chmiela, I. Poltavsky, and A. Tkatchenko, Nature Communications **14**, 3562 (2023).

[148] Z. Wu, B. Ramsundar, E. N. Feinberg, J. Gomes, C. Geniesse, A. S. Pappu, K. Leswing, and V. Pande, Chemical Science **9**, 513 (2018).

[149] V. Fung, J. Zhang, E. Juarez, and B. G. Sumpter, npj Computational Materials **7**, 84 (2021).

[150] A. Nakayama, K. Mitarai, L. Placidi, T. Sugimoto, and K. Fujii, arXiv preprint arXiv:2302.09751 (2023).

[151] L. Placidi, R. Hataya, T. Mori, K. Aoyama, H. Morisaki, K. Mitarai, and K. Fujii, arXiv preprint arXiv:2306.16627 (2023).

[152] M. Motta and J. E. Rice, WIREs Computational Molecular Science **12**, 10.1002/wcms.1580 (2021).

[153] D. A. Fedorov, B. Peng, N. Govind, and Y. Alexeev, Materials Theory **6**, 1 (2022).

[154] A. Kandala, A. Mezzacapo, K. Temme, M. Takita, M. Brink, J. M. Chow, and J. M. Gambetta, Nature **549**, 242 (2017).

[155] R. Babbush, C. Gidney, D. W. Berry, N. Wiebe, J. McClean, A. Paler, A. Fowler, and H. Neven, Physical Review X **8** (2018).

[156] R. Babbush, N. Wiebe, J. McClean, J. McClain, H. Neven, and G. K.-L. Chan, Physical Review X **8** (2018).

[157] D. W. Berry, C. Gidney, M. Motta, J. R. McClean, and R. Babbush, Quantum **3**, 208 (2019).

[158] W. Mizukami, K. Mitarai, Y. O. Nakagawa, T. Yamamoto, T. Yan, and Y. Ohnishi, Physical Review Research **2** (2020).

[159] K. Omiya, Y. O. Nakagawa, S. Koh, W. Mizukami, Q. Gao, and T. Kobayashi, Journal of Chemical Theory and Computation **18**, 741 (2022).

[160] M. Kohda, R. Imai, K. Kanno, K. Mitarai, W. Mizukami, and Y. O. Nakagawa, Physical Review Research **4**, 033173 (2022).

[161] J. M. Arrazola, O. Di Matteo, N. Quesada, S. Jahangiri, A. Delgado, and N. Killoran, Quantum **6**, 742 (2022).

[162] T. E. O'Brien, M. Streif, N. C. Rubin, R. Santagati, Y. Su, W. J. Huggins, J. J. Goings, N. Moll, E. Kyoseva, M. Degroote, C. S. Tautermann, J. Lee, D. W. Berry, N. Wiebe, and R. Babbush, Physical Review Research **4**, 043210 (2022).

[163] K. Sugisaki, H. Wakimoto, K. Toyota, K. Sato, D. Shiomi, and T. Takui, The Journal of Physical Chemistry Letters **13**, 11105 (2022).

[164] L. Erhart, K. Mitarai, W. Mizukami, and K. Fujii, Physical Review Applied **18**, 064051 (2022).

[165] F. D. Malone, R. M. Parrish, A. R. Welden, T. Fox, M. Degroote, E. Kyoseva, N. Moll, R. Santagati, and M. Streif, Chemical Science **13**, 3094 (2022).

[166] E. G. Hohenstein, O. Oumarou, R. Al-Saadon, G.-L. R. Anselmetti, M. Scheurer, C. Gogolin, and R. M. Parrish, The Journal of Chemical Physics **158** (2023).

[167] Y. O. Nakagawa, J. Chen, S. Sudo, Y. ya Ohnishi, and W. Mizukami, Journal of Chemical Theory and Computation **19**, 1998 (2023).

[168] M. Loipersberger, F. D. Malone, A. R. Welden, R. M. Parrish, T. Fox, M. Degroote, E. Kyoseva, N. Moll, R. Santagati, and M. Streif, Chemical Science **14**, 3587 (2023).

[169] K. Mitarai, K. Toyoizumi, and W. Mizukami, Quantum **7**, 1000 (2023).

[170] N. C. Rubin, D. W. Berry, F. D. Malone, A. F. White, T. Khattar, A. E. D. I. au2, S. Sicolo, M. Kühn, M. Kaicher, J. Lee, and R. Babbush, PRX Quantum **4**, 040303 (2023).

[171] Y. Yoshida, W. Mizukami, and N. Yoshida, Journal of Chemical Theory and Computation **20**, 1962 (2024).

[172] Y. Yoshida, N. Takemori, and W. Mizukami, The Journal of Chemical Physics **161** (2024).

[173] O. Oumarou, M. Scheurer, R. M. Parrish, E. G. Hohenstein, and C. Gogolin, Quantum **8**, 1371 (2024).

[174] T. Ohgoe, H. Iwakiri, M. Kohda, K. Ichikawa, Y. O. Nakagawa, H. O. Valencia, and S. Koh, Physical Review Research **6**, L022022 (2024).

[175] L. Erhart, Y. Yoshida, V. Khinevich, and W. Mizukami, Physical Review Research **6**, 023230 (2024).

[176] L. Erhart, Y. Yoshida, V. Khinevich, and W. Mizukami, arXiv preprint arXiv:2406.07364 (2024).

[177] C. L. Cortes, M. Loipersberger, R. M. Parrish, S. Morley-Short, W. Pol, S. Sim, M. Steudtner, C. S. Tautermann, M. Degroote, N. Moll, *et al.*, PRX Quantum **5**, 010336 (2024).

[178] F. Arute, K. Arya, R. Babbush, D. Bacon, J. C. Bardin, R. Barends, S. Boixo, M. Broughton, B. B. Buckley, D. A. Buell, B. Burkett, N. Bushnell, Y. Chen, Z. Chen, B. Chiaro, R. Collins, W. Courtney, S. Demura, A. Dunsworth, E. Farhi, A. Fowler, B. Foxen, C. Gidney, M. Giustina, R. Graff, S. Habegger, M. P. Harrigan, A. Ho, S. Hong,

T. Huang, W. J. Huggins, L. Ioffe, S. V. Isakov, E. Jeffrey, Z. Jiang, C. Jones, D. Kafri, K. Kechedzhi, J. Kelly, S. Kim, P. V. Klimov, A. Korotkov, F. Kostritsa, D. Landhuis, P. Laptev, M. Lindmark, E. Lucero, O. Martin, J. M. Martinis, J. R. McClean, M. McEwen, A. Megrant, X. Mi, M. Mohseni, W. Mruczkiewicz, J. Mutus, O. Naaman, M. Neeley, C. Neill, H. Neven, M. Y. Niu, T. E. O'Brien, E. Ostby, A. Petukhov, H. Putterman, C. Quintana, P. Roushan, N. C. Rubin, D. Sank, K. J. Satzinger, V. Smelyanskiy, D. Strain, K. J. Sung, M. Szalay, T. Y. Takeshita, A. Vainsencher, T. White, N. Wiebe, Z. J. Yao, P. Yeh, and A. Zalcman, Science **369**, 1084–1089 (2020).

[179] T. P. Gujarati, M. Motta, T. N. Friedhoff, J. E. Rice, N. Nguyen, P. K. Barkoutsos, R. J. Thompson, T. Smith, M. Kagele, M. Brei, *et al.*, npj Quantum Information **9**, 88 (2023).

[180] Q. Gao, G. O. Jones, M. Motta, M. Sugawara, H. C. Watanabe, T. Kobayashi, E. Watanabe, Y.-y. Ohnishi, H. Nakamura, and N. Yamamoto, npj Computational Materials **7**, 70 (2021).

[181] E. Dimitrov, G. Sanchez-Sanz, J. Nelson, L. O'Riordan, M. Doyle, S. Courtney, V. Kannan, H. Naseri, A. G. Garcia, J. Tricker, *et al.*, arXiv preprint arXiv:2311.01242 (2023).

[182] G. Kresse and J. Furthmüller, Computational materials science **6**, 15 (1996).

[183] M. Guidon, F. Schiffmann, J. Hutter, and J. VandeVondele, The Journal of Chemical Physics **128** (2008).

[184] M. e. Frisch, G. Trucks, H. Schlegel, G. Scuseria, M. Robb, J. Cheeseman, G. Scalmani, V. Barone, G. Petersson, H. Nakatsuji, *et al.*, Gaussian 16, revision c. 01 (2016).

[185] P. Giannozzi, O. Andreussi, T. Brumme, O. Bunau, M. B. Nardelli, M. Calandra, R. Car, C. Cavazzoni, D. Ceresoli, M. Cococcioni, *et al.*, Journal of physics: Condensed matter **29**, 465901 (2017).

[186] Q. Sun, T. C. Berkelbach, N. S. Blunt, G. H. Booth, S. Guo, Z. Li, J. Liu, J. D. McClain, E. R. Sayfutyarova, S. Sharma, *et al.*, Wiley Interdisciplinary Reviews: Computational Molecular Science **8**, e1340 (2018).

[187] T. Shiozaki, Wiley Interdisciplinary Reviews: Computational Molecular Science **8**, e1331 (2018).

[188] F. Neese, F. Wennmohs, U. Becker, and C. Riplinger, The Journal of Chemical Physics **152** (2020).

[189] D. G. Smith, L. A. Burns, A. C. Simmonett, R. M. Parrish, M. C. Schieber, R. Galvelis, P. Kraus, H. Kruse, R. Di Remigio, A. Alenaizan, *et al.*, The Journal of Chemical Physics **152** (2020).

[190] T. D. Kühne, M. Iannuzzi, M. Del Ben, V. V. Rybkin, P. Seewald, F. Stein, T. Laino, R. Z. Khaliullin, O. Schütt, F. Schiffmann, *et al.*, The Journal of Chemical Physics **152** (2020).

[191] G. M. Barca, C. Bertoni, L. Carrington, D. Datta, N. De Silva, J. E. Deustua, D. G. Fedorov, J. R. Gour, A. O. Gunina, E. Guidez, *et al.*, The Journal of Chemical Physics **152** (2020).

[192] S. Seritan, C. Bannwarth, B. S. Fales, E. G. Hohenstein, C. M. Isborn, S. I. Kokkila-Schumacher, X. Li, F. Liu, N. Luehr, J. W. Snyder Jr, *et al.*, Wiley Interdisciplinary Reviews: Computational Molecular Science **11**, e1494 (2021).

[193] R. Li, Q. Sun, X. Zhang, and G. K.-L. Chan, The Journal of Physical Chemistry A **129**, 1459 (2025).

[194] C. Li and G. K.-L. Chan, Journal of Chemical Theory and Computation **21**, 803 (2025).

[195] A. Bussy and J. Hutter, The Journal of Chemical Physics **160** (2024).

[196] D. A. Fedorov, M. J. Otten, S. K. Gray, and Y. Alexeev, The Journal of Chemical Physics **154** (2021).

[197] H. R. Grimsley, S. E. Economou, E. Barnes, and N. J. Mayhall, Nature Communications **10**, 3007 (2019).

[198] K. Fujii, K. Mizuta, H. Ueda, K. Mitarai, W. Mizukami, and Y. O. Nakagawa, PRX Quantum **3**, 010346 (2022).

[199] Y. Osamura, Y. Yamaguchi, and H. F. Schaefer III, The Journal of Chemical Physics **77**, 383 (1982).

[200] M. Ferrero, M. Rérat, R. Orlando, and R. Dovesi, The Journal of Chemical Physics **128** (2008).

[201] J. Paier, C. V. Diaconu, G. E. Scuseria, M. Guidon, J. VandeVondele, and J. Hutter, Physical Review B—Condensed Matter and Materials Physics **80**, 174114 (2009).

[202] A. Erba, J. K. Desmarais, S. Casassa, B. Civalleri, L. Donà, I. J. Bush, B. Searle, L. Maschio, L. Edith-Daga, A. Cossard, *et al.*, Journal of Chemical Theory and Computation **19**, 6891 (2022).

[203] S. Battaglia, M. Rossmannek, V. V. Rybkin, I. Tavernelli, and J. Hutter, npj Computational Materials **10**, 297 (2024).

[204] A. Javadi-Abhari, M. Treinish, K. Krsulich, C. J. Wood, J. Lishman, J. Gacon, S. Martiel, P. D. Nation, L. S. Bishop, A. W. Cross, B. R. Johnson, and J. M. Gambetta, arXiv preprint arXiv:2405.08810 (2024).

[205] S. J. Lee, M. Welborn, F. R. Manby, and T. F. Miller III, Accounts of chemical research **52**, 1359 (2019).

[206] I. Fdez. Galván, M. Vacher, A. Alavi, C. Angeli, F. Aquilante, J. Autschbach, J. J. Bao, S. I. Bokarev, N. A. Bogdanov, R. K. Carlson, L. F. Chibotaru, J. Creutzberg, N. Dattani, M. G. Delcey, S. S. Dong, A. Dreuw, L. Freitag, L. M. Frutos, L. Gagliardi, F. Gendron, A. Giussani, L. González, G. Grell, M. Guo, C. E. Hoyer, M. Johansson, S. Keller, S. Knecht, G. Kovačević, E. Källman, G. Li Manni, M. Lundberg, Y. Ma, S. Mai, J. P. Malhado, P. Å. Malmqvist, P. Marquetand, S. A. Mewes, J. Norell, M. Olivucci, M. Oppel, Q. M. Phung, K. Pierloot, F. Plasser, M. Reiher, A. M. Sand, I. Schapiro, P. Sharma, C. J. Stein, L. K. Sørensen, D. G. Truhlar, M. Ugandi, L. Ungur, A. Valentini, S. Vancoillie, V. Veryazov, O. Weser, T. A. Wesolowski, P.-O. Widmark, S. Wouters, A. Zech, J. P. Zobel, and R. Lindh, Journal of Chemical Theory and Computation **15**, 5925 (2019).

[207] L. Schreder and S. Luber, The Journal of Chemical Physics **161** (2024).

[208] P. Jordan and E. P. Wigner, *Über das paulische äquivalenzverbot* (Springer, 1993).

[209] Y. Suzuki, Y. Kawase, Y. Masumura, Y. Hiraga, M. Nakadai, J. Chen, K. M. Nakanishi, K. Mitarai, R. Imai, S. Tamiya, T. Yamamoto, T. Yan, T. Kawakubo, Y. O. Nakagawa, Y. Ibe, Y. Zhang, H. Yamashita, H. Yoshimura, A. Hayashi, and K. Fujii, Quantum **5**, 559 (2021).

[210] N. C. Rubin, K. Gunst, A. White, L. Freitag, K. Throssell, G. K.-L. Chan, R. Babbush, and T. Shiozaki, Quantum **5**, 568 (2021).

[211] J. R. McClean, N. C. Rubin, K. J. Sung, I. D. Kivlichan, X. Bonet-Monroig, Y. Cao, C. Dai, E. S. Fried, C. Gidney, B. Gimby, *et al.*, Quantum Science and Technology **5**, 034014 (2020).

[212] D. Feller, The Journal of Chemical Physics **96**, 6104 (1992).

[213] S.-Y. Yu, H. Kim, and J.-Y. Koo, Physical Review Letters **100**, 036107 (2008).

[214] A. Ramstad, G. Brocks, and P. Kelly, Physical Review B **51**, 14504 (1995).

[215] R. Hamers, R. Tromp, and J. Demuth, Physical Review B **34**, 5343 (1986).

[216] T. Shirasawa, S. Mizuno, and H. Tochihara, Surface Science **600**, 815 (2006).

[217] S. Swaminathan and D. L. Beveridge, Journal of the American Chemical Society **99**, 8392 (1977).

[218] L. B. Skinner, C. Huang, D. Schlesinger, L. G. Pettersson, A. Nilsson, and C. J. Benmore, The Journal of Chemical Physics **138** (2013).

[219] P. Kast, M. Asif-Ullah, and D. Hilvert, Tetrahedron Letters **37**, 2691 (1996).

[220] https://www.cp2k.org/howto:biochem_qmmm.

[221] M. Scheurer, G.-L. R. Anselmetti, O. Oumarou, C. Gogolin, and N. C. Rubin, Journal of Chemical Theory and Computation (2023).

[222] S. Käser, L. I. Vazquez-Salazar, M. Meuwly, and K. Töpfer, Digital Discovery **2**, 28 (2023).

[223] K. Choudhary, B. DeCost, C. Chen, A. Jain, F. Tavazza, R. Cohn, C. W. Park, A. Choudhary, A. Agrawal, S. J. Billinge, *et al.*, npj Computational Materials **8**, 59 (2022).

[224] J. Schmidt, M. R. Marques, S. Botti, and M. A. Marques, npj computational materials **5**, 83 (2019).

[225] Y. Mishin, Acta Materialia **214**, 116980 (2021).

[226] S. Chmiela, V. Vassilev-Galindo, O. T. Unke, A. Kabylda, H. E. Sauceda, A. Tkatchenko, and K.-R. Müller, Science Advances **9**, eadf0873 (2023).

[227] P. Liu, J. Wang, N. Avargues, C. Verdi, A. Singraber, F. Karsai, X.-Q. Chen, and G. Kresse, Physical Review Letters **130**, 078001 (2023).

[228] J. Behler, The Journal of Chemical Physics **134**, 074106 (2011).

[229] K. T. Schütt, H. E. Sauceda, P.-J. Kindermans, A. Tkatchenko, and K.-R. Müller, The Journal of Chemical Physics **148**, 241722 (2018).

[230] T. Xie and J. C. Grossman, Physical Review Letter **120**, 145301 (2018).

[231] C. Chen, W. Ye, Y. Zuo, C. Zheng, and S. P. Ong, Chemistry of Materials **31**, 3564 (2019).

[232] J. Gasteiger, F. Becker, and S. Günnemann, Advances in Neural Information Processing Systems **34**, 6790 (2021).

[233] O. T. Unke, S. Chmiela, M. Gastegger, K. T. Schütt, H. E. Sauceda, and K.-R. Müller, Nature Communications **12**, 7273 (2021).

[234] K. Choudhary and B. DeCost, npj Computational Materials **7**, 185 (2021).

[235] S. Takamoto, S. Izumi, and J. Li, Computational Materials Science **207**, 111280 (2022).

[236] I. Batatia, D. P. Kovacs, G. Simm, C. Ortner, and G. Csányi, Advances in Neural Information Processing Systems **35**, 11423 (2022).

[237] A. Musaelian, S. Batzner, A. Johansson, L. Sun, C. J. Owen, M. Kornbluth, and B. Kozinsky, Nature Communications **14**, 579 (2023).

[238] Z. Mao, J. Li, C. Liang, D. Das, M. Sumita, and K. Tsuda, arXiv preprint arXiv:2406.13265 (2024).

[239] J. T. Frank, O. T. Unke, K.-R. Müller, and S. Chmiela, Nature Communications **15**, 6539 (2024).

[240] Y. Park, J. Kim, S. Hwang, and S. Han, Journal of Chemical Theory and Computation (2024).

[241] B. Cheng, npj Computational Materials **10**, 157 (2024).

[242] J. Wang, Y. Wang, H. Zhang, Z. Yang, Z. Liang, J. Shi, H.-T. Wang, D. Xing, and J. Sun, Nature Communications **15**, 7607 (2024).

[243] A. Duval, S. V. Mathis, C. K. Joshi, V. Schmidt, S. Miret, F. D. Malliaros, T. Cohen, P. Lio, Y. Bengio, and M. Bronstein, arXiv preprint arXiv:2312.07511 (2023).

[244] A. Jain, S. P. Ong, G. Hautier, W. Chen, W. D. Richards, S. Dacek, S. Cholia, D. Gunter, D. Skinner, G. Ceder, *et al.*, APL Materials **1** (2013).

[245] S. Kirklin, J. E. Saal, B. Meredig, A. Thompson, J. W. Doak, M. Aykol, S. Rühl, and C. Wolverton, npj Computational Materials **1**, 1 (2015).

[246] J. Schmidt, H.-C. Wang, T. F. Cerqueira, S. Botti, and M. A. Marques, Scientific Data **9**, 64 (2022).

[247] J. Schmidt, T. F. Cerqueira, A. H. Romero, A. Loew, F. Jäger, H.-C. Wang, S. Botti, and M. A. Marques, Materials Today Physics , 101560 (2024).

[248] S. Haastrup, M. Strange, M. Pandey, T. Deilmann, P. S. Schmidt, N. F. Hinsche, M. N. Gjerding, D. Torelli, P. M. Larsen, A. C. Riis-Jensen, *et al.*, 2D Materials **5**, 042002 (2018).

[249] A. S. Rosen, S. M. Iyer, D. Ray, Z. Yao, A. Aspuru-Guzik, L. Gagliardi, J. M. Notestein, and R. Q. Snurr, Matter **4**, 1578 (2021).

[250] A. Sriram, S. Choi, X. Yu, L. M. Brabson, A. Das, Z. Ulissi, M. Uyttendaele, A. J. Medford, and D. S. Sholl, ACS central science **10**, 923 (2024).

[251] R. Tran, J. Lan, M. Shuaibi, B. M. Wood, S. Goyal, A. Das, J. Heras-Domingo, A. Kolluru, A. Rizvi, N. Shoghi, *et al.*, ACS Catalysis **13**, 3066 (2023).

[252] J. S. Smith, O. Isayev, and A. E. Roitberg, Scientific Data **4**, 1 (2017).

[253] J. S. Smith, R. Zubatyuk, B. Nebgen, N. Lubbers, K. Barros, A. E. Roitberg, O. Isayev, and S. Tretiak, Scientific Data **7**, 134 (2020).

[254] S. Nandi, T. Vegge, and A. Bhowmik, Scientific Data **10**, 783 (2023).

[255] M. Nakata and T. Shimazaki, Journal of Chemical Information and Modeling **57**, 1300 (2017).

[256] M. Nakata and T. Maeda, Journal of Chemical Information and Modeling **63**, 5734 (2023).

[257] C. Isert, K. Atz, J. Jiménez-Luna, and G. Schneider, Scientific Data **9**, 273 (2022).

[258] A. G. Donchev, A. G. Taube, E. Decolvenaere, C. Hargus, R. T. McGibbon, K.-H. Law, B. A. Gregersen, J.-L. Li, K. Palmo, K. Siva, *et al.*, Scientific Data **8**, 55 (2021).

[259] T. Zhou, Z. Song, and K. Sundmacher, Engineering **5**, 1017 (2019).

[260] A. Ullah, Y. Chen, and P. O. Dral, Machine Learning: Science and Technology **5**, 041001 (2024).

[261] C. Gabellini, N. Shenoy, S. Thaler, S. Canturk, D. McNeela, D. Beaini, M. Bronstein, and P. Tossou, arXiv preprint arXiv:2411.19629 (2024).

[262] A. Bochkarev, Y. Lysogorskiy, and R. Drautz, Physical Review X **14**, 021036 (2024).

[263] J. Qi, T. W. Ko, B. C. Wood, T. A. Pham, and S. P. Ong, npj Computational Materials **10**, 43 (2024).

[264] S. Takamoto, C. Shinagawa, D. Motoki, K. Nakago, W. Li, I. Kurata, T. Watanabe, Y. Yayama, H. Iriguchi, Y. Asano, *et al.*, Nature Communications **13**, 2991 (2022).

[265] K. Choudhary, B. DeCost, L. Major, K. Butler, J. Thiyagalingam, and F. Tavazza, Digital Discovery **2**, 346 (2023).

[266] A. Merchant, S. Batzner, S. S. Schoenholz, M. Aykol, G. Cheon, and E. D. Cubuk, Nature **624**, 80 (2023).

[267] H. Yang, C. Hu, Y. Zhou, X. Liu, Y. Shi, J. Li, G. Li, Z. Chen, S. Chen, C. Zeni, M. Horton, R. Pinsler, A. Fowler, D. Zügner, T. Xie, J. Smith, L. Sun, Q. Wang, L. Kong, C. Liu, H. Hao, and Z. Lu, arXiv preprint arXiv:2405.04967 (2024).

[268] T. Shiota, K. Ishihara, and W. Mizukami, Digital Discovery **3**, 1714 (2024).

[269] T. Shiota, K. Ishihara, and W. Mizukami, Digital Discovery **4**, 738 (2025).

[270] M. Neumann, J. Gin, B. Rhodes, S. Bennett, Z. Li, H. Choubisa, A. Hussey, and J. Godwin, arXiv preprint arXiv:2410.22570 (2024).

[271] B. Focassio, L. P. M. Freitas, and G. R. Schleder, ACS Applied Materials & Interfaces (2024).

[272] H. Yu, M. Giantomassi, G. Materzanini, J. Wang, and G.-M. Rignanese, Materials Genome Engineering Advances **2**, e58 (2024).

[273] J. S. Smith, B. Nebgen, N. Lubbers, O. Isayev, and A. E. Roitberg, The Journal of Chemical Physics **148** (2018).

[274] J. S. Smith, B. T. Nebgen, R. Zubatyuk, N. Lubbers, C. Devereux, K. Barros, S. Tretiak, O. Isayev, and A. E. Roitberg, Nature Communications **10**, 2903 (2019).

[275] C. Devereux, J. S. Smith, K. K. Huddleston, K. Barros, R. Zubatyuk, O. Isayev, and A. E. Roitberg, Journal of Chemical Theory and Computation **16**, 4192 (2020).

[276] R. Zubatyuk, J. S. Smith, J. Leszczynski, and O. Isayev, Science Advances **5**, eaav6490 (2019).

[277] A. Kabylda, J. T. Frank, S. S. Dou, A. Khabibrakhmanov, L. M. Sandonas, O. T. Unke, S. Chmiela, K.-R. Muller, and A. Tkatchenko, ChemRxiv preprint 10.26434/chemrxiv-2024-bdfr0 (2024).

[278] D. P. Kovács, J. H. Moore, N. J. Browning, I. Batatia, J. T. Horton, Y. Pu, V. Kapil, W. C. Witt, I.-B. Magdău, D. J. Cole, *et al.*, Journal of the American Chemical Society **147**, 17598 (2025).

[279] G. R. Schleder, A. C. Padilha, C. M. Acosta, M. Costa, and A. Fazzio, Journal of Physics: Materials **2**, 032001 (2019).

[280] B. Huang, G. F. von Rudorff, and O. A. von Lilienfeld, Science **381**, 170 (2023).

[281] G. Kresse and J. Hafner, Physical Review B **47**, 558 (1993).

[282] G. Kresse and J. Furthmüller, Physical Review B **54**, 11169 (1996).

[283] G. Kresse and J. Hafner, Physical Review B **49**, 14251 (1994).

[284] J. Hutter, M. Iannuzzi, F. Schiffmann, and J. VandeVondele, Wiley Interdisciplinary Reviews: Computational Molecular Science **4**, 15 (2014).

[285] G. te Velde, F. M. Bickelhaupt, E. J. Baerends, C. Fonseca Guerra, S. J. van Gisbergen, J. G. Snijders, and T. Ziegler, Journal of Computational Chemistry **22**, 931 (2001).

[286] F. Neese, WIRES Comput. Molec. Sci. **12**, e1606 (2022).

[287] F. Neese, WIRES Comput. Molec. Sci. **2**, 73 (2012).

[288] M. J. Frisch, G. W. Trucks, H. B. Schlegel, G. E. Scuseria, M. A. Robb, J. R. Cheeseman, G. Scalmani, V. Barone, G. A. Petersson, H. Nakatsuji, X. Li, M. Caricato, A. V. Marenich, J. Bloino, B. G. Janesko, R. Gomperts,

B. Mennucci, H. P. Hratchian, J. V. Ortiz, A. F. Izmaylov, J. L. Sonnenberg, D. Williams-Young, F. Ding, F. Lipparini, F. Egidi, J. Goings, B. Peng, A. Petrone, T. Henderson, D. Ranasinghe, V. G. Zakrzewski, J. Gao, N. Rega, G. Zheng, W. Liang, M. Hada, M. Ehara, K. Toyota, R. Fukuda, J. Hasegawa, M. Ishida, T. Nakajima, Y. Honda, O. Kitao, H. Nakai, T. Vreven, K. Throssell, J. A. Montgomery, Jr., J. E. Peralta, F. Ogliaro, M. J. Bearpark, J. J. Heyd, E. N. Brothers, K. N. Kudin, V. N. Staroverov, T. A. Keith, R. Kobayashi, J. Normand, K. Raghavachari, A. P. Rendell, J. C. Burant, S. S. Iyengar, J. Tomasi, M. Cossi, J. M. Millam, M. Klene, C. Adamo, R. Cammi, J. W. Ochterski, R. L. Martin, K. Morokuma, O. Farkas, J. B. Foresman, and D. J. Fox, Gaussian˜16 Revision C.01 (2016), Gaussian Inc. Wallingford CT.

[289] D. Zhang, X. Liu, X. Zhang, C. Zhang, C. Cai, H. Bi, Y. Du, X. Qin, A. Peng, J. Huang, *et al.*, npj Computational Materials **10**, 293 (2024).

[290] R. Ramakrishnan, P. O. Dral, M. Rupp, and O. A. Von Lilienfeld, Journal of Chemical Theory and Computation **11**, 2087 (2015).

[291] C. Chen, Y. Zuo, W. Ye, X. Li, and S. P. Ong, Nature Computational Science **1**, 46 (2021).

[292] M. Liu, A. Gopakumar, V. I. Hegde, J. He, and C. Wolverton, Physical Review Materials **8**, 043803 (2024).

[293] J. Kim, J. Kim, J. Kim, J. Lee, Y. Park, Y. Kang, and S. Han, Journal of the American Chemical Society **147**, 1042 (2024).

[294] A. Jain, G. Hautier, S. P. Ong, C. J. Moore, C. C. Fischer, K. A. Persson, and G. Ceder, Physical Review B—Condensed Matter and Materials Physics **84**, 045115 (2011).

[295] V. Stevanović, S. Lany, X. Zhang, and A. Zunger, Physical Review B—Condensed Matter and Materials Physics **85**, 115104 (2012).

[296] A. Wang, R. Kingsbury, M. McDermott, M. Horton, A. Jain, S. P. Ong, S. Dwaraknath, and K. A. Persson, Scientific Reports **11**, 15496 (2021).

[297] R. S. Kingsbury, A. S. Rosen, A. S. Gupta, J. M. Munro, S. P. Ong, A. Jain, S. Dwaraknath, M. K. Horton, and K. A. Persson, npj Computational Materials **8**, 195 (2022).

[298] A. Savin and E. R. Johnson, Density Functionals: Thermochemistry , 81 (2015).

[299] J. P. Perdew, J. Sun, A. J. Garza, and G. E. Scuseria, Zeitschrift für Physikalische Chemie **230**, 737 (2016).

[300] J. P. Perdew, K. Burke, and M. Ernzerhof, Physical Review Letters **77**, 3865 (1996).

[301] A. Najibi and L. Goerigk, Journal of Chemical Theory and Computation **14**, 5725 (2018).

[302] S. Grimme, J. Antony, S. Ehrlich, and H. Krieg, The Journal of Chemical Physics **132** (2010).

[303] S. Grimme, S. Ehrlich, and L. Goerigk, Journal of Computational Chemistry **32**, 1456 (2011).

[304] F. Weigend and R. Ahlrichs, Physical Chemistry Chemical Physics **7**, 3297 (2005).

[305] P. J. Stephens, F. J. Devlin, C. F. Chabalowski, and M. J. Frisch, The Journal of physical chemistry **98**, 11623 (1994).

[306] S.-L. J. Lahey, T. N. Thien Phuc, and C. N. Rowley, Journal of Chemical Information and Modeling **60**, 6258 (2020).

[307] C. Bannwarth, S. Ehlert, and S. Grimme, Journal of Chemical Theory and Computation **15**, 1652 (2019).

[308] J.-L. Reymond, R. van Deursen, L. C. Blum, and L. Ruddigkeit, MedChemComm **1**, 30 (2010).

[309] L. Ruddigkeit, R. van Deursen, L. C. Blum, and J.-L. Reymond, Journal of Chemical Information and Modeling **52**, 2864 (2012).

[310] R. Gómez-Bombarelli, J. Aguilera-Iparraguirre, T. D. Hirzel, D. Duvenaud, D. Maclaurin, M. A. Blood-Forsythe, H. S. Chae, M. Einzinger, D.-G. Ha, T. Wu, G. Markopoulos, S. Jeon, H. Kang, H. Miyazaki, M. Numata, S. Kim, W. Huang, S. I. Hong, M. Baldo, R. P. Adams, and A. Aspuru-Guzik, Nature Materials **15**, 1120 (2016).

[311] S. Curtarolo, G. L. W. Hart, M. B. Nardelli, N. Mingo, S. Sanvito, and O. Levy, Nature Materials **12**, 191 (2013).

[312] W. Nie, Q. Wan, J. Sun, M. Chen, M. Gao, and S. Chen, Nature Communications **14**, 6671 (2023).

[313] A. R. Oganov, C. J. Pickard, Q. Zhu, and R. J. Needs, Nature Reviews Materials **4**, 331 (2019).

[314] G. K. Pierens, Journal of Computational Chemistry **35**, 1388 (2014).

[315] J. D. Hartman, R. A. Kudla, G. M. Day, L. J. Mueller, and G. J. O. Beran, Physical Chemistry Chemical Physics **18**, 21686 (2016).

[316] J. B. K. Büning and S. Grimme, Journal of Chemical Theory and Computation **19**, 3601 (2023).

[317] G. Lauro, P. Das, R. Riccio, D. S. Reddy, and G. Bifulco, The Journal of Organic Chemistry **85**, 3297–3306 (2020).

[318] K. Hansen, F. Biegler, R. Ramakrishnan, W. Pronobis, O. A. Von Lilienfeld, K.-R. Muller, and A. Tkatchenko, The Journal of Physical Chemistry Letters **6**, 2326 (2015).

[319] J. A. Keith, V. Vassilev-Galindo, B. Cheng, S. Chmiela, M. Gastegger, K.-R. Müller, and A. Tkatchenko, Chemical Reviews **121**, 9816 (2021).

[320] P. Reiser, M. Neubert, A. Eberhard, L. Torresi, C. Zhou, C. Shao, H. Metni, C. van Hoesel, H. Schopmans, T. Sommer, *et al.*, Communications Materials **3**, 93 (2022).

[321] Z. Liu, L. Lin, Q. Jia, Z. Cheng, Y. Jiang, Y. Guo, and J. Ma, Journal of Chemical Information and Modeling **61**, 1066–1082 (2021).

[322] P. Gao, J. Zhang, Q. Peng, J. Zhang, and V.-A. Glezakou, Journal of Chemical Information and Modeling **60**, 3746 (2020).

[323] S. J. Y. Macalino, V. Gosu, S. Hong, and S. Choi, Archives of Pharmacal Research **38**, 1686 (2015).

[324] W. Gerrard, L. A. Bratholm, M. J. Packer, A. J. Mulholland, D. R. Glowacki, and C. P. Butts, Chemical Science **11**, 508 (2020).

[325] A. P. Bartók, R. Kondor, and G. Csányi, Physical Review B **87**, 184115 (2013).

[326] F. Musil, A. Grisafi, A. P. Bartók, C. Ortner, G. Csányi, and M. Ceriotti, Chemical Reviews **121**, 9759 (2021).

[327] D. Khan, S. Heinen, and O. A. von Lilienfeld, The Journal of Chemical Physics **159**, 034106 (2023).

[328] K. J. Kohlhoff, P. Robustelli, A. Cavalli, X. Salvatella, and M. Vendruscolo, Journal of the American Chemical Society **131**, 13894 (2009).

[329] Y. Guan, S. V. S. Sowndarya, L. C. Gallegos, P. C. S. John, and R. S. Paton, Chemical Science **12**, 12012 (2021).

[330] S. Liu, J. Li, K. C. Bennett, B. Ganoe, T. Stauch, M. Head-Gordon, A. Hexemer, D. Ushizima, and T. Head-Gordon, The Journal of Physical Chemistry Letters **10**, 4558 (2019).

[331] H. Han and S. Choi, The Journal of Physical Chemistry Letters **12**, 3662 (2021).

[332] Y. Kwon, D. Lee, Y.-S. Choi, M. Kang, and S. Kang, Journal of Chemical Information and Modeling **60**, 2024 (2020).

[333] E. Jonas and S. Kuhn, Journal of Cheminformatics **11**, 1 (2019).

[334] Y.-L. Liao and T. Smidt, arXiv preprint arXiv:2206.11990 (2023).

[335] Y.-L. Liao, B. Wood, A. Das, and T. Smidt, arXiv preprint arXiv:2306.12059 (2023).

[336] K. Xu, W. Hu, J. Leskovec, and S. Jegelka, arXiv preprint arXiv:1810.00826 (2018).

[337] H. Stärk, D. Beaini, G. Corso, P. Tossou, C. Dallago, S. Günnemann, and P. Liò, in *International Conference on Machine Learning* (PMLR, 2022) pp. 20479–20502.

[338] D. Jiang, Z. Wu, C.-Y. Hsieh, G. Chen, B. Liao, Z. Wang, C. Shen, D. Cao, J. Wu, and T. Hou, Journal of Cheminformatics **13**, 1 (2021).

[339] S. Kang, Y. Kwon, D. Lee, and Y.-S. Choi, Journal of Chemical Information and Modeling **60**, 3765–3769 (2020).

[340] J. Riebesell, R. E. Goodall, A. Jain, P. Benner, K. A. Persson, and A. A. Lee, arXiv preprint arXiv:2308.14920 (2023).

[341] J. Han, H. Kang, S. Kang, Y. Kwon, D. Lee, and Y.-S. Choi, Physical Chemistry Chemical Physics **24**, 26870 (2022).

[342] N. Grimblat, M. M. Zanardi, and A. M. Sarotti, The Journal of Organic Chemistry **80**, 12526 (2015).

[343] V. A. Semenov and L. B. Krivdin, Magnetic Resonance in Chemistry **58**, 56 (2020).

[344] T. Schaefer, J. Peeling, and G. H. Penner, Canadian journal of chemistry **64**, 2162 (1986).

[345] H. Fukaya and T. Ono, Journal of Computational Chemistry **25**, 51 (2004).

[346] H. Chen, S. Viel, F. Ziarelli, and L. Peng, Chemical Society Reviews **42**, 7971 (2013).

[347] J.-X. Yu, R. R. Hallac, S. Chiguru, and R. P. Mason, Progress in nuclear magnetic resonance spectroscopy **70**, 25 (2013).

[348] W. Gerrard, C. Yiu, and C. P. Butts, Magnetic Resonance in Chemistry **60**, 1087 (2022).

[349] L. B. Krivdin, Magnetic Resonance in Chemistry **61**, 507 (2023).

[350] K. Matsuzaki, S. Hayashi, and W. Nakanishi, RSC Advances **14**, 14340 (2024).

[351] T. Xie, X. Fu, O.-E. Ganea, R. Barzilay, and T. Jaakkola, arXiv preprint arXiv:2110.06197 (2021).

[352] L. Wu, C. Gong, X. Liu, M. Ye, and Q. Liu, Advances in Neural Information Processing Systems **35**, 36533 (2022).

[353] S. Zaidi, M. Schaarschmidt, J. Martens, H. Kim, Y. W. Teh, A. Sanchez-Gonzalez, P. Battaglia, R. Pascanu, and J. Godwin, arXiv preprint arXiv:2206.00133 (2022).

[354] S. Jia, A. R. Parthasarathy, R. Feng, G. Cong, C. Zhang, and V. Fung, Digital Discovery (2024).

[355] R. Elijošius, F. Zills, I. Batatia, S. W. Norwood, D. P. Kovács, C. Holm, and G. Csányi, arXiv preprint arXiv:2402.08708 (2024).

[356] F. Pedregosa, G. Varoquaux, A. Gramfort, V. Michel, B. Thirion, O. Grisel, M. Blondel, P. Prettenhofer, R. Weiss, V. Dubourg, J. Vanderplas, A. Passos, D. Cournapeau, M. Brucher, M. Perrot, and Édouard Duchesnay, Journal of Machine Learning Research **12**, 2825 (2011).

[357] T. Akiba, S. Sano, T. Yanase, T. Ohta, and M. Koyama, arXiv preprint arXiv:1907.10902 (2019).

[358] T. Kusumoto, K. Mitarai, K. Fujii, M. Kitagawa, and M. Negoro, npj Quantum Information **7**, 94 (2021).

[359] T. Haug, C. N. Self, and M. S. Kim, Machine Learning: Science and Technology **4**, 015005 (2023).

[360] T. Haug and M. Kim, Physical Review A **106**, 052611 (2022).

[361] M. Benedetti, E. Lloyd, S. Sack, and M. Fiorentini, Quantum Science and Technology **4**, 043001 (2019).

[362] `https://github.com/Qulacs-Osaka/scikit-qulacs`.

[363] A. S. Christensen, L. A. Bratholm, F. A. Faber, B. Huang, A. Tkatchenko, K. R. Müller, and O. A. von Lilienfeld, Qml: A python toolkit for quantum machine learning, `https://github.com/qmlcode/qml` (2017).

[364] N. Lopanitsyna, G. Fraux, M. A. Springer, S. De, and M. Ceriotti, Physical Review Materials **7**, 045802 (2023).

[365] M. J. Willatt, F. Musil, and M. Ceriotti, Physical Chemistry Chemical Physics **20**, 29661 (2018).

[366] S. Li, Y. Liu, D. Chen, Y. Jiang, Z. Nie, and F. Pan, Wiley Interdisciplinary Reviews: Computational Molecular Science **12**, e1558 (2022).

[367] D. Xin, C. A. Sader, U. Fischer, K. Wagner, P.-J. Jones, M. Xing, K. R. Fandrick, and N. C. Gonnella, Organic & Biomolecular Chemistry **15**, 928–936 (2017).

[368] C. Puzzarini, G. Cazzoli, M. E. Harding, J. Vázquez, and J. Gauss, The Journal of Chemical Physics **131**, 234304 (2009).

[369] R. E. Wasylishen and D. L. Bryce, The Journal of Chemical Physics **117**, 10061–10066 (2002).

[370] C. P. Rosenau, B. J. Jelier, A. D. Gossert, and A. Togni, Angewandte Chemie International Edition **57**, 9528 (2018).

[371] C. Adamo and V. Barone, The Journal of Chemical Physics **108**, 664 (1998).

[372] M. Rupp, A. Tkatchenko, K.-R. Müller, and O. A. Von Lilienfeld, Physical Review Letters **108**, 058301 (2012).

[373] A. M. El-Samman, S. De Castro, B. Morton, and S. De Baerdemacker, Canadian Journal of Chemistry (2023).

[374] B. Cantor, I. Chang, P. Knight, and A. Vincent, Materials Science and Engineering: A **375**, 213 (2004).

[375] J.-W. Yeh, S.-K. Chen, S.-J. Lin, J.-Y. Gan, T.-S. Chin, T.-T. Shun, C.-H. Tsau, and S.-Y. Chang, Advanced Engineering Materials **6**, 299 (2004).

[376] E. J. Pickering and N. G. Jones, International Materials Reviews **61**, 183 (2016).

[377] E. P. George, D. Raabe, and R. O. Ritchie, Nature Reviews Materials **4**, 515 (2019).

[378] B. Cao, C. Wang, T. Yang, and C. Liu, Scripta Materialia **187**, 250 (2020).

[379] D. Wu, K. Kusada, T. Yamamoto, T. Toriyama, S. Matsumura, I. Gueye, O. Seo, J. Kim, S. Hiroi, O. Sakata, S. Kawaguchi, Y. Kubota, and H. Kitagawa, Chemical Science **11**, 12731 (2020).

[380] D. Wu, K. Kusada, T. Yamamoto, T. Toriyama, S. Matsumura, S. Kawaguchi, Y. Kubota, and H. Kitagawa, Journal of the American Chemical Society **142**, 13833 (2020).

[381] K. Kusada, D. Wu, and H. Kitagawa, Chemistry – A European Journal **26**, 5105 (2020).

[382] D. Wu, K. Kusada, Y. Nanba, M. Koyama, T. Yamamoto, T. Toriyama, S. Matsumura, O. Seo, I. Gueye, J. Kim, *et al.*, Journal of the American Chemical Society **144**, 3365 (2022).

[383] T. A. Batchelor, J. K. Pedersen, S. H. Winther, I. E. Castelli, K. W. Jacobsen, and J. Rossmeisl, Joule **3**, 834 (2019).

[384] J. K. Pedersen, T. A. Batchelor, A. Bagger, and J. Rossmeisl, ACS catalysis **10**, 2169 (2020).

[385] H. S. Oh, S. J. Kim, K. Odbadrakh, W. H. Ryu, K. N. Yoon, S. Mu, F. Körmann, Y. Ikeda, C. C. Tasan, D. Raabe, *et al.*, Nature Communications **10**, 2090 (2019).

[386] W. Huo, S. Wang, F. J. Dominguez-Gutierrez, K. Ren, Ł. Kurpaska, F. Fang, S. Papanikolaou, H. S. Kim, and J. Jiang, Materials Research Letters **11**, 713 (2023).

[387] N. Mardirossian and M. Head-Gordon, Molecular Physics **115**, 2315 (2017).

[388] W. A. Saidi, npj Computational Materials **8**, 86 (2022).

[389] J. McClain, Q. Sun, G. K.-L. Chan, and T. C. Berkelbach, Journal of Chemical Theory and Computation **13**, 1209 (2017).

[390] I. Y. Zhang and A. Grüneis, Frontiers in Materials **6**, 123 (2019).

[391] I. Shavitt and R. J. Bartlett, *Many-body methods in chemistry and physics: MBPT and coupled-cluster theory* (Cambridge university press, 2009).

[392] A. J. Medford, A. Vojvodic, J. S. Hummelshøj, J. Voss, F. Abild-Pedersen, F. Studt, T. Bligaard, A. Nilsson, and J. K. Nørskov, Journal of Catalysis **328**, 36 (2015).

[393] J. Behler, International Journal of Quantum Chemistry **115**, 1032 (2015).

[394] J. S. Smith, O. Isayev, and A. E. Roitberg, Chemical Science **8**, 3192 (2017).

[395] K. Lee, D. Yoo, W. Jeong, and S. Han, Computer Physics Communications **242**, 95 (2019).

[396] K. T. Schütt, H. E. Sauceda, P.-J. Kindermans, A. Tkatchenko, and K.-R. Müller, The Journal of Chemical Physics **148**, 241722 (2018).

[397] C. L. Zitnick, A. Das, A. Kolluru, J. Lan, M. Shuaibi, A. Sriram, Z. Ulissi, and B. Wood, arXiv preprint arXiv:2206.14331 (2022).

[398] C. M. Clausen, J. Rossmeisl, and Z. W. Ulissi, The Journal of Physical Chemistry C **128**, 11190 (2024).

[399] F. Calle-Vallejo, J. Tymoczko, V. Colic, Q. H. Vu, M. D. Pohl, K. Morgenstern, D. Loffreda, P. Sautet, W. Schuhmann, and A. S. Bandarenka, Science **350**, 185 (2015).

[400] J. Dean, M. G. Taylor, and G. Mpourmpakis, Science Advances **5**, eaax5101 (2019).

[401] Y. Nanba and M. Koyama, ACS Omega **6**, 3218 (2021).

[402] Z. Lu, Z. W. Chen, and C. V. Singh, Matter **3**, 1318 (2020).

[403] Z. Yang and W. Gao, Advanced Science **9**, 2106043 (2022).

[404] M. Tamtaji, S. Chen, Z. Hu, W. A. G. III, and G. Chen, The Journal of Physical Chemistry C (2023).

[405] D. Roy, S. C. Mandal, and B. Pathak, ACS Applied Materials & Interfaces **13**, 56151 (2021).

[406] D. Roy, S. Charan Mandal, A. Das, and B. Pathak, Chemistry–A European Journal **30**, e202302679 (2024).

[407] M. P. Salinas-Quezada, J. K. Pedersen, P. Sebastián-Pascual, I. Chorkendorff, K. Biswas, J. Rossmeisl, and M. Escudero-Escribano, Ees Catalysis (2024).

[408] H. Nakai, Chemical Physics Letters **363**, 73 (2002).

[409] Y. Kikuchi, Y. Imamura, and H. Nakai, International Journal of Quantum Chemistry **109**, 2464 (2009).

[410] M. Yu, D. R. Trinkle, and R. M. Martin, Physical Review B **83**, 115113 (2011).

[411] Y. Huang, J. Kang, W. A. Goddard, and L.-W. Wang, Physical Review B **99**, 064103 (2019).

[412] J. J. Eriksen, The Journal of Chemical Physics **153**, 214109 (2020).

[413] D. Yoo, K. Lee, W. Jeong, D. Lee, S. Watanabe, and S. Han, Physical Review Materials **3**, 093802 (2019).

[414] Z. El-Machachi, M. Wilson, and V. L. Deringer, Chemical Science **13**, 13720 (2022).

[415] J. D. Morrow, C. Ugwumadu, D. A. Drabold, S. R. Elliott, A. L. Goodwin, and V. L. Deringer, Angewandte Chemie , e202403842 (2024).

[416] W. Jeong, D. Yoo, K. Lee, J. Jung, and S. Han, The Journal of Physical Chemistry Letters **11**, 6090 (2020).

[417] S. Watanabe, W. Li, W. Jeong, D. Lee, K. Shimizu, E. Mimanitani, Y. Ando, and S. Han, Journal of Physics: Energy **3**, 012003 (2020).

[418] H. A. Doan, C. Li, L. Ward, M. Zhou, L. A. Curtiss, and R. S. Assary, Digital Discovery **2**, 59 (2023).

[419] S. Chong, F. Grasselli, C. Ben Mahmoud, J. D. Morrow, V. L. Deringer, and M. Ceriotti, Journal of Chemical Theory and Computation **19**, 8020 (2023).

[420] F. Ø. Kjeldal and J. J. Eriksen, Journal of Chemical Theory and Computation **19**, 2029 (2023).

[421] M. Meuwly, Chemical Reviews **121**, 10218 (2021).

[422] M. Wen, E. W. C. Spotte-Smith, S. M. Blau, M. J. McDermott, A. S. Krishnapriyan, and K. A. Persson, Nature Computational Science **3**, 12 (2023).

[423] P. Singh, A. V. Smirnov, and D. D. Johnson, Physical Review B **91**, 224204 (2015).

[424] Z. Sun, C. Shi, C. Liu, H. Shi, and J. Zhou, Materials & Design **223**, 111214 (2022).

[425] K. Sheriff, Y. Cao, T. Smidt, and R. Freitas, Proceedings of the National Academy of Sciences **121**, e2322962121 (2024).

[426] K. Sheriff, Y. Cao, and R. Freitas, npj Computational Materials **10**, 215 (2024).

[427] K. Nomura, S. Hattori, S. Ohmura, I. Kanemasu, K. Shimamura, N. Dasgupta, A. Nakano, R. K. Kalia, and P. Vashishta, The Journal of Physical Chemistry Letters **16**, 6637 (2025).

[428] Ž. Ivković, J. Jover, and J. Harvey, Digital Discovery **3**, 2242 (2024).

[429] S. Maheshwary, N. Patel, N. Sathyamurthy, A. D. Kulkarni, and S. R. Gadre, The Journal of Physical Chemistry A **105**, 10525 (2001).

[430] A. Rakshit, P. Bandyopadhyay, J. P. Heindel, and S. S. Xantheas, The Journal of Chemical Physics **151** (2019).

[431] S. Goedecker, M. Teter, and J. Hutter, Physical Review B **54**, 1703 (1996).

[432] R. Salomon-Ferrer, D. A. Case, and R. C. Walker, Wiley Interdisciplinary Reviews: Computational Molecular Science **3**, 198 (2013).

[433] F. Paesani, W. Zhang, D. A. Case, T. E. Cheatham, and G. A. Voth, The Journal of Chemical Physics **125** (2006).

[434] S. B. Healy, C. Filippi, P. Kratzer, E. Penev, and M. Scheffler, Physical Review Letters **87**, 016105 (2001).

[435] H. Kim, J. Y. Park, and S. Choi, Scientific Data **6**, 109 (2019).

[436] Y. Guo, C. Riplinger, U. Becker, D. G. Liakos, Y. Minenkov, L. Cavallo, and F. Neese, The Journal of Chemical Physics **148** (2018).

[437] A. H. Larsen, J. J. Mortensen, J. Blomqvist, I. E. Castelli, R. Christensen, M. Dułak, J. Friis, M. N. Groves, B. Hammer, C. Hargus, E. D. Hermes, P. C. Jennings, P. B. Jensen, J. Kermode, J. R. Kitchin, E. L. Kolsbjerg, J. Kubal, K. Kaasbjerg, S. Lysgaard, J. B. Maronsson, T. Maxson, T. Olsen, L. Pastewka, A. Peterson, C. Rostgaard, J. Schiøtz, O. Schütt, M. Strange, K. S. Thygesen, T. Vegge, L. Vilhelmsen, M. Walter, Z. Zeng, and K. W. Jacobsen, Journal of Physics: Condensed Matter **29**, 273002 (2017).

[438] Y. Qiu, D. G. Smith, C. D. Stern, M. Feng, H. Jang, and L.-P. Wang, The Journal of Chemical Physics **152** (2020).

[439] S. P. Ong, W. D. Richards, A. Jain, G. Hautier, M. Kocher, S. Cholia, D. Gunter, V. L. Chevrier, K. A. Persson, and G. Ceder, Computational Materials Science **68**, 314 (2013).

[440] M. J. Abraham, T. Murtola, R. Schulz, S. Páll, J. C. Smith, B. Hess, and E. Lindahl, SoftwareX **1**, 19 (2015).

[441] W. L. Jorgensen, J. Chandrasekhar, J. D. Madura, R. W. Impey, and M. L. Klein, The Journal of Chemical Physics **79**, 926 (1983).

[442] J. L. Abascal and C. Vega, The Journal of Chemical Physics **123** (2005).

[443] J. V. Valle, B. H. Mendonça, M. C. Barbosa, H. Chacham, and E. E. de Moraes, The Journal of Physical Chemistry B **128**, 1091 (2024).

[444] P. Eastman, R. Galvelis, R. P. Peláez, C. R. Abreu, S. E. Farr, E. Gallicchio, A. Gorenko, M. M. Henry, F. Hu, J. Huang, *et al.*, The Journal of Physical Chemistry B **128**, 109 (2023).

[445] S. R. Bahn and K. W. Jacobsen, Computing in Science & Engineering **4**, 56 (2002).

[446] K. Kusada, H. Kobayashi, T. Yamamoto, S. Matsumura, S. Naoya, K. Sato, K. Nagaoka, Y. Kubota, and H. Kitagawa, Journal of the American Chemical Society **135**, 5493 (2013).

[447] G. Kresse and J. Hafner, Physical Review B **48**, 13115 (1993).

[448] P. E. Blöchl, Physical Review B **50**, 17953 (1994).

[449] G. Kresse and D. Joubert, Physical Review B **59**, 1758 (1999).

Acknowledgments

First and foremost, I would like to express my heartfelt gratitude to my academic advisor, Professor Keisuke Fujii of Graduate School of Engineering Science at the University of Osaka, and to Professor Wataru Mizukami of Center for Quantum Information and Quantum Biology at the University of Osaka, for providing an optimal environment and education for my research. In particular, Professor Mizukami offered invaluable advice and guidance as I began my research at the University of Osaka—a new environment different from my master's program—through research activities and collaborative projects at the center. I can only imagine the great patience this required, and I wish to express my deep appreciation for his enduring support. I am also deeply grateful to Dr. Yuichiro Yoshida, Dr. Tuan Minh Do, and Dr. Luca Erhart of the same center for their valuable advice in my daily research activities.

I extend my sincere thanks to Mr. Toshio Mori of the Center for Quantum Information and Quantum Biology at the University of Osaka for providing extensive technical support and learning opportunities through the operation of on-premises cluster machines and collaborative research. I am also deeply appreciative of my collaborator, Mr. Kenji Ishihara for the engaging discussions and shared enjoyment in our research endeavors. The members of our laboratory, with their diverse specialties in quantum information, condensed matter physics, chemistry, and machine learning, have greatly enriched my learning through reading circles and seminars we have conducted together for over a year. Lastly, I would like to express my deepest appreciation to my family for their unwavering support throughout my life.

List of Publications

Main Publications

1. T. Shiota, K. Gunst, T. Mori, T. Shiozaki and W. Mizukami, "Integrating Classical and Quantum Software for Enhanced Simulation of Realistic Chemical Systems", arXiv:2506.18877 (2025).

2. T. Shiota, K. Ishihara and W. Mizukami, "Universal neural network potentials as descriptors: towards scalable chemical property prediction using quantum and classical computers", Digital Discovery **3**, 1714-1728 (2024).

3. T. Shiota, K. Ishihara and W. Mizukami, "Lowering the exponential wall: accelerating high-entropy alloy catalysts screening using local surface energy descriptors from neural network potentials", Digital Discovery, **4**, 738-751 (2025).

4. T. Shiota, K. Ishihara, T. M. Do, T. Mori and W. Mizukami, "Taming Multi-Domain,-Fidelity Data: Towards Foundation Models for Atomistic Scale Simulations.", arXiv:2412.13088 (2024).

Other Publications

5. T. Shiota, W. Mizukami, H. Tochihara, K. Yagyu, T. Suzuki and Y. Aoki, "Microscopic Hopping Mechanism of an Isolated PTCDA Molecule on a Reactive Ge(001) Surface", The Journal of Physical Chemistry C, **124**, 45, 24704-24712 (2020).

6. T. M. Do, T. Shiota, W. Mizukami, "Optimizing adsorption configurations on alloy surfaces using Tensor Train Optimizer", arXiv:2507.20827 (2025).